ABSTRACT

Title of Dissertation:	STRUCTURAL EVOLUTION DURING THERMAL TREATMENTS AND THE RESULTANT MECHANICAL BEHAVIOR OF HIGH STRENGTH LOW ALLOY STEELS
	Matthew C. Draper, Doctor of Philosophy, 2018
Dissertation directed by:	Professor Sreeramamurthy Ankem Department of Materials Science and Engineering

HY steels were designed as a solid solution strengthened grade for both high yield strength and high impact toughness in structural applications for Naval vessels. These alloys are susceptible to both hydrogen and temper embrittlement which necessitates high expense manufacturing processes to preclude these conditions. Successful implementation of lower cost and higher reliability treatments requires an improved understanding of the structural evolution and corresponding changes in mechanical behavior for the alloy. This research combines mechanical and microstructural characterization methods along with thermodynamic and kinetic models to build a comprehensive understanding of the effects of thermal treatments on the structure-property relationship of the alloy system.

The embrittlement rate was studied between 315°C and 565°C at varied logarithmic time intervals up to 40,000 minutes. The embrittlement recovery rate was studied between 593°C and 704°C at logarithmic time intervals up to 10,000 minutes.

Finally, hydrogen aging was studied between 315°C and 565°C at varied thermodynamically equivalent time intervals. A variety of test methods were employed for characterization including: traditional metallographic techniques, mechanical testing, computational modeling, and a novel image analysis technique for carbide analysis.

Metallographic along with computational work supports a conclusion that temper embrittlement and subsequent recovery cannot be solely explained by the segregation of phosphorus and other embrittling elements to grain boundaries. Rather it is shown for the first time that alloy carbides play a key role in embrittlement for this system. The evolution of these carbides serves both to create initiation sites for cleavage fracture and deplete the matrix of Mo, which is a P scavenger. Recovery from embrittlement is thus proposed to be related to both the removal of P from the boundary and the dissolution of carbides. From these results a series of kinetic models have been developed for the nucleation, dissolution, and coarsening of alloy carbides.

Models developed for the mitigation of monatomic hydrogen show a novel treatment for hydrogen aging via performing the aging within the embrittlement range with follow on treatments designed to recover from embrittlement. This new treatment has the potential to reduce hydrogen aging times by up to 90% in industrial manufacture.

STRUCTURAL EVOLUTION DURING THERMAL TREATMENTS AND THE RESULTANT MECHANICAL BEHAVIOR OF HIGH STRENGTH LOW ALLOY STEELS

By

Matthew C. Draper

Dissertation submitted to the Faculty of the Graduate School of the
University of Maryland, College Park, in partial fulfillment
of the requirements for the degree of
Doctor of Philosophy
2018

Advisory Committee:
Professor Sreeramamurthy Ankem, Chair; University of Maryland
Professor Hugh Bruck; University of Maryland
Professor Mohamad Al-Sheikhly; University of Maryland
Professor Aristos Christou; University of Maryland
Dr. Rachel Abrahams; Air Force Research Lab – Eglin AFB

Preface

A thesis is not the end but a beginning, and while this document may be the culmination of an expansive body of work, the true purpose of this dissertation is to lay the foundation for the continued study of embrittlement and recovery mechanisms, alternative manufacturing processes, and target chemical compositions for the HY and other similar alloy systems.

The present doctoral thesis summarizes the work I have done during my nearly 8 years of study as a part time Ph.D. student in the Department of Materials Science and Engineering at the University of Maryland, College Park. During this time more than 10 tons of steel have been produced and 800 mechanical specimens have been tested to characterize the varied thermodynamic and kinetic relationships to mechanical performance in the HY alloy system. The initial work was supported by the Naval Surface Research Program - Contract no. SCRA 2015-444. The Air Force Research Laboratory, The Army Research Laboratory, The Naval Surface Warfare Center – Carderock, Scot Forge, Bradken Tacoma, Sheffield Forgemasters, and Goodwin Steel Castings provided the material, equipment, and resources necessary to conduct the experiments and obtain material response results. Without the support of numerous individuals at these institutions completion of this work would not have been possible.

It is noted that the source for each specific lot of material, while coming from one of the four manufacturer's qualified to produce HY alloys above, is not detailed here-in as to not infer an incorrect relationship between chemical composition, manufacturing parameters, heat treatments, and a given manufacture's processes and

procedures. For experimental heats, the manufacturers were requested to follow explicit experimental procedures for the purposes of this study, including procedures not currently permitted by specification. Thus, the reader is cautioned to avoid attempting to determine the source of given heat as the work described here-in was for the purposes of fundamental research and thus may lead one to draw erroneous conclusions on a manufacturer's standard practice. To retain this blind association with parent manufacturer, the heat numbers used in this text have been modified to simply be #A - #D for heats explicitly used for experimental study and, #1 - #8 when industrially processed material was selected for further study or follow on heat treatment.

It is also noted that in the early portions of this work the author studied hydrogen movement via dislocations. This work was ultimately inconclusive showing that some hydrogen transport may be accomplished by dislocation motion, but not to a degree usable in industrial applications. The results of this work are not documented herein due to their inconclusive nature and the discovery of an ultimately successful treatment for mitigation of monatomic hydrogen via thermal diffusion mechanisms.

Finally, it is noted that this work was done primarily in support of US based industrial research, and thus the temperatures selected were based on degrees F. Thus, the strong majority of temperatures selected for aging and other heat treatments do not appear as round numbers when presented in degrees C.

Portions of the contents of this work have been presented at the following conferences and in the following publications throughout my time as a student. (* Denotes publication in proceedings)

- 2013 Steel Founders Society of America Technical and Operations Conference*
    - "Control of Monatomic Hydrogen"
- 2015 Naval Shipbuilding Research Program Ship Tech Conference
- 2015 Steel Founders Society of America Technical and Operations Conference*
- 2016 Quadrennial International Hydrogen Conference
- 2016 Materials Science and Technology Conference*
    - "Hydrogen Embrittlement Mitigation Techniques in High Strength Steel Manufacture"
- 2016 Defense Manufacturing Conference
- 2016 Steel Founders Society of America Technical and Operations Conference*
    - "Control of Monatomic Hydrogen in High Strength Steels"
- 2017 Triennial International Forgemaster's Meeting*
    - "Hydrogen Embrittlement Mitigation Techniques in High Strength Steel Manufacture"
- 2017 Steel Founders Society of America Technical and Operations Conference*
    - "Mechanisms of Temper Embrittlement and Recovery in Cast HY-80"
- Journal of Material Science (2018) Accepted for Publication
    - "Mechanisms of Temper Embrittlement and Recovery in Cast HY-80 High Strength Low Alloy Steel" (JMSC-D-18-06712)
- 2018 Steel Founders Society of America Technical and Operations Conference*
    - "Thermodynamic and Kinetic Models of the HY alloy system"

Dedication

To those who have inspired me:

George H. Baker (US Navy)

1926-2015

Spencer T. Draper (US Marine Corps)

1994-2017

Acknowledgements

I express sincere gratitude to my many colleagues in industry and academia, my friends, and family, whom have given me support and guidance over the years of this work.

To my thesis advisor, Professor Ankem for his continued confidence in me, guidance, and persistence over the length of this work.

To the entire team at Bradken Tacoma for their work on this project under the Naval Shipbuilding Research Program to manufacture specialty steel samples.

To Kyle Rackers and Patrick Nowak of Scot Forge and Professor's Gregory Olson and Kathleen Stair at Northwestern University for my true training as ferrous metallurgist.

To Jeff Kruger and John Cain of Scot Forge for their continued support of my work, mentorship, and donation of laboratory time and forging resources.

To Neil Fichtelberg of the Electric Boat Corporation for all that he taught me on metallurgical principles, experimental design, and knowing to ask "how do you know?" at every corner.

To Jeff Elinski of Inducto Heat for donation of his time and laboratory space for induction treatment trials.

To Steven Roberts and Bernard Goodwin of Goodwin Steel Castings for the donation of material and time in addition to work on experimental design parameters.

To Rachel Abrahams and Richard Harris of the Airforce Research Laboratory for their donation of laboratory time and their assistance with metallographic characterization.

To the team at the Steel Founders Society of America (SFSA) for providing me an annual forum at the technical and operation conference to present and receive critical review and comments during the progression of this work.

To Billy Hornbuckle at the Army Research Lab for his help with specimen preparation and imaging of TEM foils.

To Sam Schwarm of the University of Maryland for his continued assistance with varied experiments over the last 4 years and his insight on mechanisms and characterization techniques.

To Shiv Patel of the University of Maryland for his assistance with developing statistical models for analysis of tensile data, selection of appropriate data transformations, and examination of fracture surfaces.

To Richard Gins of the University of Maryland for his assistance with developing tools and procedures for the measurement of carbide parameters.

To my partners in crime, Shelby Frasier, Jeffery Mann, and Erica Rozzero, for their continued support for my crazy ideas, for many late night discussions, debates during transatlantic flights, and for supporting me during my long road to this degree over many years of friendship, plotting, and world travels. They are truly the best friends anyone could ever ask for.

To my mother, Kathleen Draper; my father, Mark Draper Sr.; and my grandparents, George and Ione Baker, all of whom have encouraged me to continue my pursuit of higher education throughout my entire life.

To my sister Julia Draper and my mother for putting up with the varied experiments, sometimes explosive, on the back porch through our childhood.

And finally, to my wife Alison Keeley for always believing in me and supporting me even when the next steps seemed impossible to overcome, and for all of her personal sacrifice for me while I have worked on this degree.

Table of Contents

List of Tables

List of Figures

Chapter 1: Introduction

Within the field of metallurgy, it is generally accepted that hydrogen is only a contributor to failure when in its monatomic form. Thus, an important measurement in determining whether hydrogen damage is present in a material is a measure of diffusible (mobile) hydrogen. This measurement cannot currently be conducted either quickly enough or reliably enough to be used during industrial steel manufacturing. Moreover, unlike most precursors to mechanical failure, hydrogen embrittlement cannot be detected by any type of industrial nondestructive evaluation. Further complicating this issue, hydrogen assisted cracking is typically "one dimensional" and non-surface breaking such that ultrasonic, radiographic, and magnetic particle inspections are unable to reliably detect any cracks. Therefore, hydrogen damage must be precluded from engineering components.

High strength steel alloys require a monatomic hydrogen removal treatment to mitigate the occurrence of hydrogen assisted cracking. A representative treatment for hydrogen mitigation in HY-80 steel is one performed at 301°C (575°F) for 450 hours for 28 cm (11") thick HY-80 castings or 176°C (350°F) for 24 hours per each 3 cm in thickness for HY-80 submerged arc welding. The facility demands associated with these long soaking cycles in addition to the high cost of the operations necessitate an alternate, more cost-effective method for removal or neutralization of monatomic hydrogen. Furthermore, these aging treatments have been shown to be ineffective when material conditions occur outside the bounds of control samples used to calculate treatment requirements, requiring expensive removal and rework when discovered in service. Consequently, continuing study of hydrogen transport is required across many

industries to support further innovations in the development of ultra high yield materials where hydrogen limits ductility, particularly for blast resistant steel alloys.

The development of alternate treatments for current and new alloy systems is limited by the need to preclude the harmful effects of temper embrittlement. Processing controls to prevent temper embrittlement in industry are simply to avoid time in the embrittlement range. This is accomplished via furnace holds just below the temper embrittlement range for a number of hours to allow parts to thermally soak through thickness followed by a fast ramp through the embrittlement range. In addition, a fast transfer from furnace to quench tank with a highly aggressive quench for austenitization and tempering cycles also assists to limit time in the temper embrittlement zone. Current literature lacks clarity for a manufacturer in determining at what point embrittlement causes a significant loss in ductility. To create sound manufacturing processes for alloys sensitive to temper embrittlement, it is necessary to have a greater understanding of the kinetics of embrittlement mechanisms in the alloy system.

This work embarked on a study the HY alloy system with the principle objective to develop a new, more cost-effective treatment for hydrogen mitigation while precluding the onset of temper embrittlement via developing an understanding of embrittlement and recovery mechanisms. To accomplish this objective, fundamental studies have been executed to determine the hydrogen diffusion, temper embrittlement, and embrittlement recovery rates for the processing space below the AC1, along with a determination of temper embrittlement and hydrogen migration mechanisms for the HY system.

The specific goals of this work were as follows:

1. Provide an overview summary on the current understanding of hydrogen and temper embrittlement in steel alloys in order to have a meaningful discussion of past and on-going studies.
2. Carry out an experimental investigation into hydrogen aging on low and high carbon equivalent grades of HY-80 with varied parameters.
3. Carry out an experimental investigation of thermal embrittlement by thermally aging HY alloys between and 300°C and 600°C at times up to 10,000 minutes for mechanical characterization and up to 40,000 minutes for metallographic characterization.
4. Carry out an experimental investigation of embrittlement recovery by thermally aging HY samples between 593°C and 704°C at times up to 1,000 minutes for mechanical characterization and 36,000 minutes for metallographic characterization.
5. Carry out mechanical testing of all experimental samples at room temperature for tensile testing and at lower shelf temperatures for Charpy V-notch testing to measure the change in mechanical properties and note the deformation modes from the fracture surfaces.
6. Identify and characterize the fracture surfaces and microstructural evolution by characterization techniques at multiple length scales, including optical microscopy, Scanning Electron Microscopy (SEM), and Transmission Electron Microscopy (TEM).

7. Model the kinetics of carbide nucleation, coarsening, and dissolution where fracture can originate and propagate.
8. Develop and validate industrial scale parameters for new treatments for the HY alloy system based on the results provided by the mechanistic studies of hydrogen and temper embrittlement.

The structure of the thesis is as follows:

A thorough literature review and technical background is presented in Chapter 2. The characterization techniques employed and experimental procedures throughout the body of the work are detailed in Chapter 3. The analytical techniques including statistical data analysis techniques used to filter tensile ductility data are detailed in Chapter 4. Chapter 5 details the results of this work, approximately in chronological order as follows:

- Section 1 details the initial studies of alternate hydrogen soaking treatments that ultimately lead to the concept of performing hydrogen removal treatments in the embrittlement range with a subsequent subcritical recovery treatment.
- Section 2 details the extensive study of the rate of temper embrittlement and recovery for the alloy designed to study the processing space for the treatment developed in Chapter 5 in addition to carbide kinetics.
- Section 3 discusses optimization of the initial treatment developed in Section 1 based on the mechanistic understanding of embrittlement developed in Section 2. Additionally, full scale confirmation trials for the newly developed treatment at multiple industrial facilities are detailed.

- Section 4 details the results of CALPHAD analysis.
- Section 5 reviews both the bulk and microscale chemical composition.
- Section 6 discusses carbide aging and dissolution metallographic results.
- Section 7 reviews TEM analysis.
- Section 8 details the results of the analytical image analysis of carbides after aging.

Chapter 6 provides a discussion of the results and significant findings. Chapter 7 details the principle conclusions of this work in addition to detailing the recommended next steps.

Several appendices are also included as follows:

- Appendix A details the methods and results of statistical analysis of tensile ductility results
- Appendix B details the raw results of chemical composition measurements.
- Appendix C provides the direct output of Thermo-calc analysis showing the composition and volume fraction of predicted stable phases at varied treatment temperatures for the compositions studied.
- Appendix D provides the image analysis program used to determine carbide parameters from SEM images.

Figure 1 provides an overview of the study.

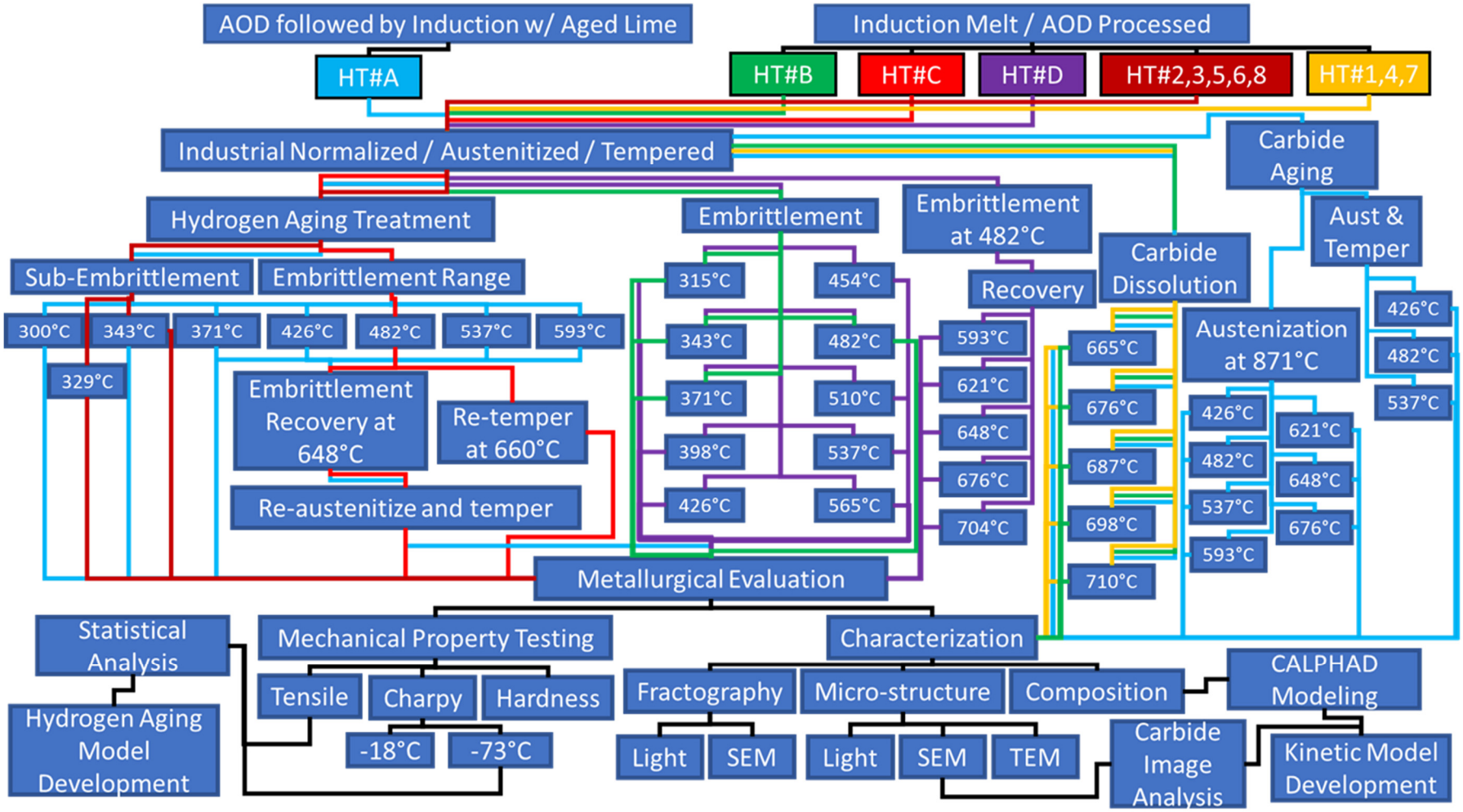

Figure 1: Overview of study. Colored tracer lines follow the varied experimental paths a given heat was used for. For most studies, samples were treated at logarithmically relevant times for each temperature listed.

Chapter 2: Background & Literature Review

In this chapter the fundamentals of hydrogen and temper embrittlement are discussed in context of their mechanistic impact on mechanical performance. Additionally, a review of the developmental work on the HY alloy series is provided. An overview of industrial arc melting, Argon Oxygen Decarburization (AOD) processing, and calcium wire injection is also provided. Finally, a review of kinetic principles relevant to this work is provided.

2.1 Hydrogen Transport and Failure Mechanisms

The causes of hydrogen embrittlement have been particularly elusive despite decades of extensive research by academia, government, and industry. Over the years, as many as 7 different models for hydrogen embrittlement mechanisms have been proposed, with many conflicting even qualitatively with one another at the most basic levels [1]. Still, to date there is little agreement on the exact mechanisms behind hydrogen embrittlement, the degree of contribution of the various mechanisms, and how hydrogen affects the mechanical properties of various alloy systems. While this review will attempt to define the failure mechanisms behind hydrogen related failures, it must be understood that in almost all cases, many of these proposed mechanisms are still aggressively debated with conflicting experimental observations.

What is clear from currently published work is that no single mechanism can describe either the motion of hydrogen throughout a steel lattice, or the reason monatomic hydrogen causes material failure. Thus far, two mechanisms have been empirically shown to operate in a continuous lattice: hydrogen enhanced localized

plasticity (HELP) [2]–[9] and hydrogen enhanced decohesion embrittlement (HEDE) [10]–[12]. In a discontinuous lattice (e.g., containing porosity, inclusions, etc.), an additional contribution to the fracture is detailed in the Zapffee and Sims Internal Pressure Model [13], though there is considerable debate as to whether this contributes to the fracture in any significant way in lower strength alloys. The formation of a brittle hydride phase has also been proposed as a possible failure mechanism [14] and is readily observable in several systems [15]–[18]. However, this has never been empirically shown to occur in iron based alloys. For this reason this mechanism will not be discussed. It should also be noted that although a number of other models have been proposed over the years with considerable debate, only those that have stood up to academic rigor are discussed herein.

2.1.1 Hydrogen Enhanced Localized Plasticity (HELP)

The basis of the HELP mechanism is that the presence of hydrogen in the lattice increases the ease of dislocation motion and/or generation [19]. This change in dislocation mobility drives a change in the microscopic failure mechanism of the material to that of shear localization [20]. Brittle fracture is traditionally characterized by a loss of macroscopic ductility, observed as a decrease in reduction of area and elongation in a tensile sample. However, high resolution fractography has shown that brittle fracture characteristics do not actually occur at the microscopic scale within hydrogen damaged material. In these cases, hydrogen damage is associated with locally enhanced plasticity at initiation sites [2].

Mechanical stresses can enhance the solubility of a diffusion species in the lattice and under an applied stress (possibly occurring below the yield stress of the bulk

matrix), the distribution of hydrogen in the lattice becomes highly non-uniform. Since dislocations are surrounded by a stress field, they can attract an appreciable number of dissolved atoms. This system is similar to the model of carbon diffusion to dislocations with the exception that as the mobility of hydrogen is higher than that of carbon, the dislocations in this case would not be locked in place by the diffusing atom, but rather the hydrogen will be locked to the dislocation. [4], [21] The consequences of this theory are that dislocations are now highly mobile rather than pinned [15], and that moving dislocations can drag monatomic hydrogen atoms along [22]. The exact mechanism behind the preference of hydrogen at the dislocation core, over larger elements such as carbon diffusing to the core, to conserve lattice strain energy, is not entirely understood; however, this effect has recently been empirically shown in the literature [23], [24].

The localized stress field around a dislocation has the capability to attract and entrap several monatomic hydrogen atoms forming a Cottrel atmosphere around the compression side of the dislocation core. [25], [26] With dislocations now mobile under a low applied stress, the normal dynamics of dislocation motion come into play, with dislocation pile-ups at impediments to dislocation motion, such as grain boundaries and discontinuities, under an applied load. [27], [28] The implications are that as dislocations move through the matrix, they pick up monatomic hydrogen atoms in the lattice while leaving alloying elements such as carbon behind as interstitials in the lattice. Finally, once the dislocations begin to pile-up, the majority of the hydrogen within the matrix that was not originally attracted to hydrogen-sinks, such as inclusions and shrinkage porosities, is no longer equally distributed, but preferentially lined up along dislocation pile-ups in the matrix and along grain boundaries. This creates a

condition where the HEDE mechanism can cause a failure of the material by localized plasticity. [29]

2.1.2 Hydrogen Enhanced Decohesion Embrittlement (HEDE)

The HEDE mechanism postulates embrittlement due to localized reduction in cohesive strength induced by the segregation of hydrogen to defects such as grain boundaries, microcracks, notches, and second phase particles, among others. In this case, embrittlement is directly attributable to a decrease in the strength of atomic bonding of the parent matrix in regions of hydrogen loading [30]. The mechanism only activates under conditions where hydrogen is not equally distributed in the lattice. [31], [32] Such a condition occurs readily in cast steels, as hydrogen is preferentially located at hydrogen sinks as described above.

The essential premise behind the HEDE mechanism is that hydrogen damage occurs at a crack tip when the local crack tip opening tensile stress exceeds the maximum-local atomic cohesion strength, which is lowered by the presence of hydrogen. The model postulates that hydrogen will concentrate at areas just ahead of a crack initiation site due to the influence of the localized stress field on hydrogen diffusion where tensile stresses are maximized [33]. The consensus throughout the literature is that the HEDE mechanism is the dominant mechanism for internal hydrogen assisted cracking in alloys where hydride phases do not form. More recent work has demonstrated that the HEDE contribution to crack tip advancement is the dominant mechanism in hydrogen loaded materials over the slip plane advancement process. [34]–[36]

Additionally, the HEDE mechanism can cause early yielding of material resulting in a loss of macroscopic ductility. [29] The local flow stress at hydrogen loaded areas is reduced, resulting in localized deformation along the grain boundaries and dislocation pile-ups at stresses far below the yield of the bulk matrix. [30] This localized early yielding causes failure by a ductile process at the microscopic level along the flow lines created between grains in the matrix, as the yield strength along the flow lines is decreased by the hydrogen decohesion, while the actual deformation of the parent matrix remains small. The net result is macroscopic brittle failure with the bulk matrix largely un-deformed. It should be noted that the mechanism describing how microscopic softening along dislocation lines leads to macro scale shear localization in the presence of hydrogen has not yet been fully determined, but the occurrence of this phenomenon has been demonstrated repeatedly. [39], [40]

2.1.3 Hydrogen Failure Modes in High Strength Steels

Tensile specimens can be used to identify hydrogen damage as opposed to direct measurement as hydrogen related failures only occur under slow strain rate conditions and will not be apparent in impact specimens. Hydrogen damage has been observed as two distinct fracture morphologies on the fracture surfaces of tensile specimens. The first morphology can be definitively characterized as transgranular fracture (Figure 1a). The second has some transgranular features; however areas between facet-like structures appear featureless (Figure 2b). These different morphologies are likely a result of the altered constraint conditions operating when hydrogen trapping sites interrupt the lattice as discontinuities. As one would normally

anticipate a highly ductile fracture mode in high strength steels, the difference in appearance of these fracture modes is immediately apparent.

2.1.3.1 Effect of Trapping Sites on Failure Mode

The amount of hydrogen loading in the system has been shown to have an effect on the failure mode [41]. It appears that lower affinity hydrogen traps are only activated if all of the more preferential trapping sites have already been filled reasonably close to their capacity.[42], [43] This is typically observed in casting hydrogen failures due to the large variety of different trapping sites in cast materials including but not limited to solidification voids, gas porosities, inclusions, dislocations, grain boundaries, and lattice voids.

At the lowest degree of hydrogen damage observed throughout a cast sample fracture surface, hydrogen damage appears to only occur in the vicinity of shrinkage porosity (Figure 1b). The increased affinity of this trapping site can likely be attributed to the ease of dislocation termination at a free surface. At some unidentified level of hydrogen charging, gas porosities will begin to appear in the fracture surface surrounded by hydrogen damage (Figure 1d). This appears to be caused by the collection of hydrogen at normal vacancy clusters in the lattice, reaching pressures high enough to deform and expand the lattice. Only in samples where hydrogen damage is extremely prevalent is hydrogen damage observed in the vicinity of inclusions alone (Figure 1c). This is most likely due to stronger attraction to a dislocation core, allowing only a minimal number of hydrogen atoms to leave the dislocation Cottrel atmosphere. This appears to be a physical response which can be directly correlated back to the hydrogen affinity of different trapping site types. [41]

The failure mode in these cases is dominated by transgranular fracture. Transgranular hydrogen assisted fracture is a quasi-cleavage like fracture mechanism differing only slightly from cleavage, in that there is a lack of defined cleavage bands running through the fracture surface with a mixture of occasional intergranular (IG) separation (Mills, 1987), as shown in Figure 1a. At some distance away from the trapping site, the failure mode transitions to ductile. The macroscopic failure mode of the sample is then simply dependent on the size of the transgranular region vs. the ductile region, and will be either a brittle fracture along the 45 degree shear plane, or ductile cup-cone.

2.1.3.2 Failure Mode in a Porosity/Inclusion Free Matrix

The partial transgranular fracture, while also having hydrogen as its root cause, has its own independent morphology (Figure 2). At lower magnification, the fracture appears slightly faceted with the area in between the facets appearing mostly featureless. The size of these facets ranges between 152.4 microns (0.006 inches) to as small as 10.2 microns (0.0004 inches). Furthermore, some areas are completely devoid of facets, instead having only a featureless appearance. In these areas dominated by only featureless appearing fracture, bands are occasionally observed traveling through the fracture. Possible mechanisms for the formation of the bands are mechanical twinning and yield-point phenomenon such as Lüders bands. The bands are also similar in appearance to tongues common in cleavage fracture of body-centered cubic metals, especially ferritic steels, which are caused by mechanical twinning. This may be a direct observation of failure along slip planes, in accordance with the HELP mechanism.

Only at high magnification does it become apparent that the featureless regions have rough, and not smooth, surfaces. Energy Dispersive Spectroscopy (EDS) analysis of this surface reveals no discernible chemical composition differences to explain these micro-scale topography differences.

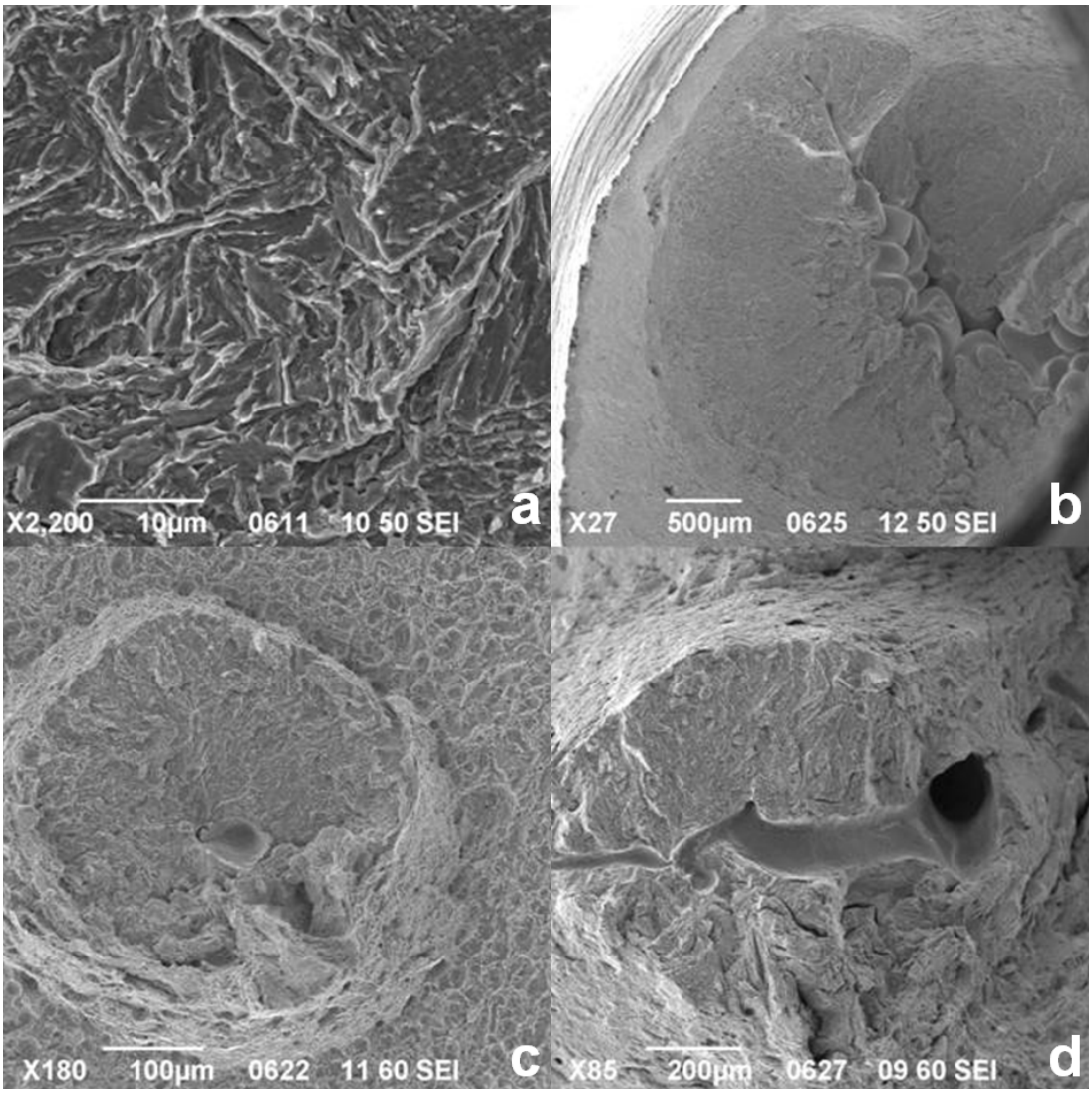

Figure 2: Hydrogen Sinks – a: High magnification image of hydrogen damage; b: Shrinkage porosity surrounded by a large region of hydrogen damage; c: Inclusion surrounded by hydrogen damage; d: Gas porosity surrounded by hydrogen damage. [41]

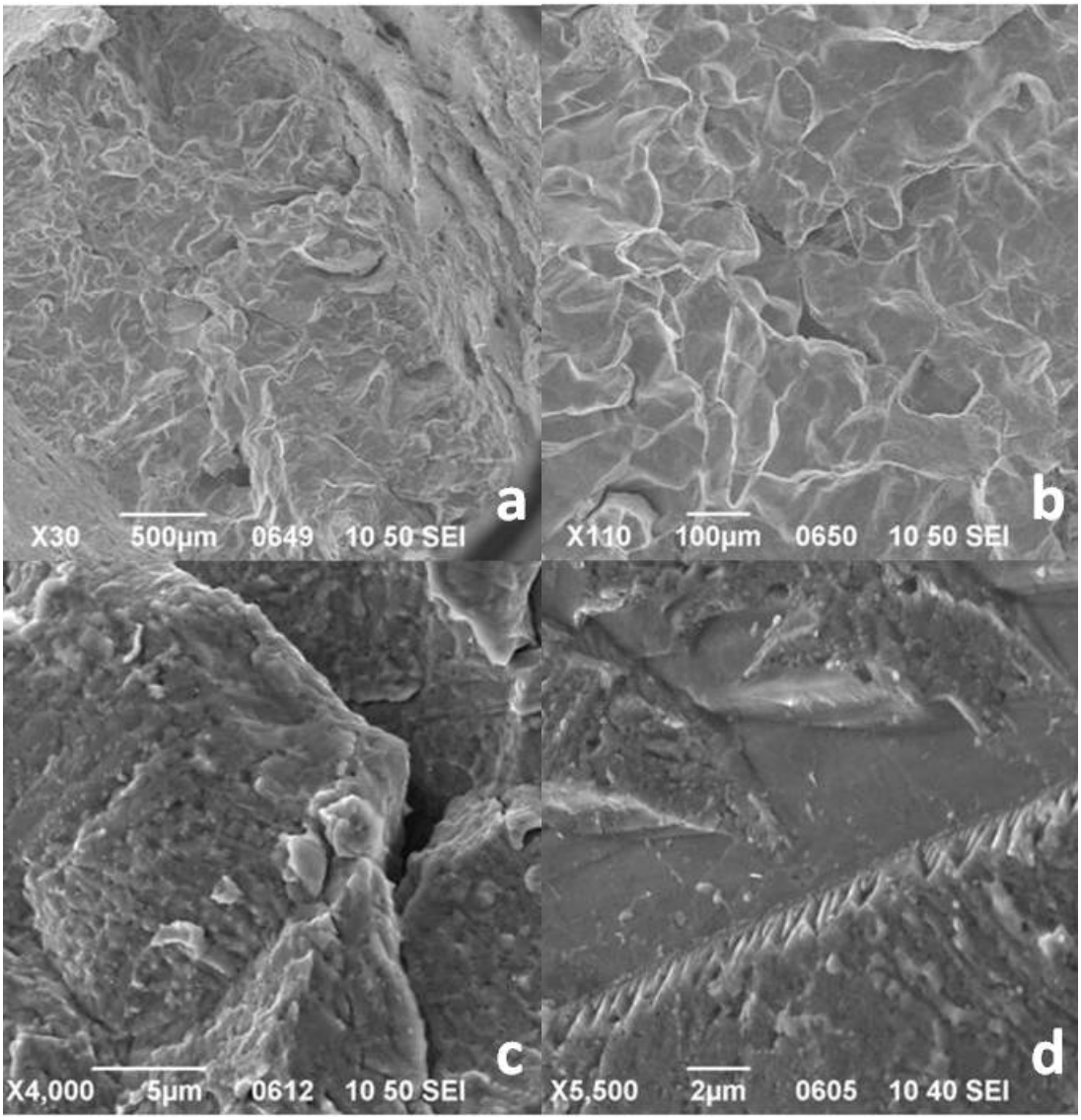

Figure 3: Characteristics of Hydrogen Embrittlement Fracture Mechanism – a: Low magnification view of a large area dominated by the mechanism with no apparent initiation site (such as a pore). b: Higher magnification view of the first image clearly shows that facets are present as part of the fracture. c: Very high magnification shows that the surface is not completely featureless. d: What appears to be cleavage bands or mechanical twins are found running through areas associated with this fracture mechanism where the facets are less prevalent. [41]

2.1.4 Current Practices to Prevent and Preclude Hydrogen

The movement of hydrogen in a static lattice free from discontinuities is largely dominated by thermal diffusion. As a result, the typical mitigation strategy to prevent

hydrogen induced failures is the removal of hydrogen from the lattice by performing a low temperature hydrogen soak treatment. As discussed in the introduction, this treatment is typically performed at 575°F for 450 hours for thick section (greater than 11") high strength steel castings [44], with an approximate cost of $50,000 to $100,000 at current natural gas prices depending on location. The method for determining these requirements is included below in section 2.1.5. Furthermore, the prevention of hydrogen damage in high strength steel welds may require both controlled preheat and interpass temperatures (varied by alloy, weld consumable, and process) as well as a post-production heat soak (example: 350F for 12 hours in 2 inch thick welded sections). For HY-80, the implementation of these controls can account for a significant portion of overall energy consumption for the manufacture of an article.

Confirmation of the effectiveness of a hydrogen soaking treatment is necessary in all new applications, including welded structures, where new process parameters, fluxes (where used) and consumables are used. This analysis is conducted via tensile testing in all materials and for high strength steel alloys percent reduction of area is generally the best indicator of hydrogen damage. For cast products, a low reduction of area is generally caused by only two types of material conditions, porosity in the tensile sample or hydrogen damage. If porosity is determined not to be the driving cause of the tensile test failure, a reduction of area measurement above 55% is generally indicative of a lattice free from any harmful levels of monatomic hydrogen. Between 45% and 55% reduction of area generally indicates some level of hydrogen in the material, but not to an extent that detrimental material performance would be anticipated. Below 45% reduction of area indicates detrimental hydrogen damage with

lower values indicating greater levels of hydrogen damage. For welded structures, an additional analysis beyond tensile testing is performed by reviewing transverse macro sections across the weld metal, heat affected zone, and base metal, and longitudinal macro sections through the heat affected zone and weld metal. During the analysis of these macro specimens, the polished surfaces are reviewed for micro-cracks.

In industry, first article testing in addition to meaningful conformance testing in general should preclude any hydrogen related material performance issues. This only holds true, however, if the first article evaluation is conducted under the worst case scenario for hydrogen. In the case of steel castings this can be summarized by two factors, the initial level of hydrogen in the lattice, and the average spacing between hydrogen trapping sites. For the first factor, any first article casting should be produced using the practices which will produce the highest allowable hydrogen levels during manufacture. For the second factor, the traditional test block, with a proper feeding system, is a reasonable worst case condition for hydrogen as test blocks are typically cleaner than the castings they accompany, resulting in greater diffusion distances for monatomic hydrogen to reach trapping sites. The resulting requirements for hydrogen removal can be both onerous and expensive for the manufacturer.

2.1.5 Hydrogen Soaking Requirements Calculation

Using the trigonometric series solution to Fick's law and an Arrhenius expression for diffusivity, the following estimates can be made [41]:

$$\bar{C} = C_m \frac{8}{\pi^2} exp\left[-\frac{\pi^2}{h^n} Dt\right] \quad and \quad D = D_o \exp\left[-\frac{Q}{RT}\right] \tag{1}$$

$Where$:
$\bar{C} = the\ average\ bulk\ hydrogen\ concentration$
$C_m = The \max hydrogen\ concentration\ immediatly\ after\ fabrication$
$h^n = Diffusion\ path\ where\ n$
$= 1.5\ or\ 2\ for\ planer\ or\ compact\ shapes\ respectivley$
$t = Time$
$D = Diffusivity$
$D_o = Diffusion\ coefficient$
$Q = Activation\ energy$
$R = The\ gas\ constant$
$T = Temperature\ (°K)$

Due to the difficulty in obtaining reliable hydrogen measurements, experimental calculations are very difficult to make for anything other than very small samples for the starting and ending hydrogen concentrations. However, if one knows an effective hydrogen soak treatment based on empirical test results, it is still possible to calculate other effective soaking parameters.

Substituting for D and rearranging the expression yields:

$$\ln\left[\frac{\bar{C}}{C_m}\frac{\pi^2}{8}\right] = -\frac{t\pi^2}{h^n} D_o \exp\left[-\frac{Q}{RT}\right] = Constant\ (X) \qquad (2)$$

This constant provides a relative measure of degassing over an effective thickness, time and temperature. For a known set of hydrogen soak parameters, solving for X is relatively straight forward. Given a value for X, the equation can be rearranged to give the required amount of time needed for a new hydrogen soak under a new set of soaking conditions as follows:

$$t = Xh^n \exp\left[+\frac{Q}{RT}\right] \qquad (3)$$

There are several limitations with this approach as the assumptions necessary to use the calculated constant X may not be true for all situations. Namely, it must be assumed

that the starting hydrogen conditions from the sample selected to calculate X are equal or greater to that of any castings upon which one desires to apply the new calculated treatment. Although these assumptions could result in incorrect hydrogen soak treatment parameters, given no better method at the time, this approach has been used to generate several current requirements for hydrogen soaking treatments in industry [45] (see **Table 1** for example of requirements in HY-steel alloys).

Table 1 Hydrogen Soak Time at 301°C [44]

Section Size	Minimum Soak Time
< 203.2mm (8”)	24 hours
203.2mm – 234.95mm (8” – 9 ¼”)	150 hours
> 234.95mm – 279.4mm (9 ¼” – 11”)	300 hours
greater than 279.4mm (11”)	450 hours

Several researchers have attempted to create varied other models of hydrogen diffusion and as with the study of hydrogen failure modes, the subject remains contested with wide ranging and sometimes conflicting models presented just as with hydrogen failure modes. Most current work focuses on attempts to describe how the influence of both hydrogen trapping sites and stress fields impact diffusion. The principle methods discussed in the literature are:

- Varied methods for accounting for hydrogen traps firms by McNabb and Foster [46]
- Diffusion by random-walk [47], [48]
- The Kirchhiem model, which calculates the chemical diffusion coefficient of hydrogen in amorphous metals [49]
- The method of configuration sums, that refines the Kirchhiem model by attempting account for hydrogen – hydrogen interactions [50]–[52]

2.2 Temper Embrittlement

Temper embrittlement in low alloy carbon steels causes a severe reduction in ductility usually measured as a decrease in the ductile to brittle transition temperature of the material [53]–[55]. This is a problem in several industries as the condition cannot be detected via non-destructive techniques in service. In addition some forms of temper embrittlement are irreversible [56], [57]. As a result temper embrittlement, like hydrogen embrittlement, must be precluded and in service conditions controlled or understood to ensure freedom from embrittling conditions. In addition, the necessity to limit time in the temper embrittlement temperature range decreases the available treatment temperature for tempering, hydrogen removal, and stress relief treatments.

2.2.1 Embrittlement Fundamentals

Traditional temper embrittlement is caused by elemental grain boundary segregation and is a time dependent process [58], [59]. The kinetics of embrittlement are dependent on both starting concentration of embrittling constituents and time at temperature [60]–[63]. Olson determined in 1994 that the reason for embrittlement at the grain boundaries was associated with the morphology of electron density distribution. Olson further determined that impurity-induced reduction of Fe-Fe bonding is not the primary mechanism for grain boundary embrittlement. Rather, the spatial anisotropy of the bounding interaction between the impurity states with the surrounding Fe atoms is fundamental to grain boundary embrittlement. Impurities with stronger vertical and weaker lateral bonding across the grain boundary enhance grain boundary cohesion, where as weak vertical and strong lateral bonding enhance grain boundary decohesion [64], [65].

2.2.2 Fracture Mechanics of Grain Boundary Embrittlement

The cohesive energy of a grain boundary ($2\gamma_{int}$); the energy difference between surface energy after fracture and grain boundary energy before fracture, is the controlling parameter in grain boundary embrittlement [66] Per the mechanics for brittle fracture, the crack growth condition for elastic-plastic materials for the case of plane strain follows equation 4.

$$\frac{(1-v^2)(\sigma^*)^2\pi a_c}{E}\left(Energy\ Release\ Rate\ in\frac{J}{m^2}\right) \geq \gamma_p + 2\gamma_{int} \qquad (4)$$

Where:
v is Poisson's ratio
$\boldsymbol{\sigma}^*$ is the local applied fracture stress
$\mathbf{a_c}$ is a half-length of crack
E is Young's modulus
$\boldsymbol{\gamma_p}$ is plastic work
$\boldsymbol{2\gamma_{int}}$ is the cohesive energy of the G

Equation 4 indicates that the crack can grow if the elastic energy released by the crack growth becomes larger than the energy that is necessary for the formation of new fracture surfaces and the plastic work associated with the crack growth. As shown in **Figure 1**, the concentrated stress σ at the sharp crack tip becomes so strong by the stress concentration as to break atomic bonds.

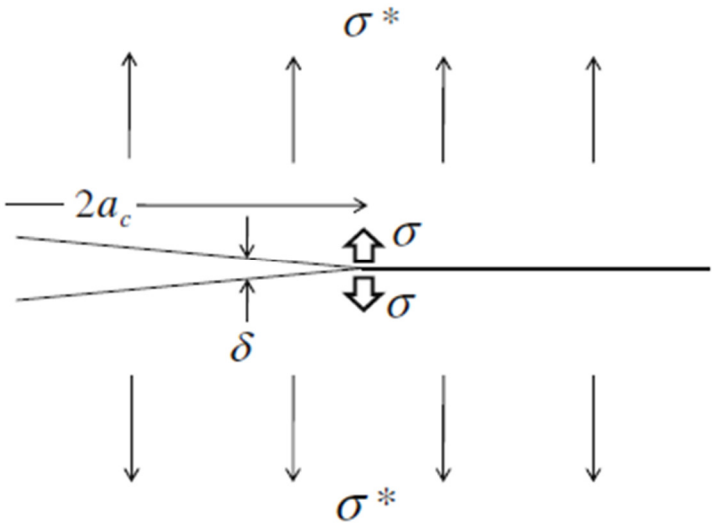

Figure 4: Schematic illustration of a crack tip. [67]

(Note: σ is different from σ^*; σ is a concentrated stress in an atomic scale at the crack tip, while σ^* is the local fracture stress applied on the entire crack in micrometer scale.) The longer the crack length is, the larger the stress concentration at the crack tip is. The relation between the concentrated stress σ at the crack tip and the displacement of crack opening d are shown in **Figure 2**.

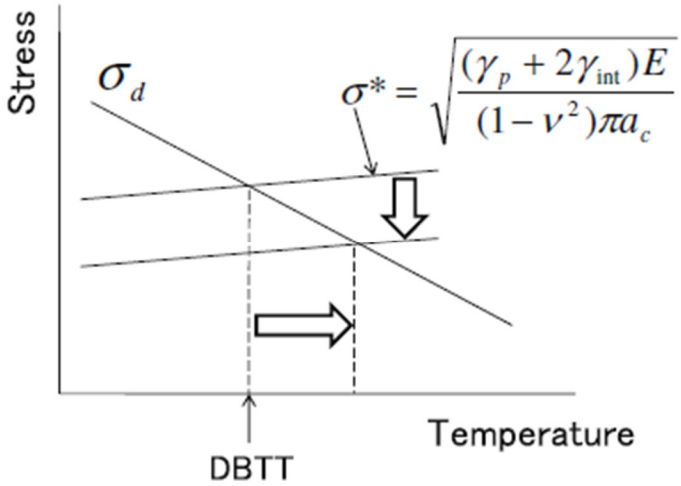

Figure 5: Schematic illustration showing the increase of the ductile to brittle transition temperature with decreasing the local fracture stress that depends on the grain boundary cohesive energy. [67]

The integration of the σ-d curve corresponds to the cohesive energy (work of separation) of the GB, $2\gamma_{int}$ per equation 5. [68]

$$2\gamma_{int} = 2\gamma_s - \gamma_{gb} \tag{5}$$

Here, γ_s is the fracture-surface energy after fracture, and γ_{gb} is the GB energy before fracture. The maximum value of the concentrated stress σ is denoted by σ_{max}; this is an ideal strength of a GB. If $\sigma \geq \sigma_{max}$ the atomic bonds at the crack tip are broken and then the fracture surfaces appear. Usually, the stress condition for fracture, $\sigma \geq \sigma_{max}$, is easily satisfied by a large stress concentration at the sharp crack tip rather than the energy condition of equation 5 for fracture. Therefore, the crack growth is dominated by the energy condition of equation 4.

Traditionally the brittle fracture of deformable solids is accompanied by a significant plastic work γ_p, which is often much larger than the cohesive energy term $2\gamma_{int}$. [66], [68] When the crack growth condition of equation 4 was suggested, the plastic work term γ_p was assumed to be independent from the cohesive energy, $2\gamma_{int}$. However, this assumption cannot explain the GB embrittlement of metals by impurity segregation in steels with P, Sn, or Sb, and in Ni alloys with S. In all cases, the segregation is limited to a very narrow region along the grain boundaries. Thus, the plastic work term γ_p, which depends on dislocation mobility, cannot be affected by the segregation. Impurity segregation can bring about a drastic embrittlement (a large energy decrease in the right-hand side of equation 4). To resolve this dilemma, Jokl *et al.* resolved that there was a dependency relation between the two terms, [68].

$$\gamma_p = \gamma_p(2\gamma_{int}, other\ paramaters) \tag{6}$$

Jokl *et al.* suggested that γ_p was a monotonically increasing function of $2\gamma_{int}$ from their analysis using the Dugdale–Billy–Cottrell–Swinden model. Their model suggests that a large decrease in γ_p is induced by a small decrease in $2\gamma_{int}$. This indicates that the crack growth condition (equation 4) can be controlled by $2\gamma_{int}$. Because γ_p depends on $2\gamma_{int}$, the DBTT is also considered to be controlled by $2\gamma_{int}$. To understand this relation, the illustration in **Figure 2** can be used. From this figure, it is shown that the ductile-to-brittle transition occurs at the intersection of the two lines of brittle fracture stress (σ^*) and ductile fracture stress (σ_d), where the ductile fracture stress depends highly on temperature. Thus, the decrease of $2\gamma_{int}$ brings about a large decrease of γ_p. This further results in a decrease in σ^*, as shown in equation 4, which brings about a shift of the DBTT. Therefore, the decrease of $2\gamma_{int}$ brings about the increasing shift of DBTT. [67]

2.2.3 Equilibrium Grain Boundary Embrittlement

During the onset of process development at major steel manufacturing facilities in the early 1900's, observations of embrittlement led to the development of thermodynamic based assessments of the temperature ranges that needed to be avoided to prevent embrittlement. These analyses were fundamentally flawed as there was a lack of understanding on the root cause of embrittlement. The legacy of thermodynamic based calculation can still be observed today in industry as the guidance for prevention of embrittling conditions is simply to avoid a critical temperature range, rather than detailing the time limits within a temperature bound to prevent loss of mechanical performance. [69]

McLean proposed the Langmuir–McLean segregation equation for equilibrium grain boundary segregation (EGS) according to equations 7 - 9. The model predicted that the segregation of a second atom species to grain boundaries in a polycrystalline material increases with decreasing temperature. While this is a simplistic analysis, McLean's model predicting impurity segregation via kinetics made major improvements upon the previous work.

$$C_{\infty}(T) = \frac{AC_g \exp\left(\frac{Q}{kT}\right)}{1 + AC_g \exp\left(\frac{Q}{kT}\right)}; \quad (7)$$

Where:
$C_g = Concentration\ of\ Impurity\ in\ the\ Matrix$
$A\ is\ a\ constant\ representing\ the\ vibrational\ entropy\ of\ the\ GB\ region$
$k\ is\ the\ Boltzman\ constant$
$Q = impurity\ binding\ energy\ to\ the\ lattice$
$C_{\infty} = concentration\ of\ impurity\ in\ a\ monolayer\ on\ boundaries\ \&\ interfaces$

$$\frac{C_b(t) - C_{\infty}(T_i)}{C_{\infty}(T_j) - C_{\infty}(T_i)} = 1 - \exp\left(\frac{4D_i t}{\alpha_i^2 d_e^2}\right) erfc\left(\frac{2(D_i t)^{\frac{1}{2}}}{\alpha_i d_e}\right); \quad (8)$$

Where:
$C_b(t) = Concentration\ of\ impurity\ on\ the\ boundry\ after\ time\ t$
$d_e = thicknes\ of\ the\ boundary\ (\sim 1nm)$
$D_i = Diffusivity\ of\ the\ impurity\ in\ the\ matrix$

$$\alpha_i = \frac{C_{\infty}(T_j)}{C_g}; \quad (9)$$

Where:
$T_i = Quenching\ Temperature\ ;\ T_j = Treatment\ Temperature$

2.2.4 Non-Equilibrium Grain Boundary Embrittlement

With the advent of better characterization tools where elemental segregation at the grain boundary started to be measured, errors in the McLean model were observed. Aust *et al.* and Anthony proposed another grain boundary segregation mechanism via

non-equilibrium diffusion of embrittling elements to vacancies sites in the vicinity of grain boundaries. However, refinement of characterization tools took over a decade to validate the kinetics equations developed to detail the non-equilibrium condition. Williams *et al.* provided the first experimental results showing non-equilibrium segregation of boron in steel to confirm the mechanism of diffusion. When type 316 steel was solution treated at the normal temperature of 1050°C and cooled in a stream of cold argon, it was observed that the higher the solution treatment temperature, the greater the amount of boron segregated to grain boundaries after cooling in argon. This behavior was opposite to that predicted by Langmuir–McLean equilibrium segregation detailed above in equations 7 - 9. Thus, it was referred to as thermally induced non-equilibrium grain boundary (NGS) segregation according to equations 10 – 13. [54], [58], [70], [71]

$$C_b^m(T) = C_g\left(\frac{E_b}{E_f^v}\right)\exp\left(\left[\frac{E_b - E_f^v}{kT_i}\right] - \left[\frac{E_b - E_f^v}{kT_j}\right]\right); \tag{10}$$

Where:

$C_b^m(T) = The\ maximum\ concentration\ of\ non - equilibrium\ grain\ boundary\ segregation$

$E_f^v = Energy\ of\ Vacancy\ Formation$

$E_b = Vacancy\ impurity\ atom\ binding\ energy$ (0.36 $eE_b\ for\ P\ in\ an\ \gamma - Fe\ matrix$)

$$\frac{C_b(t) - C_b^m(T_i)}{C_b^m(T_j) - C_b^m(T_i)} = 1 - \exp\left(\frac{4D_c t}{\alpha_j^2 d_n^2}\right) erfc\left(\frac{2(D_c t)^{\frac{1}{2}}}{\alpha_j d_n}\right); \tag{11}$$

Where:

$D_c = Coefficient\ of\ diffusion\ of\ complexes\ in\ the\ matrix$

$d_n = width\ of\ the\ concentrated\ layer\ of\ impurities$

$$\alpha_j = \frac{C_b^m(T_j)}{C_g} \tag{12}$$

$$erfc\left(\frac{2(D_c t)^{\frac{1}{2}}}{\alpha_j d_n}\right) = 1 - \frac{2}{\pi^{\frac{1}{2}}}\int_0^{\frac{2(D_c t)^{\frac{1}{2}}}{\alpha_j d_n}} \exp(-Y^2)\, dY \tag{13}$$

2.2.5 Critical Time

Thermally induced non-equilibrium grain boundary segregation is considered to be a consequence of the formation of solute vacancy complex within the matrix, where the three parts: solute atom (I), vacancy (V) and their recombined complex (C) are in equilibrium with each other [53], [61] such that:

$$I + V = C \tag{14}$$

If an alloy is solution treated at a higher temperature and subsequently cooled to a lower temperature and held at this temperature, then there must be an isothermal holding time at the lower temperature, at which the grain boundary segregation concentration reaches a maximum value. This holding time is defined as the critical time of TNGS according to equation (15).

$$t_c = \frac{B^2 \ln(D_c/D_i)}{4\delta(D_c - D_i)}\ ; \tag{15}$$

Where:
$t_c = critical\ time$
$\delta - numerical\ factor$
$B = Grain\ Size$

When the holding time is shorter than the critical time, the grain boundary concentration of solute will increase with holding time, referred to as the segregation phase. Lastly, when the holding time is longer than the critical time, the grain boundary concentration of solute decreases with holding time, and represents the desegregation phase. When the effective time is longer than the critical time desegregation is

dominant. **Figure 6** below shows the relationship between Phosphorus, temperature, and critical time in low carbon steel. These relationships are typically more important for in service conditions of materials at longer time as it permits evaluation of the worst case condition, due to similar kinetic conditions at higher temperatures, without need to conduct full time scale through life testing.

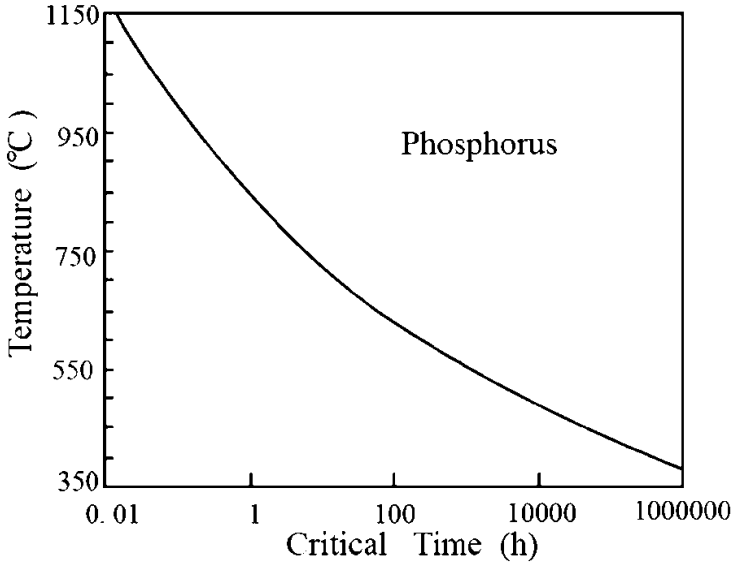

Figure 6: Calculation of the critical time for phosphorus in low carbon steel from equation 15. [53]

2.2.6 Segregation During Cooling

Manufacturing processes and in service conditions are not always at constant temperature. As a result, the kinetics of elemental segregation during variable temperature distributions over time must also be detailed. The cooling temperature difference $Ti - Ti_{+1}$ between solution temperature Ti and aging temperature Ti_{+1} is an important precondition under which TNGS phenomena can take place. The relationship between the maximum solute boundary concentration and the cooling temperature difference $Ti - Ti_{+1}$ is given by:

$$C_m(T_{i+1}) = C_g\left(\frac{E_b}{E_f}\right)\exp\left\{\left[\frac{E_b - E_f}{kT_i}\right] - \left[\frac{E_b - E_f}{kT_{i+1}}\right]\right\}; \quad (16)$$

$C_g = Concentration\ of\ solute\ atoms\ within\ the\ grain$
$E_b = Vacancy - Impurity\ binding\ energy$
$E_f = Vacancy\ formation\ energy$

The TNGS kinetic equations for a sample aged at temperature $Ti+1$ after quenching from a higher temperature Ti are given by:

$$\frac{C_b(t) - C_b^m(T_i)}{C_b^m(T_{i+1}) - C_b^m(T_i)} = 1 - \exp\left(\frac{4D_c t}{\alpha_{i+1}^2 d_n^2}\right) erfc\left(\frac{2(D_c t)^{\frac{1}{2}}}{\alpha_{i+1} d_n}\right); \quad (17)$$

for aging times shorter than the critical time ($t < t_c$) , and

$$\left[C_b(t_c) - C_g\right]\left\{\text{erf}\left[\frac{\frac{d}{2}}{[4D_i(t - t_c)]^{\frac{1}{2}}}\right] - erf\left[\frac{-\frac{d}{2}}{[4D_i(t - t_c)]^{\frac{1}{2}}}\right]\right\}; \quad (18)$$

for aging times longer than the critical time ($t > t_c$), where $Cm(Ti+1)$ is obtained with Eqs. (16, 17, and 18) give the concentration at the grain boundary, $C_b(t)$, as a function of aging time t at temperature $Ti+1$. [53]

2.3 The HY Alloy System

2.3.1 History

At the end of World War II, the United States Naval Bureau of Ships recognized the need for the development of a high yield strength steel to increase the combat effectiveness of submarines. To fulfill this need an investigation was commissioned with the United States Steel Company and the International Nickel Company to develop a nonballistic, weldable, structural steel with a minimum yield strength of 552 MPa (80 ksi) in the water quenched and tempered condition. This material, which

would come to be known as HY-80, began its use in 1951 but it was not until a decade later that studies began into understanding its processing dependence on mechanical response and metallurgical properties. In the early 1960s a program was established and executed to perform metallurgical studies on isothermal transformation, variations in chemistry, and impurities to determine their relation to the mechanical properties and weldability of high-strength steels, principally HY-80. The majority of the foundational understanding of the HY alloy system comes from this work conducted by A.R. Willner and M.L Salive at the Department of the Navy David Taylor Model Basin. Since the completion of this work, no expansive study has been executed for the alloy system. Rather the focus has been on further development of welding parameters.

2.3.2 Current Processing Limitations and Mechanical Requirements

The acquisition requirements of HY components today is dictated by NAVSEA Technical Publication 0300 (TP-0300). [44] The requirements re-printed from TP-0300 in **Figure 7** through **Figure 9** below will be considered the benchmark for successful experimental treatments in this work. It is also noted that there are processing restrictions within TP-0300 to which this work has adhered to in order to assure that any newly developed processes would be implementable in a commercial environment.

The principle processing restrictions are on the austenitizing and tempering temperatures that can be employed. Inter-critical treatments are prohibited in accordance with early studies showing inconsistent and non-uniform yielding characteristics. Subsequently, tempering is restricted to not exceed 689°C in order to avoid passing the AC1, measured to 721°C. It is noted that the early studies that measured the AC1 at 721°C were of a different composition than that used today and

that SSDTA measurements on nominal industrial compositions currently in use show the AC1 as low as 687°C. [72] The minimum tempering temperature is also restricted depending on product form to either 621°C for forgings and rolled plate or 638°C for castings. This limitation is associated with the objective to preclude time in the temper embrittlement region for the alloy, considered to be from 371°C to 615°C in nearly all publications on the alloy to date.

Element	Weight Percent (single values are maximums)	
	Grade HY-80	Grade HY-100
Carbon	0.20	0.22
Manganese	0.55 – 0.75	
Phosphorus	0.014	
Sulfur	0.005	
Silicon	0.50	
Nickel	2.75 – 3.25	3.00 – 3.50
Chromium	1.35 – 1.65	
Molybdenum	0.30 – 0.60	
Vanadium 2/	0.03	
Titanium 2/	0.02	
Copper 2/	0.25	
Arsenic 2/	0.025	
Tin 2/	0.03	
Antimony 2/	0.025	
Aluminum	0.04	
Nitrogen	100 ppm 3/	

NOTES:

1/ For definition of lot for heat analysis, see D.4.4.1.2 and D.4.4.2.
2/ Elements shall not be intentionally added.
3/ Nitrogen content shall be determined with samples and instrumentation in accordance with ASTM E1019 or by other NAVSEA approved method. Nitrogen analysis may be performed during refining, in the ladle, or from samples removed from the final product.

Figure 7: Chemical composition requirements of Technical Publication 0300 Revision 2 [44]

Property	Required Value			
	Grade HY-80		Grade HY-100	
T ≤ 6 inches (152 mm) 1/, 2/				
Location	T/2 or 2 inches (51 mm)		T/2 or 2 inches (51 mm)	
Yield strength, 0.2% offset, ksi [MPa]	80 – 99.5 [552 – 686]		100 – 120 [690 – 827]	
Elongation in 2 inches, minimum percent	20		18	
Reduction of area, minimum percent	50		50	
6 inches (152 mm) < T ≤ 10 inches (254 mm) 1/				
Location	T/4 or 2 inches (51 mm) 2/	T/2 3/	T/4 or 2 inches (51 mm) 2/	T/2 3/
Yield strength, 0.2% offset, ksi [MPa]	80 – 99.5 [552 – 686]	78 – 99.5 [538 – 686]	100 – 120 [690 – 827]	98 – 120 [676 – 827]
Elongation in 2 inches, minimum percent	20	18	18	15
Reduction of area, minimum percent	50	50	50	50
T > 10 inches (254 mm) 1/				
Location	T/4	T/2 3/	T/4	T/2 3/
Yield strength, 0.2% offset, ksi [MPa]	80 – 99.5 [552 – 686]	76 – 99.5 [524 – 686]	100 – 120 [690 – 827]	93 – 120 [641 – 827]
Elongation in 2 inches, minimum percent	20	14	18	12
Reduction of area, minimum percent	50	50	50	45

NOTES:

1/ Ultimate tensile strength is reported for information only.

2/ For T up to and including 4 inches (102 mm), sample location shall be T/2. For T greater than 4 inches, sample location shall be T/4 or 2 inches (51 mm), whichever is greater.

3/ For T greater than 6 inches (152 mm), a second set of specimens shall be taken at T/2, unless otherwise specified (see D.6.2).

Figure 8: Tensile property requirements of Technical Publication 0300 Revision 2

[44]

Impact Requirements at T/2 and T/4 Test Locations for Both HY-80 and HY-100, Unless Otherwise Specified in this Table 1/, 2/, 3/			
	Charpy V-Notch Temp: -100 °F (-73 °C)	Charpy V-Notch Temp: 0 °F (-18 °C)	Dynamic Tear Temp: -40 °F (-40 °C)
HY-80/HY-100: T ≤ 4 inches (102 mm), T/2	50 ft-lb (68 J) Avg Min; % Shear Required	70 ft-lb (95 J) Avg Min; % Shear Required	For Info Only 4/
HY-80/HY-100: T > 4 inches (102 mm), T/4 or 2 inches (51 mm), whichever is greater			
HY-80/HY-100: T< 5/8 inch (16 mm)	50% Avg Min Shear	% Shear for Info Only	Not Required
HY-80: 5/8 inch (16 mm) ≤ T ≤ 6 inches (152 mm)	50% Avg Min Shear	% Shear for Info Only	For Info Only 4/
HY-100: 5/8 inch (16 mm) ≤ T ≤ 4 inches (102 mm)			
HY-80: 6 inches (152 mm) < T < 12 inches (305 mm)	40% Avg Min Shear	% Shear for Info Only	For Info Only 4/
HY-100: 4 inches (102 mm) < T < 12 inches (305 mm)			
HY-80/HY-100: T ≥ 12 inches (305 mm)	35% Avg Min Shear	% Shear for Info Only	For Info Only 4/
Impact Requirements for Second Set of Specimens Taken at T/2 for Both HY-80 and HY-100 1/, 2/, 5/			
	Charpy V-Notch Temp: -100 °F (-73 °C)	Charpy V-Notch Temp: 0 °F (-18 °C)	Dynamic Tear Temp: -40 °F (-40 °C)
6 inches (152 mm) < T < 10 inches (254 mm), unless otherwise specified (see D.6.2)	50 ft-lb (68 J) Avg Min; % Shear Not Required	70 ft-lb (95 J) Avg Min; % Shear Not Required	For Info Only 3/, 4/
T ≥ 10 inches (254 mm)	30 ft-lb (41 J) Avg Min; % Shear Not Required	50 ft-lb (68 J) Avg Min; % Shear Not Required	For Info Only 3/, 4/

NOTES:

1/ Sampling and location of test specimens shall be as specified in D.4.3.2.2, D.4.3.2.5, and D.4.3.2.6 for first article and D.4.4.3, D.4.4.3.3, and D.4.4.3.4 for conformance inspection.

2/ Average of three specimens. No single Charpy V-notch energy value shall be below the minimum required average by more than 5 ft-lb (7 joules).

3/ The percent shear fracture shall be measured on each specimen.

4/ Data shall be forwarded to the NAVSEA Materials Engineering Group until otherwise advised by NAVSEA.

5/ Unless otherwise specified (see D.6.2), for T greater than 6 inches (152 mm), additional Charpy V-notch impact tests and dynamic tear tests shall be conducted at a depth of T/2.

Figure 9: Impact property requirements of Technical Publication 0300 Revision 2

[44]

2.3.3 Chemical Composition and Microstructure

HY is a fully killed, low alloy steel which acquires its strength and toughness through quenching and subsequent tempering. In industrial manufacture the microstructure is typically a combination of tempered martensite with some percentage of upper transformation productions. [33], [74] **Figure 10** shows the time-temperature-transformation diagram for the alloy which shows the slow kinetics of austenite decomposition. This slow response to transformation results in an effective duplex martensite/bainite microstructure.

The alloying elements each serve a key role in establishing the mechanical response of the HY alloy system.

- Carbon is controlled to ensure good weldability while simultaneously achieving the desired strength level. [75], [76]
- Nickel is added primarily to increase the hardenability. It has been observed that nickel also lowers the NIL ductility temperature of the alloy. [77]
- Chromium is also added to increase the hardenability and secondary hardening during the tempering treatment. The Cr limits were set to act as a carbide former in hardening. Chromium also improved the corrosion resistance.
- Manganese additions prevent the formation of detrimental sulfides by preferentially forming manganese sulfides and limiting the available sulfur for reacting with iron to form iron-sulfides. The addition of manganese also provides solution strengthening to the alloy; however excess manganese is known to cause embrittlement.

- Molybdenum is used to improve hardenability, creep resistance, and machineability.
- Phosphorous and Sulfur are both detrimental elements and have had increased limits placed on their content over numerous specification revisions. Sulfur combines with iron to form an iron-sulfide, which liquifies at rolling and forging temperatures, as where P is the principle constituent of GB embrittlement.
- Finally, Silicon is added as a deoxidizer during processing and to modify the viscosity during solidification for castings and to control the basistivity during melting processes.

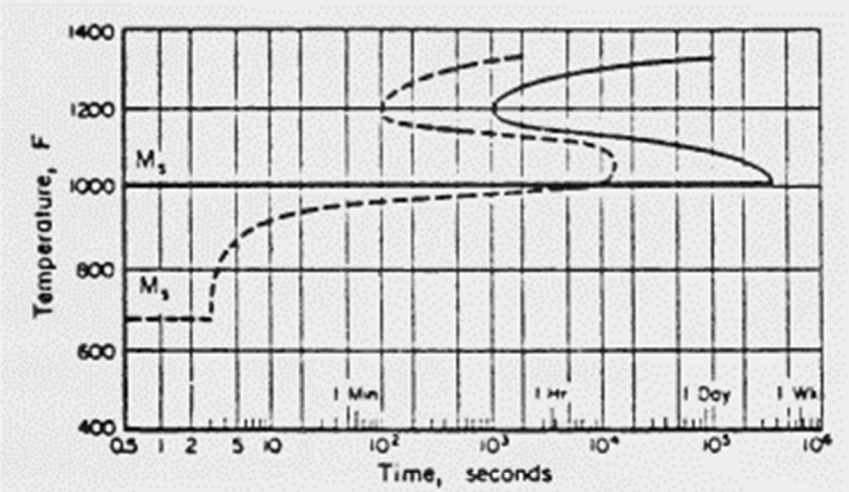

	Solid Curve	Dotted Curve
C	0.16	0.13
Mn	0.34	0.16
P	0.014	0.009
S	0.024	0.013
Si	0.25	0.10
Ni	2.87	3.08
Cr	1.52	1.76
Mo	0.41	0.49
Austenitizing Temperature	2400 F	1650 F

Figure 10: CCT Diagram for HY-80. Reprinted from Willner and Salive

2.3.4 General Characteristics and Heat Treatment Response

The work of Willner and Salive provides numerous observations for heat treatment of what would today be considered a low carbon equivalent grade of HY-80 (See **Table 2**). From the 1960's through 2000's heat X would have been considered representative of a low carbon equivalent and heat Y would have been identified has a high carbon equivalent grade for plate product. Heat A represents one of the heats used for this study that is more representative of a high carbon equivalent of cast HY-80 today.

Table 2: Historical chemical compositions investigated (wt%)

Heat	C	Mn	P	S	Si	Ni	Cr	Mo	Cu
X	0.14	.028	0.010	0.018	0.18	2.18	0.87	0.21	0.03
Y	0.15	0.24	0.011	0.014	0.14	2.85	1.44	0.45	0.03
A	0.205	0.64	0.005	0.003	0.41	3.15	1.48	0.42	0.03

Principle of Salive and Willner's work were results associated with the impact of varied heat treatment parameters on the mechanical response of HY-80. The most important conclusions from this work between 1958 and 1972 are summarized below:

- The austenitization temperature does not influence the mechanical tensile properties of a quenched heat with subsequent tempering between 621°C and 688°C. [78]
- Transverse Charpy V-notch impact energies can be reliably obtained above 68 Joules (50 ft-lbs) tested at -120°C for specimens quenched from austenitization temperatures ranging between 843°C and 927°C and subsequently tempered between 621°C and 688°C. [79]

- Tempering times up to 16 hours do not have an appreciable impact on notch-brittleness. [78]
- With increasing austenitization temperature, particularly in the range from 982°C to 1093°C, and decreasing tempering temperature, the ductile to brittle transition temperature is shifted to the right. [79]–[81]
- Material quenched to 100% martensite require higher tempering temperatures; whereas the tempering ranges for samples containing non-martensitic products are lower. [82]
- The effective hardenability and the lower shelf Charpy V-notch energy are proportional to each other. [78]

For the heats studied by Willner and Salive two tempering ranges for HY were revealed. In the range between 260°C and 427°C tempers have the effect of increasing the transition temperature and strength level. For tempering between 621°C and 649°C two competing effects were observed. The first change impacting mechanical performance was presumed to be the precipitation of a carbide phase resulting in secondary hardening or aging. The second effect was theorized to be a softening effect due to the coalescence of carbides. These two effects being competing was presumed to be the reason why the strength level remains relatively constant, however the fibrous fracture transition temperatures were observed to decrease. [78] At the time of this work it was viewed that the CVN fibrous fracture appearance would be the most sensitive to changes in the microstructure of the material. [77]

The work presented in this dissertation has shown for the first time that in the HY alloy system two different types of carbides exist that may form depending on the

chemical composition of the heat, an $M_{23}C_6$ and M_7C_3 carbide. A review of these carbides in adjacent alloy systems is provided in the next section.

2.4 Carbides in Steel

The $M_{23}C_6$ carbide is the most extensively studied due to their ubiquitous occurrence, where the metal atom (M) is most likely to be chromium. The $M_{23}C_6$ carbide has a f.c.c lattice and forms on phase, twin, and lathe boundaries. It is aligned with the austenite phase during the austenitizing treatment, $(11\text{-}1)_{M23C6}//(111)_{\gamma}$ and satisfies a cube-on-cube orientation relationship. [33] While carbide-forming alloying elements, primarily Cr, were added to the HY system to serve as strengtheners, excessive alloying has been shown to bring ductility loss in adjacent alloy systems. As the carbon supply is limited, the amount of $M_{23}C_6$ is mainly determined by C content.[34] M_7C_3 carbides have a pseudo-hexagonal lattice and is found when the carbon levels are sufficiently high. [85], [86]

The $M_{23}C_6$ carbide has an incoherent boundary with the ferrite phase, featuring curved boundaries further into the ferrite phase in comparison to the straight boundaries at the edge of the austenite phase (with which the carbide is coherent). The $M_{23}C_6$ carbide depletes the parent phase of Cr and ejects Ni and Si into it. Some researchers state that near the carbide, there is a eutectoid transformation of $\delta \rightarrow M_{23}C_6 + \gamma_2$, thus propagating a ferrite to austenite transformation, perhaps influencing the reactions at the boarder of the AC1.

Adjacent work on NiCrMo [87], [88], NiCrMoV [89]–[91], and CrMo [83], [92], [93] steels has investigated the presence and role of alloy carbides on mechanical properties. Their worked showed via various experimental techniques that $M_{23}C_6$ and

M_7C_3 carbides (in addition to others) can form in these alloys and are primarily made up of Cr and Mo. The presence of these carbides on prior austenite grain boundaries has been shown to have a detrimental effect on impact strength. [92], [94] This decrease in impact strength has been correlated to the carbides serving as initiation sites for cracks. [95]–[97] As a result, the failure mode transitions from intergranular (traditionally associated with temper embrittlement) to that of transgranular cleavage.

Most recently, a small number of researchers have used the new technique of atom probe tomography to examine the grain boundaries of ferritic steel alloys. Via this technique a high aspect ratio tip of material is biased at a high DC voltage. Using a laser or HV pulsing, atoms are evaporated from the surface of a tip on a layer by layer basis. The evaporated atoms impact a position sensitive detector which enables reconstruction of the material. This type of work has shown that phosphorus appears to be the primary grain boundary embrittling segregate in steels containing Ni, Cr, and Mo as alloying elements. [98] In addition, this work has shown that phosphorus can surround grain boundary carbides.

2.5 Kinetic Fundamentals

2.5.1 Particle Growth

At an interface between a matrix and precipitate phase, the structure, composition, or both can change discontinuously. The discontinuities are maintained during the motion of this interface, thus constituting the growth of the precipitate phase. In many cases of transformation, the product has a different chemical composition than

the parent phase. In these cases the velocity of interfacial motion depends on the mobility of the atoms in the matrix and rate of transfer across the interface.

If we consider the precipitation of a particle growing in a matrix in a multicomponent system, mass balance must be satisfied at the interface for each element. Zener [99] presented the solution for a binary system assuming (1) growth is isothermal, (2) growth is controlled by diffusion of solute into the matrix; (3) the interface compositions are given by local equilibrium; (4) the diffusion coefficient in the matrix is independent of composition; (5) the growth preserves the precipitate shape; and (6) growth occurs in a semi-infinite medium.

Under these assumptions, the one-dimensional solution for particle growth is shown in **Figure 11** where the solute concentration profile is adjacent to the moving interface in a two component system.

From Fick's first law, the flux at the interface is given by:

$$J_{x=x^I} = -D\left(\frac{d\chi}{dx}\right)_{x=x^I} \tag{19}$$

Where:
$\boldsymbol{x}$ is the coordinate normal to the interface
D is the diffusion coefficient of the solute
$\boldsymbol{x^I}$ is the position of the interface

To maintain the concentrations and at the interface, the flux must be equal to the rate at which the solute is partitioned such that:

$$J_{x=x^I} = v\left(\chi^{\beta\alpha} - \chi^{\alpha\beta}\right) \tag{20}$$

Where v is the interface velocity. Using the Zener approximation:

$$\left(\frac{d\chi}{dx}\right)_{x=x^I} = \frac{\left(\chi^{\alpha\beta} - \bar{\chi}\right)}{L} \tag{21}$$

Where L in the nominal diffusion distance, which from conservation of mass can be calculated as:

$$L = 2x^I \frac{(\chi^{\beta\alpha} - \bar{\chi})}{(\bar{\chi} - \chi^{\alpha\beta})} \tag{22}$$

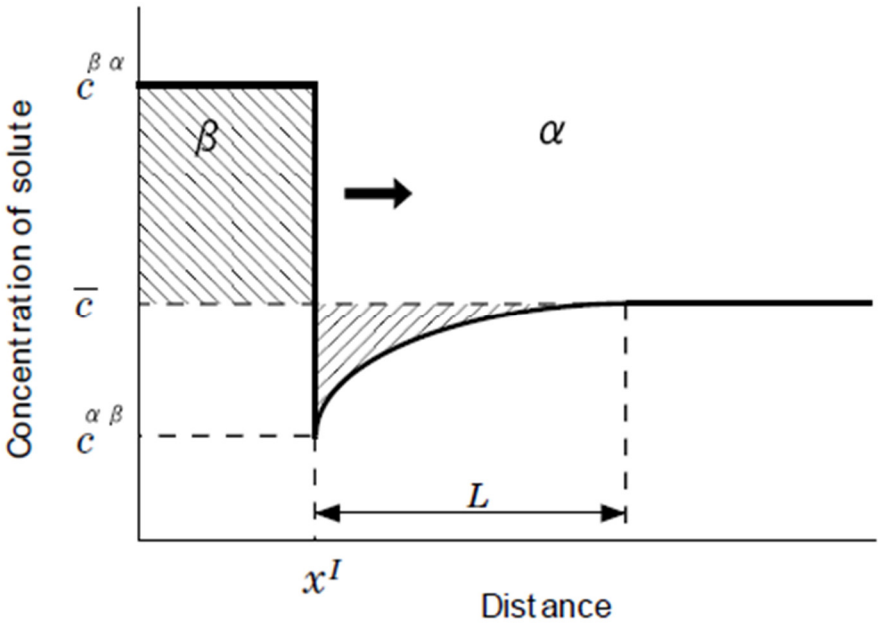

Figure 11: General model of solute mole fraction at the interface between a matrix phase α and a growing precipitate phase β.

From equations 19 through 22 above, the interface velocity can be determined as:

$$v = \frac{D}{2x^I} \frac{(\bar{\chi} - \chi^{\alpha\beta})^2}{(\chi^{\beta\alpha} - \chi^{\alpha\beta})(\chi^{\beta\alpha} - \bar{\chi})} \tag{23}$$

For the case investigated in this study of alloy carbide precipitation, in which the solute elements are Cr and Mo present as intentional alloying elements in the HY system, $\chi^{\beta\alpha}$ is much larger than $\bar{\chi}\ and\ \chi^{\alpha\beta}$. As a result, it can be assumed that $(\chi^{\beta\alpha} - \chi^{\alpha\beta})$ is nearly equal to $(\chi^{\beta\alpha} - \bar{\chi})$ such that equation 23 is reduced to:

$$2x^I v = D\Omega^2 \tag{24}$$

Where Ω is the supersaturation of the solute equal to:

$$\Omega = \frac{(\bar{\chi} - \chi^{\alpha\beta})}{(\chi^{\beta\alpha} - \chi^{\alpha\beta})} \tag{25}$$

Integrating equation 25 above considering that $v = dx^I/dt$ the parabolic growth law can be derived as:

$$x^I = \Omega\sqrt{Dt} \tag{26}$$

The precipitate dimension is thus found to be proportional to $\sqrt{Dt}$ and growth is parabolic such that the diffusion distance increases as the particle grows.

In three dimensions the parabolic growth expected for the diffusion-controlled growth of spherical particles can be defined as:

$$r^I = \alpha_3\sqrt{Dt} \tag{27}$$

Where r^I is the radius of the growing particle and α_3 is a proportionality constant similar to Ω in the 2-D solution. The growth velocity in the 3-D case is given by:

$$v = \frac{dr^I}{dt} = \frac{D}{c^{\beta\alpha} - c^{\alpha\beta}} \left(\frac{\partial c}{\partial r}\right)_{r=r^I} \tag{28}$$

In order to solve α_3 a solution to Fick's second law is necessary. The boundary conditions for the solution in this case are $c(r, o) = \bar{c}$ and $c(r^I, t) = c^{\alpha\beta}$. Zener showed that if $c^{\alpha\beta}$ is constant, then the distribution of solute is given by:

$$c(r,t) = \bar{c} + (c^{\alpha\beta} - \bar{c}) \frac{\phi\left(\frac{r}{\sqrt{Dt}}\right)}{\phi\left(\frac{r^I}{\sqrt{Dt}}\right)} \tag{29}$$

$$where\ \phi(x) = \int_x^{\infty} \eta^{-2} \exp\left(\frac{-\eta^2}{4}\right) d\eta \tag{30}$$

For 3-D growth:

$$\frac{r^I}{\sqrt{Dt}} = \alpha_3 = C_2\sqrt{2}\sqrt{\frac{\bar{c} - c^{\alpha\beta}}{c^{\beta\alpha} - \bar{c}}} \tag{31}$$

Where C_2 varies from 1 to $\sqrt{3}$ as $\bar{c}$ varies from $c^{\alpha\beta}$ to $c^{\beta\alpha}$. Thus the parabolic growth law in 3-D is defined and can be applied for cases where any capillary effect on the equilibrium concentration is sufficiently small, which is valid for spherical particles such as $M_{23}C_6$ carbides.

For the case of carbides with a needle morphology, such as M_7C_3 carbides, a different model must be used as the growth is substantially impacted by the capillary effect due to the small radius of curvature at the interface. The Zener model assumes that the tip of a needle is a hemispherical head such that the composition of the α phase at the interface, $c_r^{\alpha\beta}$, is constant over a curved surface. **Figure 12** is a schematic of the compositional profile across the interface in which the equilibrium mole fraction in the matrix at the tip is increased relative to that for a planar interface, $c^{\alpha\beta}$, due to the Gibbs-Thomson effect. The mole fraction gradient of the solute element is $\left(\bar{c} - c_r^{\alpha\beta}\right)/L$. If the curvature of the interface does not change during growth than the growth velocity can be given as:

$$v = \frac{D}{r^{IC}}\Omega_r \tag{32}$$

Where the supersaturation due to the capillary effect is given by:

$$\Omega_r = \frac{\bar{c} - c_r^{\alpha\beta}}{c_r^{\beta\alpha} - c_r^{\alpha\beta}} \tag{33}$$

Assuming $c_r^{\beta\alpha} - c_r^{\alpha\beta}$ is approximately equal to $c_r^{\alpha\beta} - c_r^{\beta\alpha}$ this can be reduced to:

$$\Omega_r = \left(1 - \frac{r_c}{r^{IC}}\right)\Omega \tag{34}$$

Where r_c is the critical tip radius of a needle such that $\Omega_r = 0$ and no growth proceeds.

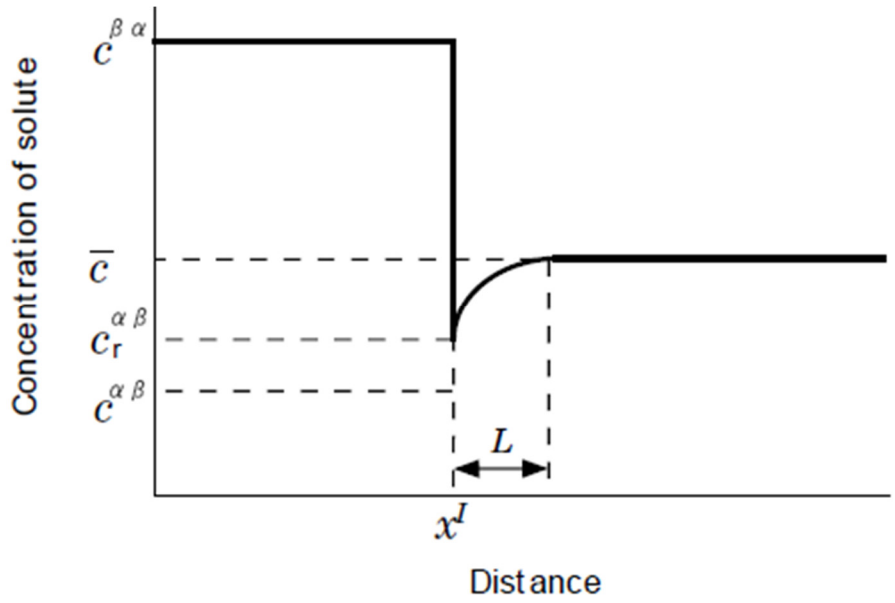

Figure 12: Solute mole fraction at the interface between a matrix phase α and a growing precipitate phase β for the case of a needle shaped precipitate.

2.5.2 Particle Coarsening

Coarsening occurs due to the total energy reduction of the system by eliminating interfaces. To accomplish the energy reduction, large particles grow more rapidly than small particles, and they grow at the expense of smaller particles in classical coarsening. The average particle size thus increases with aging time. Coarsening has slow kinetics because of the small energies associated with the interfaces compared with the free energy change that accompanies precipitation. Ostwald ripening can therefore be assumed to occur after the predominant precipitation as already occurred. For spherical particles coarsening theory is defined as follow [100], [101]:

$$\bar{r}^3 - r_0^3 = \left(\frac{8\sigma v^\beta D c^{\alpha\beta}}{9kT}\right) t \tag{35}$$

Where:
$\bar{r}^3$ is the average particle volume
r_0^3 is the initial average particle volume
v^{β} is the atomic volume of the β phase
D is the solute diffusion coefficient
σ is the interfacial energy
$c^{\alpha\beta}$ is the equilibrium solute concentration in the matrix
k is Boltzmann's constant
t is time

This relationship remains valid when the equilibrium volume fraction of the β phase is small.

The theory of particle coarsening was developed by Lifshitz and Slyozov and independently by Wagner, and is known as LSW theory. The LSW theory applies to Ostwaldian systems consisting of a solute-lean matrix with solute-rich particles. Excess free energy associated with the particles' interfacial surface area leads to thermodynamic instability tending to decrease this surface free energy by the process of particle coarsening. The dissolution of the particles depends on their radius of curvature, described by the Gibbs-Thompson relation in Equation 36.

$$C_r = C_\infty \left(1 + \frac{2\gamma V_m}{RTr}\right) \tag{36}$$

Where C_r is the solute concentration of matrix near a particle of radius r, C_∞ is the equilibrium solute concentration in matrix, γ is the interface free energy, V_m is the molar volume, R is the gas constant and T is the temperature.

As the curvature of the particle increases, the solute concentration in the matrix adjacent to the particle increases. The concentration gradient drives the solute to diffuse from the small particles towards the large particles via particle coarsening. While maintaining a constant volume fraction, the small particles shrink as the larger ones

grow. With time, the number density of the particles decreases as the mean radius increases.

2.5.3 Activation Energy

To determine the activation energy, the parameter, $Ln[K]$, is the intercept and is related to temperature by:

$$Ln[K] = Ln[K'] - Q/RT \tag{37}$$

The change in slope Q/R of the line $Ln[K]\ vs\ 1/T$ would suggest that the rate-controlling mechanism changes towards bulk diffusion as the temperature is increased. In the LSW theory, n represents the diffusion path mechanism and Q represents the 'bottleneck' or barrier for the slowest diffusing species.

The coarsening kinetics may not solely be controlled by dislocation pipe, interface, or bulk diffusion. **Figure 13** shows the rate controlling mechanisms as a function of inverse temperature. Bulk diffusion has larger diffusivity at higher temperatures, while grain boundary diffusion is larger at lower temperatures. The apparent diffusivity is the contribution of both mechanisms, given by:

$$\mathrm{D_{app}} = \mathrm{D_l} + \mathrm{D_b}\,\delta/\mathrm{d} \tag{38}$$

where D_l is the diffusivity of the lattice or bulk, D_b, is the diffusivity of grain boundary or interface, δ is the effective width of grain boundary, and d is the effective mean grain size.

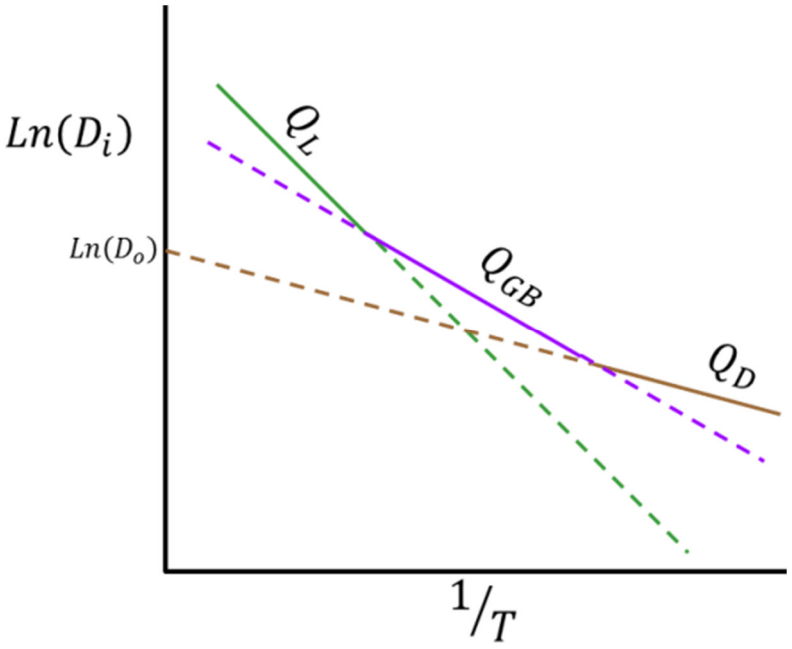

Figure 13: Diffusion mechanism changes as a function of temperature

The mutual exchange of fluxes in coarsening can only occur by the process of long-range diffusion. Diffusion is a process of mass transport by atomic movement under the influence of thermal energy and chemical potential gradient. Small atoms, such as C, can diffuse via interstitial mechanism. Larger atoms, such as Fe and Cr, proceed via substitutional diffusion. Defects, such as dislocations and grain boundaries, play a role in diffusion due to their open structure. The lower activation barrier in defects provides a higher diffusion rate than through the lattice. Diffusion on the surface has the lowest activation energy because the top layer is effectively entirely vacancies.

The slope of the diffusion coefficient versus inverse temperatures gives the activation barrier of diffusion (Q) from the Arrhenius equation given by:

$$D = D_o \, Exp[-Q/RT] \tag{39}$$

Where:
D is m^2/s
T is temperature in *K*
R is the ideal gas constant 8.314 J/mol K
Q is in J/mol

Activation energies increase in order from surface to dislocation pipe to grain boundary to lattice or bulk diffusion. Lower activation energy implies higher rates of diffusion. Lattice diffusion is dominant at high temperatures, where there is sufficient energy from atomic vibrations to overcome the activation barrier. Lattice diffusion is faster in b.c.c open crystal structures compared to f.c.c closed packed ones.

2.6 Industrial Steel Manufacturing Processes

2.6.1 Melting

Electric arc and induction are the most common methods of melting metal for steel manufacture. In this work only direct electric arc furnace melting has been used. The three phase direct arc furnace consists of a vessel with a refractory bottom and sidewalls, and a refractory roof with three carbon electrodes projecting down toward the charge. An electric current arcs from the graphite electrodes to the metal in the furnace. The arc is controlled by continuous repositioning of the individual electrodes. The electric current leaves an electrode via the arc, flows through the metal charges, and exits the furnace via the arcs developed by the other electrodes. The metal is subsequently heated by the current flow and from the heat generated in the arcs.

Several types of refractories are used during the melting and refining process. The principle types of refractories are classified as basic, acid, and neutral where the basicity (V) of the slag formed on the surface of the molten metal bath is defined in

Equation 40. When V is less than one, the basicity is considered acid, more than one is basic, and approximately one is neutral.

$$V = {\%\, CaO + \%\, MgO}/{\%\, SiO_2} \tag{40}$$

The most ideal set-up is for the refractories to be inert, and results in no reactions with the molten steel. The refractories used strongly influence the type of processing as detailed below.

After initial melting is completed, the primary reaction used for processing of the molten metal is called boiling and occurs at temperature above (1510°C). Oxygen reacts with carbon causing the production of carbon monoxide gas bubbles at the bottom of the molten bath. These bubbles rise through the metals such that the surface appears to be boiling, hence the name of the reaction. Oxygen is injected into the bath or added via the introduction of iron oxide. As hydrogen and nitrogen are highly soluble in liquid iron these levels must be reduced below the solid solubility level in order to prevent defect formation upon solidification. This is accomplished via hydrogen migration into the rising bubbles of carbon monoxide, which then leaves the metal during the bubble. The governing reactions are:

$$4\, Cr_{(bath)} + 3\, O_2 \rightarrow 2\, Cr_2O_{3(slag)} \tag{41}$$

$$Cr_2O_{3(slag)} + 3C_{(bath)} \rightarrow 3CO_{(gas)} + 2Cr_{(bath)} \tag{42}$$

Removal of harmful embrittling elements is key for the manufacturing of steel with high impact toughness such as the HY alloys used in this study. To remove phosphorus, a high calcium oxide content slag is used which contains large amounts of iron oxides. Phosphorous and all other oxidizable elements react with the oxidizing slag and become part of the slag which can then easily be removed. If the high oxide

content of the slag is not retained, the slag containing the phosphorous can revert and return phosphorous to the melt. [102] To prevent this revert process the usual practice is to manually remove the slag from the molten bath, thus permanently removing the phosphorous from the furnace. New slag is then charged and melted for follow on operations.

The removal of sulfur from the molten bath is done under a slag with a high content of calcium oxide and high basicity. In order to remove sulfur, this slag must be reducing such that it is free of iron oxides, the opposition of the condition required for the removal of phosphorus. The slag is generally made reducing by the addition of silicon, carbon, aluminum, or other reducers to the slag in order to either remove or tie up the non-desirable iron oxides. The sulfur from the metals then chemically combines into the reducing slag and becomes part of it as long as the composition of the slag remains reducing. Just as with the removal of phosphorous, the sulfur laden slag can then simply be mechanically removed from the top of the melt.

It is during this process that the majority of hydrogen and nitrogen gas pick up is accomplished. Hydrogen is readily available during any non-vacuum based melting process simply from the water vapor in the air. **Figure 14** shows the hydrogen and nitrogen solubility in steel and a function of temperature.

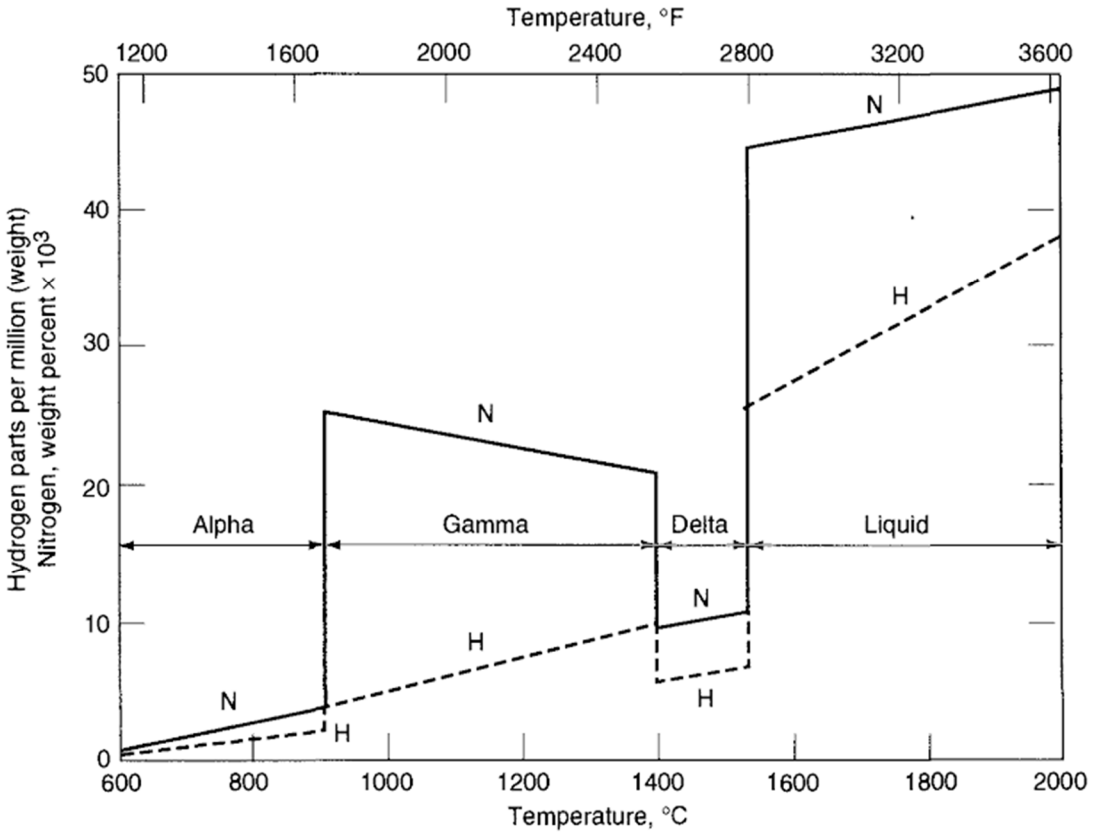

Figure 14: Hydrogen and nitrogen solubility in iron, reprinted with permission from the Steel Founders Society of America from the 6th addition of the steel castings handbook [103]

2.6.2 AOD Processing

Argon Oxygen Degasser (AOD) vessels are used to further process the metal for use in applications where primary furnaces are unable to obtain the desired chemical composition. The AOD vessel permits easier control, refining, and removal of gases from the molten metal and is considered a stage of secondary refining. The metal is first melted and processed in a conventional arc or induction furnace as detailed in the preceding section. Prior to transfer to the AOD a slag cover is added to the vessel.

During the AOD secondary refinement process, gaseous nitrogen or argon is combined with oxygen gas and injected into the metal through multiple pipes known

as tuyeres near the bottom of the vessel or through a submerged top lance, or combination of both. Gaseous oxygen is injected in combination with argon or nitrogen at carefully controlled flow rates and specific ratios to control the oxidation of elements contained within the molten bath while controlling molten bath temperature.

Heat is generated by the exothermic oxidation of silicon, manganese, chromium, iron, and aluminum, where the oxidation of silicon and aluminum provide the majority of the heat source. As with the electric arc furnace, a synthetic slag is usually calcium rich to maintain a high basicity ratio, and is added to the steel to provide a medium for oxidation products. [103]

The first stage of the AOD process is the removal of carbon via the injection of oxygen called decarburization, but first before this is initiated naturally any residual Al and/or Si is removed due to their higher affinity for oxygen as depicted by the Ellingham diagram. During de-carburation phosphorous can be oxidized, low melting point elements such as tin, zinc, and lead are volatilized, and hydrogen and nitrogen concentrations are reduced via the same process previously discussed for the electric arc furnace. The removal of carbon to carbon monoxide via the reaction:

$$2\,C_{(bath)} + O_{2_{(gas)}} \rightarrow 2CO_{(gas)} \qquad (43)$$

is an endothermic reaction and provides no heat into the molten steel bath. However, in parallel with the carbon reaction, removal of Mn, Cr, and Fe which are exothermic in nature counteract the cooling effect of carbon removal. [104]

The second phase of the AOD operation is commonly known as the reduction phase. This is where desirable elements which have been inadvertently oxidized during decarburization can be reverted back into the steel from the convertor slag. These

elements may include Mn, Cr, Fe and others. The process involves adding to the AOD convertor vessel an element of sufficient quantity having a higher affinity for oxygen than the metal oxides within the slag which are to be recovered into the molten metal bath. [105]

Sulphur removal is performed similarly to the practices discussed previously for the basic arc furnace with the primary difference being that the AOD process increases reaction speeds mainly due to the better stirring of the molten bath accomplished via the AOD convertor argon injection.

The final operations bring the metal to the target chemical composition and temperature. Analytical sampling is followed by alloying additions to either increase or dilute measured heat elemental composition. Heating is accomplished by adding aluminum or silicon along with oxygen gas injection in order to drive an exothermic reaction. Finally, nitrogen is controlled by either bubbling argon at the conclusion of composition refining or bubbling nitrogen to either remove or add it respectively. [105]

Chapter 3: Experimental Techniques

This chapter provides the details of the characterization techniques employed throughout the course of this work. The evaluation of mechanical response via tensile, Charpy, and Dynamic Tear testing is discussed. The evaluation of microstructures and carbides via optimal, SEM, and TEM techniques is subsequently detailed. The specific sample manufacturing techniques used in the follow on work is then detailed along with test specimen locations.

Section 3.1 through 3.3 details the general techniques for mechanical testing, metallographic characterization, and sample manufacture that were employed throughout this work. Sections 3.4 through 3.7 detail specific experimental procedures employed for the primary studies in approximately chronological order; Hydrogen treatment studies (3.4), Embrittlement and recovery rate studies (3.5), Carbide studies (3.6), and Industrial treatment development (3.7). Finally, sections 3.8 and 3.9 detail the methods of analytical techniques employed of CALPHAD and statistical analysis, respectively.

3.1 Mechanical Testing

3.1.1 Quasi Static Tensile Testing

Tensile test specimens were machined following specifications established in ASTM E8-13a for cylindrical specimens with dimensions containing a 12.5mm +/- 0.2mm (0.500” +/- 0.010”) gauge diameter and a 50mm +/- 0.1mm (2.000” +/- 0.005”) gauge length. The cylindrical specimens are machined with threaded ends on either side of the gauge which are then able to be screwed into the tensile test fixtures. The

specimens were tested at room temperature in tension using a Tinius Olsen 60,000lb Super "L" machine and a Denison Mayes Universal Tensile testing machine with 500kN capacity, calibrated from 450kN to 5.5 kN calibrated to E8/E370 ASTM standards. 0.2% offset yield stress (σ_y), ultimate tensile strength (UTS), and ductility were measured following standard procedures laid out in the ASTM standards. Errors are calculated as twice the standard error of the mean.

The ductility of the specimens were measured in two different ways: total elongation (%EL), and percent reduction of area (%RA). The %EL values were measured by marking the initial gauge length as delineated by the extensometer and measuring the final elongated length by a standard caliper. Likewise, the %RA values were measured using a standard caliper and averaging the maximum and minimum diameter of the necked region following fracture. Tensile ductility measurements are important for measuring the degree of hydrogen embrittlement, as this is characterized by a reduction in ductility under slow strain rate testing.

3.1.2 Rockwell and Brinell Hardness

Specimens were ground and polished to 800 grit surface finish employing standard procedures. The specimens were tested using a Wilson Universal Hardness Tester – Model Reicherter UH250 tester with a Brinell 5mm indenter, a load of 250 kgf, and dwell time of 10 s in accordance with the ASTM E10-17 standard procedures. The average of five measurements was reported and the ± 2σ errors were based on the standard error of the mean. The hardness measurements were calculated by dividing the parameters of load force (F) over the area of the indent diagonals (d_1 and d_2).

3.1.3 Charpy V-notch Impact Toughness (CVN)

The CVN specimens were fabricated in accordance with the ASTM E23-12c standard from the specimen blanks. The $55\,\text{mm} \times 10\,\text{mm} \times 10\,\text{mm}$ CVN specimens were tested at -73°C and -18°C employing a Tinius Olsen IT406 and IT264 test frames and a Denison Mayes 300J capacity pendulum Charpy tester Model number 6705U calibrated to ASTM E23 and used following the ASTM standard test procedures. Specimens were chilled via use of a Charpy-Cool and a methanol bath with temperature measured via a thermocouple in the bath. Each test specimen was left to soak in the bath for a minimum of 1 hour in accordance with specification requirements to ensure a uniform temperature profile throughout the specimen. The absorbed impact energy was measured, and fracture morphology was observed for each specimen. The average of three measurements is reported for each treatment condition, and the reported errors are based on the standard error of the mean.

3.2 Microstructural Characterization and Fractography

3.2.1 Optical Microscopy

Bulk fractography images of the broken Charpy impact specimen and Tensile specimens were taken with a Keyence VHX digital microscope. Light Metallography was performed employing a Buehler ViewMet, a Zeiss Inverted Metallograph, and the Keyence VHX digital microscope. The metallographic specimens were prepared by hot mounting in polyfast followed by polishing via carbon grit paper with water, and polishing with a diamond suspension of 9um, 3um, and 1um with a final polish using

0.1um OPU. Samples were etched for 10 seconds using a 2% nital solution and/or a Vielle's solution to reveal the microstructure and highlight the carbides.

3.2.2 Scanning Electron Microscope (SEM)

The scanning electron microscope (SEM) in the present investigation was used for numerous purposes: examining fracture surfaces of Charpy impact specimens at the micro-level; Energy Dispersive Spectroscopy (EDS) mapping of chemical partitioning; examination of carbide sizes, distributions, and compositions; and Electron Backscatter Diffraction (detailed in the next section).

Imaging of fractography surfaces, carbides, and EDS mapping were done by a Hitachi S-3400 Variable Pressure (VP) SEM instrument equipped with a Bruker QUANTAX XFLASH 4010 energy dispersive spectrometer (EDS) at acceleration voltages between 5 kV and 20 kV located at the Naval Surface Warfare Center – Carderock (NSWC-CD). In addition, the FEI Quanta 200FE SEM with EDAX and EBSD detectors was used at the Air Force Research Lab Munitions Directorate (AFRL/RW) at Eglin Air Force Base. Elemental maps of carbides in the bulk, at prior austenite grain boundaries, and martensite lathe boundary interfaces were acquired for 1200 s at 15 kV and low probe current. Line scales across carbides were acquired for 4000 x at 15 kV and low probe current. 15 kV was selected in each case to ensure the detection of all primary constituents of the carbides.

3.2.3 Electron Backscattered Diffraction (EBSD)

EBSD and/or Orientation Image Microscopy (OIM) is used to examine crystallographic orientation, texture and/or phase content of materials. EBSD is

performed using collected diffracted electrons, which produce a pattern of intersecting bands referred to as Kikuchi patterns or electron backscattered patterns (EBSP). This technique is performed using a scanning electron microscope equipped with a phosphor screen electron collector. In order for the electron capture to be sufficient, the sample is tilted in the chamber to allow for reflected electrons to be easily collected, typically at an angle of 70 degrees. The patterns of the collected electrons can be related to crystallographic features of the specimen. The bands themselves provide information about lattice structure, orientation, and spacings of atoms in crystal planes. Bands are transformed using Fourier patterns into Hough Patterns, where they correspond to peaks that give information about orientation and structure. These patterns are then computationally fit to possible user-identified candidate structures and expressed in terms of statistical confidence.

To prepare specimens for EBSD analysis an additional preparation step was taken of vibratory polishing at an intensity of 40% for 3 hours just prior to imaging. Both the SEMs and ARFL/RW and NSWC-CD were used to examine varied sample microstructure. Specimens were examined at 30kv with an excitation voltage of 2.00kv, a medium probe current, and 5.0 conditioning length. 5x5 detector binning was used with no EBSD gain and 11.58 exposure (~170 fps) at a tilt of 70 degrees. The static background was corrected, and the sub-dynamic background deleted. Finally, a normalized detector intensity of 600x was used with a 200nm step size and an approximate 200 x 140 μm scan area. OIM Analysis EDAX software was employed for the collection and analysis of EBSD data.

3.2.4 Transmission Electron Microscope (TEM)

The scanning/transmission electron microscope (STEM/TEM) in the present investigation were performed at the Army Research Lab in Aberdeen, MD.

In FEI, Bright field (BF) and high angle annular dark field (HAADF) micrographs were obtained in STEM mode on a Talos F200X equipped with XFEG and Super-X EDS technology. A JEOL 2100 LaB6 TEM instrument operating at 200 kV and a JEOL 2100 field emission gun (FEG) TEM instrument operating at 200 kV and equipped with an Oxford INCA 250 X-ray energy dispersive spectrometer (EDS) were employed to study the microstructural evolution.

TEM specimen preparation:

Two techniques to prepare TEM specimens were used, including ion milling to permit targeting of a grain boundary for investigation and jet-polishing.

At the Army Research Lab, the grain boundary area specimen for STEM imaging was prepared using Helios Plasma Dual Beam FIB. The process was the standard FIB prep process, thinning with 30 kV for the bulk of the milling then final polishing with 5 kV.

The specimens were punched from a mechanically thinned foil sample of approximately 200 μm. The foils were single-jet electropolished in 10 vol% perchloric acid ($HClO_4$) solution in acetic acid (CH_3COOH) at 0 °C and 20 V for 10 min. The foils were then subsequently ion-beam milled at a 10° milling angle, 5 kV, and 3 mA until perforation in a Fischione Model 1010 milling system.

TEM analysis:

The selected area electron diffraction (SAED) technique was used to identify the ferrite, austenite, cementite, $M_{23}C_6$ carbide, and M_7C_3 carbide in the foils. The TEM images and SAED patterns were analyzed using the Gatan Digital Micrograph Microscopy Suite software.

3.3 Study Sample Manufacturing Processes & Testing Locations

3.3.1 High Hydrogen Heat

The primary heat (#A) used for this study to determine the effectivity of varied heat treatment operations to neutralize monatomic hydrogen was manufactured with a modified process to introduce a high level of diffusible hydrogen. It was first melted in an electric arc furnace. Next it was transferred to an AOD vessel and refined via the standard treatments developed for an HY-80 heat. After refining and perfecting the chemical composition, the heat was tapped into a ladle and poured back into the arc furnace along with lime that had been intentionally aged for 48 hours. As quick-lime is hygroscopic, this aging resulted in pick-up of moisture from the environment and thus a source for hydrogen. The heat was then held in the arc furnace for one hour to adsorb as much hydrogen from the quick-lime as possible up to the solubility limit. Finally, the heat was tapped into a bottom pour ladle from which the test coupons were all poured. The resultant high hydrogen heats chemical composition is detailed in below.

3.3.2 High Phosphorus Heat

The second heat (#B) was also melted in an electric arc furnace followed by a transfer to an AOD and tap out in a bottom pour ladle for final pouring of test coupons. However, in this case aged lime was not used, and rather the best practices for

producing lower hydrogen content steel was employed. Residuals, particularly Phosphorus, were permitted to be at the higher end of specification allowable in order to have a heat that would bound the worst case for the rate and degree of temper embrittlement.

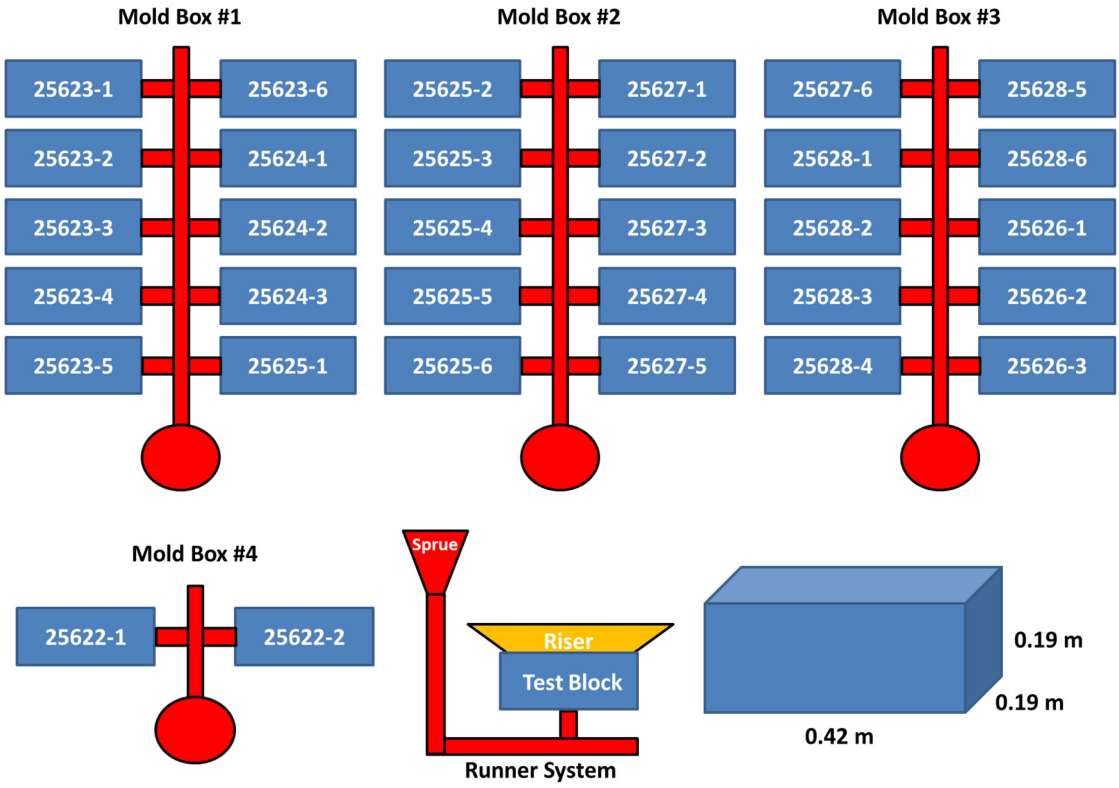

Figure 15: Runner system layout for high hydrogen blocks produced for Heat#A. The mold box size for the first three set of ten blocks was 1.52m x 2.44m (60" x 96"). The final mold box was 0.91m x 0.91m (36" x 36") and contained the last two test blocks. Samples were poured on Tuesday, 09/08/15. Pour temperature was 2850F. Nozzle size 3, R861-2519 Liner. Total pour weight 10800.

3.3.3 Industrial heats with standard melting practice

A set of industrial heats were selected from production material for follow-on study of hydrogen aging treatments. These test samples were processed with identical conditions as detailed in section 3.3.1 with the exception that the additional step of treated under aged lime was not included, such that these heats should have a nominal

level of absorbed hydrogen. The chemical composition of these heats is detailed in **Table 3** and **Table 4** with the remainder for all being Fe.

The third experimental heat (#C) explicitly for experimental studies was used to manufacture 8 test blocks for the purpose of further investigating the performance of hydrogen soaking treatments in the embrittlement range. The heat was similarly melted under electric arc and AOD processed with final taping out of a bottom pour ladle into the test coupon runner system. In this case all optimal processing conditions were followed with a target for a lower carbon equivalent composition. The residual levels for phosphorus and sulfur were considerably below specification requirements.

In the case of the test specimens produced to manufacture HT#C an alternate test block and testing configuration were used to match that used in industrial production. In this configuration four blanks were extracted in addition to the tensile and Charpy specimens from mid-thickness and quarter thickness. Three sets of blanks were used for Dynamic Tear test specimens for the samples achieving the closest to compliant mechanical response, with the remaining blanks used for follow on heat treatment studies.

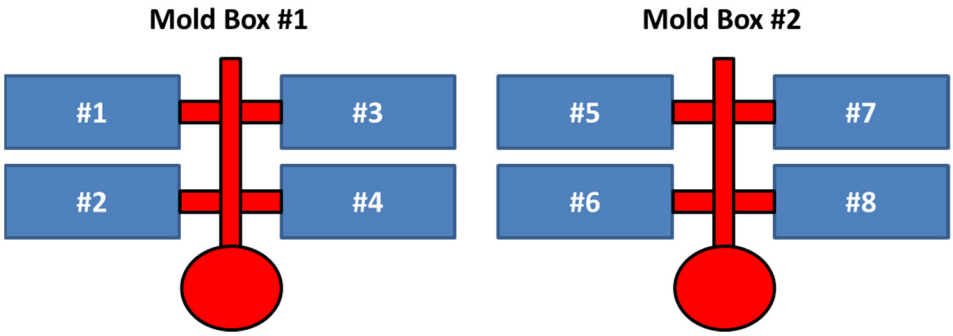

Figure 16: Heat #C mold design. Two identical flasks were used each containing 4 test blocks. The pour temperature was 1577°C.

Table 3: HY Chemical Composition – Experimental Heats (wt%)

Element	HT#A	HT#B	HT#C	HT#D
Carbon	0.205	0.15	0.15	0.18
Manganese	0.64	0.70	0.66	0.66
Silicon	0.41	0.39	0.33	0.41
Phosphorus	0.005	0.013	0.010	0.004
Sulfur	0.003	0.001	0.002	0.002
Molybdenum	0.42	0.56	0.57	0.37
Chromium	1.48	1.55	1.62	1.38
Nickel	3.15	3.17	3.15	2.96
Aluminum	0.007	0.018	0.017	0.011
Vanadium	0.004	0.005	0.004	0.006
Copper	0.03	0.06	0.013	0.10
Titanium	0.002	0.004	0.002	0.006
Tin	0.002	0.003	0.002	0.018
Arsenic	0.002	0.002	0.002	-
Antimony	<0.001	<0.001	<0.001	-
Nitrogen	0.01	0.005	0.006	-

Table 4: HY Chemical Composition – Selected Industrial Heats (wt%)

HEAT #	1	2	3	4	5	6	7	8
CARBON	0.150	0.170	0.172	0.175	0.181	0.184	0.190	0.190
MANGANESE	0.70	0.29	0.58	0.61	0.61	0.61	0.64	0.64
SILICON	0.39	0.33	0.42	0.34	0.30	0.36	0.38	0.35
PHOSPHORUS	0.013	0.005	0.003	0.007	0.004	0.004	0.004	0.004
SULFUR	0.001	0.002	< 0.001	0.004	< 0.001	< 0.001	< 0.001	< 0.001
MOLYBDENUM	0.56	0.48	0.32	0.41	0.39	0.45	0.48	0.53
CHROMIUM	1.55	1.74	1.44	1.44	1.45	1.50	1.42	1.42
NICKEL	3.17	3.13	3.06	2.97	3.09	3.20	3.12	3.16
ALUMINUM	0.018	-	0.009	0.037	-	0.011	-	0.014
VANADIUM	0.005	0.01	0.003	0.008	0.003	0.004	0.003	0.003
COPPER	0.06	0.11	0.17	0.11	0.10	0.07	0.10	0.13
TITANIUM	0.004	<0.01	< 0.001	0.003	< 0.001	< 0.001	< 0.001	< 0.001
TIN	0.003	0.01	0.005	0.009	0.005	0.003	0.005	0.006
ARSENIC	0.002	0.01	0.006	0.013	0.005	0.004	0.007	0.006
ANTIMONY	<0.001	<0.01	< 0.001	0.003	< 0.001	< 0.001	< 0.001	< 0.001
NITROGEN	0.005	-	0.0036	0.005	-	0.0053	-	0.0038

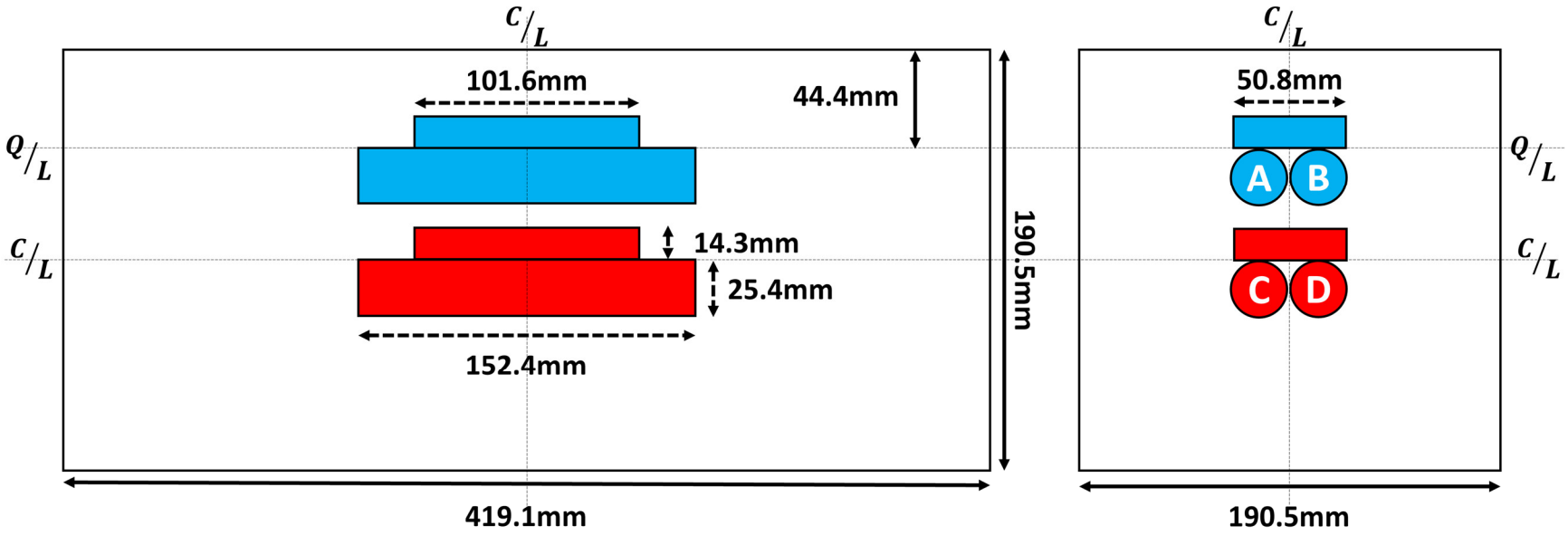

Figure 17: Test Specimen Layout for the varied assays detailed in **Table 5**, **Table 6**, and **Table 7**. (Note: Larger section size cast test blocks detailed in **Table 8** had specimen extraction in accordance with Ref. [44]) Q/L refers to quarterline or T/4, C/L refers to centerline or T/2. Red specimens are mid thickness (T/2) samples and blue specimens are quarter thickness (T/4) specimens. Round specimens are 12.827mm (0.505") diameter tensile samples, square specimens are 10mm x 10mm x 55mm. Charpy V-notch samples. Dimensions on drawings for specimens represent the extracted blanks that were subsequently machined into the mechanical test specimens. Cast tapers are not shown on this diagram. The cast riser was located at the bottom of the figure.

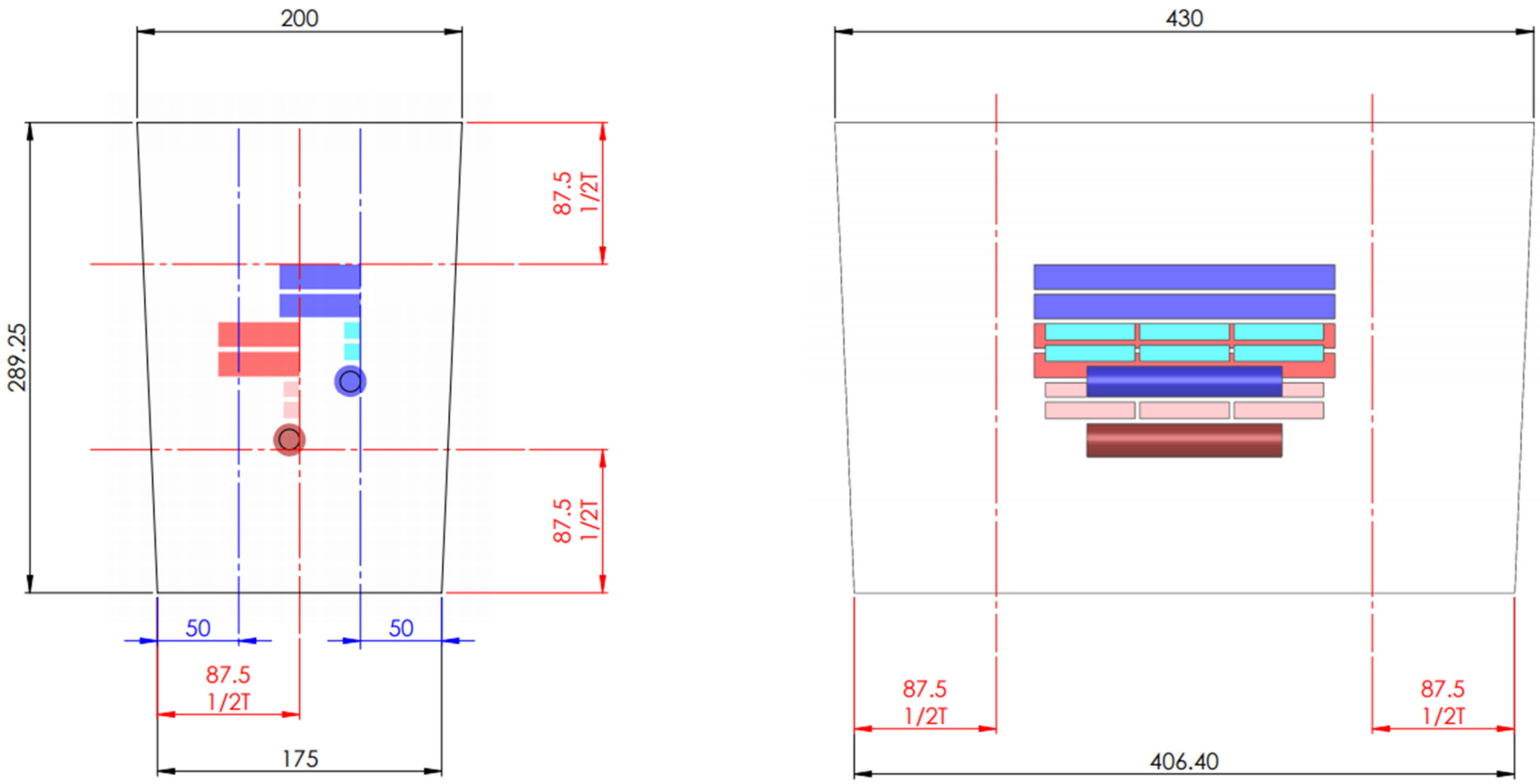

Figure 18: Test Specimen Layout for Embrittlement Range Soaking assays detailed in **Table 9**. Red specimens are mid thickness (T/2) samples and blue specimens are quarter thickness (T/4) specimens. Round specimens are 12.827mm (0.505") diameter tensile samples, square specimens are 10mm x 10mm x 55mm. Charpy V-notch samples, and the large rectangular specimens are for adjacent heat treatment studies. All dimensions are in mm.

3.4 Hydrogen Treatment Studies

3.4.1 High Hydrogen Heat Assays

From Heat#A; that was intentionally charged with hydrogen, an initial set of high hydrogen soak treatments were calculated using the equations and methodology present in section 2.5.1 at each 343°C and 371°C (650°F and 700°F) and executed in accordance with the heat treatment schedule detailed in **Figure 19** and **Table 5**.

A second set of trials was intended to study the ability to remove hydrogen via soaking in the embrittlement zone. 482°C (900°F) was selected as the heat soak temperature based on the literature review showing that at long soaking times that the embrittling element phosphorus diffused fastest in the range from 482°C to 510°C (900°F to 950°F). After the hydrogen removal treatment the steel samples were then re-austenitized and re-tempered with the intent of reversing the embrittlement in accordance with the heat treatment plan detailed in **Figure 20** and **Table 6**.

Follow on testing was designed to iterate on previous assays for determining optimal parameters for conducting hydrogen soaks within the embrittlement range. These trials explored the entire temper embrittlement range from 371°C – 593°C (700°F to 1100°F). For these trials an additional embrittlement recovery treatment was also added prior to re-austenitization conducted at 648°C (1200°F). In addition, the impact of aging time was examined at 537°C (1000°F). This second round of temper embrittlement soak trials were conducted in accordance with the heat treatment plan in **Figure 21** and **Table 7**.

Finally, industrial scale material was used to extrapolate results for 190.5 mm (7.5”) thick test block to test blocks up to 330.2 mm (13”) in thickness. The confirmation trial heat treatments were conducted in accordance with the heat treatment plan presented in **Figure 22** and **Table 8**. Note: The test blocks from Heat#A that were not detailed above were used for dislocation based treatments that were ultimately inconclusive and not presented in this dissertation.

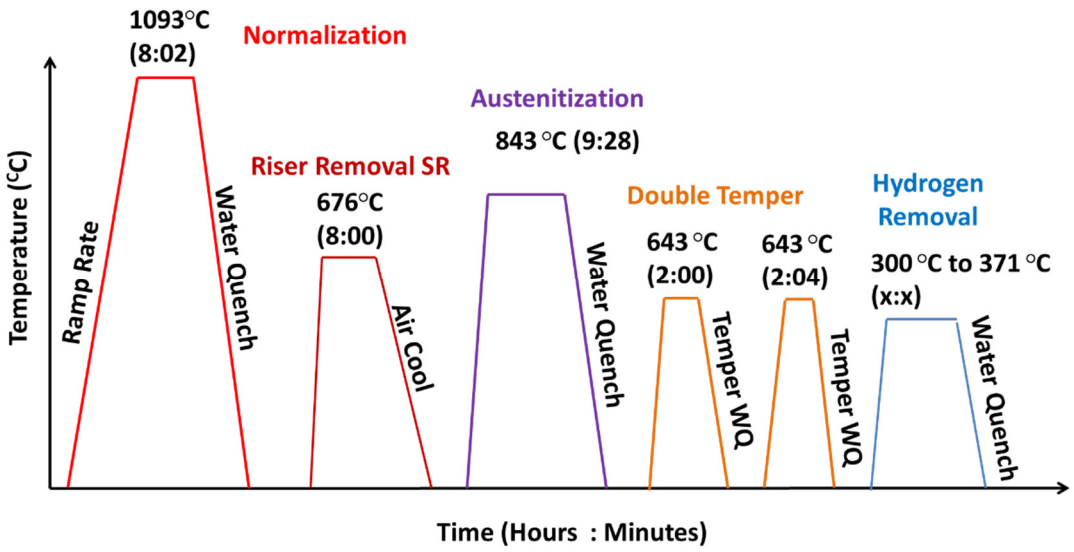

Figure 19: Heat Treatment for Initial Diffusion Based Treatments below the Embrittlement Range

Table 5: Hydrogen Aging Treatments below Embrittlement Range

SERIAL	ID	NORM	SR	AUST	TEMPER	TEMPER	SOAK TEMP	SOAK TIME
25625	1	1093°C for 8hrs 2 min WQ	767°C for 8 hrs Air Cool	843°C for 9 hrs 28 min WQ	646°C for 2hrs WQ	646°C for 2hrs 4 min WQ	N/A	N/A
25625	6						300°C	100 hrs
25623	1						343°C	20 hrs 53 min
25623	2						343°C	42 hrs 61 min
25623	3						343°C	66 hrs 39 min
25623	4						371°C	13 hrs 38 min
25623	5						371°C	31 hrs 10 min
25623	6						371°C	45 hrs 15 min

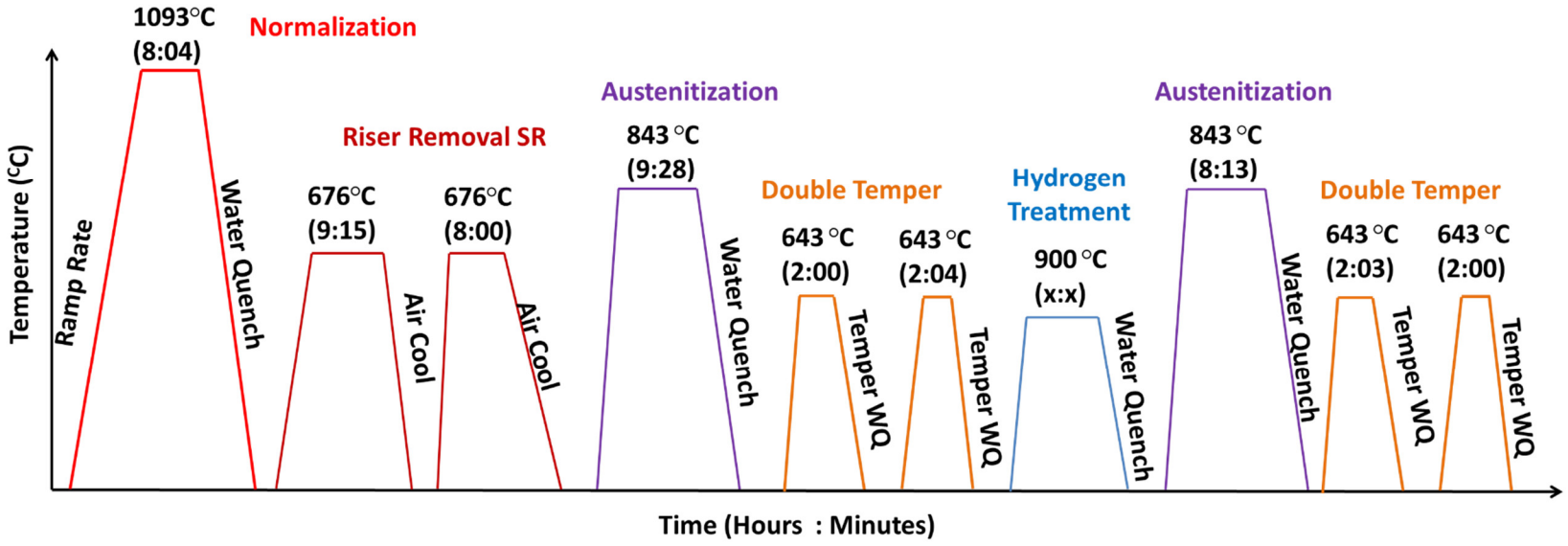

Figure 20: Heat Treatment for initial treatments at 482°C in the Embrittlement Range

Table 6: Hydrogen Aging Treatments within the Embrittlement Range

SERIAL	ID	NORM	SR	SR	AUST	TEMPER	TEMPER	SOAK TEMP	SOAK TIME	AUST	TEMPER	TEMPER
25625	5	1093°C for 8hrs 4 min WQ	676°C for 9 hrs 15 min AC	676°C for 8 hrs AC	843°C for 9 hrs 28 min WQ	646°C for 2hrs WQ	646°C for 2hrs 4 min WQ	N/A	N/A	843°C for 8 hrs 13 min WQ	646°C for 2hrs 3 min WQ	646°C for 2hrs WQ
25624	1							482°C	9 hrs 26 min			
25624	2							482°C	18 hrs 36 min			
25624	3							482°C	37 hrs 18 min			

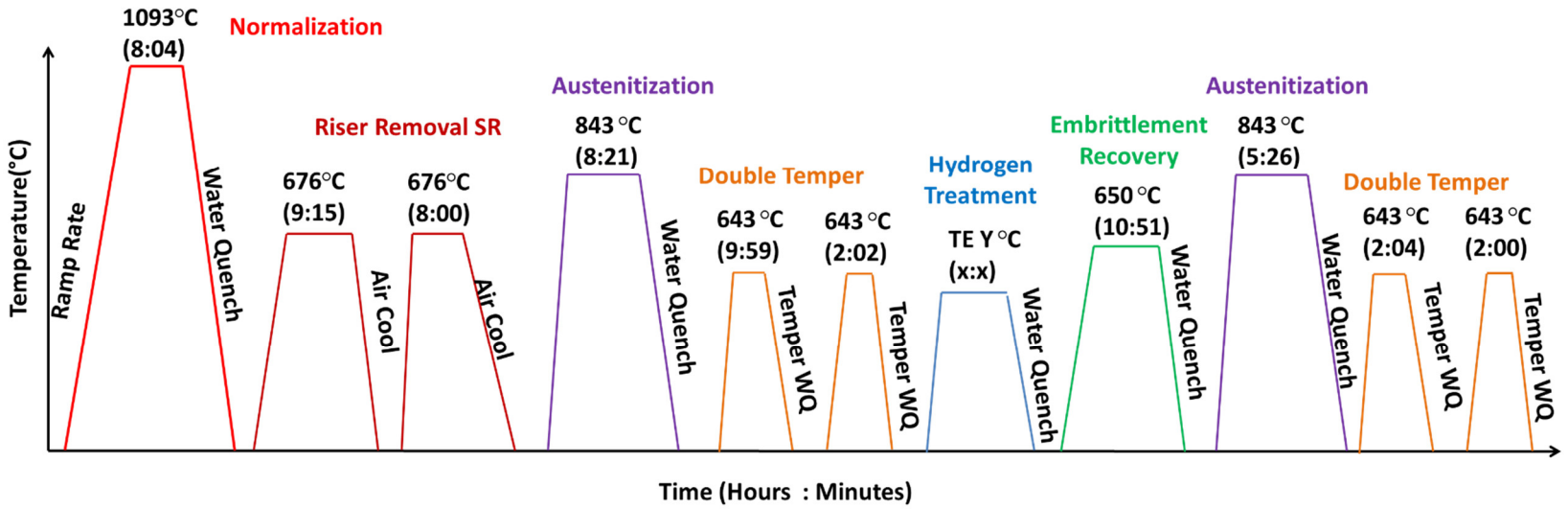

Figure 21: Heat Treatment for the second set of assays with hydrogen aging in the embrittlement range

Table 7: Hydrogen Aging Treatments within the embrittlement range with post soak recovery

SERIAL	ID	NORM	SR	SR	AUST	TEMPER	TEMPER	SOAK TEMP	SOAK TIME	RECOVER	AUST	TEMPER	TEMPER
25628	1	1093°C for 8hrs 4 min WQ	767°C for 8 hrs 15 min Air Cool	767°C for 8 hrs Air Cool	843°C for 8 hrs 21 min WQ	646°C for 2 hrs 1 min WQ	646°C for 2 hrs 2 min WQ	N/A	N/A	648°C for 10 hrs 51 min WQ	843°C for 5 hrs 26 min WQ	646°C for 2 hrs 4 min WQ	646°C for 2hrs WQ
25628	2							593°C	6 hrs				
25628	3							537°C	10 hrs				
25622	1								24 hrs				
25622	2								76 hrs 8 min				
25628	4							482°C	15 hrs				
25628	5							426°C	29 hrs 29 min				
25628	6							371°C	50 hrs				

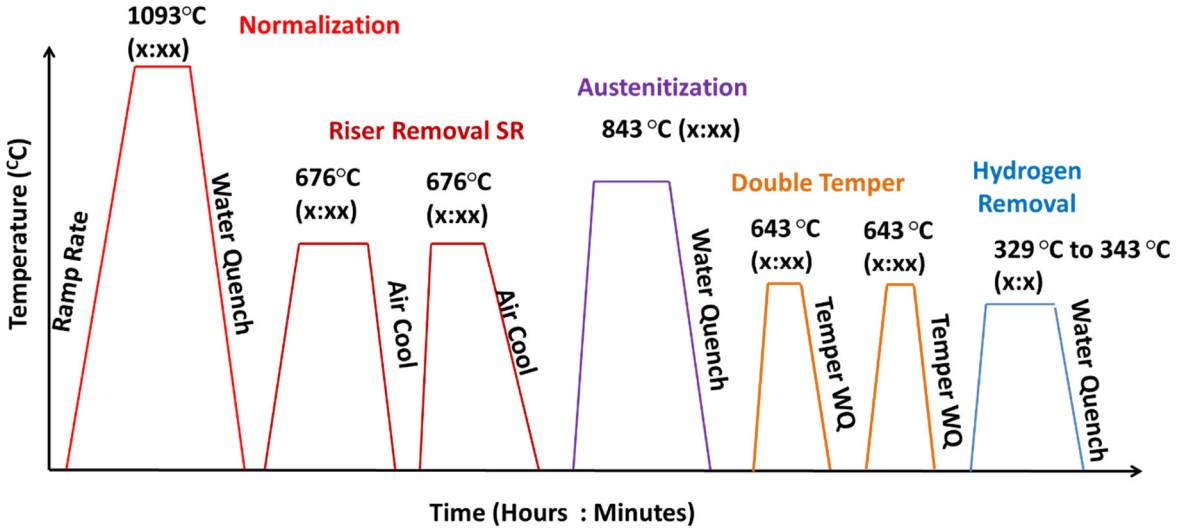

Figure 22: Heat treatment for industrial samples with hydrogen aging below the embrittlement range

Table 8: Hydrogen aging treatments below embrittlement range on production heats

SERIAL	ID	HT#	NORMALIZE		STRESS RELIEF		STRESS RELIEF		AUSTENTIZE		TEMPER		TEMPER		SOAK	
			°C	(Hr:min)	°C	(Hr:min)	°C	(Hr:min)	°C	(Hr:min)	°C	(Hr:min)	°C	(Hr:min)	°C	(Hr:min)
25626	3	279415	1093 - WQ	8:04	676 - AC	9:15	676 - AC	8:00	643 - WQ	8:21	643 - WQ	2:01	643 - WQ	2:02	625 - AC	87:00
25724	17	429614		8:17		13:07		8:16		6:41		2:00		2:00		87:00
25725	3	429615		8:05		9:54		14:19		7:00		2:04		2:00		205:04
25739	1	443015Y		8:54		12:11		13:59		20:31		2:34		2:34		314:06
25626	2	279415		8:04		9:15		8:00		8:01		2:05		2:02	650 - AC	72:25
25724	27	431214		10:01		10:00		10:20		5:20		2:10		2:00		72:25
25725	5	427115		8:35		10:08		10:17		19:08		2:00		2:00		161:15
25739	2	443015Y		8:54		12:11		13:59		20:31		2:34		2:34		324:47

3.4.2 Embrittlement range soak optimization

From Heat #C the eight test blocks were treated with varied heat treatments in accordance with the details in **Figure 23** and **Table 9**.

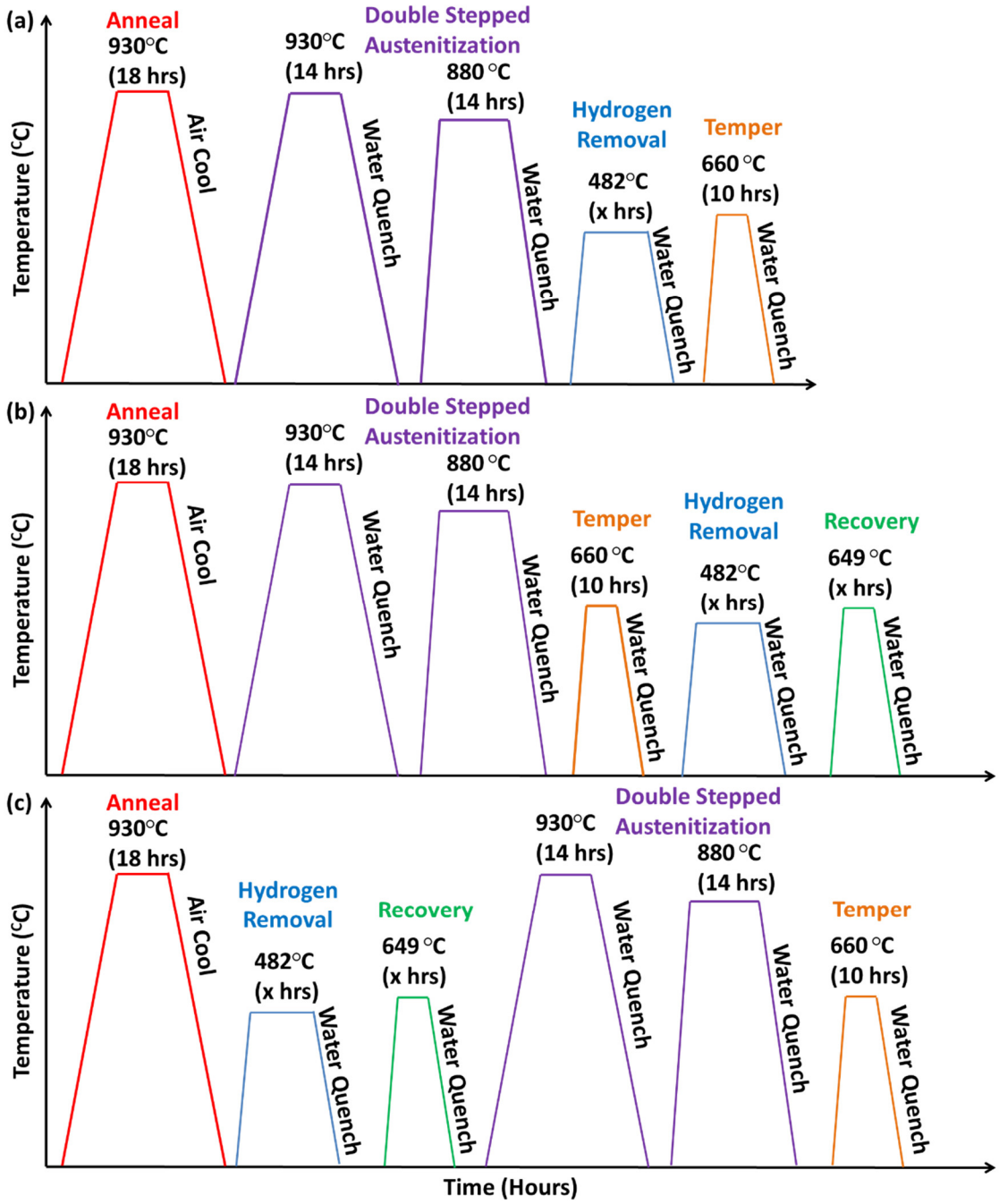

Figure 23: Heat treatment for heat #C studies on the impact of sequencing on embrittlement range hydrogen aging treatments

Table 9: Hydrogen aging treatments on HT#C

TREATMENT	ASSAY SET (A)			ASSAY SET (B)		ASSAY SET (C)	
	Block 1	Block 2	Block 3	Block 4	Block 5	Block 6	Block 7
	Mid-Treatment			Post-Treatment		Pre-Treatment	
482°C HYDROGEN AGE	2 hrs	6 hrs	15 hrs	2 hrs	15 hrs	2 hrs	15 hrs
649°C RECOVERY	Temper	Temper	Temper	6 hrs	10 hrs	6 hrs	10 hrs

These studies were done to determine the influence of treatment sequencing on the effectiveness of the hydrogen aging treatment. In addition, the use of temper operation as a dual purpose treatment that both tempers quenched martensite and recovers from temper embrittlement was studied.

The test blocks for this study were produced using a Zircon mould wash. Primary melting was executed in a 12 ton capacity inductotherm high frequency induction furnace and secondary refinement was done using a 9.5 ton capacity AOD convertor vessel.

3.5 Embrittlement and Recovery Rate Studies

To better understand the mechanisms and rate of temper embrittlement in cast HY-80, samples were subjected to embrittlement and recovery treatments after a typical industrial heat treatment from HT#D. The embrittlement rate was studied between 315°C and 565°C (600°F and 1050°F) at varied logarithmic time intervals up to 10,000 minutes. The embrittlement recovery rate was studied between 593°C and 704°C (1100°F and 1300°F) at logarithmic time intervals up to 1,000 minutes.

3.5.1 Material

The material used in this study is a commercial grade of HY-80 steel processed via standard electric arc melting techniques with follow-on secondary refining in an Argon Oxygen Degasser (AOD) (Heat #D in **Table 4**). The heat was poured into a series of 190mm (7.5 inch) square test blocks by 430 mm's (17 inches) in length. The test blocks for study received a standard industrial heat treatment for HY-80 of an austenitization followed by a double temper and low temperature hydrogen soak at shown in **Figure 25**. Blanks orientated transverse to the length of the test blocks were then extracted from the blanks for embrittlement and recovery rate treatments and marked for identification in accordance with **Figure 24**.

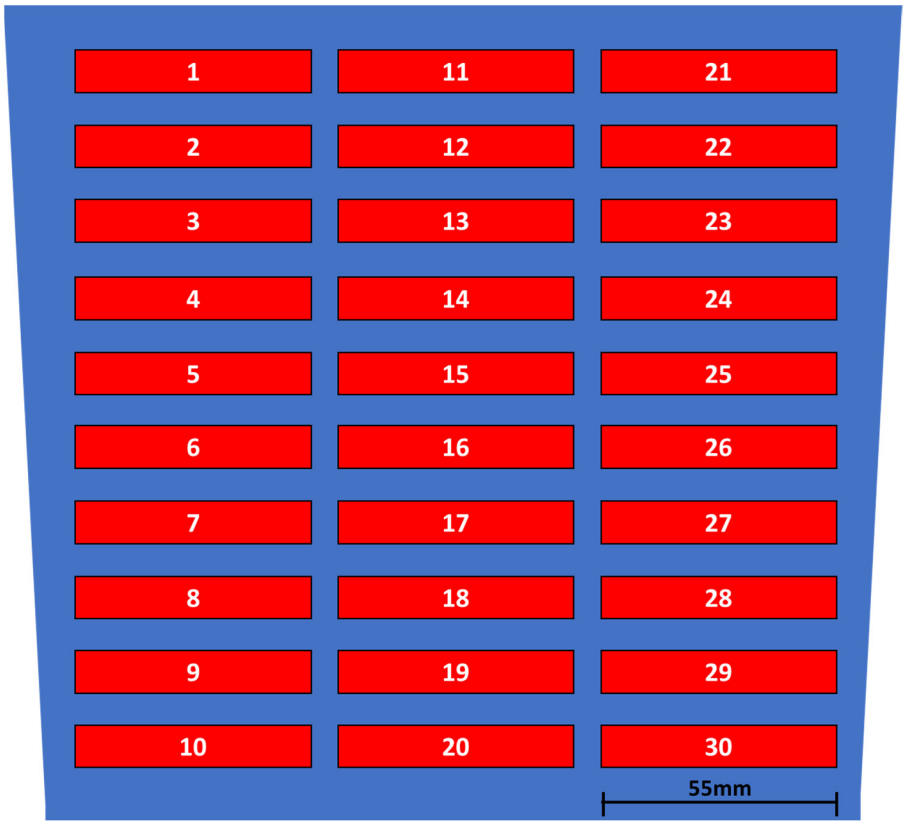

Figure 24: Charpy specimen extraction diagram for transverse test block slices from HT#D. Drag: bottom of the sheet; Cope: top of the sheet.

Specimens for each test temperature were all extracted from a transverse sheet of equal length from the end of a test block in order to normalize quench end effect. For each set of three Charpy specimens, one was extracted from a sub-surface location, one from a quarter thickness location, and one from the centerline of a transverse sheet again to normalize any differences starting microstructure and/or chemical segregation across a block.

3.5.2 Heat Treatment

The industrial heat treatments were carried out in a furnace certified to MIL-STD-1684D. The furnace was rated to within plus or minus 13.9°C. Three K type thermocouples were placed into the load and attached to test blocks. The attached thermocouples showed that the heat treatments were within 7°C degrees across the furnace load.

The subsequently applied embrittlement and recovery heat treatments were executed in a laboratory size oven (Model FB1315M Muffle Furnace) with an internal volume of 1.3L, manufactured by Thermo Scientific Thermolyne. The furnace was controlled by a K type thermocouple and the furnace was rated to be with plus or minus 1% of the set point temperature. Continuous monitoring of the furnace temperature was also conducted via a set of two K type thermocouples. Readouts were recorded on an Omega RDXL-SD thermocouple data logger.

The first set of specimens was extracted for the study of the embrittlement rate. The samples were treated between 315°C (600 °F) and 565°C (1050°F). In accordance with **Table 11** and **Table 10**.

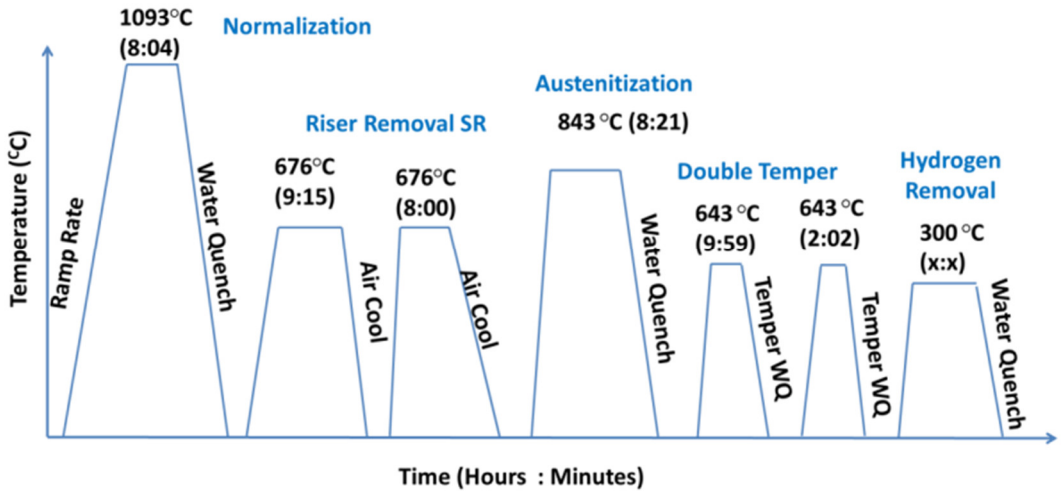

Figure 25: Initial Sample Heat Treatment

Table 10: Details of embrittlement rate treatment assays (510-565°C)

SET	IDS	NORM		AUST		TEMPER		TREATMENT	
		Temp	**Time**	**Temp**	**Time**	**Temp**	**Time**	**Temp (°C)**	**Time (min)**
C	**2,12,22**	1093°C (2000°F)	8 hrs 3 min - Water Quench	843°C (1550°F)	9 hrs 28 min - Water Quench	643°C (1190°F)	2 hrs - WQ / 2 hrs 4 min -WQ	510.0	500
C	**4,14,24**							510.0	1000
C	**6,16,26**							510.0	2000
C	**8,18,28**							510.0	5000
C	**10,20,30**							510.0	10000
A	**2,12,22**							537.8	500
A	**4,14,24**							537.8	1000
A	**6,16,26**							537.8	2000
A	**8,18,28**							537.8	5000
A	**10,20,30**							537.8	10000
D	**2,12,22**							565.6	500
D	**4,14,24**							565.6	1000
D	**6,16,26**							565.6	2000
D	**8,18,28**							565.6	5000
D	**10,20,30**							565.6	10000

Table 11: Details of embrittlement rate treatment assays (315-482°C)

SET	IDS	NORM		AUST		TEMPER		TREATMENT	
		Temp	**Time**	**Temp**	**Time**	**Temp**	**Time**	**Temp (°C)**	**Time (min)**
E	**9,19,29**	1093°C (2000°F)	8 hrs 3 min - Water Quench	843°C (1550°F)	9 hrs 28 min - Water Quench	643°C (1190°F)	2 hrs - Water Quench / 2 hrs 4 min - Water Quench	315.6	1000
E	**7,17,27**							315.6	2000
E	**3,5,25**							315.6	5000
E	**11,21,23**							315.6	10000
A	**9,19,29**							343.3	1000
A	**7,17,27**							343.3	2000
A	**3,5,25**							343.3	5000
A	**11,21,23**							343.3	10000
B	**9,19,29**							371.1	1000
B	**7,17,27**							371.1	2000
B	**3,5,25**							371.1	5000
B	**11,21,23**							371.1	10000
C	**9,19,29**							398.9	1000
C	**7,17,27**							398.9	2000
C	**3,5,25**							398.9	5000
C	**11,21,23**							398.9	10000
B	**2,12,22**							426.7	500
B	**4,14,24**							426.7	1000
B	**6,16,26**							426.7	2000
B	**8,18,28**							426.7	5000
B	**10,20,30**							426.7	10000
G	**2,12,22**							454.4	500
G	**4,14,24**							454.4	1000
G	**6,16,26**							454.4	2000
G	**8,18,28**							454.4	5000
G	**10,20,30**							454.4	10000
E	**2,12,22**							482.2	500
E	**4,14,24**							482.2	1000
E	**6,16,26**							482.2	2000
E	**8,18,28**							482.2	5000
E	**10,20,30**							482.2	10000

A second set of specimens was extracted for the study of the recovery rate from embrittlement. For these studies samples were pre-treated at 482°C (900°F) for 10,000 minutes, consistent with the maximum embrittlement temperature in previous work. Follow on treatments were executed between 593°C (600 °F) and 704°C (1050°F).

3.5.3 Mechanical Testing

Following either the embrittlement or recovery experimental treatments each blank was machined into a 10mm x 10mm x 55mm Charpy V notch specimen. Testing was performed at -73°C (100°F) in all cases with cooling achieved via a methanol bath with a 1 hour soak time in accordance with the procedure detailed in section 3.1.

3.5.4 Computational

The chemical composition was evaluated in Thermocalc to examine the thermodynamically stable system. Principally the projected amounts of all phases over the temperature ranges employed were found as well as the composition of those phases.

Table 12: Details of embrittlement recovery rate treatment assays

SET	IDS	NORM		AUST		TEMPER		PRE - TREAT		TREATMENT	
		Temp	**Time**	**Temp**	**Time**	**Temp**	**Time**	**Temp**	**Time**	**Temp (°C)**	**Time (min)**
I	**2,12,22**	1093°C (2000°F)	8 hrs 3 min - Water Quench	843°C (1550°F)	9 hrs 28 min - Water Quench	643°C (1190°F)	2 hrs - Water Quench / 2 hrs 4 min - Water Quench	482°C (900°F)	10000 min - Water Quench	593.3	50
I	**4,14,24**									593.3	100
I	**6,16,26**									593.3	200
I	**8,18,28**									593.3	320
I	**10,20,30**									593.3	500
I	**9,19,29**									593.3	1000
H	**2,12,22**									621.1	50
H	**4,14,24**									621.1	100
H	**6,16,26**									621.1	200
H	**8,18,28**									621.1	320
H	**10,20,30**									621.1	500
H	**9,19,29**									621.1	1000
J	**2,12,22**									648.9	50
J	**4,14,24**									648.9	100
J	**6,16,26**									648.9	200
J	**8,18,28**									648.9	320
J	**10,20,30**									648.9	500
J	**9,19,29**									648.9	1000
I	**7,17,27**									676.7	50
I	**3,5,25**									676.7	100
I	**11,21,23**									676.7	200
H	**7,17,27**									676.7	320
H	**3,5,25**									676.7	500
H	**11,21,23**									676.7	1000
G	**7,17,27**									704.4	50
G	**3,5,25**									704.4	100
G	**11,21,23**									704.4	200
J	**7,17,27**									704.4	320
J	**3,5,25**									704.4	500
J	**11,21,23**									704.4	1000

3.6 Metallographic Studies of Carbides

During the course of this work it became readily apparent that carbides may play a key role in mechanical response in the HY alloy system. A separate set of experiments was devised to determine kinetic constants.

3.6.1 Material

For this portion of the study four heats with varied target chemical compositions from four different manufacturers were used. They were selected in order to study a range of carbon equivalents. Each of the four compositions were HY-80 steel processed via standard electric arc melting techniques with follow-on secondary refining in an Argon Oxygen Degasser (AOD). They consisted of Heat #A, Heat #1, Heat #2, and Heat #7. The material for study received a standard industrial heat treatment for HY-80 according to each manufacturer's production heat treatment procedures prior to receipt. The specific austenitization and tempering treatments are proprietary and will not be detailed here-in; however, the main objective of the study of these samples was associated with the impact of chemical composition.

After receipt, the material was sectioned into 25.4 mm (1") thick sections for batch heat treatments followed by sectioning into approximately 10mm cubed specimens for individual specimen heat treatments.

3.6.2 Heat Treatment

The industrial heat treatments were carried out in varied furnaces all rated to within plus or minus 13.9°C. Three K type thermocouples were placed into the load

and attached to test blocks in each case. All furnaces used were surveyed to MIL-STD-1684D to ensure furnace uniformity.

The subsequently applied heat treatments were executed in a laboratory size oven (Model FB1315M Muffle Furnace) with an internal volume of 1.3L, manufactured by Thermo Scientific Thermolyne. The furnace was controlled by a K type thermocouple and the furnace was rated to be with plus or minus 1% of the set point temperature.

The first set of treatments was designed to generate a carbide time, temperature, transformation diagram for aging after austenitization from HT#A. The treatments were executed between 426°C and 676°C for aging times between 60 minutes and 10,000 minutes as detailed in **Table 13**.

The second set of treatments was designed to examine carbide coarsening and nucleation after austenitization and tempering in the range of temperatures of interest for hydrogen aging from HT#A and HT#7. The treatments were executed between 426°C and 537°C for aging times between 100 minutes and 40,000 minutes as detailed in **Table 14**.

The third set of treatments examined carbide dissolution in the tempering temperature range up to and exceeding the AC1 for each of the four selected heats in order to examine the validity of CALPHAD results. The treatments were executed between 665°C and 710°C for aging times between 120 minutes and 36,000 minutes as detailed in **Table 15**.

Table 13: Details of carbide aging TTT diagram treatments

ASSAY SET	AUST	AGING						
	843°C	426°C	482°C	537°C	593°C	621°C	648°C	676°C
CONTROL	120 min	N/A						
1		60 min - Water Quench						
2		200 min - Water Quench						
3		1,000 min - Water Quench						
4		2,000 min - Water Quench						
5		10,000 min - Water Quench						

Table 14: Details of carbide aging after temper treatments

ASSAY SET	AUST	TEMPER	AGING		
	843°C	637°C	426°C	482°C	537°C
CONTROL	120 min	240 min	N/A		
1			100 min - Water Quench		
2			1,000 min - Water Quench		
3			10,000 min - Water Quench		
4			40,000 min - Water Quench		

Table 15: Details of carbide aging TTT diagram treatments

ASSAY SET	NORM	AUST	TEMPER	AGING				
				665°C	676°C	687°C	698°C	710°C
CONTROL	898°C to 1093°C	843°C to 898°C	637°C to 676°C	N/A				
1				120 min - Water Quench				
2				840 min - Water Quench				
3				2,580 min - Water Quench				
4				36,000 min - Water Quench				

3.7 Chemical Composition Testing

Heat chemical composition was measured with an ARL 3460 Optical Emission Spectrometer using certified reference material traceable to NIST . Additional chemical composition measurements were made using a LECO Glow Discharge Spectrometer (GDS) 900 at Eglin Air Force Base. Drift calibrations were made prior to any measurements using reference material traceable to NIST. Finally, microscale chemical composition was measured via EDS on each the SEM at NSWCCD and AFRL/RW.

Chapter 4: Analytical Procedures Employed

This chapter provides the details of the analytical tools used to interpret data from tensile ductility mechanical response and SEM images of carbides within a microstructure. In addition, the details of CALPHAD modeling are provided.

The details of statistical analysis tools used to prepare data sets for filtering to determine what data sets could be reliably used for the development of models is included separately as Appendix A. Specifically, the presence of porosity on the fracture surface of tensile specimens and their detrimental impact on specimen ductility is addressed in the appendix, which can provide a false indication of the loss of ductility. A general overview of CALPHAD modeling and the methods used in this study is provided for the study of the anticipated volume fractions, nucleation regimes, and phase dissolution. Finally, methodologies for image analysis are detailed that extract carbide size, morphology, and distributions within a microstructure.

4.1 CALPHAD Modeling

Phase diagrams present visual representations of phase content and stability at equilibria as a function of state variables such as composition, pressure, temperature, etc. However, constructing phase diagrams for complex alloys is extremely time-consuming as well as expensive. An overview of CALPHAD (CALculation of PHAse Diagrams) methods and uses is detailed below, adopted from reference literature [106]–[109].

Multi-component phase-equilibria can be modeled using the CALPHAD methodology, which operates on finding states with minimized free energy. The Gibbs

free energy expresses the thermodynamic/chemical potential to perform work. At any given equilibrium state, Gibbs free energy is at a minimized state in a closed system, and can be represented as a general equation for chemical phases:

$$G_{system} = \min \sum_{p} G_p G_n \tag{44}$$

The contributions to the Gibbs energy of a phase ϕ can be written as the following:

$$G^{\phi} = G_T^{\phi}(T,x) + G_p^{\phi}(p,T,x)\ G_m^{\phi}(T_c,\beta_0,T,x) \tag{45}$$

Where:
$G_T(T,x)$ is the partial input to energy
T is temperature
x is composition
$G_p(p,T,x)$ is the contribution of the pressure
p is pressure
$G_m(T_C, \beta_o, T, x)$ is the magnetic contribution of the Curie temperature, and the average magnetic moment per atom.
Temperature dependence of the Gibbs free energy is commonly expressed as a power series of T:

$$G = a + bT + cT(\ln T) + \sum d_n * T^n \tag{46}$$

Where a, b, c and d_n are coefficients and n is an integer.

If solution phases are considered, the following equation describes Gibbs energy of formation in a binary model. This model can be extended to ternary and higher order solutions:

$$G^{\phi} = x_A G_A^0 + x_B G_B^0 + RT\{x_A ln x_A + x_B ln x_B\} + x_A x_B \sum_{i=0}^{n} G_i (x_A - x_B)^i \tag{47}$$

Where x_A and x_B represent mole fractions of each solution constituent and G_A^0 and G_B^0 are the states at standard temperature and pressure (reference state) of element A and B. The third term is the energy contribution from mixing. The final term consists of excess Gibbs energy. The sum of the terms $(x_A - x_B)^i$ refers to the Redlich-Kister polynomial used in regular solutions. As the term i changes, the shape of the Gibbs energy contribution from fourth polynomial also changes.

To extend values into higher component systems, free energy models are often simply added together to form higher order systems. Higher component systems can become much more complex; in many cases, binary component systems are assessed and data is extrapolated and extended to ternary and higher-order equations. Experiments are then done on higher order systems to correct discrepancies seen due to the extrapolation.

Thermocalc software was used to model systems at different equilibrium conditions. In most cases, the custom steel database included with Thermocalc were used to provide estimates of phase contents at equilibrium, primarily the TCFE9 database with parameters for steels in particular.

It should be noted that in castings, phase equilibrium is not fully achieved, particularly at lower temperatures and this is not accounted for in Thermocalc. This is particularly true at lower temperatures where diffusion of substitutional elements is orders of magnitude slower than at higher temperatures. Similarly, temperature gradients within the material are not taken into account in the modeling software. Metal closest to the mold-interface is expected to solidify faster than that of the center of a casting. The same holds true upon cooling from high heat temperature treatments.

The segregation of alloying elements during initial solidification is also not considered in this analysis. In true solidification, alloy-rich intercelluar regions can be expected to undergo different reactions and yield different distributions of phases as compared to alloy-poor interdendritic regions. This may be particularly influential when considering local carbide formation where alloy rich regions may have considerably different characteristics than the bulk in terms of stable carbides.

In addition, results are dependent upon the data quality of the thermodynamic database, and with multicomponent systems, data must be extrapolated from established experimental data from simpler systems. In the case of the HY alloy system, no direct model exists such that extrapolation is the only available methodology.

Despite these limitations in determining phase equilibria and phase percentages, Thermocalc and similar programs can give a relative measure of the effects of composition on high-temperature phases. Running validation experiment studies is possible; but is also extremely expensive, requiring difficult setup, and can be inconclusive because of interference due to experimental limitations. Experimental results for phase stability in the HY alloys system are non-existent as it is used primarily for non-commercial applications. Useful information on the role of carbide stabilizers and the feasibility of reactions and transformations in multicomponent systems can lead to an understanding of how chemistry influences phase stability for expected chemistry variation in industrial heats.

Using these thermodynamic tools made easily usable by CALPHAD modeling software packages like Thermocalc, each of the chemical compositions measured for

the varied heat used here-in were examined. In each case the stable phases were determined as a function of temperature, with particular attention to alloy carbides and their associated stable temperature ranges.

4.2 Image Analysis

Image analysis of HY-80 SEM images of various magnifications ranging from 6kx to 40kx were analyzed to determine the trend between carbide formation and temperature of the heat treatment. Analysis was carried out using Clemex Vision PE. The measurements taken via the program in Appendix D for each image were:

- Carbide average size distribution
- Average separation between like and dislike carbides
- Volume fraction of carbides; total, $M_{23}C_6$, and M_7C_3
- Carbide aspect ratio distribution
- Carbide number density

4.2.1 Procedure

In SEM images high points and ridges appear as bright spots on the image. As such, the grain boundaries and the carbides both being seen as bright white spots on the image must be deconvoluted. The basis of the image analysis technique employed works by thresholding the image based on differences in contrast. This is difficult, however, considering the brightness and contrast between the carbides and grain boundaries are very similar. In order to compensate for the similarities between the grain boundary and the carbides, the grain boundaries are first found and removed from an image. This is done by subtracting a series of relative contrast threshold from

a grayscale threshold. This allows for all of the carbides within the bulk of the grain to be imaged relatively clearly, while nothing on the grain boundary is seen.

After the bulk carbides are found, the carbides that were removed along with the grain boundary must be found. This is accomplished by using various binary functions including convex hull and propagate dilate. These functions are used to the effect of highlighting the grain boundary and propagating the thresholding so that a dark scale image remains where the carbides are left untouched, thereby finding most of the carbides situated on the grain boundary. Although this routine finds most of the carbides, it is noted that a significant population of the smaller carbides at a boundary are seen as a conglomerate of one carbide. To correct this error, carbide refining using binary functions is employed. These functions include bride removal and separate. Separate works by highlighting all of the known single carbides and subtracting it from the threshold.

4.2.2 Advantages and Limitations

Small carbides that are close together often from a conglomerate into one particle and are difficult to separate. This routine works at its best when the contrast and brightness of the images being analyzed are the same. If there is a large deviation in the contrast and brightness between the images, then the routine will not work properly. In order to attain the most comparable results, SEM images are selected that have approximately the same image properties.

High magnification SEM images that show formation of the quench un-tempered martensite phase resulting from aging temperature above the AC1 struggle with the base routine. This is related to martensite phase contrast being very similar to

the carbides as well as all of the carbides being situated on a grain boundary. The grain boundary itself, however, is less of an issue as its morphology is different from the carbides.

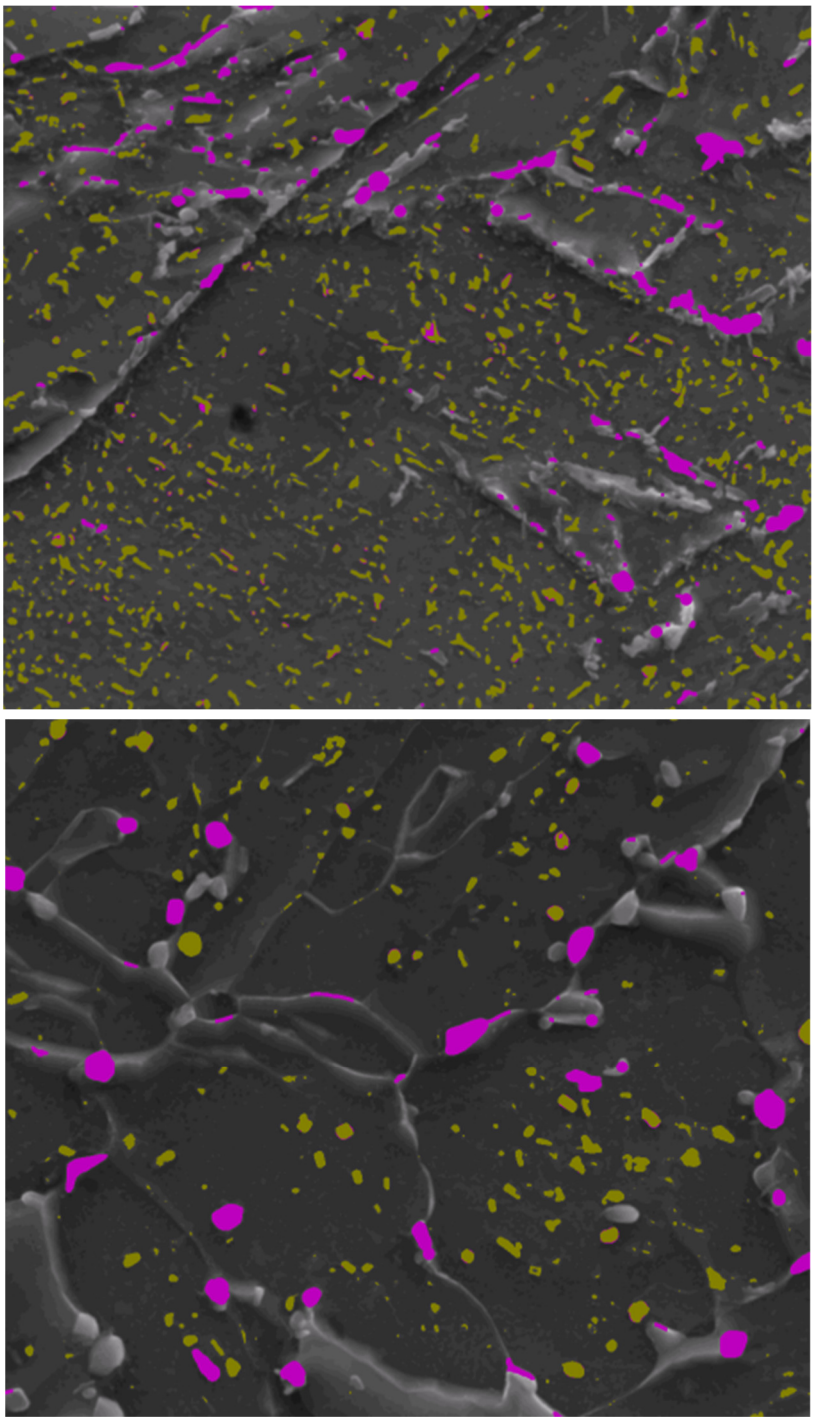

Figure 26: Examples of carbide analysis results. Yellow highlights bulk carbides. Pink highlights boundary carbides.

Chapter 5: Results

This Chapter documents both the experimental and analytical results from the procedures detailed in Chapters 3 and 4. First, the results of lower temperature aging treatments below the literature embrittlement range are presented in section 5.1. Section 5.2 reviews the results for the determination of the embrittlement rate and recovery from embrittlement rate for a high carbon equivalent grade of HY-80. Results for the embrittlement rate in a low carbon grade are also presented. In section 5.3 the results for varied experimental treatments of hydrogen aging within the temper embrittlement regime are detailed. The results of analytical statistical techniques used to identify specimens with porosity affecting tensile ductility, that were used to filter data sets in section 5.1 and 5.3, are presented in section 5.4. The metallographic results of studies on carbide nucleation, aging, and dissolution are detailed in Section 5.5. Finally, in Section 5.6 the analytical results of analysis on SEM images from Section 5.5 are presented for determination of carbide volume fraction and size.

5.1 Hydrogen Aging below the Embrittlement Range

5.1.1 Mechanical Response

Initial heat treatments conducted on the high hydrogen test blocks at 343°C and 371°C (650°F and 700°F) were intended to investigate the ability of increasing the hydrogen soak temperature to increase thermal diffusion speed, while not exceeding the temper embrittlement start temperature for the material. At both aging temperatures, the reduction of area and elongation increase with increasing aging time as shown in **Figure 27**. This is indicative of an increasing amount of monatomic hydrogen diffusing

from lattice sites to trapping sites such as porosity. At each temperature the improvement in tensile ductility occurs more rapidly at the T/4 quarter line location than with the T/2 center line specimens. This is consistent with literature and may be explained by the higher starting concentration of diffusible monatomic hydrogen at the center location.

At 343°C no statistically significant loss in toughness as measured by Charpy specimens tested at -100°F was observed; however, a clear loss in toughness was observed at 371°F as shown in **Figure 29**, potentially a result of the onset of temper embrittlement. The percent shear at both temperatures drops slightly with increasing aging time, with a more pronounced drop at 371°C.

The tensile yield and ultimate results show a set of unexpected results in **Figure 29**. While the T/4 quarter line results show a negligible to minor impact of increasing aging time on tensile results, both the yield and ultimate strength at the centerline T/2 location are shown to increase with extended aging time. For aging at 371°C an increase of approximately 30 MPa is observed for yield strength between the control and 40 hours of aging time with an associated increase of 50 MPa in the ultimate strength. Similar but less pronounced increases are observed for aging at 343°C.

In order to determine the applicability of the results obtained from the high hydrogen heat to steel produced using optimal manufacturing processes, two sets of two 7.5” test blocks were soaked at 625°F and 650°F respectively. In each set of test blocks, one was selected from the high hydrogen heat, and a second from one produced under optimal manufacturing processing. As expected, these results show that for an identical hydrogen soaking treatment, the mechanical response for reduction of area

and elongation of the standard production heat is measurably higher than the high hydrogen heat as shown in **Table 16**. Of particular note is the difference in reduction of area for hydrogen aging at 329°C where the high hydrogen heat had a response of 36.7% at the T/2 centerline location and the production heat of identical design and thickness had a response of 59.9% at the same depth.

It is noted that this relationship is not demonstrated by the raw results for aging at 343°C shown in **Figure 30**. In this case both tensile samples from the centerline location of the production heat had significant porosity on the fracture surface that affected the ductility results. Thus, these results were not used for the creation of empirical models. Section 5.4 details the results of statistical analysis that was used to identify these and other occurrences of low ductility due to porosity rather than hydrogen and how they were filtered from the data sets used for model generation.

Table 16: Comparison of Mechanical Response at 329°C [1]

TESTING DEPTH	HIGH HYDROGEN				STANDARD PRODUCTION				% RA DELTA
	YS (ksi)	El (%)	RA (%)	CVN	YS (ksi)	El (%)	RA (%)	CVN	
T/4	115.9	21.0	54.9	89.2	108.5	21.8	60.5	98.0	10.29%
T/2	115.6	14.8	36.7	68.5	106.5	22.5	59.9	65.7	63.32%

The impact of increasing thickness on the resultant Charpy impact energy and percent shear is shown in **Figure 31**. As expected, a decrease in impact energy is observed with increased thickness at both the centerline and quarter line location. This

[1] Noted: Calibration samples were also completed at 343°C, but the results of these samples could not be utilized due to excessive porosity on the fracture surface of most tensile samples.

is likely a result of the slower quench from austenitization temperatures creating a lower percentage of martensite with increasing thickness.

An unexpected decrease in Charpy results is also observed between the high hydrogen and production 0.19m (7.5”) test block results for each aging temperature, with a more pronounced delta between centerline specimens. The principle differences between these two samples are a longer austenitization time performed on the high hydrogen blocks (6 hrs 41 min and 5 hrs 20 min vs 8 hrs 21 min and 8 hours 1 min on the 329° and 343°C set of blocks respectively) and a higher carbon concentration with the high hydrogen blocks (0.205 vs 0.181 and 0.190). The production heats may have also received a less effective quench as they were combined with production materials that may have retarded the transfer time to the quench tank after austenitization and the rate of cooling during the quench due to local heat masses. This should be noted as the results from controlled test blocks studies may exhibit higher Charpy response than would be observed in a production environment.

The results for tensile yield and ultimate strength with increasing section size are shown in **Figure 32**. At both aging temperatures the anticipated reduction in tensile response is observed for the 0.33m block. The results for smaller thicknesses are scattered but are all higher than observed for the thickest cross section. This is consistent with an assumed microstructure with a lower percentage of martensite due to a retarded cooling rate in a thick section.

Table 17: Mechanical results for sub-embrittlement range hydrogen aging (HT#A)

BLOCK ID	AGING	DEPTH	UTS (MPA)	YIELD (MPA)	EL (%)	ROA (%)	CHARPY IMPACTS -73'C		
							Individual	AVG	% Shear
25623-1	343°C 20.8hrs	1/4 T (1)	785.0	635.7	16.0	35.7	106, 79, 91	92	70
		1/4 T (2)	788.5	639.2	16.0	39.2			
		1/2 T (1)	741.1	648.0	8.0	26.0			
		1/2 T (2)	785.0	649.7	12.0	20.4			
25623-2	343°C 41.7hrs	1/4 T (1)	781.5	614.6	19.5	47.9	94, 77, 90	87	60
		1/4 T (2)	783.2	632.2	17.5	44.3			
		1/2 T (1)	779.7	632.2	17.5	35.7			
		1/2 T (2)	788.5	641.0	14.5	33.4			
25623-3	343°C 62.5hrs	1/4 T (1)	769.1	632.6	19.5	42.6	84, 94, 76	84.8	60
		1/4 T (2)	788.5	637.5	19.0	44.9			
		1/2 T (1)	795.5	646.2	18.0	30.4			
		1/2 T (2)	783.2	637.5	12.0	27.4			
25623-4	371°C 13.3hrs	1/4 T (1)	783.6	640.2	13.5	27.0	106, 117, 84	102.6	65
		1/4 T (2)	788.5	642.7	15.5	32.1			
		1/2 T (1)	782.8	647.1	10.5	22.6			
		1/2 T (2)	788.1	652.4	12.5	26.4			
25623-5	371°C 26.7hrs	1/4 T (1)	775.8	627.7	18.5	42.6	54, 68, 102	74.8	53.3
		1/4 T (2)	777.9	626.9	18.0	44.3			
		1/2 T (1)	769.2	628.7	14.0	21.5			
		1/2 T (2)	783.2	642.7	12.5	17.2			
25623-6	371°C 40.0hrs	1/4 T (1)	793.7	644.5	19.0	45.2	73, 67, 50	63.5	53.3
		1/4 T (2)	786.7	635.7	17.0	37.0			
		1/2 T (1)	799.0	655.0	15.5	36.0			
		1/2 T (2)	800.8	655.0	18.0	39.5			
25626-1	Control No Aging	1/4 T (1)	771.2	624.9	13.5	24.8	75, 92, 102	89.8	61.7
		1/4 T (2)	772.2	626.4	14.0	17.1			
		1/2 T (1)	732.3	607.6	6.0	17.6			
		1/2 T (2)	754.6	634.7	8.0	17.6			

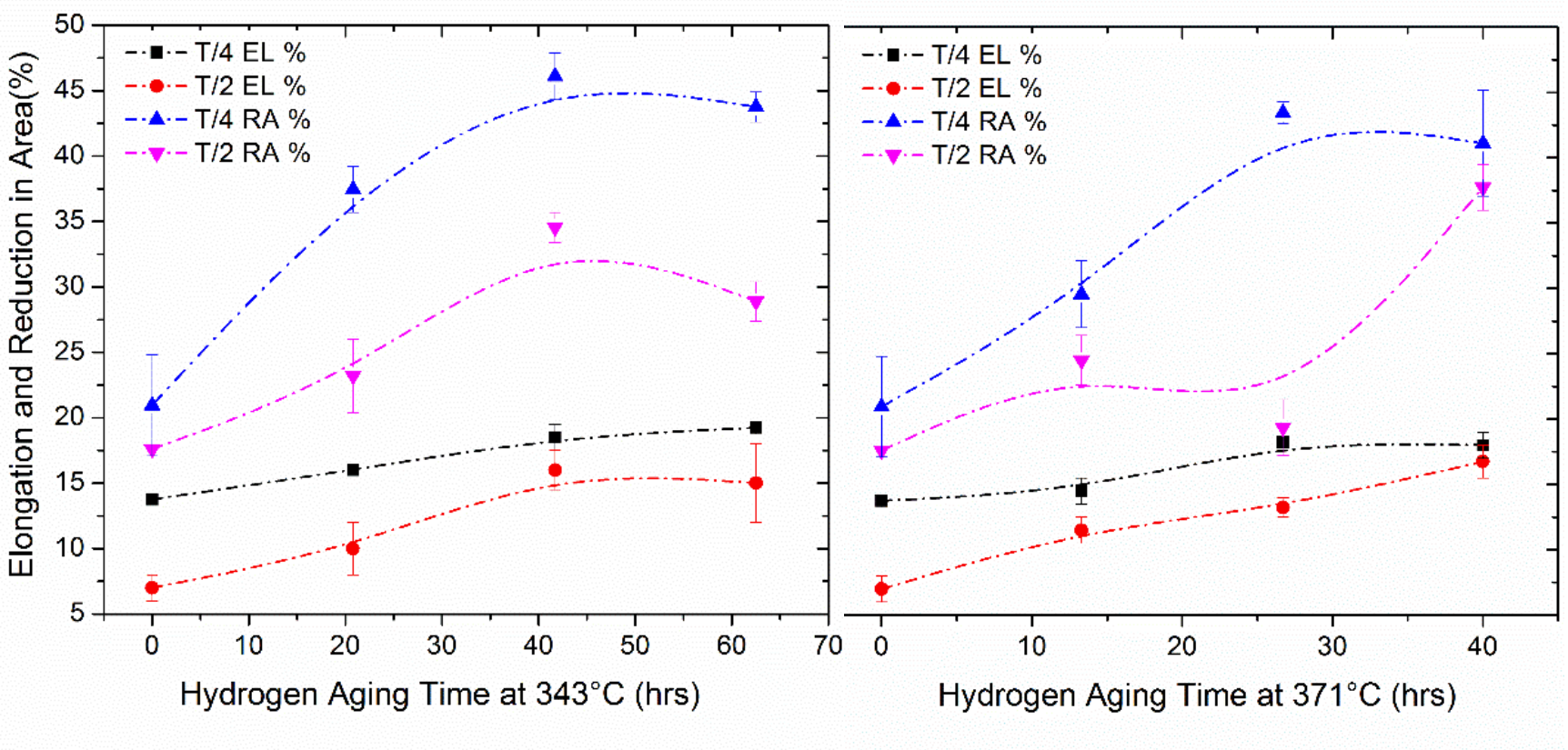

Figure 27: Elongation and reduction of area in tensile samples vs hydrogen aging time at 343°C and 371°C at the quarter-line and centerline location of 0.19m (7.5") test blocks from the hydrogen charged HT#A.

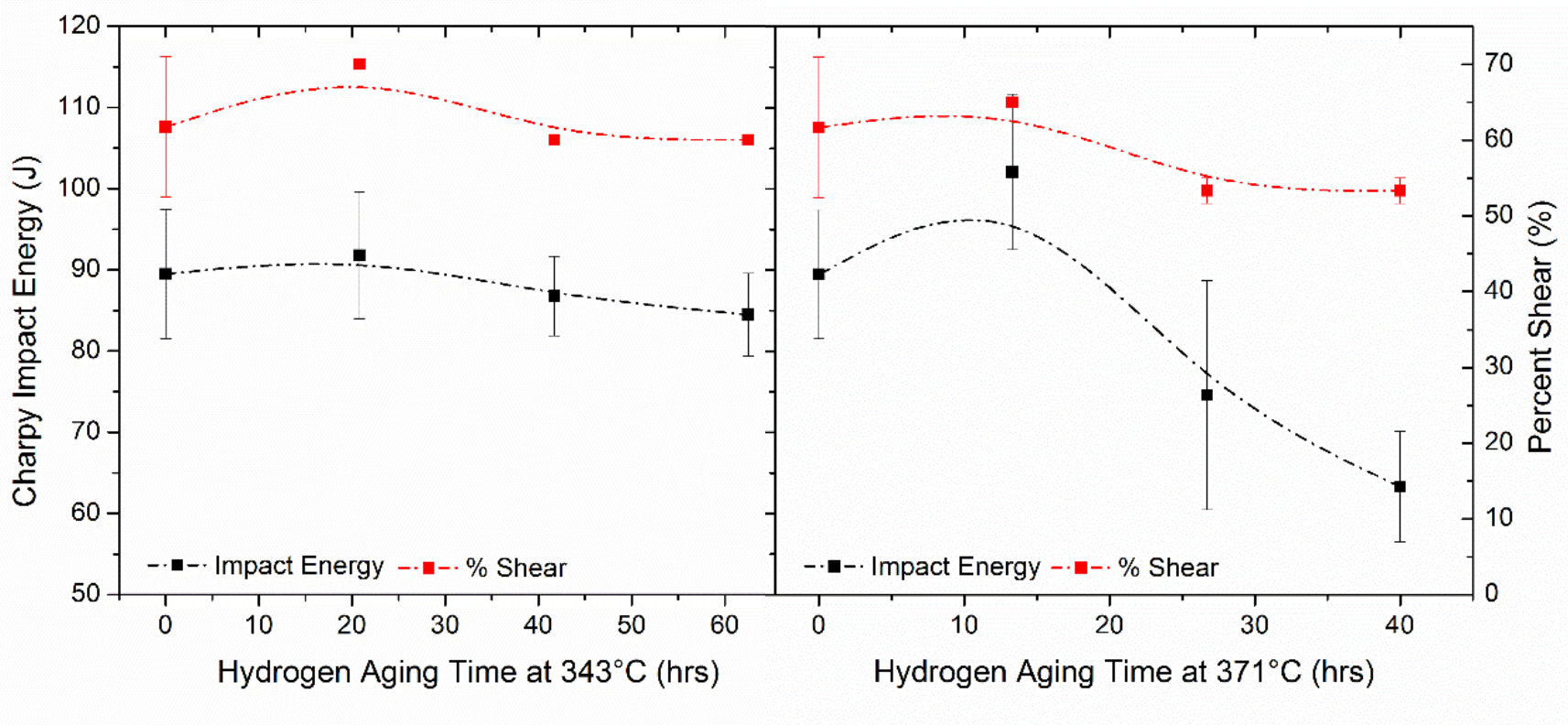

Figure 28: Charpy impact energy and percent shear vs hydrogen aging time at 343°C and 371°C at the centerline location of 0.19m (7.5") test blocks from the hydrogen charged HT#A.

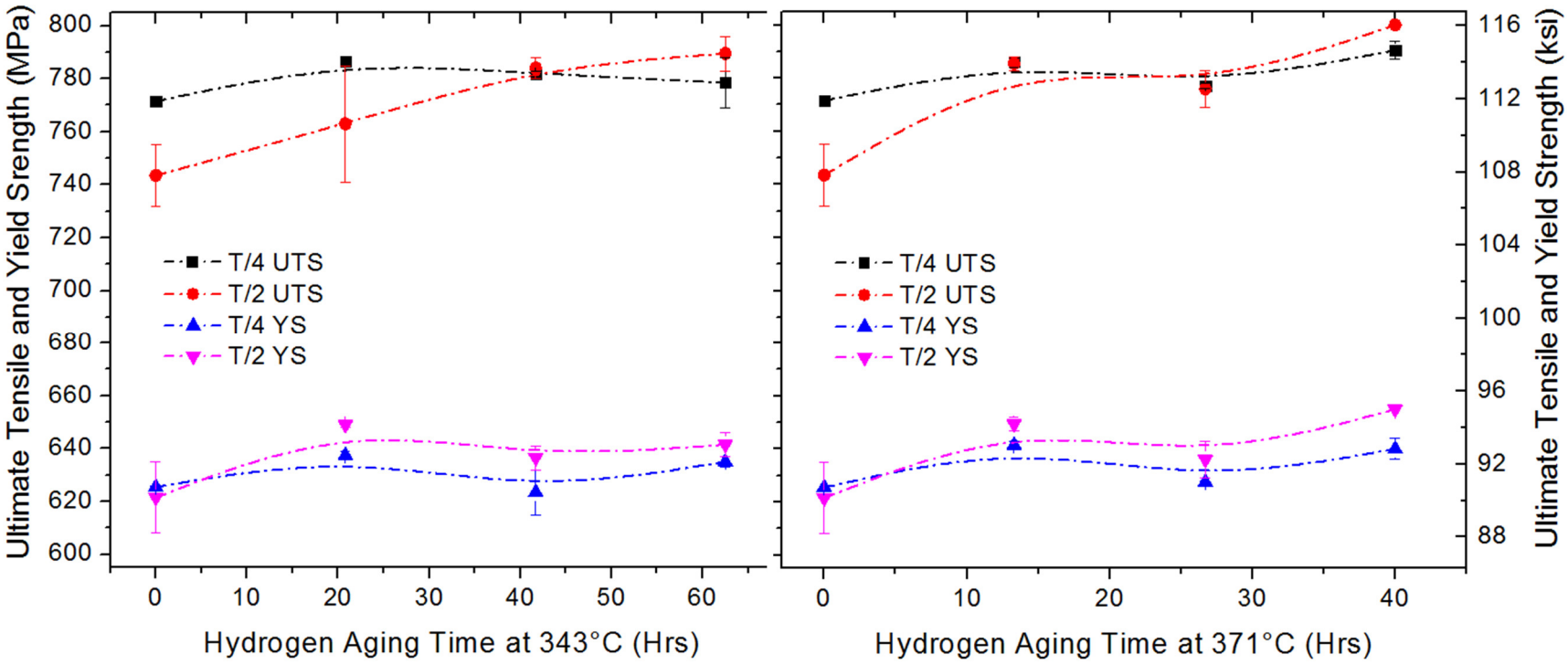

Figure 29: Tensile yield and ultimate strength vs hydrogen aging time at 343°C and 371°C at the quarter-line and centerline location of 0.19m (7.5”) test blocks from the hydrogen charged HT#A.

Table 18: Mechanical results for sub-embrittlement range hydrogen aging (HT#A and industrial heats)

BLOCK ID	AGING	DEPTH	UTS (MPA)	YEILD (MPA)	EL (%)	ROA (%)	CHARPY IMPACTS -73'C		
							Individual	AVG	% Shear
25626-3	329°C 87hrs	1/4 T (1)	799.3	643.7	21.0	56.9	124, 122, 117	121.3	98.3
		1/4 T (2)	799.3	643.7	21.0	52.9			
		1/2 T (1)	795.8	643.7	13.0	32.4	84, 88, 97	93.2	91.7
		1/2 T (2)	797.6	640.2	16.5	40.9			
25724-17	329°C 87hrs	1/4 T (1)	748.1	597.1	21.0	57.8	134, 136, 130	133.3	100.0
		1/4 T (2)	748.1	593.6	22.5	63.3			
		1/2 T (1)	731.7	576.5	21.5	57.8	86, 98, 84	89.3	53.3
		1/2 T (2)	737.0	580.1	23.5	61.9			
25725-3	329°C 191hrs	1/4 T (1)	804.9	677.7	20.0	59.6	58, 69, 56	61.2	57.7
		1/4 T (2)	806.6	682.9	20.0	59.9			
		1/2 T (1)	775.2	641.1	21.0	61.1	67, 86, 60	70.7	39.0
		1/2 T (2)	766.5	620.2	21.0	57.0			
25739-1	329°C 287hrs	1/4 T (1)	738.7	573.2	21.0	56.8	58, 64, 63	61.7	32.7
		1/4 T (2)	744.6	576.0	21.0	55.1			
		1/2 T (1)	740.2	578.4	20.0	48.9	38, 54, 71	54.4	44.3
		1/2 T (2)	735.8	572.5	22.0	50.2			
25626-2	343°C 72hrs	1/4 T (1)	797.3	642.7	20.5	57.0	99, 110, 103	104.3	94.3
		1/4 T (2)	800.8	644.5	20.5	54.6			
		1/2 T (1)	761.3	599.3	21.0	57.8	106, 116, 125	115.6	92.7
		1/2 T (2)	767.0	633.3	10.0	25.2			
25724-27	343°C 72hrs	1/4 T (1)	770.0	609.7	21.0	56.5	101, 84, 112	98.8	85.0
		1/4 T (2)	772.2	614.3	21.0	59.3			
		1/2 T (1)	794.4	632.4	14.0	28.3	73, 126, 75	91.6	80.0
		1/2 T (2)	801.4	649.8	15.0	30.0			
25725-5	343°C 159hrs	1/4 T (1)	822.1	668.1	14.5	41.6	44, 46, 50	46.7	57.0
		1/4 T (2)	828.9	677.8	18.0	43.8			
		1/2 T (1)	836.1	690.9	17.0	44.0	80, 73, 56	69.8	52.7
		1/2 T (2)	822.1	680.4	18.0	44.3			
25739-2	343°C 238hrs	1/4 T (1)	741.1	583.0	18.5	39.5	54, 56, 68	59.4	55.0
		1/4 T (2)	744.6	579.5	18.5	40.7			
		1/2 T (1)	741.1	577.7	20.5	53.8	56, 58, 48	53.9	32.7
		1/2 T (2)	746.3	584.8	19.5	51.3			

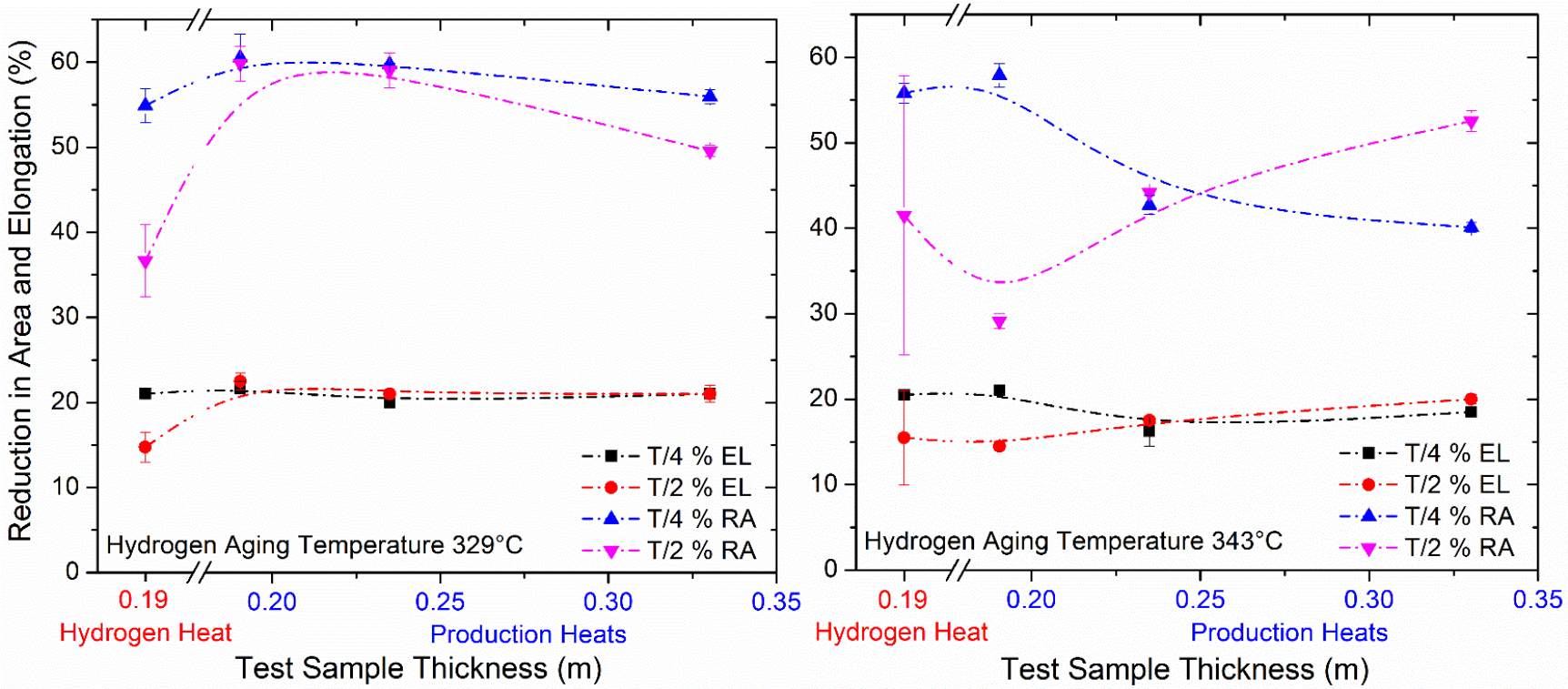

Figure 30: Elongation and reduction of area in tensile samples vs test sample thickness at 329°C and 343°C at the quarter line and centerline location of both a 0.19m (7.5") test block from the hydrogen charged HT#A and from three industrial heats at thickness of 9.25" (HT#5 and 7), 11" (HT#3 and 8), and 13" (HT#6) where the first heat designates the block treated with a 329°C aging treatment and the second heat designates those blocks treated at 343°C.

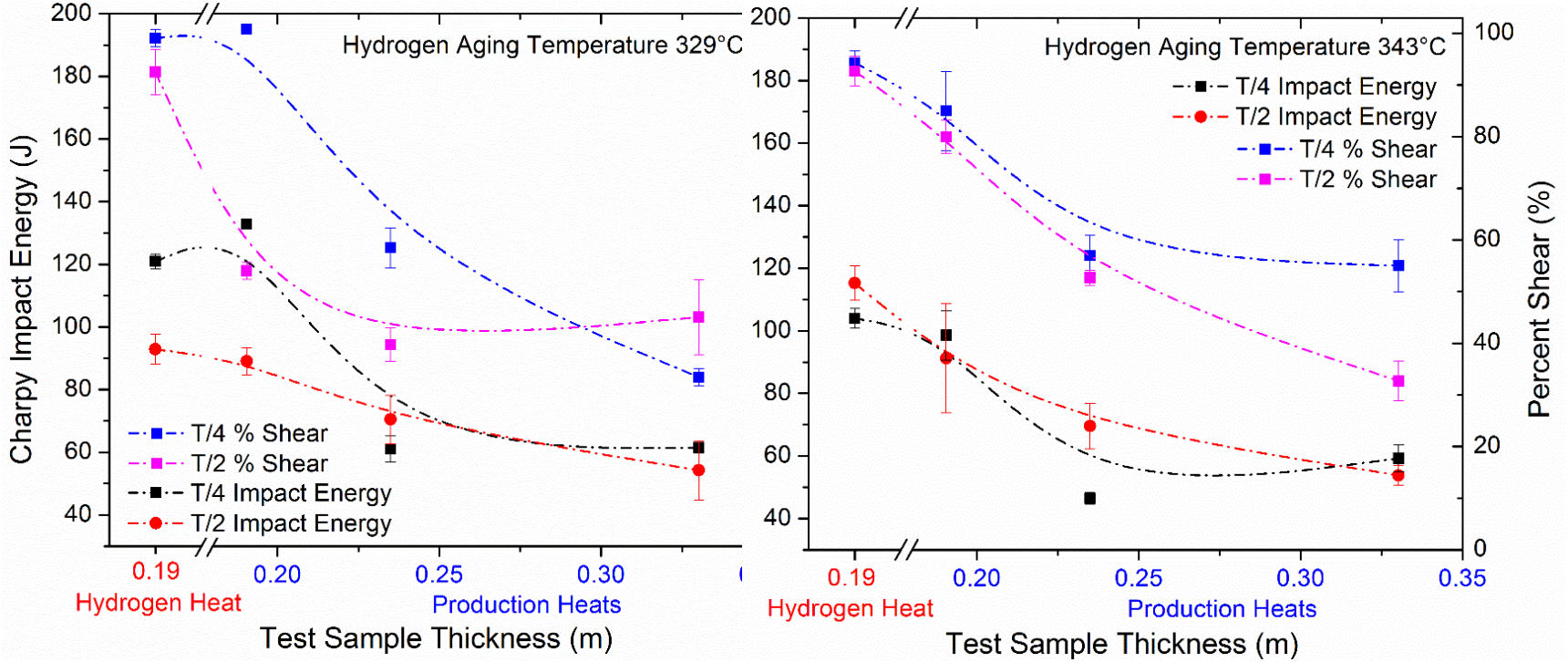

Figure 31: Charpy impact energy and percent shear vs test sample thickness at 329°C and 343°C at the quarter line and centerline location of both a 0.19m (7.5") test block from the hydrogen charged HT#A and from three industrial heats at thickness 9.25" (HT#5 and 7), 11" (HT#3 and 8), and 13" (HT#6) where the first heat designates the block treated with a 329°C aging treatment and the second heat designates those blocks treated at 343°C.

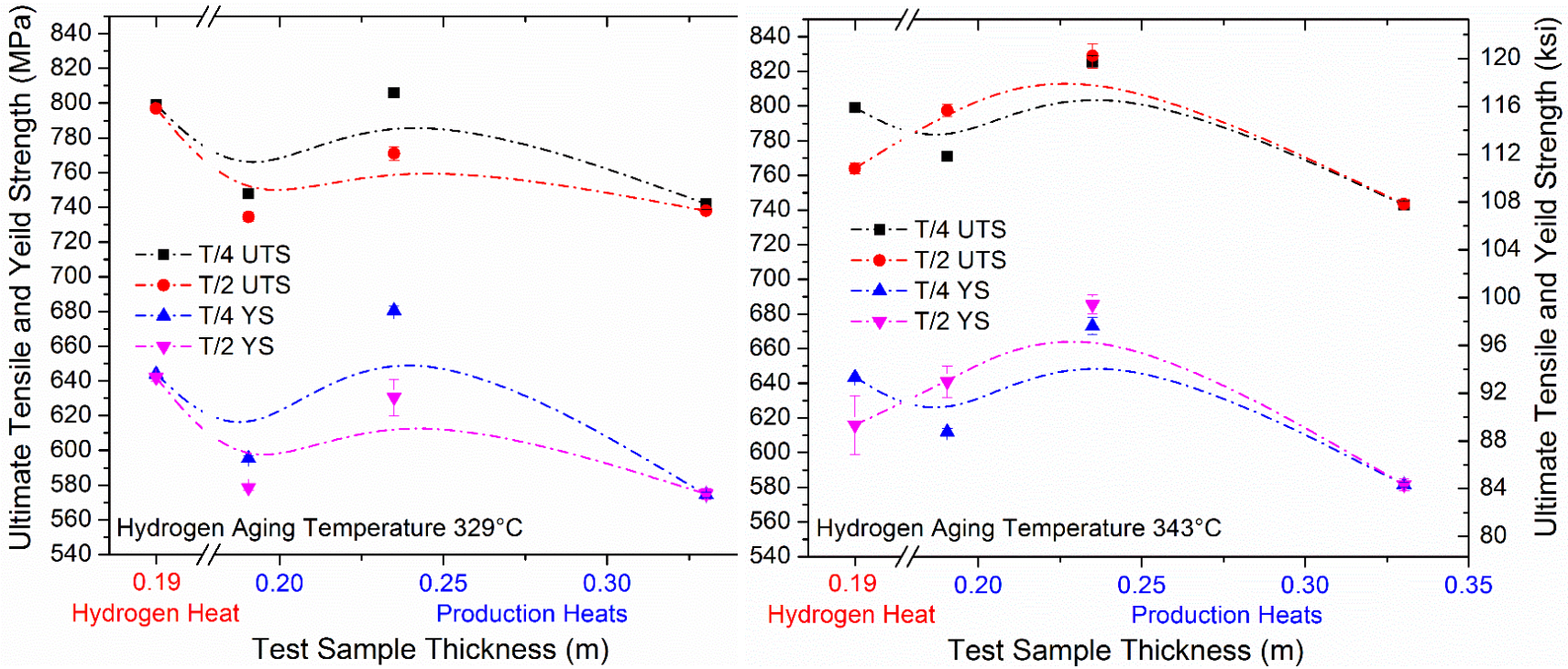

Figure 32: Tensile ultimate and yield strength vs test sample thickness at 329°C and 343°C at the quarter line and centerline location of both a 0.19m (7.5") test block from the hydrogen charged HT#A and from three industrial heats at thickness of 9.25" (HT#5 and 7), 11" (HT#3 and 8), and 13" (HT#6) where the first heat designates the block treated with a 329°C aging treatment and the second heat designates those blocks treated at 343°C.

5.1.2 Fractography

Numerous specimens exhibited varied levels of hydrogen damage that resulted in a depression of the tensile reduction of area. **Figure 33** and **Figure 34** show examples of tensile fracture surfaces with high levels of hydrogen damage and low associated reductions in area. The characteristic feature is the hydrogen "fish eye" appearing as a shiny region surrounding a hydrogen trapping sites. The most common trapping site for hydrogen observed in these assays is a porosity as shown in **Figure 34**.

This fractography is in stark contrast to that observed for specimens exhibiting ductile fracture. **Figure 35** is an example of such a ductile specimen where the applied hydrogen aging treatment has successfully migrated all monatomic hydrogen either out of the material or to trapping sites where it forms non-harmful H_2 gas. For purposes of analysis, the reduction of area is used in most cases to indicate the level of hydrogen damage based on the observed relationship here, as with adjacent literature for castings.

Figure 33: Specimen showing excessive hydrogen "fish eyes" (examples highlighted by arrows) and very low ductility and with nearly no observable reduction in the gauge diameter [Left] Vertical view [Right] 45 degree showing slant fracture (254D)

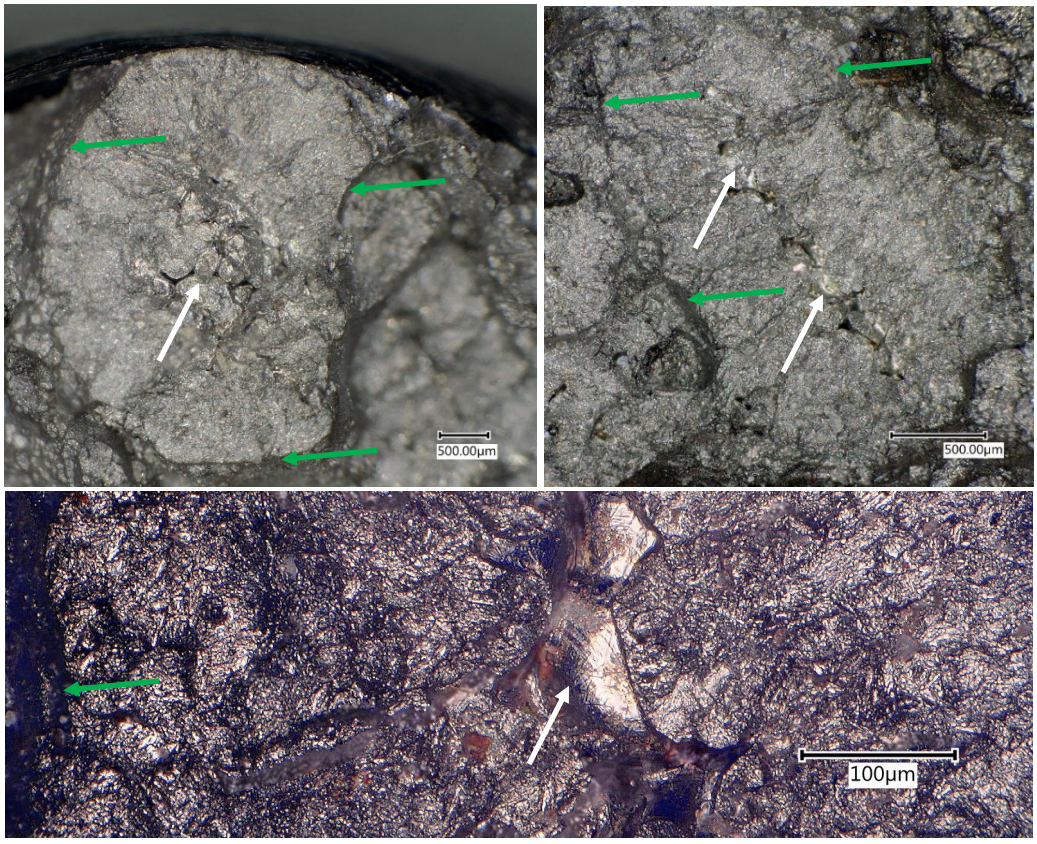

Figure 34: Specimens [Left] 253 C [Right & Bottom] 252 B; highlighting regions of hydrogen damage surrounding a porosity on the fracture surface. White arrows highlight porosity, green arrows highlight rim of hydrogen damage region.

Figure 35: Example specimen (256 B) showing high ductility with a traditional "cup and cone" morphology with considerable observable reduction in the gauge diameter

5.2 Embrittlement and Recovery

In initial work prior to the development of the embrittlement range as a potential hydrogen aging treatment, the embrittlement rate was investigated. This work was principally done on the high embrittling element heat #B to define the speed of embrittlement and characterization of the fracture surface. After this work was completed, various trials were attempted to determine the possibility of recovery from embrittlement. Once it became evident that recovery was not only possible but that 100% recovery from embrittlement could be achieved, the study of the use the embrittlement range for hydrogen aging began. This section details the results of the foundational work on determining the embrittlement and recovery from embrittlement rate and critical temperatures.

5.2.1 Embrittlement Rate of High Phosphorus Heat (#B)

The results of the initial work on the temper embrittlement rate as measured by Charpy impact strength at -73°C (-100°F) with treatments conducted at 482°C (900°F) are shown in **Figure 36**. The initial control results using the Heat #B had a surprising low starting impact strength averaging at 54J (40 ft-lbs), where for a standard production heat this would be anticipated to be in excess of 68J (50 ft-lbs). It was theorized that these low mechanical results were due to the initiation of temper embrittlement that would have been caused by the heat-up and cooling cycles the blocks went through during the initial quality heat treatment on the basis of SEM results showing the presence of both intergranular and cleavage fracture. Review of the fracture surfaces for zero time of intentional exposure in the embrittling range supports this conclusion as there is clear evidence of a non-ductile failure mode.

Of interesting note, at very short time scales a decrease in impact strength for aging times less than 100 min is followed by an increase in impact strength at 100 min. This is then followed by a sharp decrease in impact energy for times longer than 100 min. As this observation cannot be clearly described by any single known embrittlement mechanism, this implies that more than one competing mechanism is active. This will be discussed in more detail later in this chapter.

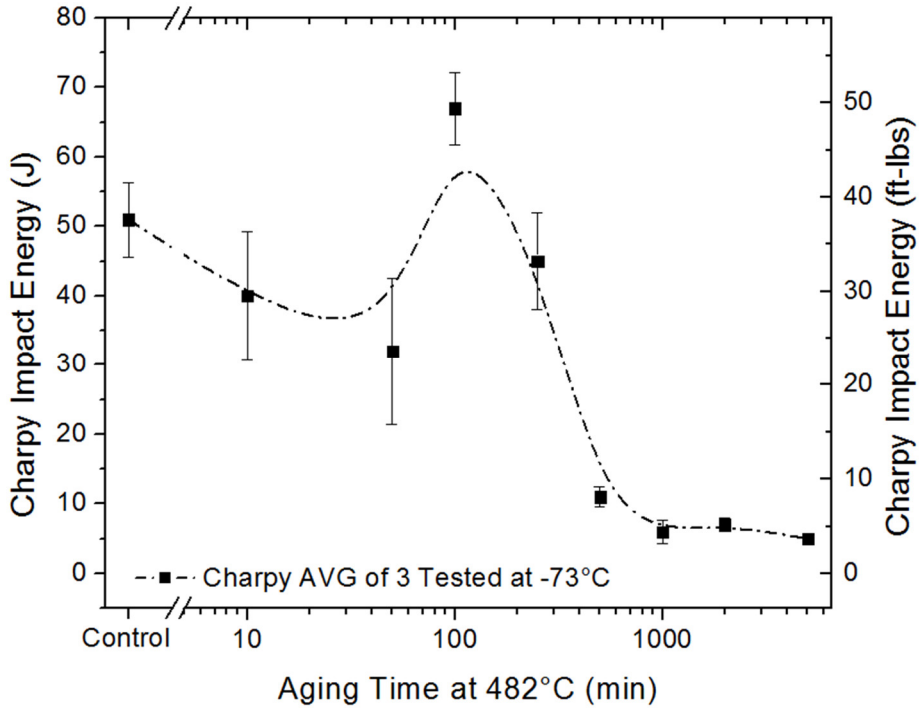

Figure 36: Speed of temper embrittlement onset at 482°C (900°F) for Heat #B.

In order to study this further, the test block samples were reduced to 15.875mm x 15.875mm (5/8" x 5/8") cross section blanks and re-heat treated. This follow on work is summarized in **Table 19** and **Figure 37** shows the delta in the speed of embrittlement for the temperature range from 343°C to 482°C (650°F to 900°F). The rate of embrittlement significantly increases with increasing temperature up to a maximum at 482°C.

Table 19: Charpy impact results for HT#B

TEMPERATURE	CHARPY (J)	TIME (MINUTES)									
		100	250	500	1000	2000	5000	10000	20000	50000	100000
482.2°C	1	29.5	37.6	11.8	22.1	7.4					
	2	39.8	37.6	33.9	16.2	11.1					
	3	26.6	45.7	42.8	21.4	7.4					
	AVG	31.7	39.1	29.5	19.9	8.9					
426.7°C	1		39.8	48.7	17.7	23.6	16.2				
	2		54.6	39.8	22.1	19.2	17.7				
	3		35.4	42.8	20.7	19.9	No Test				
	AVG		43.5	43.5	19.9	20.7	17.0				
398.9°C	1			38.4	25.8	33.2	24.3	26.6			
	2			17.7	26.6	21.4	16.2	16.2			
	3			28.0	44.3	32.5	24.3	17.0			
	AVG			28.0	32.5	28.8	21.4	19.9			
357.2°C	1				47.2	64.2	19.2	49.4	28.8	28.8	42.8
	2				39.8	29.5	18.4	28.8	36.9	22.1	38.4
	3				45.0	42.8	24.3	23.6	45.0	28.0	27.3
	AVG				44.3	45.7	20.7	33.9	36.9	26.3	36.1
343.3°C	1								36.9	No Test	35.4
	2								22.1	22.1	33.9
	3								27.3	32.5	37.6
	AVG								28.8	27.3	35.7

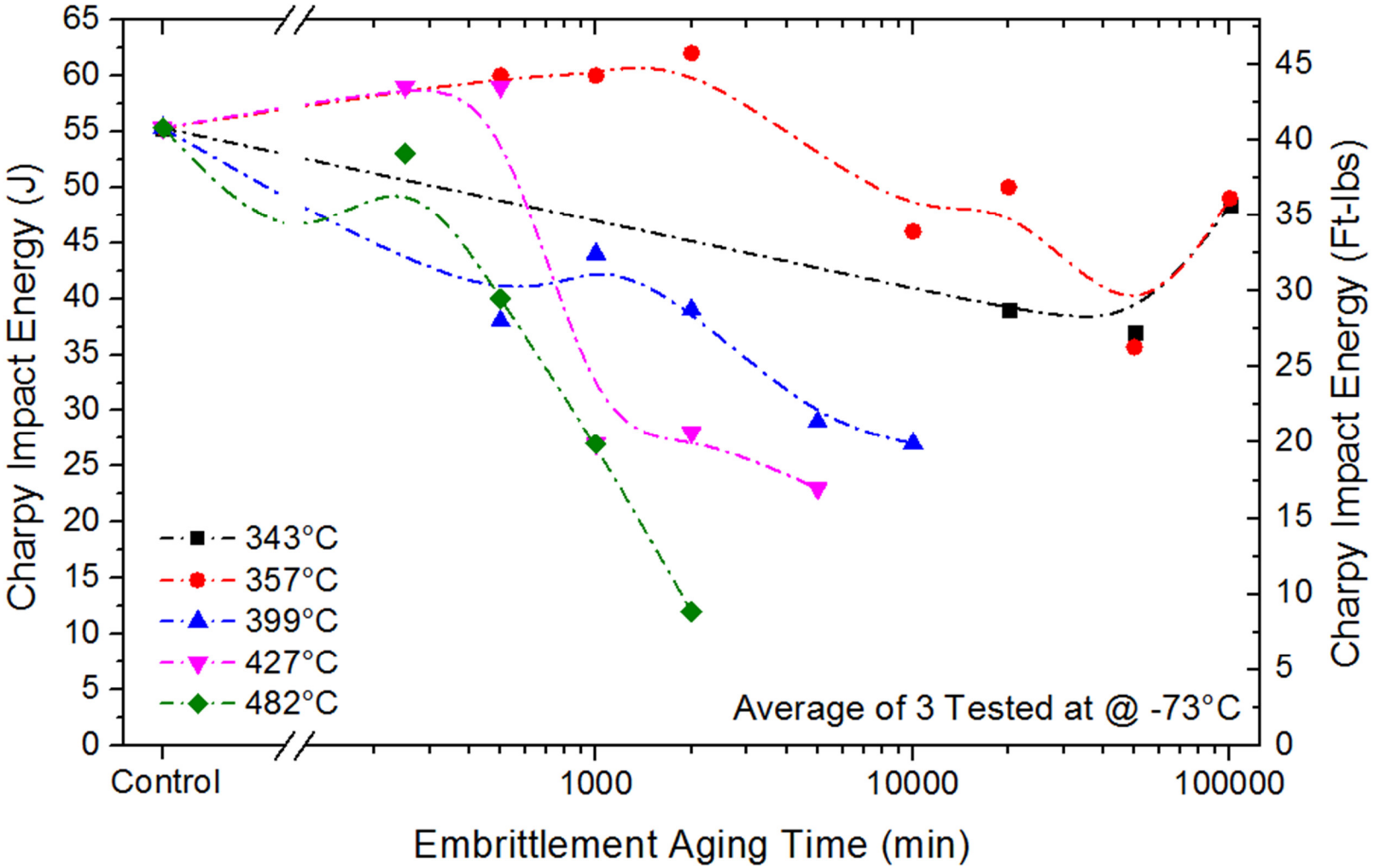

Figure 37: Embrittlement Rate in HY-80 as measured by average of 3 Charpy impact specimens tested @ -73°C for HT#B

5.2.2 Embrittlement Rate of High Carbon High Hydrogen Heat

HT#D was used to examine the rate of embrittlement. The incoming material had variable impact strength of 68.5 to 155.2 Joules (50.5 to 114.5 ft-lbs), which is suspected to be a result of both differences in the local quenching rate of the test block in addition to the variability associated with impact results in the transition region. The upper shelf is measured in excess of 271J (200 ft-lb) while the lower shelf is less than 41J (30 ft-lbs) for a non-embrittled sample of HY-80. In order to normalize these results, all impact properties for the embrittlement rate are presented as a percent of the control specimen set for that temperature. The results as a function of temperature are presented in **Figure 38** and as a function of time in **Figure 39**. There are three characteristic regions to the embrittlement rate diagram with temperature:

- From 315°C up to approximately 420°C there is a region of a slight increase in the impact strength,
- From 420°C to 485°C there is a region of rapid increase in the embrittlement rate, and
- From 485°C to 565°C there is a region of slowing embrittlement rate with increasing temperature.

It is also shown that as expected the Charpy impact energy is reduced with increasing aging time in the embrittlement range. It can be inferred that at 482°C there is a mechanistic inflection point in embrittlement. This will be discussed further in Chapter 6.

Table 20: Charpy impact results for temper embrittlement rate

Temperature	Time	Set	C1	C2	C3	AVG	STD
426°C	Control	B	1	13	15	114.50	21.86
			100.32	139.67	103.51		
426°C	500 min	B	2	12	22	105.73	1.45
			107.32	105.38	104.48		
426°C	1000 min	B	4	14	24	107.42	6.70
			106.07	101.5	114.69		
426°C	2000 min	B	6	16	26	94.69	14.89
			105.38	77.685	101.01		
426°C	5000 min	B	8	18	28	83.63	11.10
			89.38	70.841	90.682		
426°C	10000 min	B	10	20	30	36.44	4.47
			32.177	41.092	36.05		
454°C	Control	G	1	13	15	114.50	21.86
			100.32	139.67	103.51		
454°C	500 min	G	2	12	22	96.26	3.92
			92.536	95.907	100.35		
454°C	1000 min	G	4	14	24	71.24	20.97
			84.123	47.037	82.559		
454°C	2000 min	G	6	16	26	62.71	15.42
			80.185	51.038	56.892		
454°C	5000 min	G	8	18	28	34.21	5.83
			39.114	27.77	35.746		
454°C	10000 min	G	10	20	30	25.91	3.44
			28.835	22.114	26.768		
482°C	Control	E	1	13	15	71.43	16.64
			53.087	75.664	85.553		
482°C	500 min	E	2	12	22	32.97	4.81
			31.827	38.253	28.835		
482°C	1000 min	E	4	14	24	32.54	0.48
			32.719	32.899	31.997		
482°C	2000 min	E	6	16	26	19.11	2.08
			20.908	19.595	16.826		
482°C	5000 min	E	8	18	28	12.30	1.59
			13.379	10.483	13.049		
482°C	10000 min	E	10	20	30	8.92	0.28
			8.597	9.134	9.026		
510°C	Control	C	1	13	15	50.51	14.32
			42.21	67.052	42.272		

Temperature	Time	Set	C1	C2	C3	AVG	STD
510°C	500 min	C	2	12	22	30.97	9.69
			20.393	33.08	39.422		
510°C	1000 min	C	4	14	24	22.97	1.86
			23.442	20.908	24.545		
510°C	2000 min	C	6	16	26	17.61	2.65
			20.45	17.163	15.206		
510°C	5000 min	C	8	18	28	14.41	1.56
			12.609	15.317	15.317		
510°C	10000 min	C	10	20	30	10.20	3.78
			7	9.2416	14.373		
538°C	Control	A	1	13	15	103.38	10.53
			115	100.67	94.461		
538°C	500 min	A	2	12	22	74.51	18.61
			85.826	53.022	84.668		
538°C	1000 min	A	4	14	24	52.90	9.43
			48.81	46.217	63.685		
538°C	2000 min	A	6	16	26	37.00	3.80
			32.899	37.701	40.411		
538°C	5000 min	A	8	18	28	48.35	8.22
			50.591	39.237	55.211		
538°C	10000 min	A	10	20	30	44.10	0.42
			44.458	44.207	43.644		
566°C	Control	D	1	13	15	73.17	4.34
			70.308	71.041	78.157		
566°C	500 min	D	2	12	22	40.51	4.27
			40.658	36.172	44.709		
566°C	1000 min	D	4	14	24	33.44	5.49
			38.991	33.321	28.006		
566°C	2000 min	D	6	16	26	37.97	4.49
			37.701	33.623	42.584		
566°C	5000 min	D	8	18	28	38.74	4.08
			43.394	35.746	37.089		
566°C	10000 min	D	10	20	30	39.51	2.74
			38.315	42.646	37.578		
316°C	Control	E	1	13	15	71.43	16.64
			53.087	75.664	85.553		
316°C	1000 min	E	9	19	29	65.06	6.76
			67.251	70.441	57.476		
316°C	2000 min	E	7	17	27	74.76	8.29
			74.79	83.035	66.456		

Temperature	Time	Set	C1	C2	C3	AVG	STD
316°C	5000 min	E	3	5	25	65.34	6.32
			72.578	62.502	60.929		
316°C	10000 min	E	11	21	23	56.86	9.97
			54.115	48.556	67.914		
343°C	Control	A	1	13	15	103.38	10.53
			115	100.67	94.461		
343°C	1000 min	A	9	19	29	132.10	4.35
			135.92	133.01	127.37		
343°C	2000 min	A	7	17	27	107.83	22.79
			112.39	83.103	128		
343°C	5000 min	A	3	5	25	108.60	6.84
			116.36	103.44	106		
343°C	10000 min	A	11	21	23	102.90	23.09
			99.98	81.405	127.3		
371°C	Control	B	1	13	15	114.50	21.86
			100.32	139.67	103.51		
371°C	1000 min	B	9	19	29	120.57	8.40
			111.42	127.93	122.35		
371°C	2000 min	B	7	17	27	112.79	13.37
			120.47	97.355	120.54		
371°C	5000 min	B	3	5	25	113.09	4.40
			110.38	110.72	118.17		
371°C	10000 min	B	11	21	23	102.94	12.60
			102.95	90.339	115.53		
399°C	Control	C	1	13	15	50.51	14.32
			42.21	67.052	42.272		
399°C	1000 min	C	9	19	29	63.88	5.35
			57.736	67.516	66.39		
399°C	2000 min	C	7	17	27	56.99	15.13
			58.386	41.216	71.375		
399°C	5000 min	C	3	5	25	52.31	11.90
			65.927	43.957	47.037		
399°C	10000 min	C	11	21	23	42.10	9.38
			46.406	31.338	48.556		

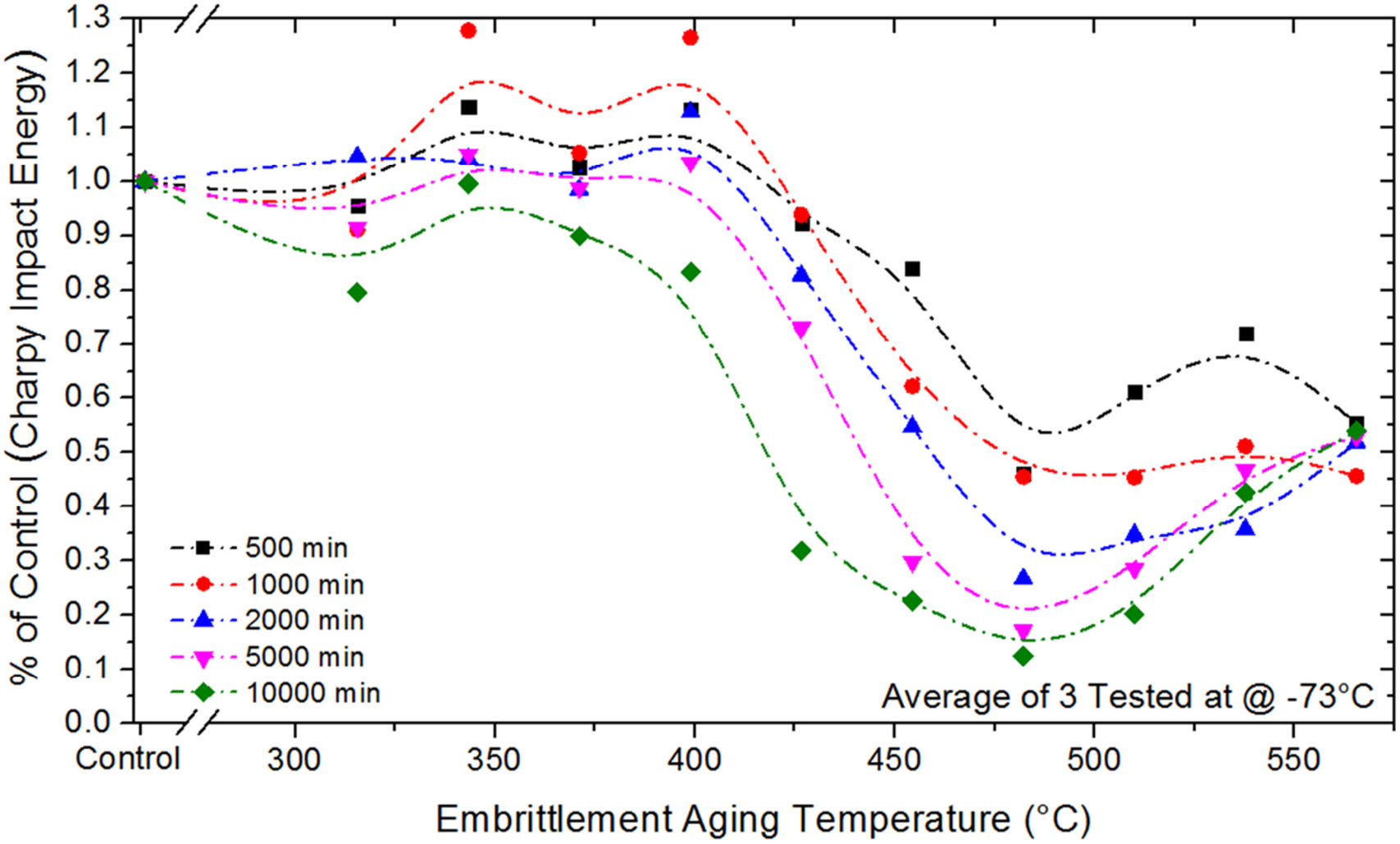

Figure 38: Embrittlement results as measured by the % of control from Charpy impact specimens tested at -73°C for HT#A

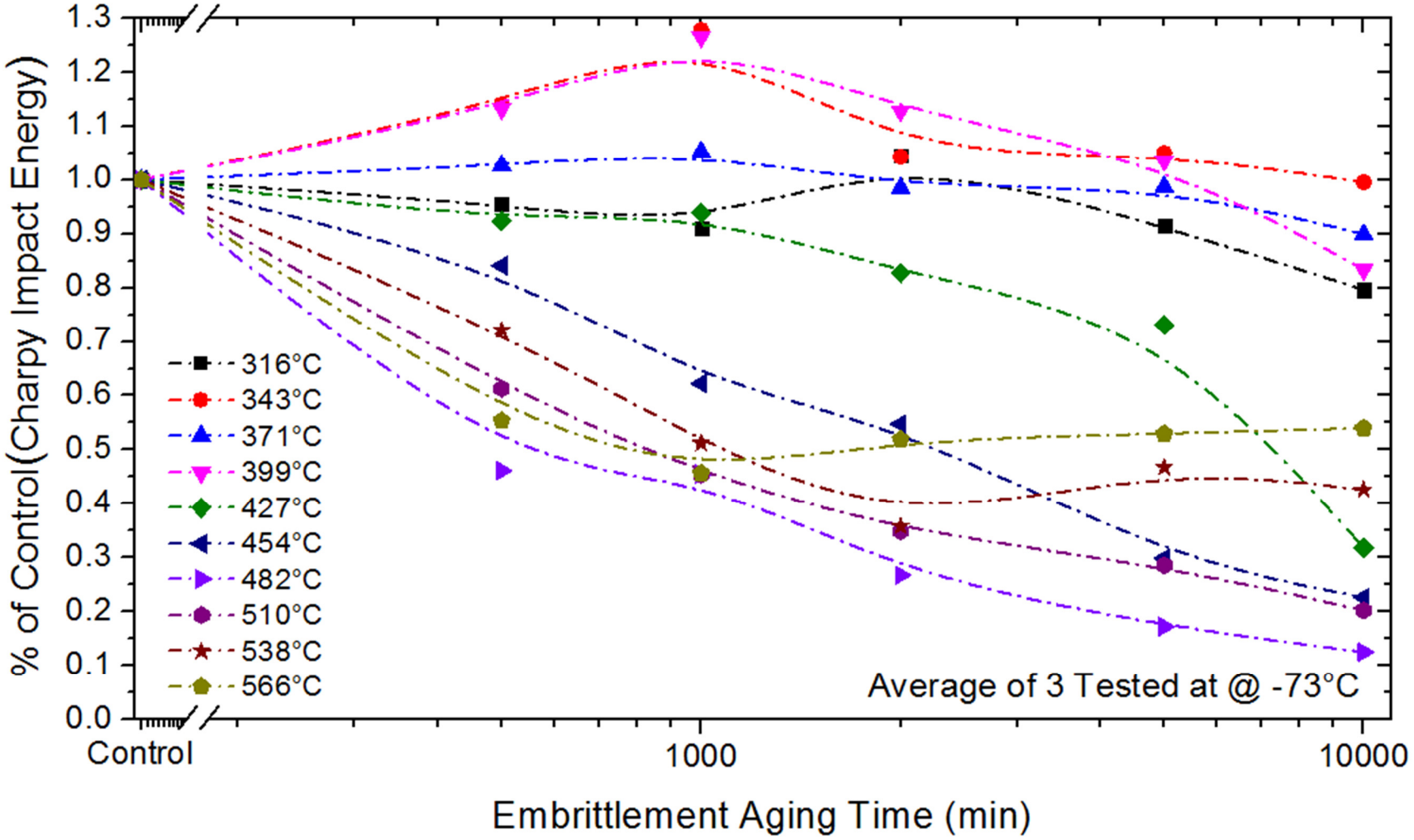

Figure 39: Embrittlement results as measured by the % of control from Charpy impact specimens tested at -73°C for HT#A

5.2.3 Embrittlement Recovery Rate of High C High H Heat #A

As the maximum rate of embrittlement was determined to be at 482°C in the results detailed above, this was selected as the temperature to pre-treat specimens for evaluation of the rate of recovery from embrittlement. Control specimens for embrittlement recovery rate studies that had been aged at 482°C for 10,000 minutes were relatively equal ranging from 10.7 to 27.5 Joules (7.9 to 20.3 ft-lbs). As a result, the actual Charpy impact results are presented for the recovery rate diagrams as an average of 15 Charpy specimens. The results as a function of temperature are presented below in **Figure 40** with the results as a function of time in **Figure 41**.

There are three characteristic regions to the embrittlement recovery rate diagram as a function of temperature:

- Fast recovery across the entire temperature range to > 50J within 50 minutes.
- An isolated region centered at 649°C (1200°F) with complete recovery from embrittlement and a further increase in the impact strength beyond the incoming material as detailed in the preceding text.
- A region of decreased impact strength at long times above 675°C (1250°F).

When the results are examined as a function of time three additional characteristics become clear:

- A steady, continuous increase in impact strength with increasing time for samples treated at 593°C and 621°C.
- An immediate and sustained increase in impact strength by nearly an order of magnitude at 649°C.

- A significant increase in impact strength at short time scales for treatments at 677°C and 704°C followed by a decrease in impact strength with increasing treatment time, with a dramatic decrease at 704°C to levels at or below the starting condition.

The decrease in impact strength for aging at higher temperatures was not expected but will be explained in the follow on section detailing metallographic observations.

Table 21: Charpy impact results for temper embrittlement recovery rate

Temperature	Time	Set	C1	C2	C3	AVG	STD
593°C	Control	I	1	13	15	9.37	1.73
			11.298	7.956	8.865		
593°C	50 min	I	2	12	22	43.29	6.40
			36.05	45.651	48.176		
593°C	100 min	I	4	14	24	41.19	8.40
			33.201	40.411	49.954		
593°C	200 min	I	6	16	26	57.01	9.21
			63.487	46.469	61.06		
593°C	320 min	I	8	18	28	70.73	2.21
			72.846	70.908	68.445		
593°C	500 min	I	10	20	30	58.30	2.21
			58.256	60.537	56.115		
593°C	1000 min	I	9	19	29	69.69	1.95
			68.246	68.91	71.91		
621°C	Control	H	1	13	15	7.93	1.73
			6.046	8.2761	9.458		
621°C	50 min	H	2	12	22	69.07	6.91
			62.043	69.309	75.866		
621°C	100 min	H	4	14	24	72.04	15.00
			69.841	58.256	88.012		
621°C	200 min	H	6	16	26	80.40	12.73
			81.744	67.052	92.398		
621°C	320 min	H	8	18	28	92.80	10.80
			84.123	89.38	104.89		
621°C	500 min	H	10	20	30	68.19	6.57
			72.11	71.843	60.602		
621°C	1000 min	H	9	19	29	82.57	12.95
			94.461	84.463	68.777		
649°C	Control	J	1	13	15	20.29	2.38
			22.171	21.08	17.613		
649°C	50 min	J	2	12	22	136.92	3.33
			138.84	138.84	133.08		
649°C	100 min	J	4	14	24	130.82	8.25
			122.49	138.98	130.99		
649°C	200 min	J	6	16	26	135.11	7.09
			126.95	138.56	139.81		

Temperature	Time	Set	C1	C2	C3	AVG	STD
649°C	320 min	J	8	18	28	144.47	20.99
			142.3	124.65	166.47		
649°C	500 min	J	10	20	30	128.09	5.46
			131.68	121.8	130.78		
649°C	1000 min	J	9	19	29	132.07	6.59
			124.51	135.16	136.55		
677°C	Control	H & I	1	13	15	See Above	
			See Above				
677°C	50 min	I	7	17	27	104.87	4.39
			109.82	103.37	101.43		
677°C	100 min	I	3	5	25	95.34	4.46
			98.183	97.631	90.202		
677°C	200 min	I	11	21	23	86.64	17.97
			87.806	68.113	103.99		
677°C	320 min	H	7	17	27	74.15	4.93
			79.847	71.175	71.442		
677°C	500 min	H	3	5	25	72.11	1.40
			73.717	71.509	71.108		
677°C	1000 min	H	11	21	23	50.37	3.08
			50.782	47.1	53.215		
704°C	Control	J & G	1	13	15	16.38	3.46
			18.178	18.572	12.39		
704°C	50 min	G	11	21	23	99.96	3.77
			102.88	95.7	101.29		
704°C	100 min	G	3	5	25	96.17	23.57
			121.52	92.055	74.925		
704°C	200 min	G	7	17	27	42.94	1.70
			44.892	41.775	42.148		
704°C	320 min	J	11	21	23	14.72	2.61
			17.726	13.324	13.104		
704°C	500 min	J	3	5	25	11.14	1.67
			11.407	12.664	9.349		
704°C	1000 min	J	7	17	27	8.82	1.60
			10.591	7.476	8.381		

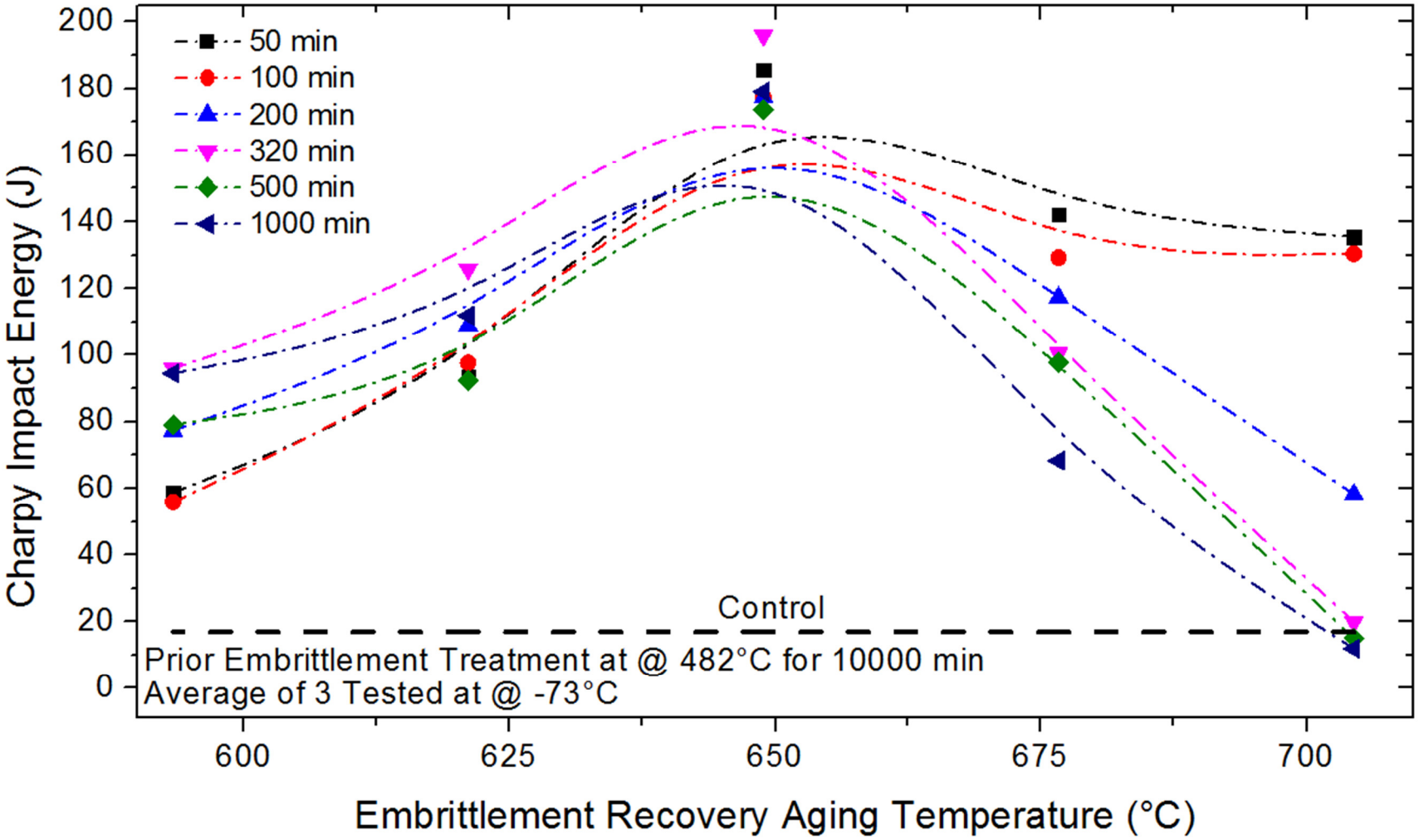

Figure 40: Embrittlement recovery rate results as measured by Charpy impact specimens tested at -73°C with treatments per Table 3. Selected embrittlement treatment (control result) corresponds to the maximum embrittlement measured in **Figure 39**.

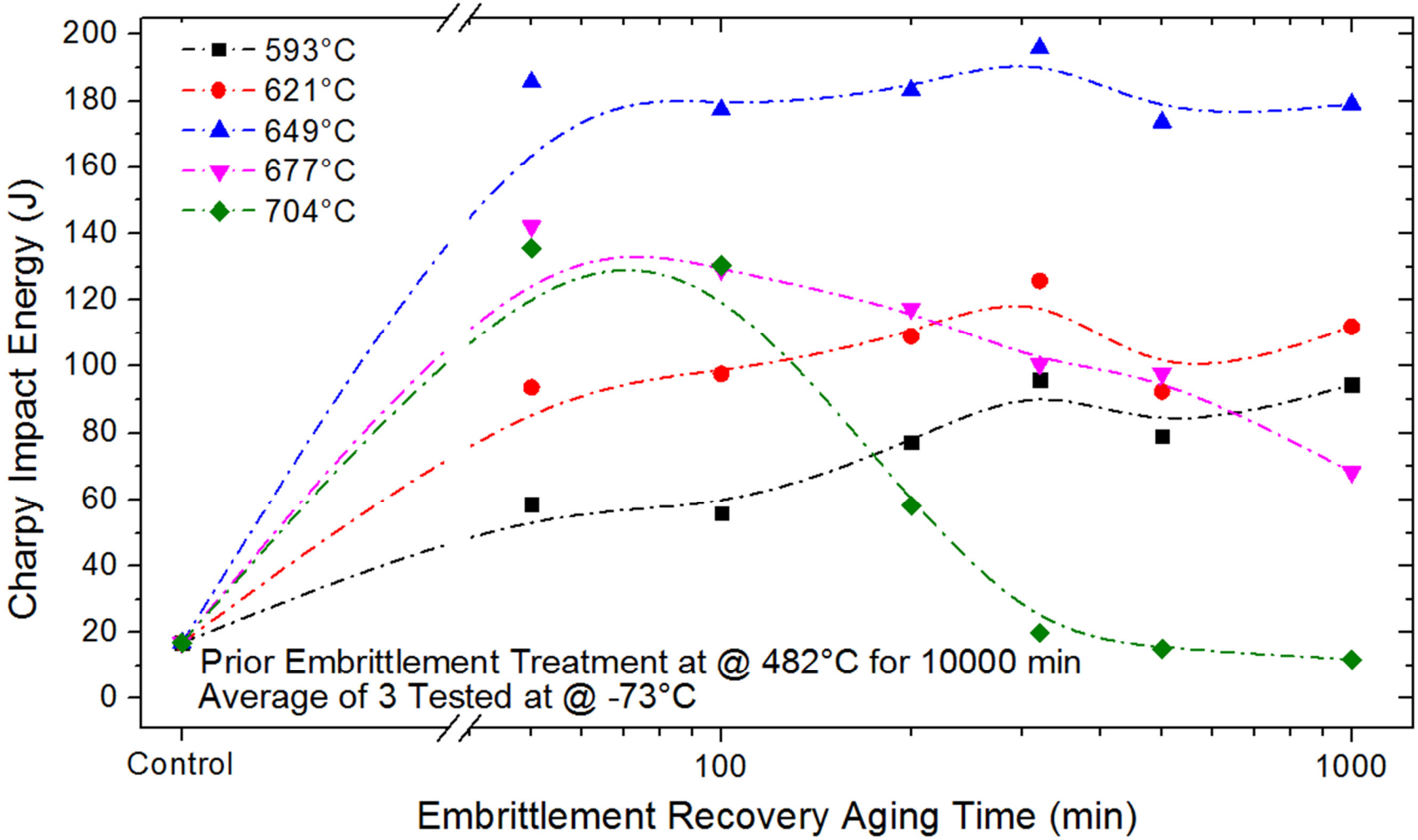

Figure 41: Embrittlement recovery rate results as measured by Charpy impact specimens tested at -73°C with treatments per Table 3. Selected embrittlement treatment corresponds to the maximum embrittlement measured in **Figure 39**.

5.2.4 Metallographic Observations of Embrittlement & Recovery

The incoming material had a mixed microstructure consisting primarily of tempered martensite with a small percentage of tempered bainite, in addition to some percentage of un-tempered products as shown in **Figure 42**. After embrittlement at 482°C, even at long treatment times, little to no observable difference can be identified in the primary microstructure of the sample shown in **Figure 43**. Therefore, as expected, no macroscale microstructural reason is present to explain the observed decrease in impact strength. In samples recovered from embrittlement via treatment at 648°C, the microstructure is nearly 100% tempered products as shown in **Figure 44**. This likely accounts for the additional increase in impact strength beyond the control sample. Finally, of note is the decrease in impact strength observed for recovery samples treated at 704°C for long time periods. In these samples it is immediately evident that the AC1 for the material has been exceeded and as a result the microstructure is mixed between the prior tempered martensitic structure and un-tempered martensite as shown in **Figure 45**. It should be noted that prior historical work on this alloy system noted an AC1 of approximately 721°C, which has been lowered by the additional alloying content of the current system being studied.

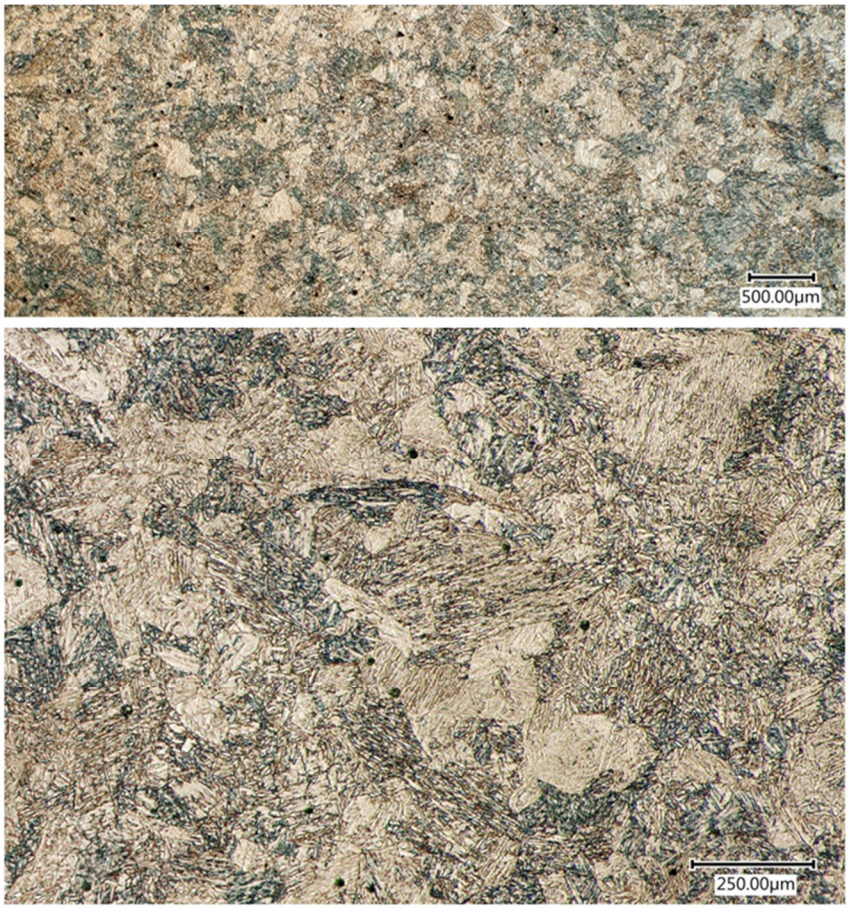

Figure 42: Control sample Heat Treatment, etched with 2% Nital. Tempered martensite microstructure.

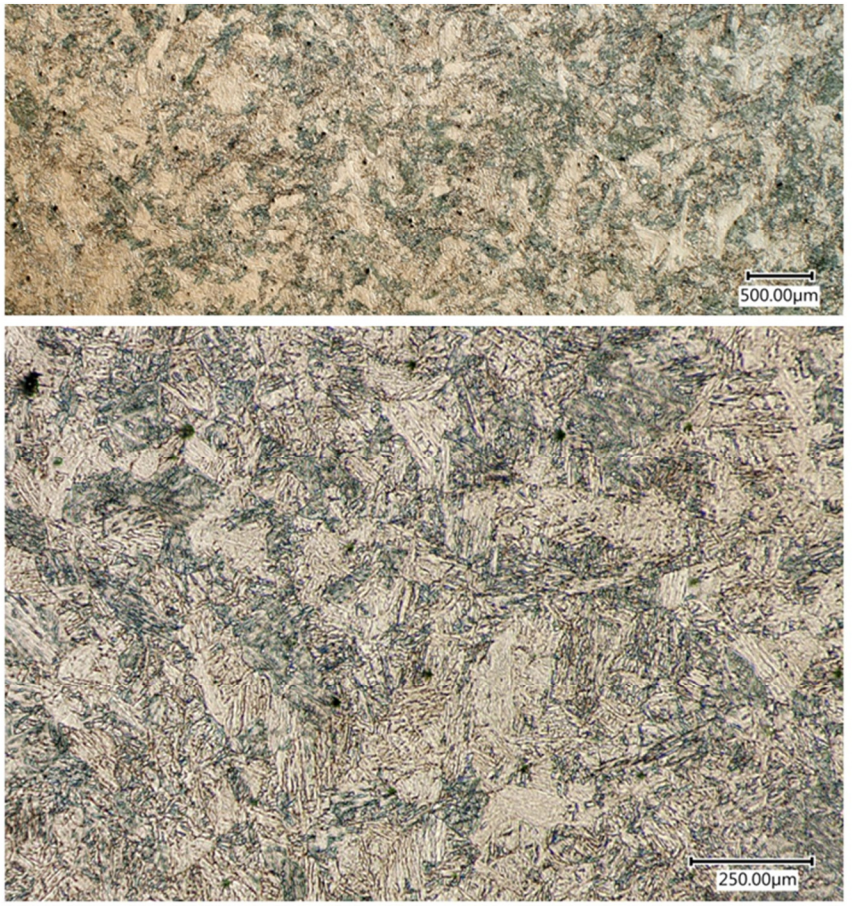

Figure 43: Sample treated at 482°C for 10,000 minutes after initial heat treatment, etched with 2% Nital. Tempered martensite microstructure.

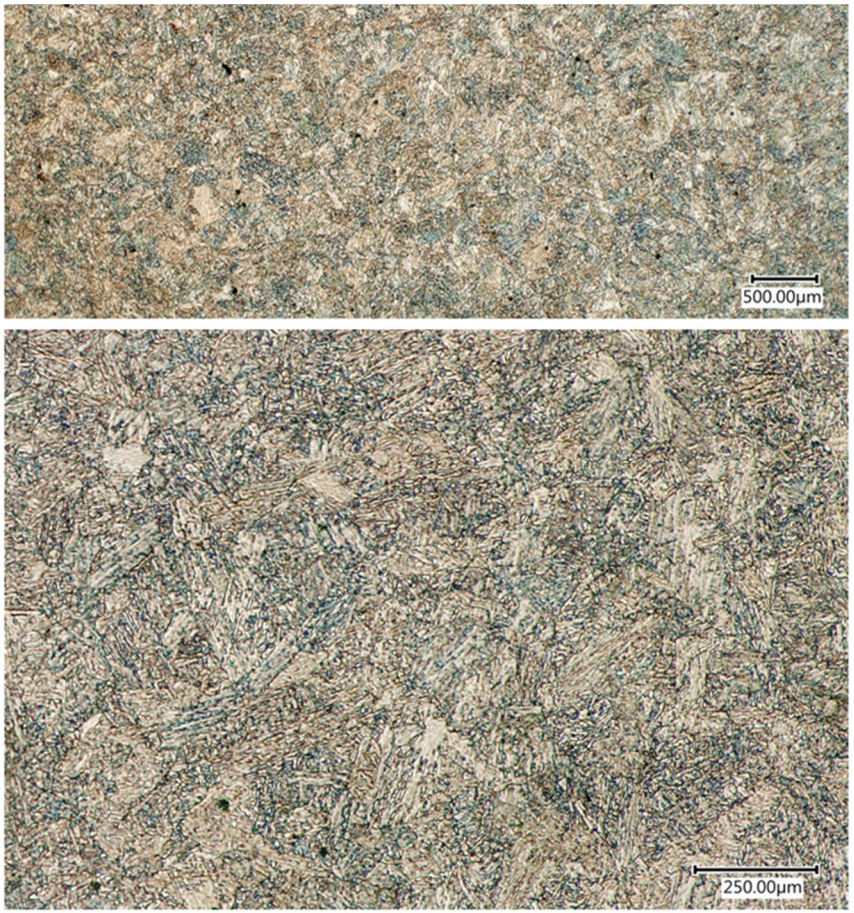

Figure 44: Sample treated at 649°C for 500 minutes with a pre-treatment of 482°C for 10,000 minutes after initial heat treatment, etched with 2% Nital. Tempered martensite microstructure

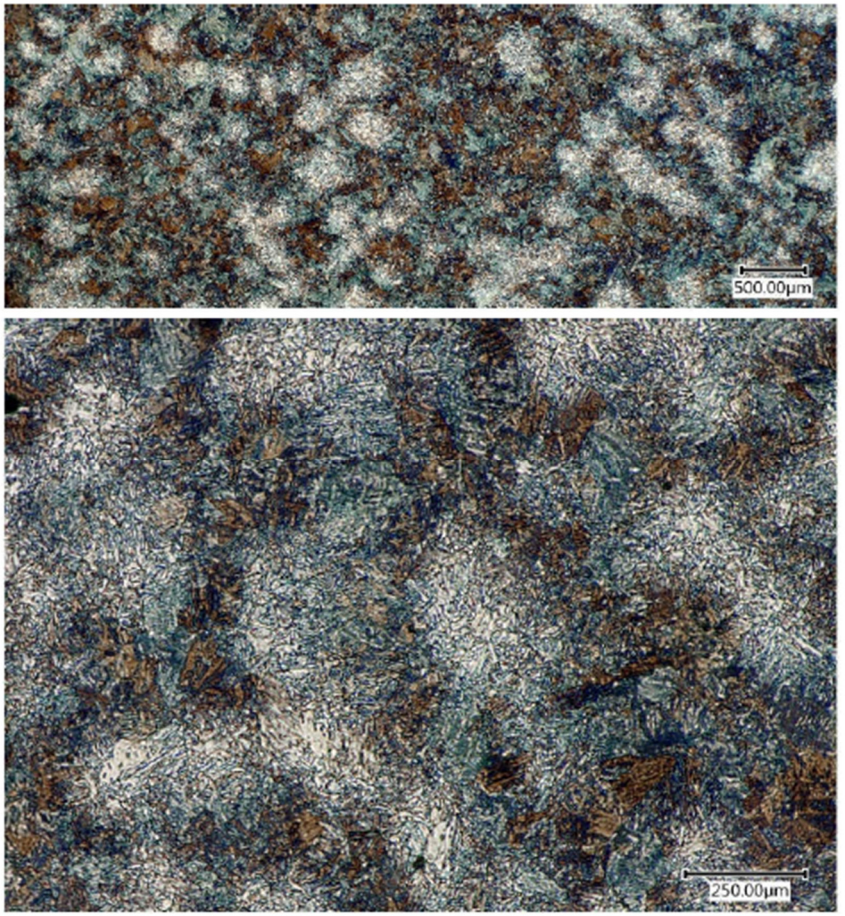

Figure 45: Sample treated at 704°C for 500 minutes with a pre-treatment of 482°C for 10,000 minutes after initial heat treatment, etched with 2% Nital. Mixed tempered and untempered martensite microstructure.

5.2.4 Fractography Observations of Embrittlement & Recovery

Specimens show a consistent transgranular cleavage failure mode at reduced impact strength (**Figure 47**) with a transition to mixed mode with an increasing percent of ductile fracture with increasing impact strength (**Figure 48**). The lack of any substantial area of intergranular fracture, even on samples with extremely low impact strengths <10 J is particularly noteworthy.

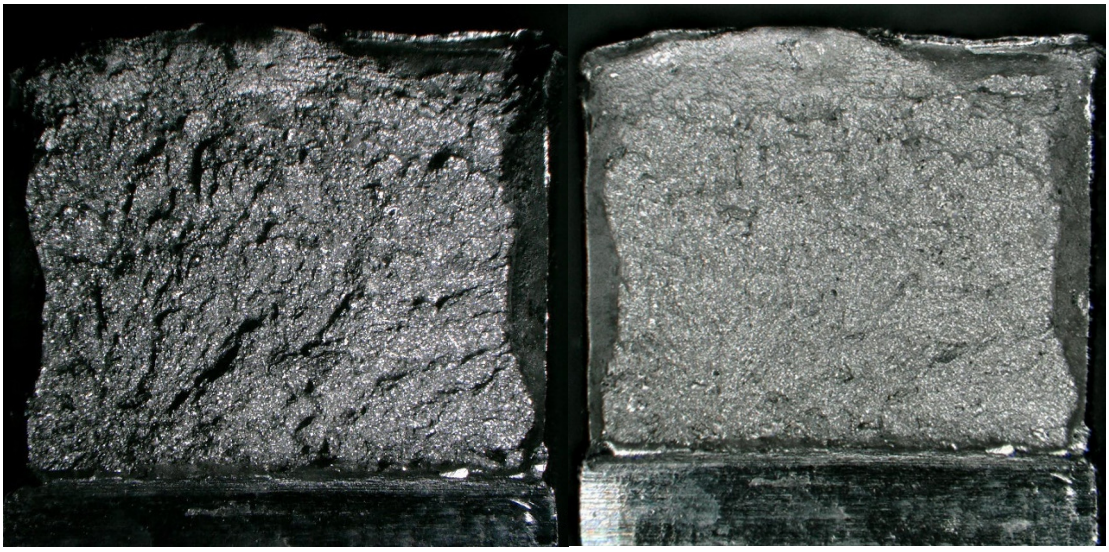

Figure 46: Optical fractography image of specimen 4F-3 under different lighting conditions to reveal the surface structure.

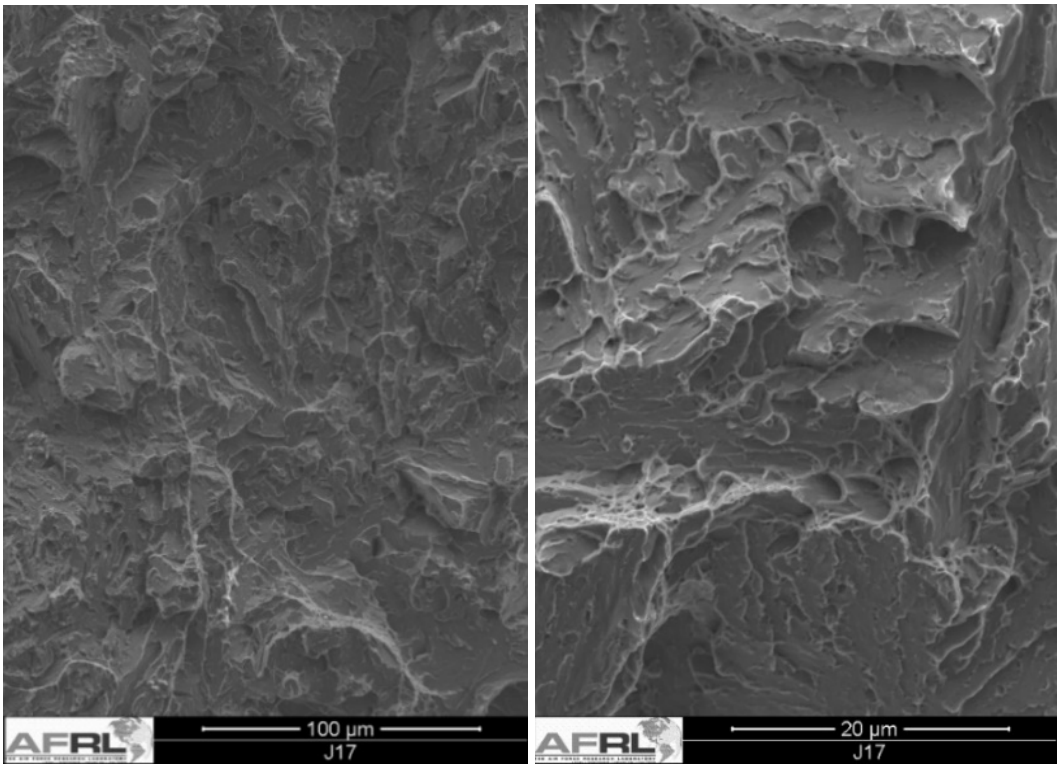

Figure 47: Trans granular quasi cleavage failure on specimen treated at 482°C for 10,000 min and tested at -73°C.

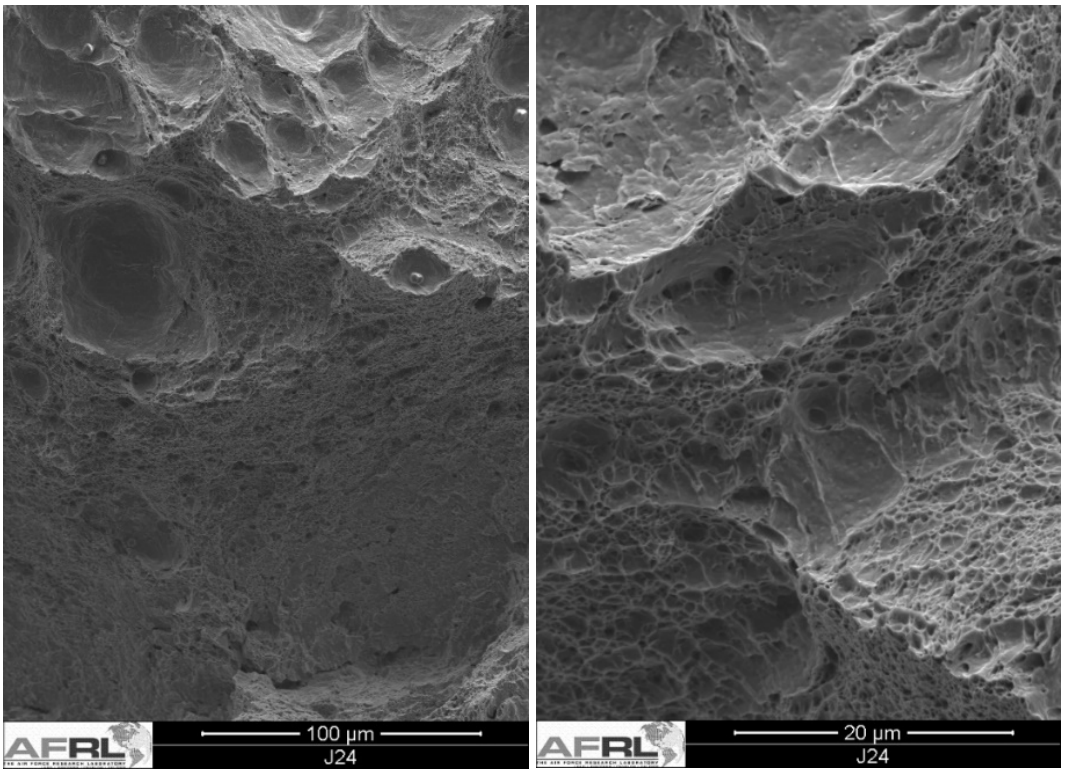

Figure 48: Ductile failure on control sample treated with a quench and double temper and tested at -73°C.

5.2.5 General Metallography of Embrittlement & Recovery

Examination of specimens via SEM reveals the presence of two distinct carbides, a round/blocky type and a needle-like type alloy carbide (**Figure 49**). Review of the literature along with results of computational analysis and TEM analysis shows that these are $M_{23}C_6$ and M_7C_3 carbides, respectively. In addition, specimens with lower impact strength after treatment within the embrittlement range show the presence of numerous carbide clusters. Examples of these clusters are shown in **Figure 50** and **Figure 51** with varied levels of severity. Of particular note in **Figure 51** is the large delta in carbide density is observed where the bottom left quadrant of the image shows a relatively small number of carbides when grain and martensite lathe boundaries show high density $M_{23}C_6$ clusters. M_7C_3 clusters are also observed in the bulk.

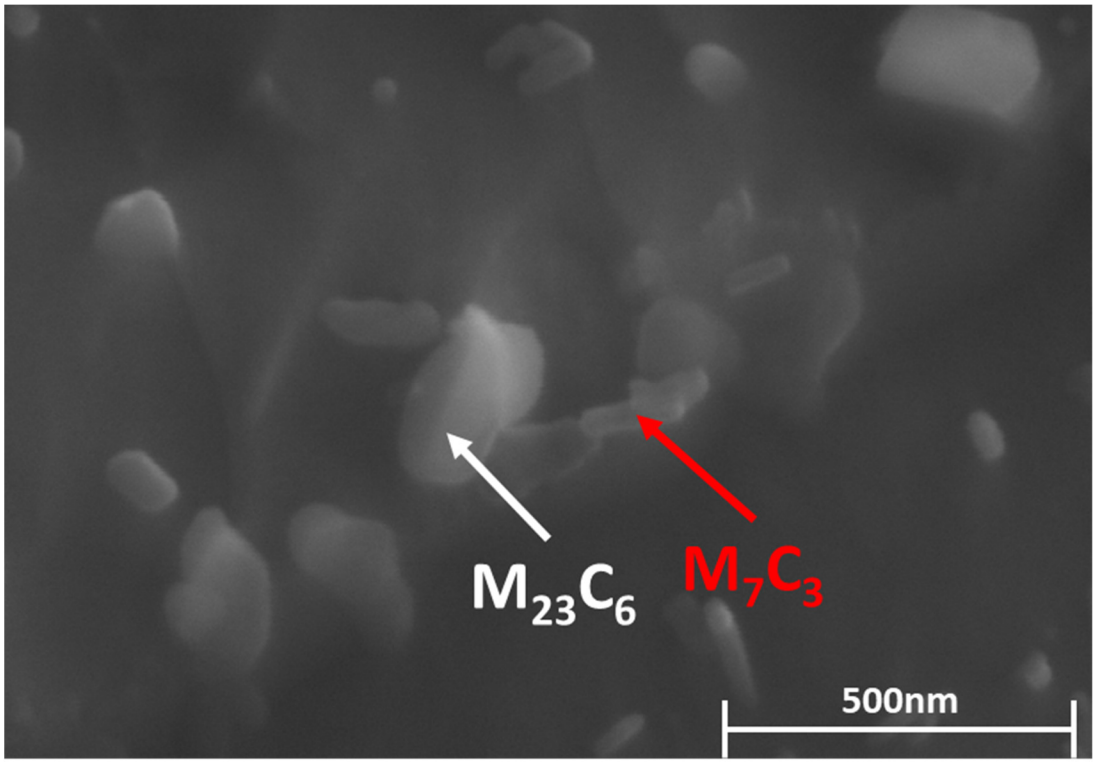

Figure 49: High magnification image; HT#A sample treated at 482°C for 10,000 minutes, etched with 2% Nital; $M_{23}C_6$ and M_7C_3 carbides identified

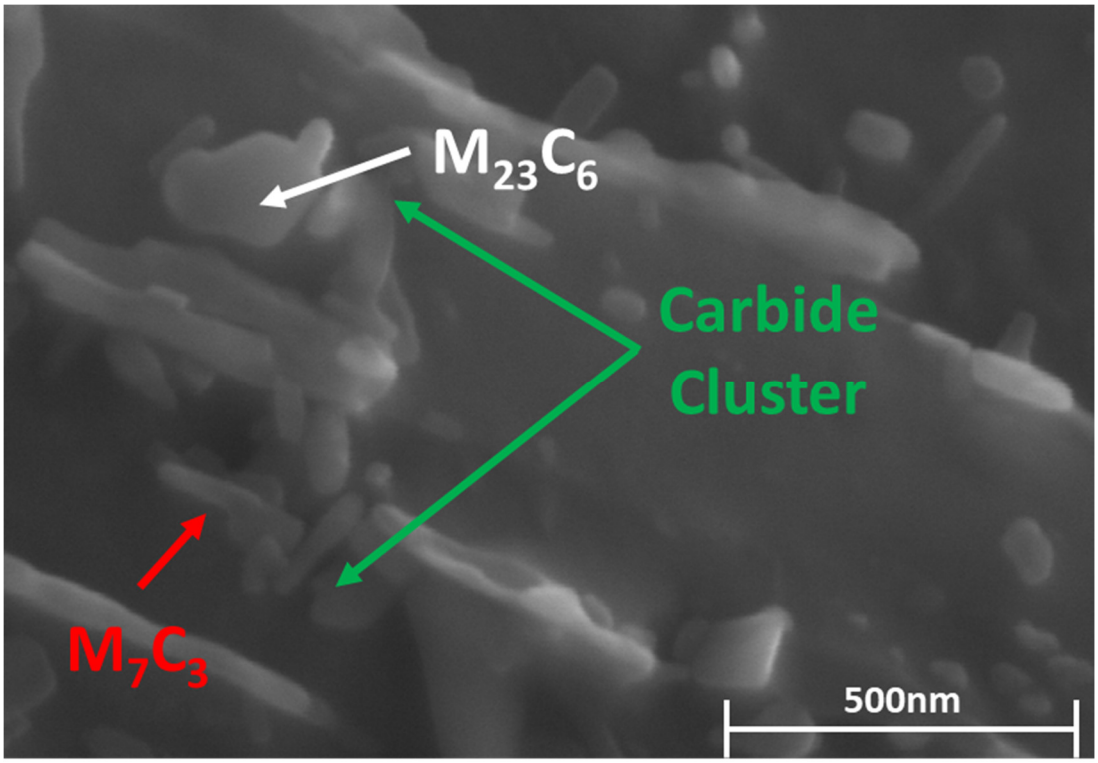

Figure 50: High magnification image; HT#A sample treated at 482°C for 10,000 minutes, etched with 2% Nital; Area of carbide cluster

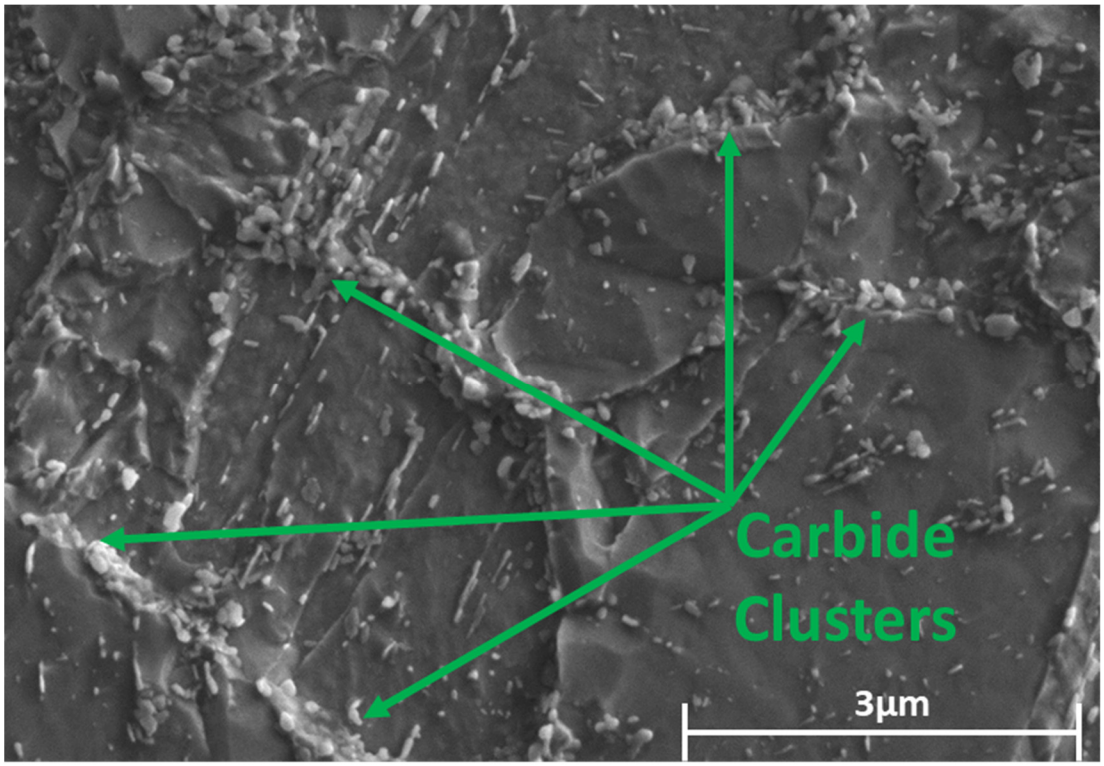

Figure 51: High magnification image; HT#2 sample treated at 482°C for 10,000 minutes, etched with 2% Nital; Multiple areas of carbide clusters present

5.2.6 Grain Boundary Metallography of Embrittlement & Recovery

Examination of the prior austenite grain boundaries for embrittled samples reveals the presence of numerous carbides. Samples treated for long times in the embrittlement range show an apparent increase in carbide content and larger carbides at boundaries. Samples treated to recovery from embrittlement show these carbides have begun dissolution from the PAGBs and from within the grains. It is noted that both $M_{23}C_6$ and M_7C_3 carbides of small size (<0.1 microns) appear throughout the bulk in the specimens. (**Figure 52** - **Figure 54**)

EDS of these carbides in comparison with results obtained via Thermocalc analysis in addition to their morphology indicate the carbides are $M_{23}C_6$ at PAGBs (**Figure 55** and **Table 22**). Analysis via EDS mapping (**Figure 56**) shows two different dominant compositions within the carbides of Mo and Cr. It appears that all bulk carbides have Cr as their dominant constituent. However, boundary carbides are observed that are predominantly Mo or Cr. Thermocalc CALPHAD predictions do show that Cr should be the dominate element in M_7C_3 carbides at 58.7 % mass fraction. The predictions for $M_{23}C_6$ carbides expect a balance between Cr and Mo, with a strong preference for Cr at 37% mass fraction Cr and 19% mass fraction Mo. However, it is indeed possible to have two stable $M_{23}C_6$ compositions dominant in different elements within the same material. (Complete results of CALPHAD analysis for composition are included as **Appendix C.**)

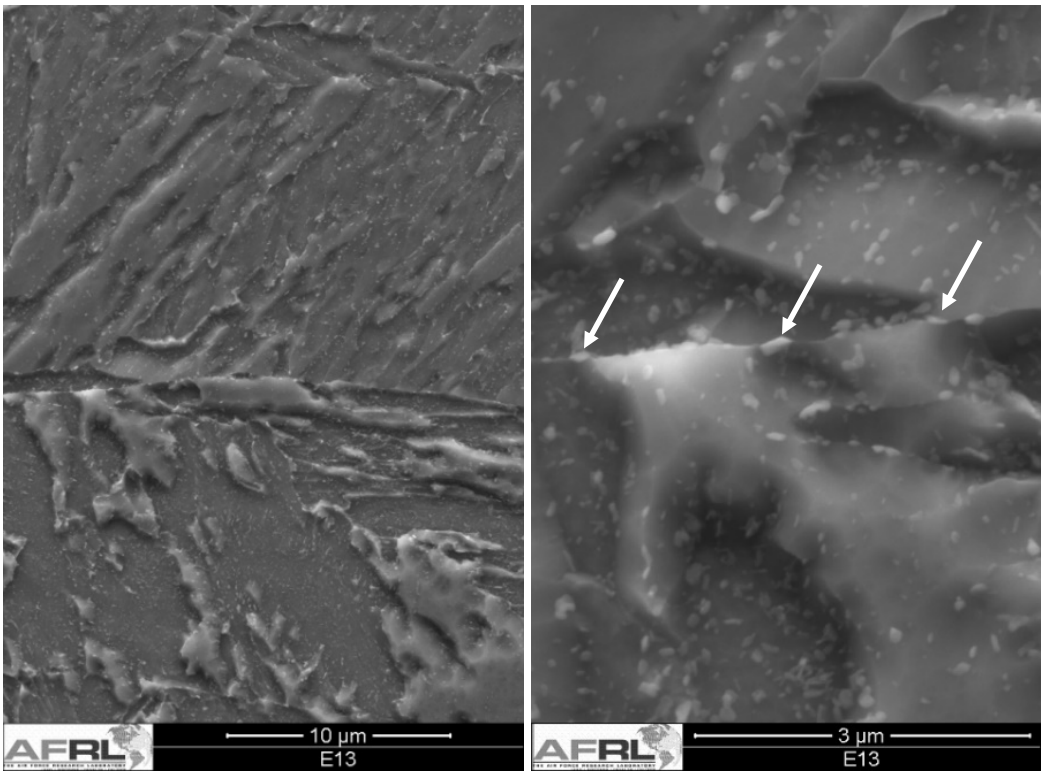

Figure 52: Initial Sample Heat Treatment, etched with 2% Nital, Prior austenite grain boundary [Boundary carbides noted by arrows]

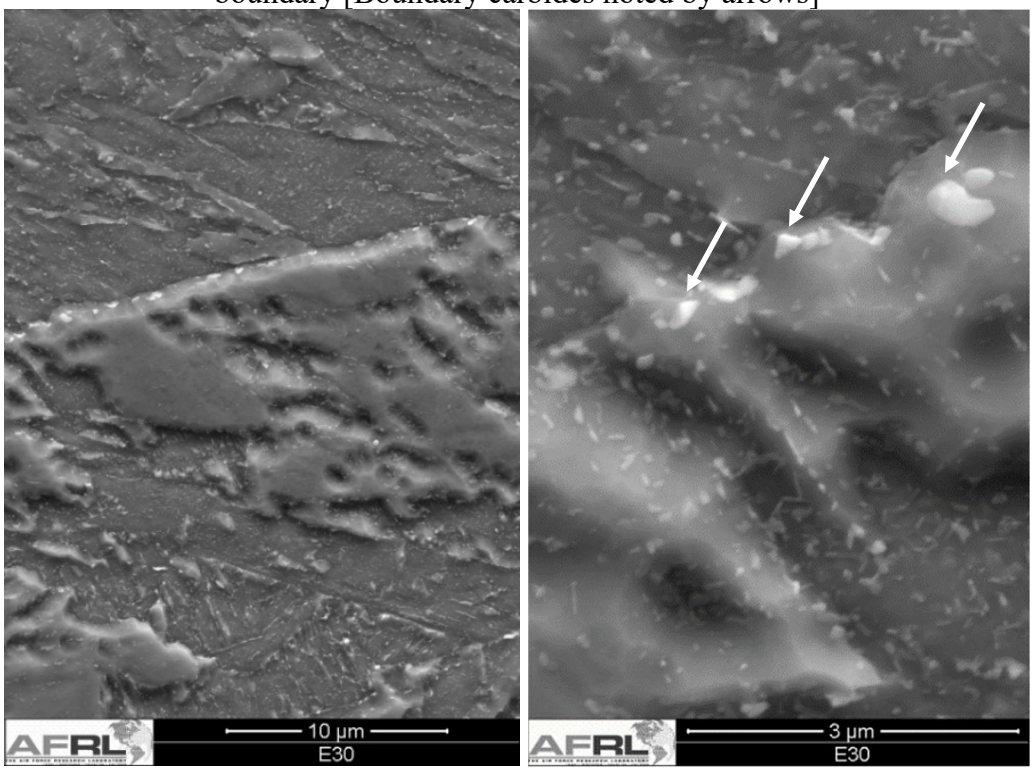

Figure 53: Sample treated at 482°C for 10,000 minutes, etched with 2% Nital, Prior austenite grain boundary. Carbides appear both larger and more semi-continuous than in the control specimen [Boundary carbides noted by arrows]

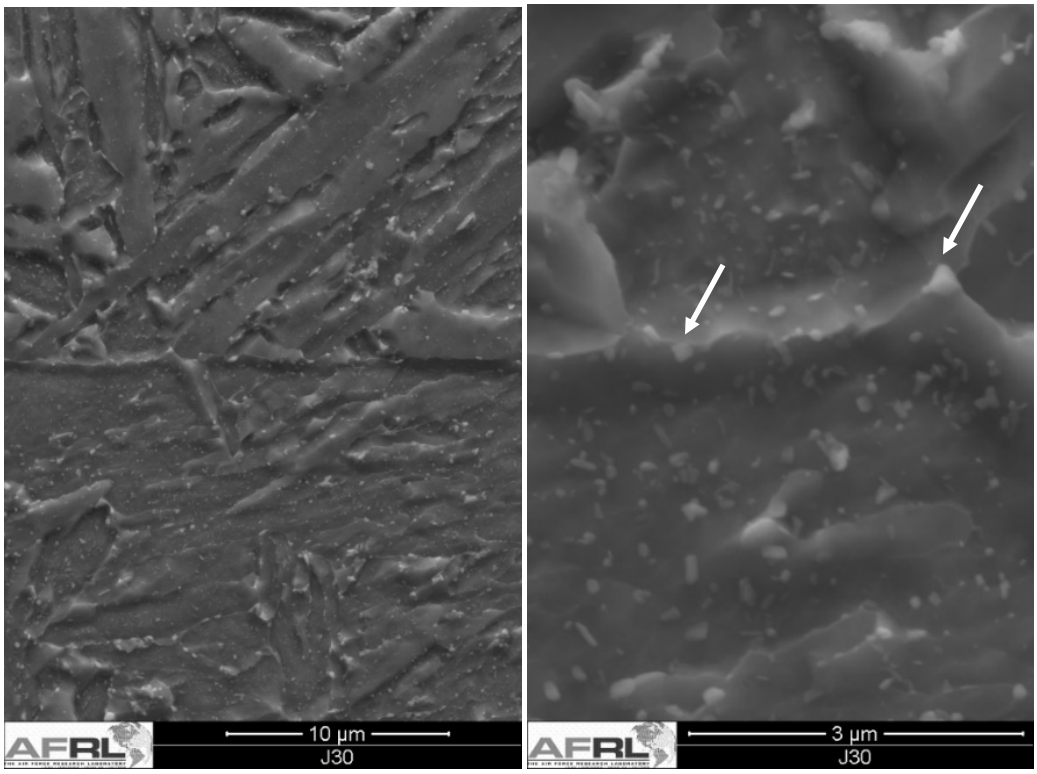

Figure 54: Sample treated at 482°C for 10,000 minutes with follow on embrittlement recovery treatment at 648°C for 500 minutes, etched with 2% Nital, Prior austenite grain boundary. Carbides are once again small and discontinuous at the boundary [Boundary carbides noted by arrows]

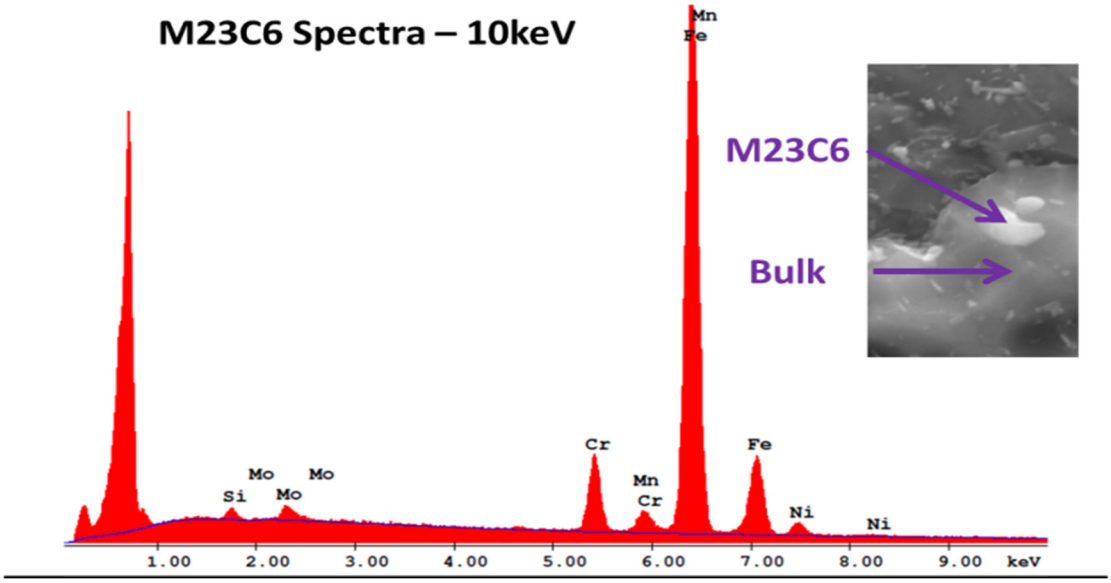

Figure 55: EDS spectra for the bulk and M23C6 carbide

Table 22: Thermocalc determinations for the bulk and M23C6 carbide chemical composition

Location		Si	Mo	Cr	Mn	Ni	Fe	C
EDS	M23C6	0.69	1.66	6.51	1.81	3.06	86.27	NM
	Bulk	0.60	0.49	1.57	0.99	3.10	93.25	NM
TC	M23C6	0	17.29	31.7	1.44	1.79	42.66	5.05
	Bulk	0.42	< 0.01	0.24	0.5	3.21	95.6	< 0.01

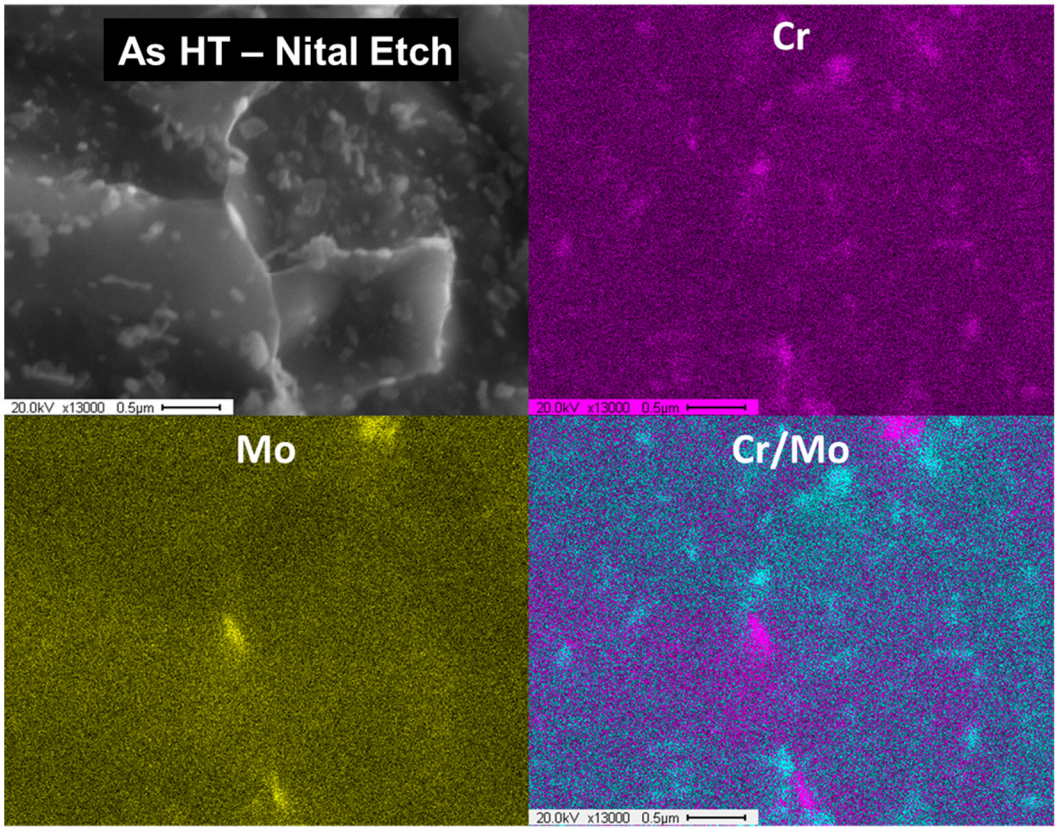

Figure 56: EDS of grain boundary carbides showing the presence of at least two distinct phases of Mo and Cr rich composition respectively.

No substantial difference is evident in either the grain size or the average width of the martensite lathes between initial, embrittlement, and recovery samples based on EBSD analysis shown in **Figure 57**. Thus, the differences in carbide location, morphology, density, and volume fraction appear to be the only significant differences between sample microstructures to explain differences in mechanical response other than those samples that exceeded the AC1.

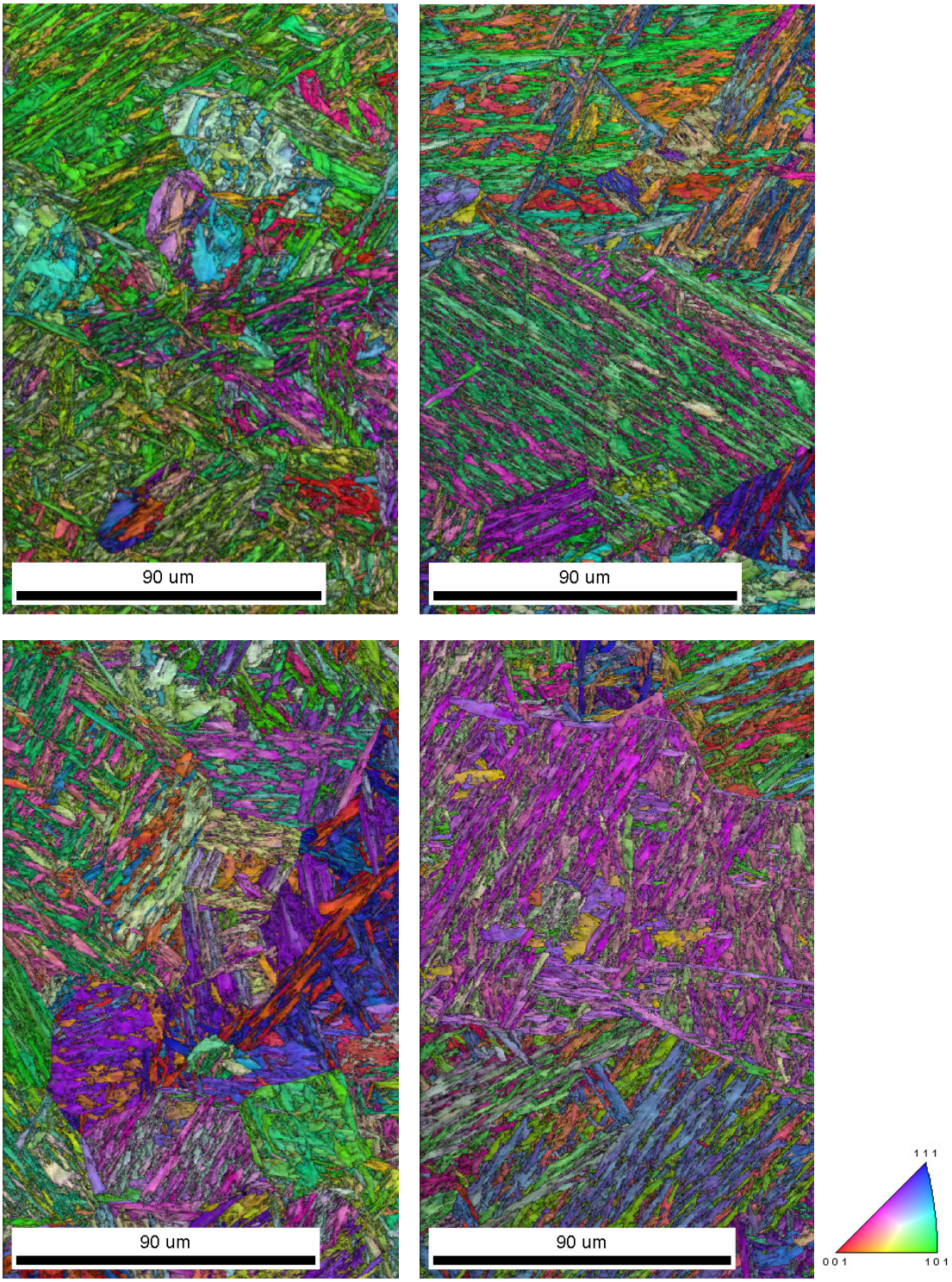

Figure 57: EBSD Images (TL) A10 [Control]; (TR) E13[Treated at 482°C for 10k min.]; (BL) E30[Treated at 649°C after being embrittled at 482°C]; (BR) J30 [Treated at 704°C after being embrittled at 482°C]

5.3 Hydrogen Aging within the Temper Embrittlement Range

5.3.1 Soaking in the Embrittlement Range with a Sub-Critical Anneal

An alternate set of treatments was conducted within the embrittlement range with a post austenitization and tempering treatment. The work presented in section 5.2 indicated that a heat treatment step would be required to recover from embrittlement and that the maximum embrittlement recovery rate could be obtained at 648°C. Thus, for these treatments, a sub-critical diffusion treatment at 648°C was added after the completion of the hydrogen soak treatment, but before the austenitization and tempering cycles. This added treatment was intended to migrate the embrittling elements away from the PAGBs prior to austenitization to ensure that some portion of these embrittling elements do not stay locked at boundaries in high concentrations, and to dissolving embrittling carbides back into the matrix phase generating a microstructure with limited to no continuous/semi-continuous grain boundary carbides.

Upon initial confirmation of the effectiveness of this treatment, a complete set of assays was performed investigating the effectiveness of soaking treatments throughout the embrittlement range. The normalizing factor for these treatments was the use of the empirically developed equation presented in section 6.1.1 to determine the soaking time for each given temperature range.

The results of these assays for tensile ductility are shown below in **Figure 58**. The initial control is the identical control from earlier hydrogen aging treatments where the sample from HT#A has been normalized, austenitized, and double tempered, but has received no hydrogen aging treatment. The second control “Post RAT” (Post Recovery, Austenitization, and Temper) has received a second austenitization and

double temper such that it has the same thermal history as the trial test blocks with the only exception being that it did not receive a hydrogen aging treatment between the first and second set of austenitization and tempering treatments.

The difference in tensile ductility between the initial and Post RAT control is significant. With no specifically designed hydrogen aging treatment the reduction of area at both the T/4 and T/2 location is increased significantly in the RAT control, with the T/4 location improving from 22% reduction of area and 8% elongation to 47% reduction of area and 11% elongation. While these samples still have significant levels of hydrogen (shown via low RoA), it is observed that the normal sequence of heat treatments for thicker section materials does, in itself, perform a minor hydrogen aging treatment.

Through the range of hydrogen aging temperatures used it is shown that all have been effective in increasing the tensile ductility above the Post RAT control sample. Test samples aged between 371°C and 482°C have approximately equal effectiveness, with T/4 reductions in area in excess of 57% and T/2 reductions in area measured between 43% and 52%, which is above the Post RAT T/2 control of 28%. Decreased aging effectiveness is observed for thermodynamically equivalent times above 482°C. The decrease in relative effectiveness is particularly prominent for the sample aged at 593°C, where the reduction of area at the T/2 location dropped from 52% at 482°C to 36% at 593°C with a similar decrease in elongation from 18% to 12%.

Figure 59 shows the Charpy impact strength and percent shear results across the range of hydrogen aging treatments. The difference in T/2 impact strength and percent shear between the initial and post RAT controls is striking, and a greater delta

in Charpy response exists than that observed for any other set of treatments executed in this study; from 90J to 133J and 65% to 100% shear. A slight increase is also observed at the T/4 specimen location. This is predominantly explained by the influence of the double austenitization in grain refinement.

Through most of the hydrogen aging temperature range studied there is minimal difference between the measured Charpy response with the post RAT control and the experimental assays. However, with increasing temperature; with a more pronounced effect at 593°C, the T/2 impact strength is decreased. This decrease is not observed at the T/4 testing depth.

Tensile yield and ultimate strength are shown in **Figure 60**. Once again the striking difference between the initial and post RAT control samples is immediately apparent, with increases of at least 50 MPa for both ultimate and tensile strength at both testing depths within the test blocks. This is attributed to the effect of the double austenitization as with the increases observed in Charpy response.

Throughout the range of hydrogen aging treatments studied there is an increase in yield and ultimate strength from 371°C to 482°C, followed by a decrease from 482°C to 593°C. A reason for the increase in tensile response is not immediately apparent, but the decrease for high temperature treatments could be explained simply as tempering.

It is noted that of all the thermal diffusion based treatments employed, the treatments in the embrittlement range with a sub-critical embrittling element diffusion treatment were the most effective as an alternate hydrogen soaking treatment. Furthermore, the resultant Charpy impact strength from these treatments exceeds that typically observed during manufacture of identical cross section castings using the

currently employed 300°C treatment at a yield strength near the maximum for the alloy. This indicates that the treatment is highly robust and should be capable of transitioning to industrial manufacture.

Table 23: Mechanical property results for embrittlement range hydrogen aging

BLOCK ID	AGING	DEPTH	UTS (MPA)	YEILD (MPA)	EL (%)	ROA (%)	CHARPY IMPACTS -73°C		
							Individual	AVG	% Shear
25628-1	Post RAT Control	1/4 T (1)	816.6	670.8	17.8	42.5	131, 141, 135	135.8	100.0
		1/4 T (2)	818.3	670.8	19.0	49.3			
		1/2 T (1)	807.5	664.7	12.0	21.9	128, 139, 131	132.6	100.0
		1/2 T (2)	806.0	665.6	12.0	35.0			
25628-2	593°C 6hrs	1/4 T (1)	822.1	668.1	20.0	54.8	137, 126, 139	134	100.0
		1/4 T (2)	823.4	680.6	18.0	52.8			
		1/2 T (1)	797.3	665.6	12.5	32.8	103,118, 135	118.8	98.3
		1/2 T (2)	795.5	662.0	13.0	35.7			
25628-3	538°C 10hrs	1/4 T (1)	826.5	677.2	19.0	51.0	124, 122, 145	130.3	99.3
		1/4 T (2)	812.0	667.4	19.0	48.5			
		1/2 T (1)	811.0	678.8	9.5	12.4	126, 129, 131	129	100.0
		1/2 T (2)	819.9	675.3	16.0	43.5			
25628-4	482°C 15hrs	1/4 T (1)	830.4	687.6	20.0	58.1	130, 112, 148	129.9	100.0
		1/4 T (2)	826.9	685.9	21.0	58.9			
		1/2 T (1)	832.2	687.6	14.5	32.5	146, 125, 116	128.7	100.0
		1/2 T (2)	828.7	677.0	20.0	54.1			
25628-5	426°C 6hrs	1/4 T (1)	826.2	672.8	20.0	58.1	139, 129, 150	139.2	100.0
		1/4 T (2)	825.1	675.3	20.0	56.8			
		1/2 T (1)	825.4	674.3	18.5	44.6	114, 113, 148	134.9	100.0
		1/2 T (2)	825.1	675.3	16.5	42.6			
25628-6	371°C 29.5hrs	1/4 T (1)	811.3	662.0	20.5	55.4	139, 147, 129	138.3	99.3
		1/4 T (2)	814.6	645.3	21.5	61.7			
		1/2 T (1)	807.8	660.3	23.0	59.0	139, 127, 124	129.9	100.0
		1/2 T (2)	804.3	653.3	15.0	37.6			
25622-1	538°C 24hrs	1/4 T (1)	800.5	643.5	20.0	48.5	107, 99, 129	112	100.0
		1/4 T (2)	799.0	639.2	18.5	47.0			
		1/2 T (1)	797.3	632.2	16.5	37.6	107, 99, 129	112	96.7
		1/2 T (2)	765.6	604.1	16.0	36.6			
25622-2	538°C 76hrs	1/4 T (1)	797.3	641.0	21.0	59.8	120, 122, 117	129.9	100.0
		1/4 T (2)	802.8	645.4	21.0	59.2			
		1/2 T (1)	804.3	649.7	20.5	45.2	84, 99, 97	95.9	86.7
		1/2 T (2)	793.7	621.7	13.0	31.1			

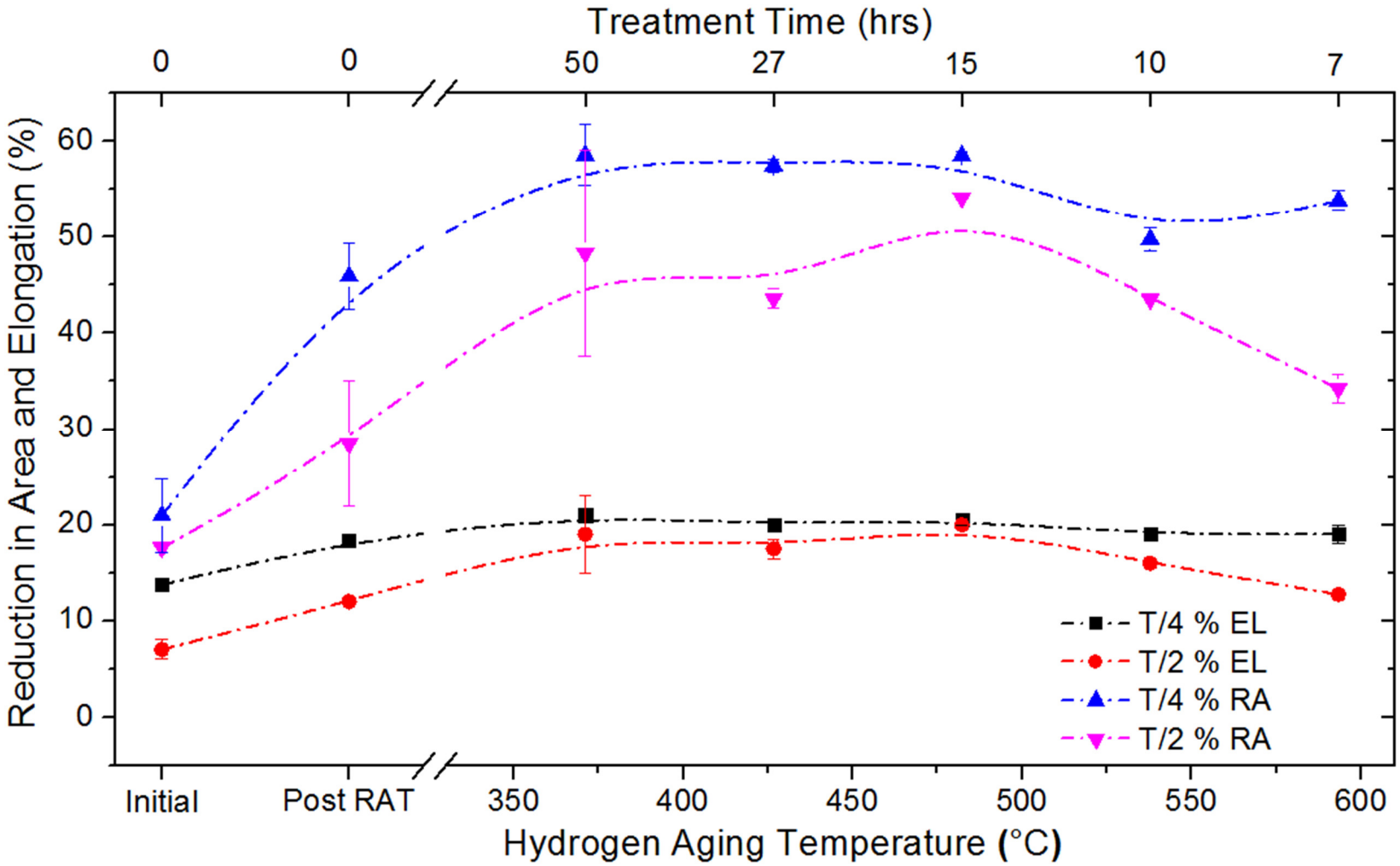

Figure 58: Tensile ductity for temper embrittlement range hydrogen aging. All treatment times are thermodynamically equivalent based on the Arrhenius derivation of Fick's second law. RAT = Recovery, Austenitization, and Temper.

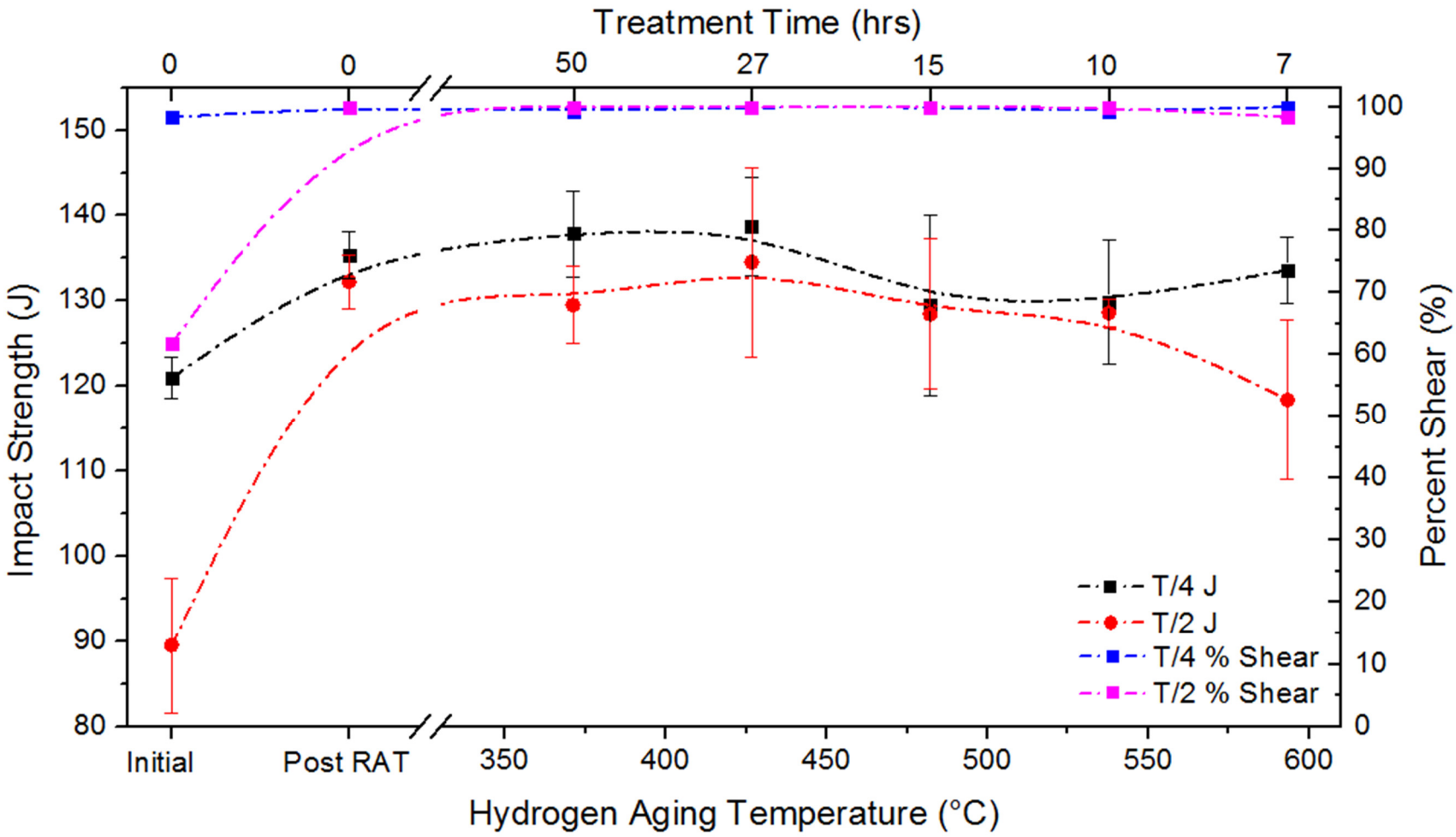

Figure 59: Charpy impact strength and percent shear results for temper embrittlement range hydrogen aging

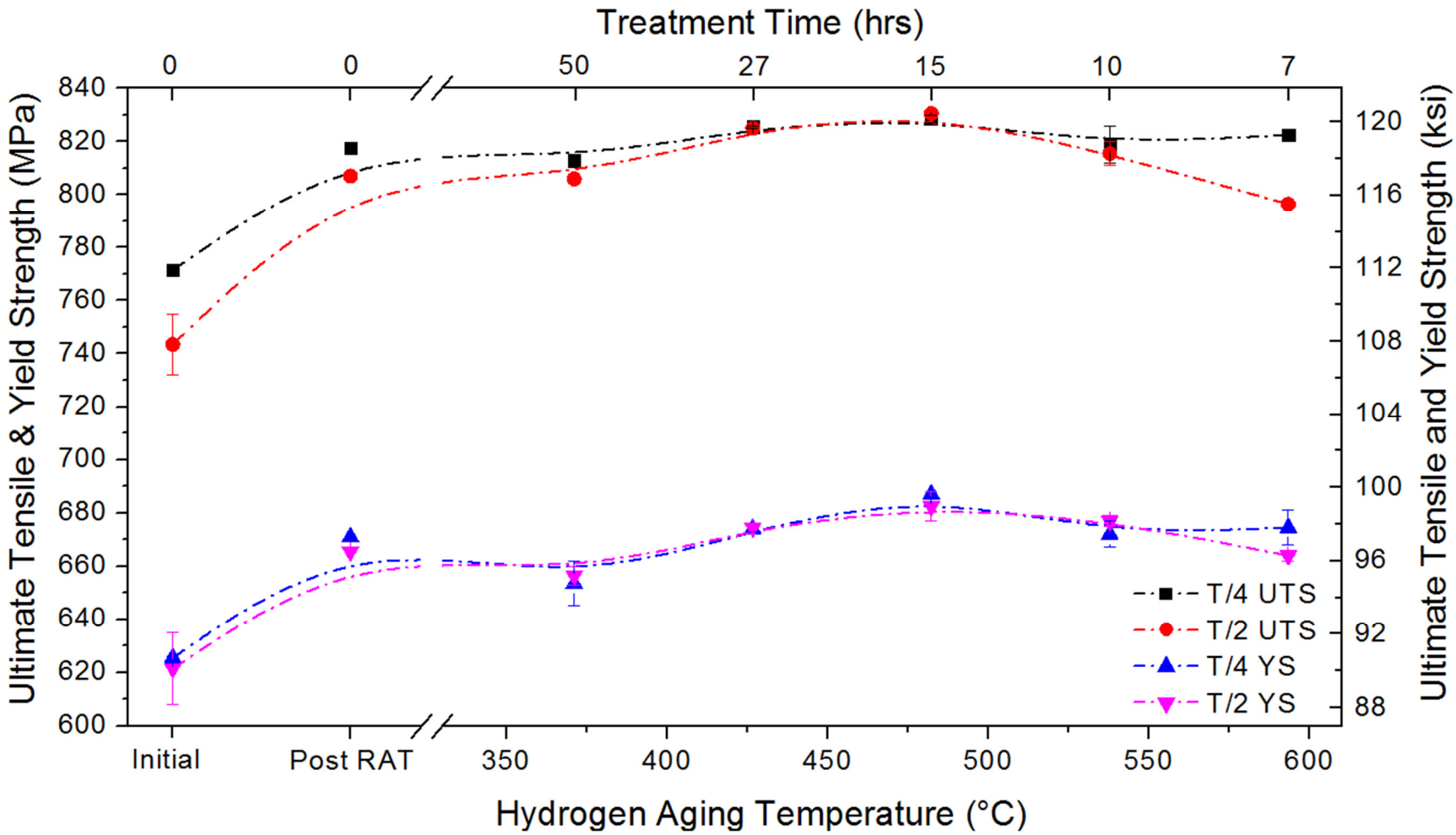

Figure 60: Tensile yield and ultimate mechanical response for temper embrittlement range hydrogen aging.

Of the treatments evaluated, the best balance between achieving the desired removal of monatomic hydrogen against time were those treatments conducted at 482°C (900°F) and 538°C (1000°F) for 15 hours and 10 hours respectively. In each case the test blocks from HT#A were subsequently treated with a sub-critical anneal at 648°C (1200°F) intended to recover from embrittlement followed by a re-austenitization and temper. These three treatments added an additional 22 hours to each cycle time. Based on the solution to Ficks' second law presented in section 2.1.5, in order to increase the thickness of specimens from 0.19m to 0.28m (7.5" to 11") an increase from 15 hours at 482°C (900°F) to 27 hours would be required. In addition, an increase to the austenitizing treatment time of 4 hours would be required. The resulting new hydrogen soak treatment would require 43 furnace hours for a 0.28m thick casting vs. the current treatment of 450 furnace hours; a decrease of 90%. However, this solution neither accounts for the increased starting concentration of hydrogen in a thicker test specimen, nor a complete understanding of the influence of approaching the solubility limit for achieving less than 1ppm diffusible hydrogen. It is noted that as the requirements at both T/4 and T/2 were met with this treatment at 482°C (900°F) on the high hydrogen heat, it would be expected that for a normal production heat the required mechanical performance could be achieved with significant margin.

Additional work was done to examine the influence of increasing aging time at 538°C with the post treatment sub-critical anneal and re-austenitization and temper. The results for reduction of area and elongation are detailed in **Figure 61**. In this case the expected trend of an increase in tensile ductility as measured by both reduction of area and elongation is observed. Similar to lowering aging temperatures, the

improvements observed at the T/4 depth were significantly higher than at the T/2 location.

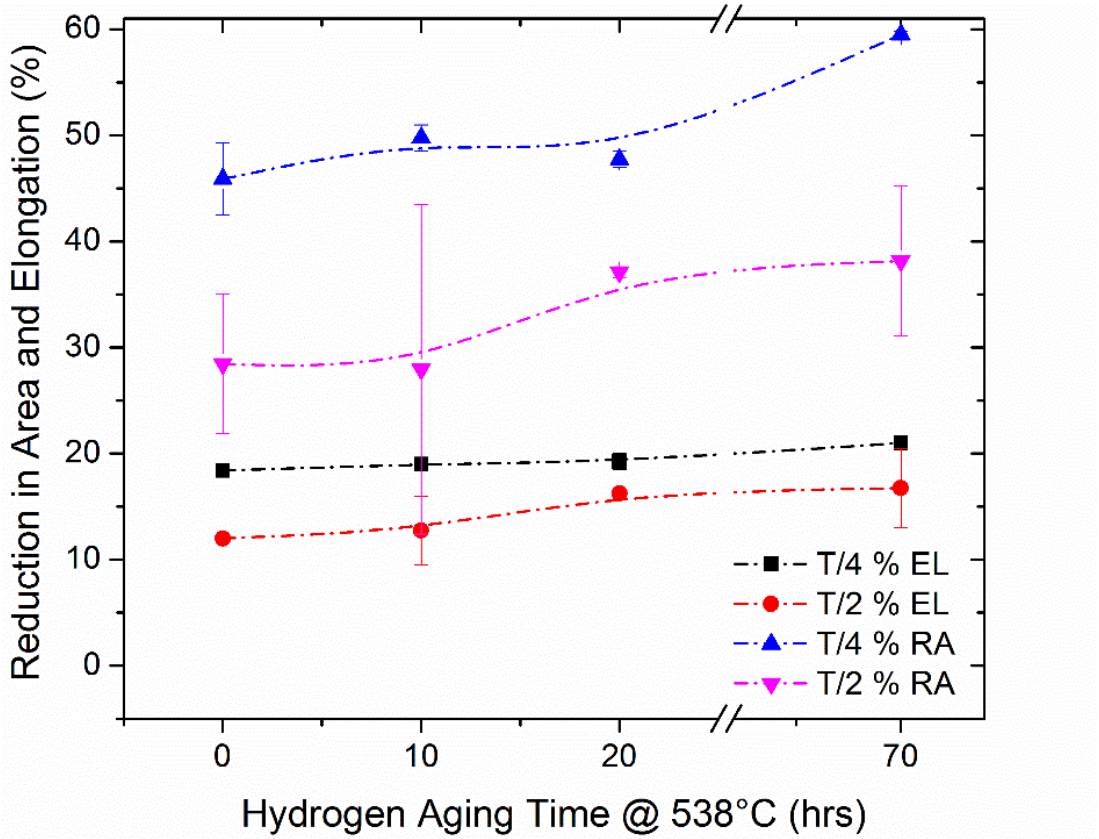

Figure 61: Reduction of area and elongation for hydrogen aging at 538°C on HT#A test blocks. Post aging 648°C treatment followed by re-austenitization and temper.

The Charpy response for 538°C hydrogen aging is detailed in **Figure 62**. Unexpectedly, a significant decline in Charpy impact strength, particularly at the T/2 location, is observed with a corresponding decrease in percent shear. The reason for this decrease is not immediately clear as it cannot be explained as an effect of low temperature tempering where a slight increase would be expected as was observed for increasing aging time at 482°C.

Figure 63 details the tensile yield and ultimate response. For both measurements a slight decrease in tensile response is observed, potentially explained

by the influence of a low temperature temper. That both the tensile and Charpy response decreases is of note and indicates that either some embrittlement phenomenon is occurring, or that the embrittlement observed during the hydrogen aging treatment has not been completely reversed. Such a conclusion could imply that for longer hydrogen aging times, additional time is required to recover from embrittlement. This is significant as it implies an embrittlement mechanism is present that is not entirely associated with embrittling trace elements such as phosphorous and sulfur.

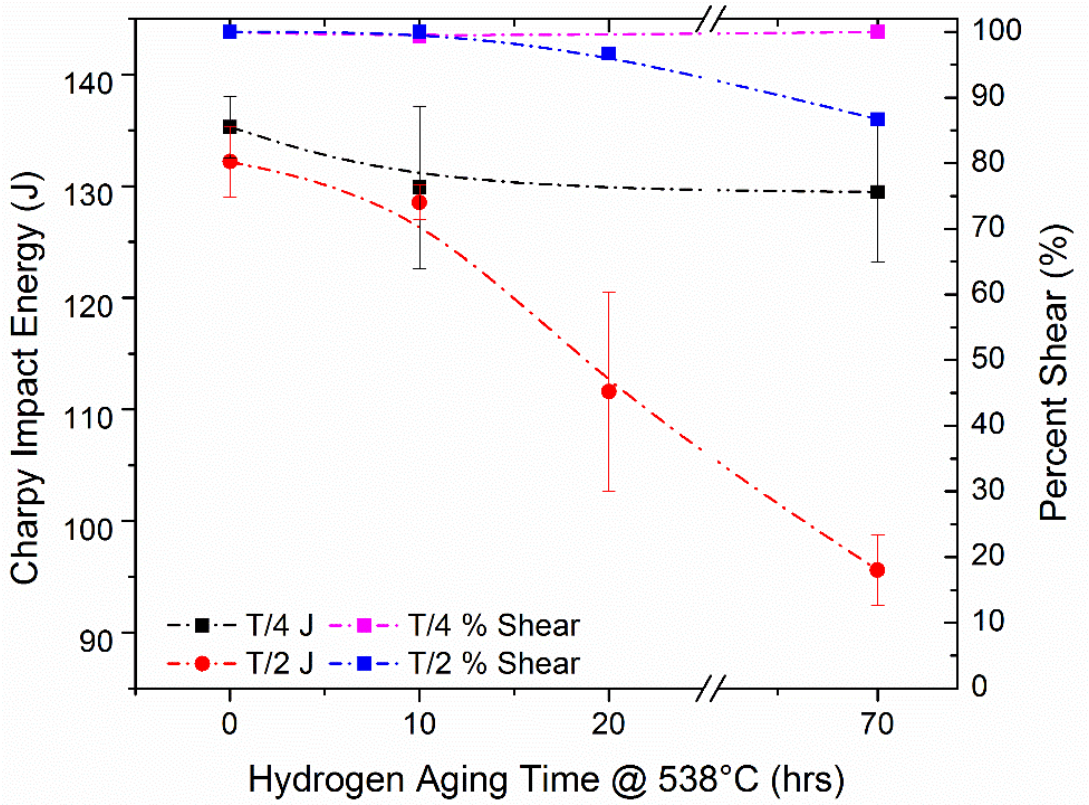

Figure 62: Impact strength and percent shear for hydrogen aging at 538°C on HT#A test blocks. Post aging 648°C treatment followed by re-austenitization and temper. (Note: A T/4 specimen for 20 hours has a machining error and is thus not included)

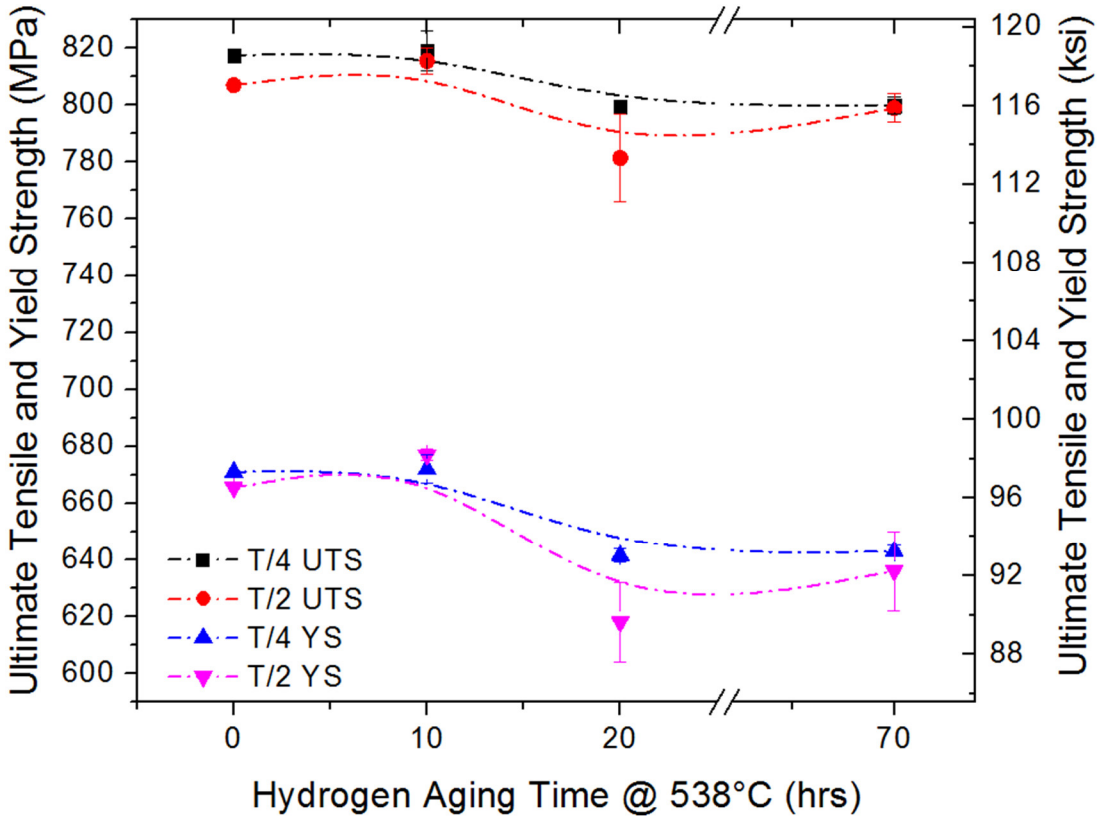

Figure 63: Tensile yield and ultimate strength for hydrogen aging at 538°C. Samples received a post aging 648°C embrittlement recovery treatment followed by re-austenitization and temper.

5.3.3 The Influence of Process Sequence

The initial hydrogen aging treatments were executed after the traditional quality heat treatment of normalization, austenitization, and tempering had already been completed. The follow on set of assays specifically examined the influence of process sequence on mechanical response.

The first assay, set A, examined performing the hydrogen aging treatment after austenitization, such that alloy carbides would be dissolved into the matrix at the start of the aging treatment. Subsequently the samples were tempered, with the objective to perform the dual role of both tempering the quenched martensitic structure and reversing temper embrittlement from the hydrogen aging treatment. (Block IDs 1, 2,

and 3 treated for 2, 6, and 15 hours during the 482°C hydrogen age) The results for tensile ductility are shown in **Figure 64**. The first three data points on the left show the response of the hydrogen aging treatment where both the elongation and reduction of area are shown to increase with increasing aging time. However, the minimum specification threshold of 50% reduction of area has not been achieved. The set of data points on the right of the graph represent the results for the traditional 300°C hydrogen age for 188 hours and the maximum reduction of area that the alloy with the applied temper is capable of receiving.

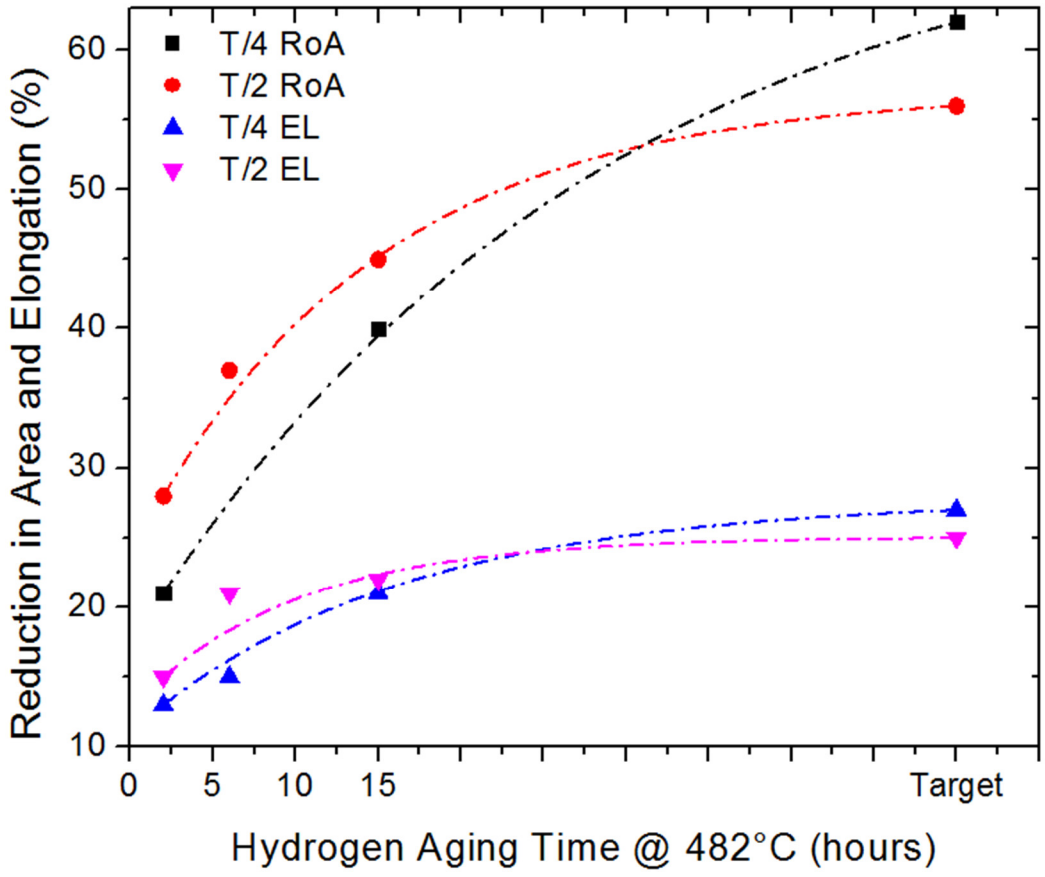

Figure 64: Reduction of area and elongation at the quarter line and center line for Industrial Heat #C with hydrogen aging at 482°C. Samples (Block IDs 1, 2 and 3) were austenitized, hydrogen annealed, and tempered. An exponential fit is applied to each data set. Target properties are from Block ID 8 aged at 300°C for 188 hours.

The exponential fit to the tensile ductility data projects that "target" mechanical properties matching that of the Block 8 control condition would be reached in approximately 50 hours. This projection would also anticipate achieving the minimum reduction of area (50%) and elongation (20%) after approximately 30 hours. This compares favorably with the 188 hours used for aging at 300°C, but requires further modeling and validation as will be discussed further in Chapter 6.

The impact strength at -73°C did not change significantly with aging time. However, a decrease of 20J is observed at -18C between aging for 2 hours vs aging for 15 hours (**Figure 65**). Slight increases in tensile response are observed at the centerline for increasing hydrogen aging time consistent with the results discussed above for embrittlement range hydrogen aging on HT#A (**Figure 66**). However, the degree of increase in response is less than observed for similar aging times on HT#A with the UTS increasing 10 MPa and the YS increasing 14 MPa.

In order to determine the materials' maximum ductility capability, three tensile specimens from each of the different assay sets were extracted. A low temperature hydrogen age at 300°C for 48 hours after austenitization and tempering was employed after the specimens were cut to 25.4mm, which removes or neutralizes all monatomic hydrogen down to the solubility limit at that temperature of approximately 0.16 ppm. These results are shown in **Table 24** along with the results from block 8.

Table 24: Mechanical Testing Results after Hydrogen Degassing from 25.4mm cross sections at 300°C for 40 hours for Studies on HT#C

MATERIAL	YIELD (MPA)	UTS (MPA)	EL (%)	ROA (%)	BHN
7 - CONTROL	735	604	25	59	227
5 – CONTROL	688	539	26	59	212
3 – CONTROL	740	601	24	59	224
BLOCK 8	702	557	25	56	214

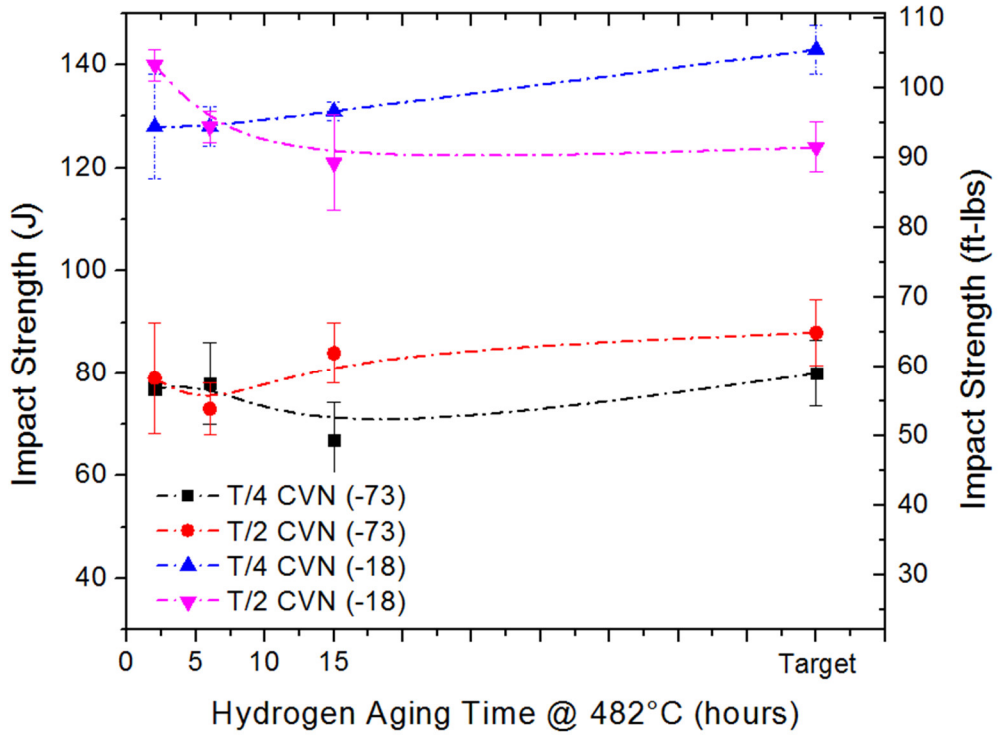

Figure 65: Charpy impact strength at -73°C and -18°C at the quarter line and center line for Industrial Heat #C (Assay Set A) with hydrogen aging at 482°C.

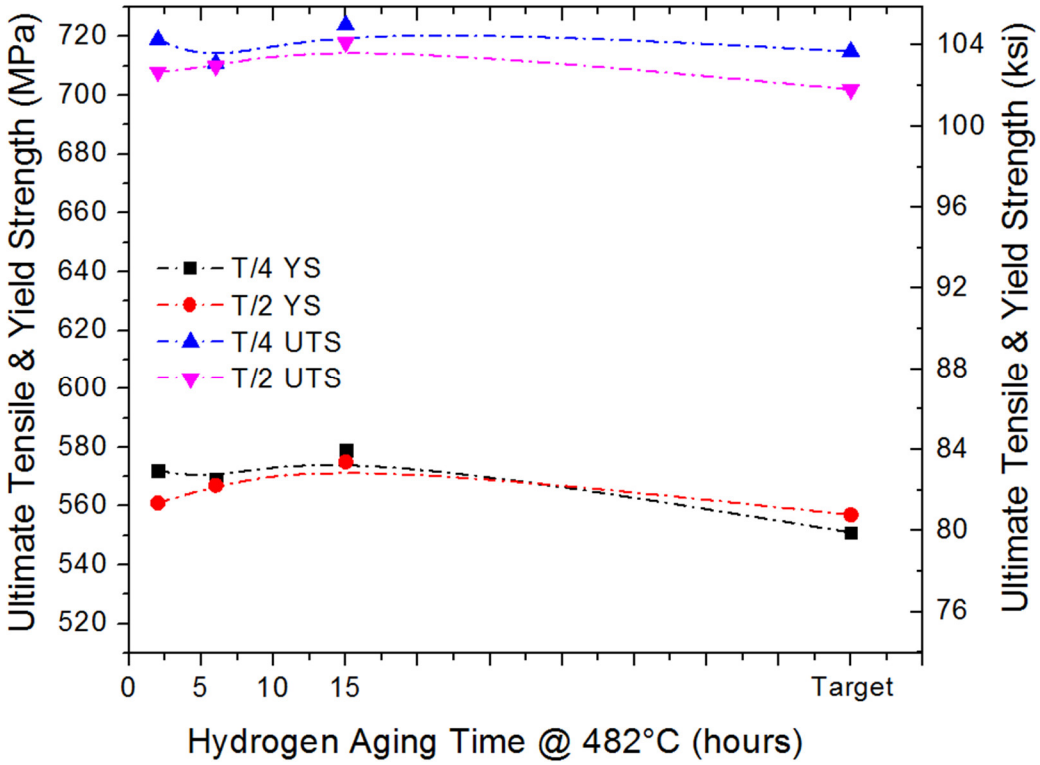

Figure 66: Tensile and Ultimate strength at the quarter line and center line for Industrial Heat #C (Assay Set A) with hydrogen aging at 482°C.

The second assay, set B (Block IDs 4 and 5), was treated with a hydrogen age and subsequent recovery treatment after all traditional heat treatments were completed. The third assay, set C (Blocks IDs 6 and 7), was treated with a hydrogen age and embrittlement recovery anneal prior to the austenitization treatment.

During the second assay set (B) the additional time in the tempering region has lowered both the Ultimate and Tensile strength by 25 to 40 MPa. In addition, the increase in aging time is shown to decrease the tensile response for assay set B while no significant change is observed for assay set C (**Figure 67**). This is particularly noteworthy as every other treatment on this and every other heat resulted in a neutral or positive impact on the tensile response.

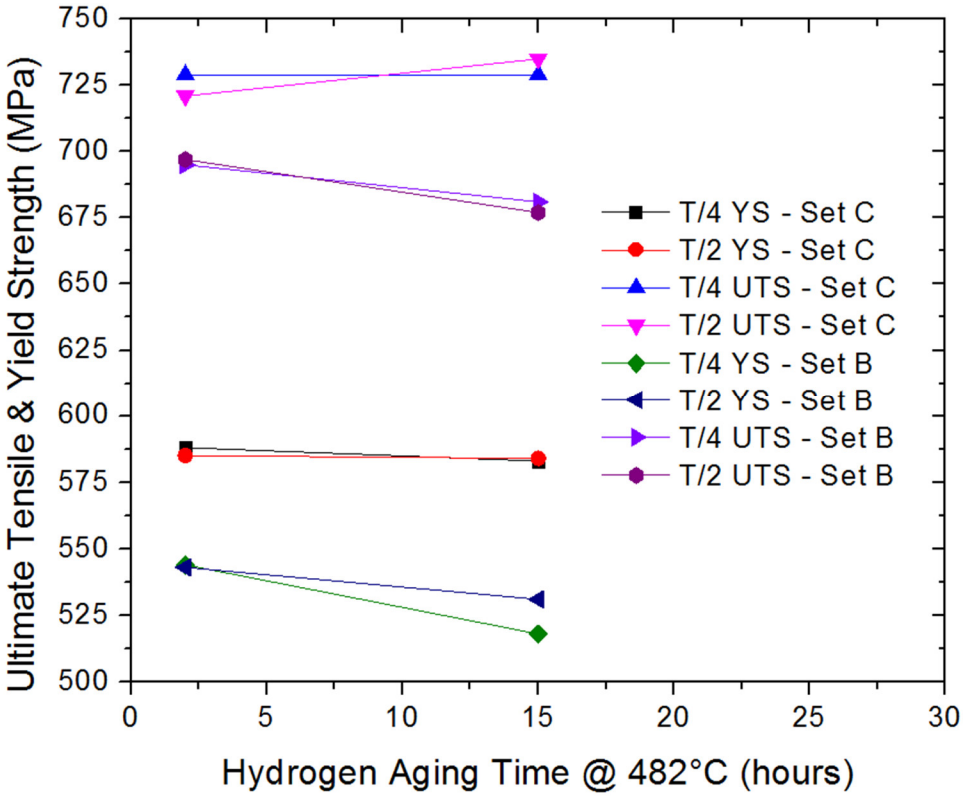

Figure 67: Tensile and Ultimate strength at the quarter line and center line for Industrial Heat #C (Assay Set B and C) with hydrogen aging at 482°C.

There are no discernable patterns to material response that are observed when examining the Charpy impact response between assay sets B and C (**Figure 68**). However, it is noted that as with assay set A, the applied treatment has resulted in complete recovery from embrittlement.

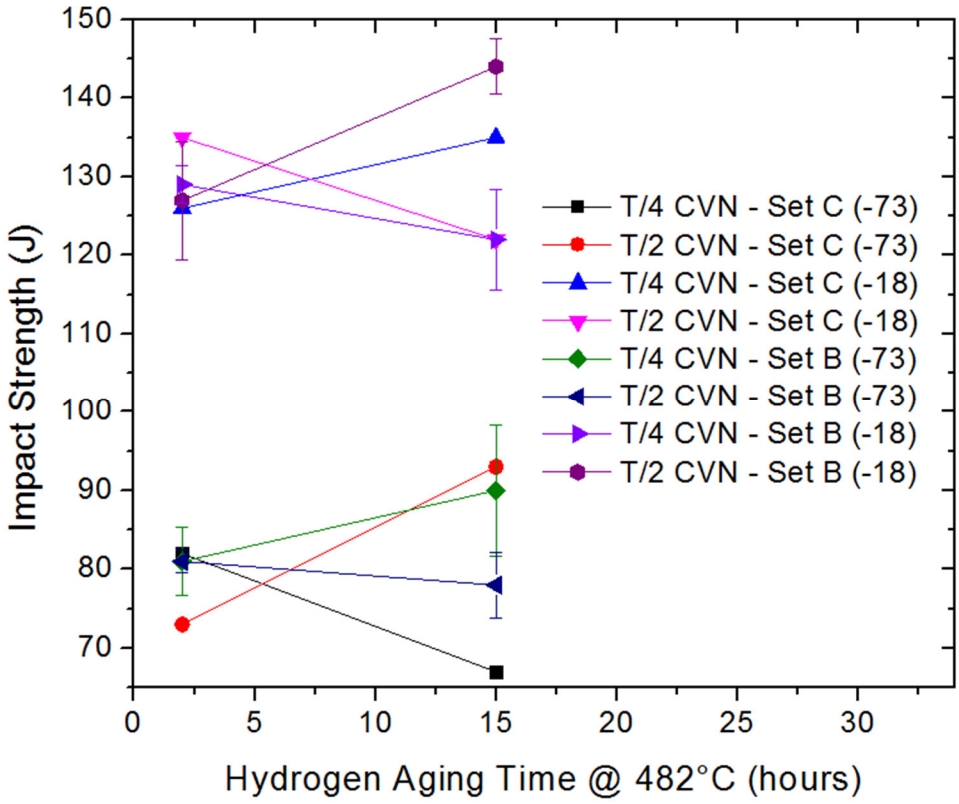

Figure 68: Charpy impact strength at -73°C and -18°C at the quarter line and center line for Industrial Heat #C (Assay Set B and C) with hydrogen aging at 482°C.

A significant delta in the increase to the tensile ductility is observed between assay set B and C (**Figure 69**). The mechanical response for set B are nearly universally higher at both aging temperatures. The largest delta between the sets is observed in the reduction of area measured at 15 hours of aging at 13%. It is also noted that the treatment applied to Block 5 is the only treatment that achieved specification acceptable reduction of area at the centerline location.

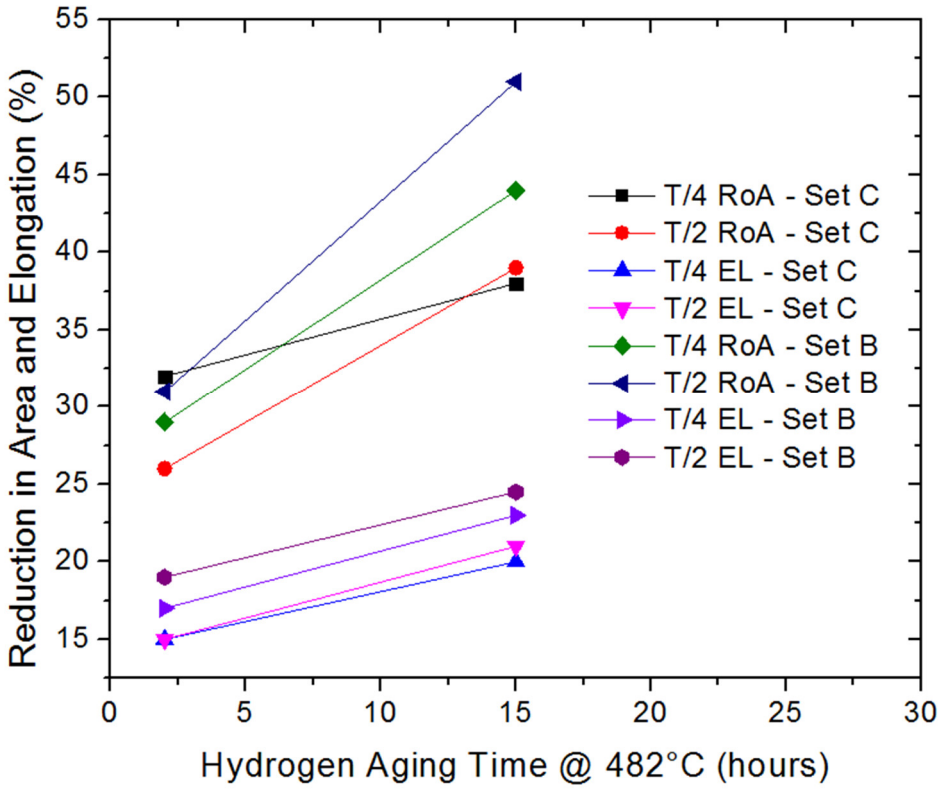

Figure 69: Reduction of area and elongation at the quarter line and center line for Industrial Heat #C (Assay Set B and C) with hydrogen aging at 482°C.

The specimens treated with a recovery treatment anneal had a significantly different carbide structure than those that received a traditional heat treatment apart from the hydrogen age before the temper as shown in **Figure 70**. Sample 3 (which was treated with an austenitization, hydrogen age, and temper) has both a higher number count and volume fraction of carbides as compared to Sample 5 (treatment was an austenitization, temper, hydrogen age, and anneal). While the concentration of carbides is higher on sample 3, it is clear that the boundary carbides are discontinuous in both sample 3 and 5. It should also be noted that in both samples, only round $M_{23}C_6$ carbides are present in the microstructure, consistent with CALPHAD predictions for this chemical composition.

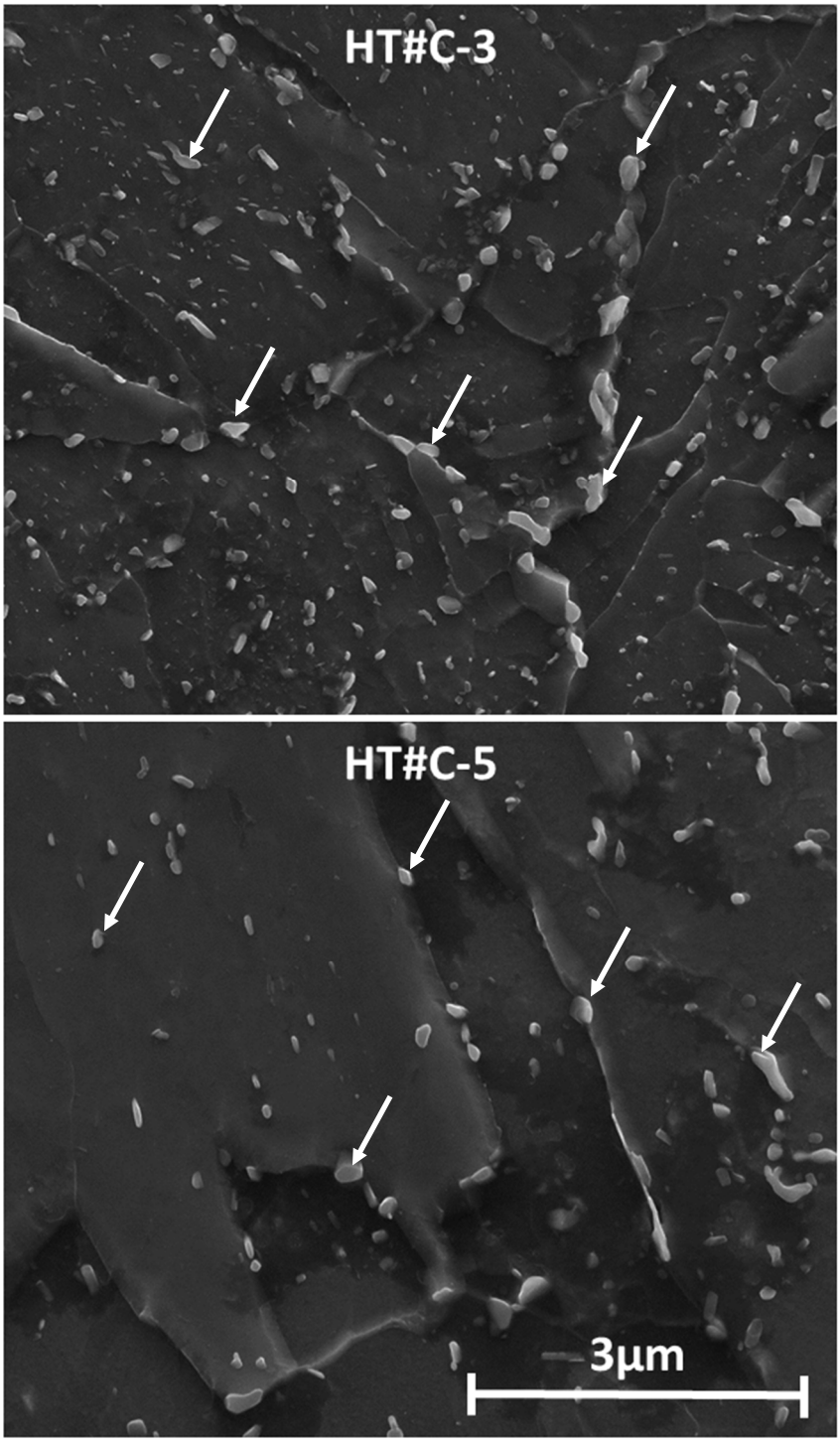

Figure 70: SEM Images of carbide structure on HT#C. [Top] Sample treated with an austenitization, 482°C aging treatment and 660°C temper. [Bottom] Sample treated with an austenitization, 660°C temper, 482°C aging treatment, and a 649°C anneal. (White arrows highlight carbide examples)

Table 25: Mechanical Testing Results for Studies on HT#C

BLOCK ID	DEPTH	YIELD (MPA)	UTS (MPA)	EL (%)	ROA (%)	BHN	CHARPY IMPACTS -18°C			CHARPY IMPACTS -73°C		
							Individual (J)	AVG (J)	% Shear	Individual (J)	AVG (J)	% Shear
8 CONTROL	1/4T	551	715	27	62	215	134,150,146	143	65	92,70,78	80	60
	1/2T	557	702	25	56	214	120,134,119	124	60	100,87,78	88	50
1	1/4T	572	719	13	21	217	141,116,126	128	85	76,76,78	77	50
	1/2T	561	708	15	28	217	142,134,144	140	80	64,73,100	79	55
2	1/4T	569	711	15	20	219	121,130,134	128	60	64,78,92	78	60
	1/2T	567	710	21	37	217	132,122,130	128	60	80,76,63	73	60
3	1/4T	579	724	21	40	228	130,128,134	131	70	58,61,81	67	60
	1/2T	575	718	22	45	220	108,116,139	121	70	89,72,90	84	60
4	1/4T	544	695	17	29	214	124,132,130	129	70	73,82,88	81	60
	1/2T	543	697	19	31	213	140,127,114	127	65	83,81,78	81	60
5	1/4T	518	681	23	44	206	126,130,109	122	55	104,90,75	90	70
	1/2T	531	677	25	51	201	151,140,141	144	65	70,79,84	78	55
6	1/4T	588	729	15	32	221	123,138,117	126	70	89,76,80	82	60
	1/2T	585	721	15	26	220	147,136,122	135	70	64,64,92	73	60
7	1/4T	583	729	20	38	223	122.128.154	135	60	60.66.74	67	60
	1/2T	584	735	21	39	223	130,123,108	122	60	89,76,114	93	60

5.4 Computational CALPAD Results

Thermocalc analysis shows the existence of three stable carbides for HT#A as shown in **Figure 71**.

- Vanadium carbides
    - Dissolving completely @ 440°C
    - Primarily C, V, and Fe in composition
- $M_{23}C_6$ carbides
    - Dissolving completely @ 740°C
    - Primarily Fe, Cr, C, Mo in composition
- M_7C_3
    - Dissolving completely @ 690°C
    - Primarily Cr, C, Mn, Fe in composition

It is interesting to note that this composition varies from the historical HY-80 grades used during the original development of the alloy in the 1950s and 60s. With the need for increasingly thick articles, the carbon equivalent has nominally increased over time to drive increases in the material's hardenability. In lower carbon equivalent grades (such as HT#B and #C) Thermocalc analysis predicts three principle differences vs. current high carbon equivalent grades (such as HT#A) being evaluated that should be considered when examining historical literature.

- An increase in the volume fraction of vanadium carbides and a shift up of the dissolution temperature by 100°C.
- An increase in the volume fraction of $M_{23}C_6$ carbides.
- No presence of M_7C_3 carbides in the treatment range being studied associated with a shift down in the dissolution temperature by 300°C.

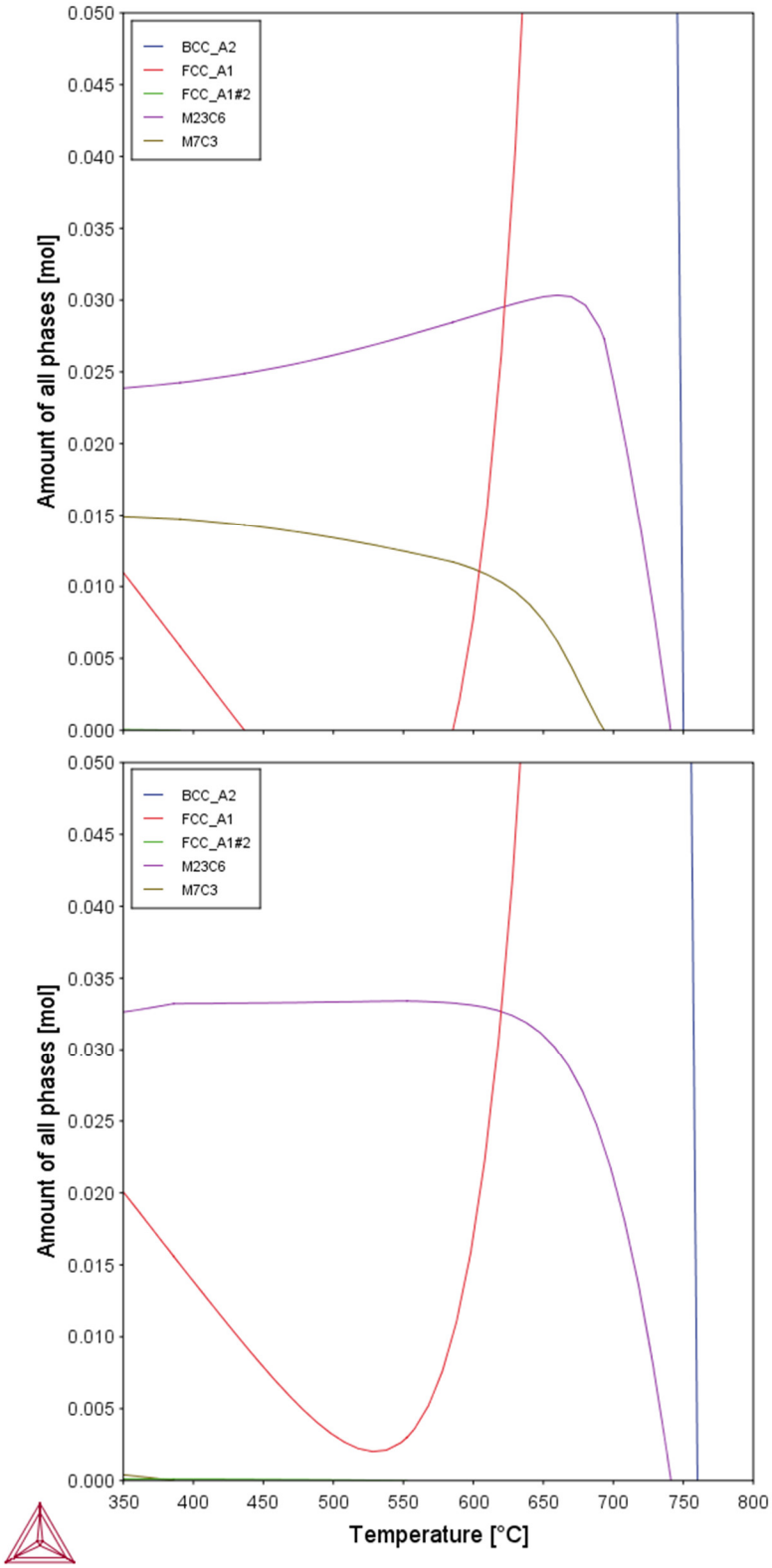

Figure 71: Thermocalc results for stable phases at equilibrium for the chemical composition in Table 1 [Top] and for a low carbon equivalent grade of HY-80 [Bottom]

5.5 Chemical Composition

5.5.1 Uniformity of composition through thickness

In order to determine if any trends in mechanical response could be associated with macroscale segregation throughout a test block, a transverse slice from HT#D was examined at the center of each location where a Charpy specimen was to be extracted. The results collected via GDS for all major alloying elements through the center line of a slice are shown in **Figure 72**. No elemental segregation is discernable. **Figure 73** shows all locations plotted for Carbon. Again, no elemental segregation trends are discernable. Thus, for the purposes of the studies using HT#D no influence of chemical composition needs to be considered in the analysis of mechanical response.

In addition, the chemical composition was measured from the end of one tensile specimen at both the T/4 quarter line and T/2 centerline locations within a test block for each sample tested. In general, the results show only a slight variation from location to location. **Figure 74** shows the weight percent differences from the average of all measurements between the T/2 and T/4 locations for HT#C. For each of the six major alloying elements, the T/4 location had a slightly higher weight percent alloy content than the T/2 location. In the case of HT#A, only Ni and Cr varied between the two locations, with slightly high Ni at T/2 and higher Cr at T/4. In each case the variation at an individual location is large enough that the average of the alternate depth falls within the standard error of the results from the first depth. Thus, as with HT#D, no local influence of chemical composition within an individual test block is considered in the analysis of mechanical response.

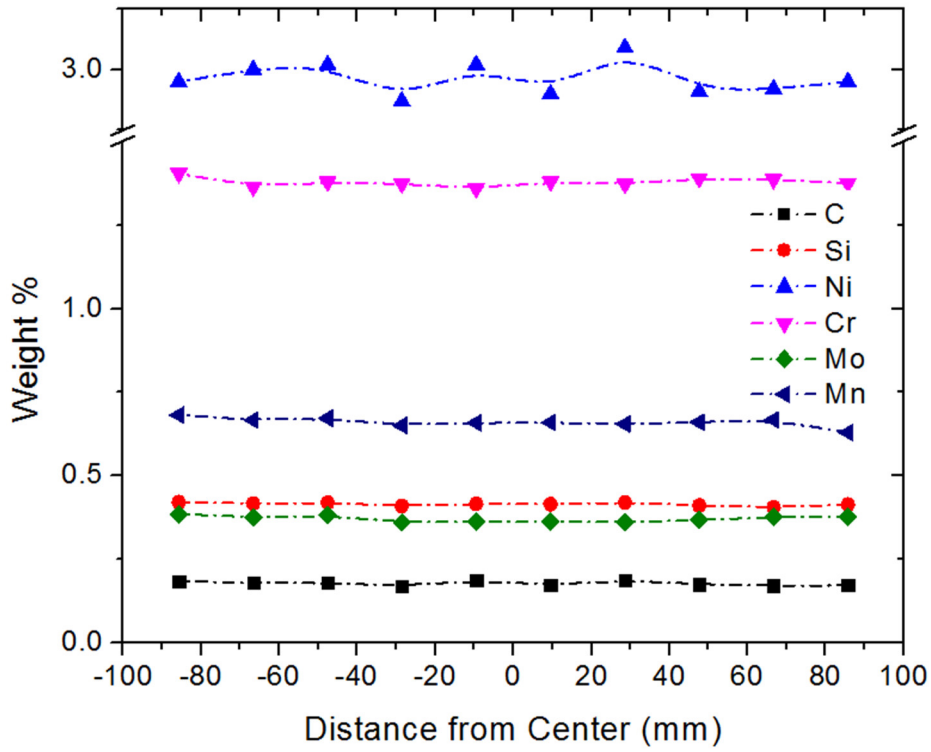

Figure 72: Chemical composition of major alloying elements from industrial heat number D through the thickness of transverse slice of a 0.19m test block sample.

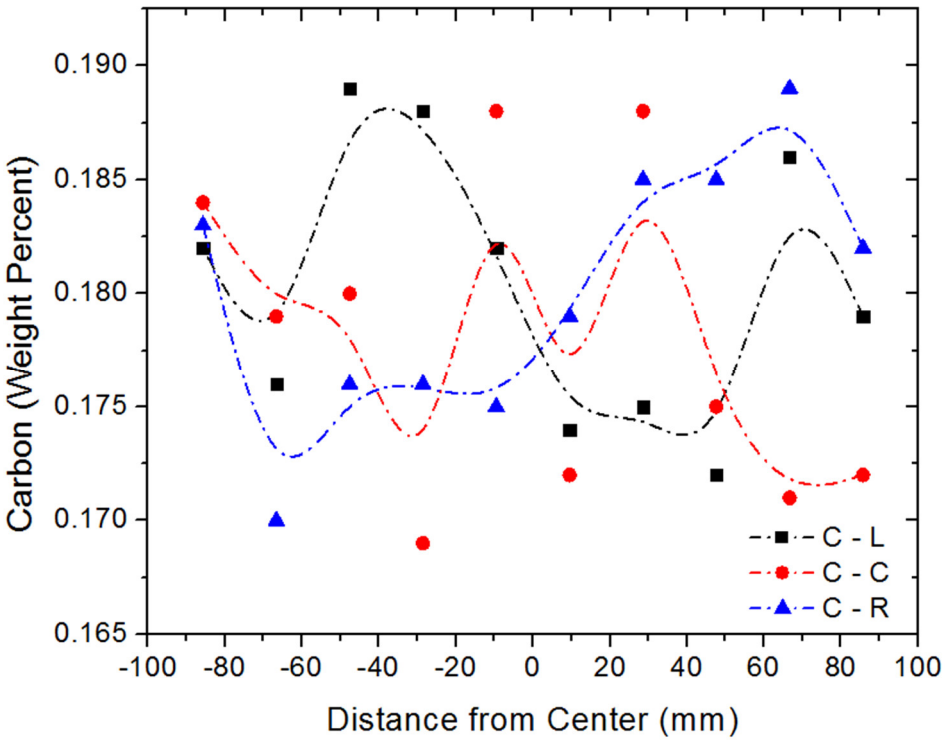

Figure 73: Carbon weight percent from industrial heat #D through the thickness of transverse slice of a 0.19m test block sample. (L, Left / C, Center / R, Right)

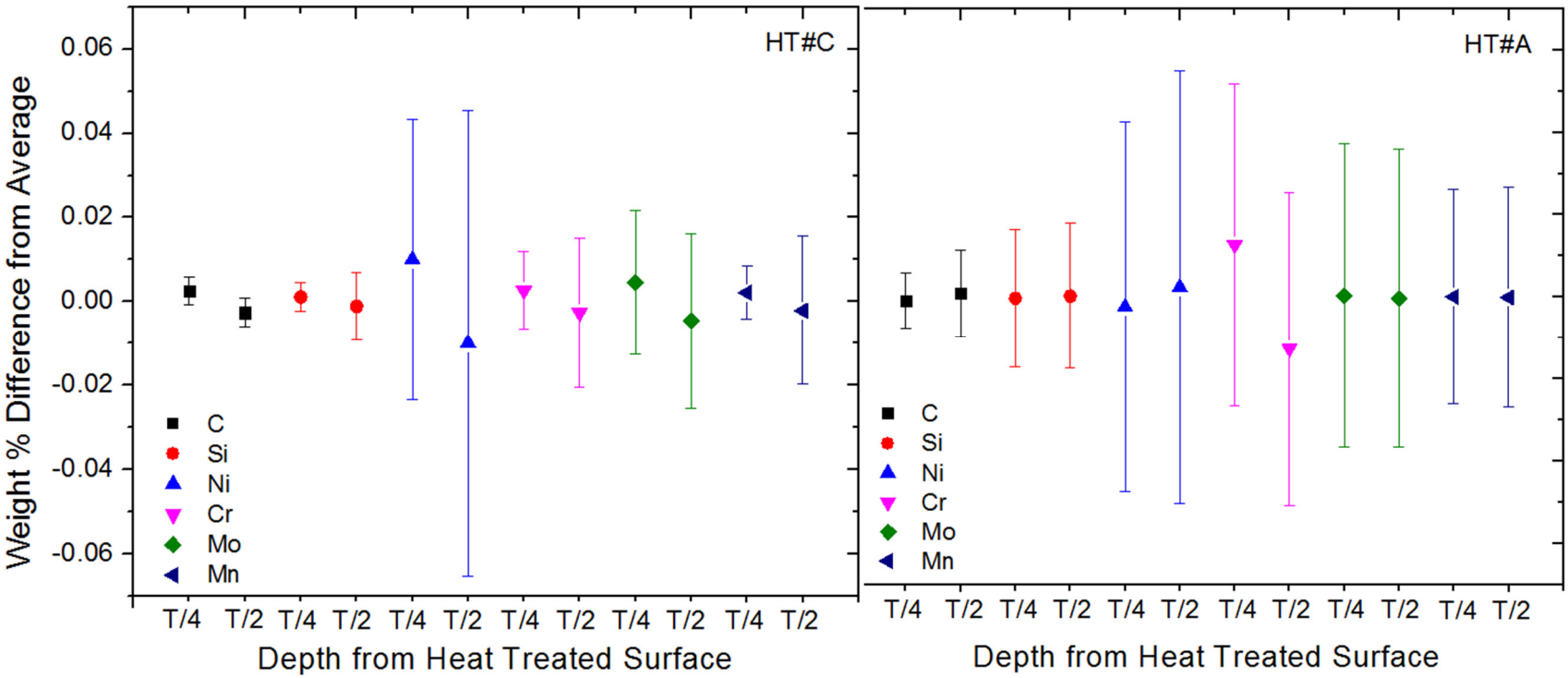

Figure 74: Chemical composition of major alloying elements from heat number #C [Left] and #A [Right]. All results are shown as the difference from the average of all mechanical specimens at each the quarter line and centerline of the 0.19m test block samples.

5.5.2 Carbide Analysis

In order to experimentally determine the chemical composition of the carbides present in numerous samples used in this study EDS measurements were taken in an SEM. Measurements on a carbide discern the presence of Mo and Cr as anticipated by CALPHAD modeling and consistent with the literature for $M_{23}C_6$ and M_7C_3 carbides. Of significant interest were the results of line scans across a carbide. **Figure 75** shows the results of one such scan in this case over an $M_{23}C_6$ on a specimen from HT#A that had been embrittled at 482°C for 10,000 minutes. The expected peaks as a raster is executed across a carbide of Mo, Cr, and C are found in addition to an unexpected peak of P. This result also appears for a line scale across an M_7C_3 carbide.

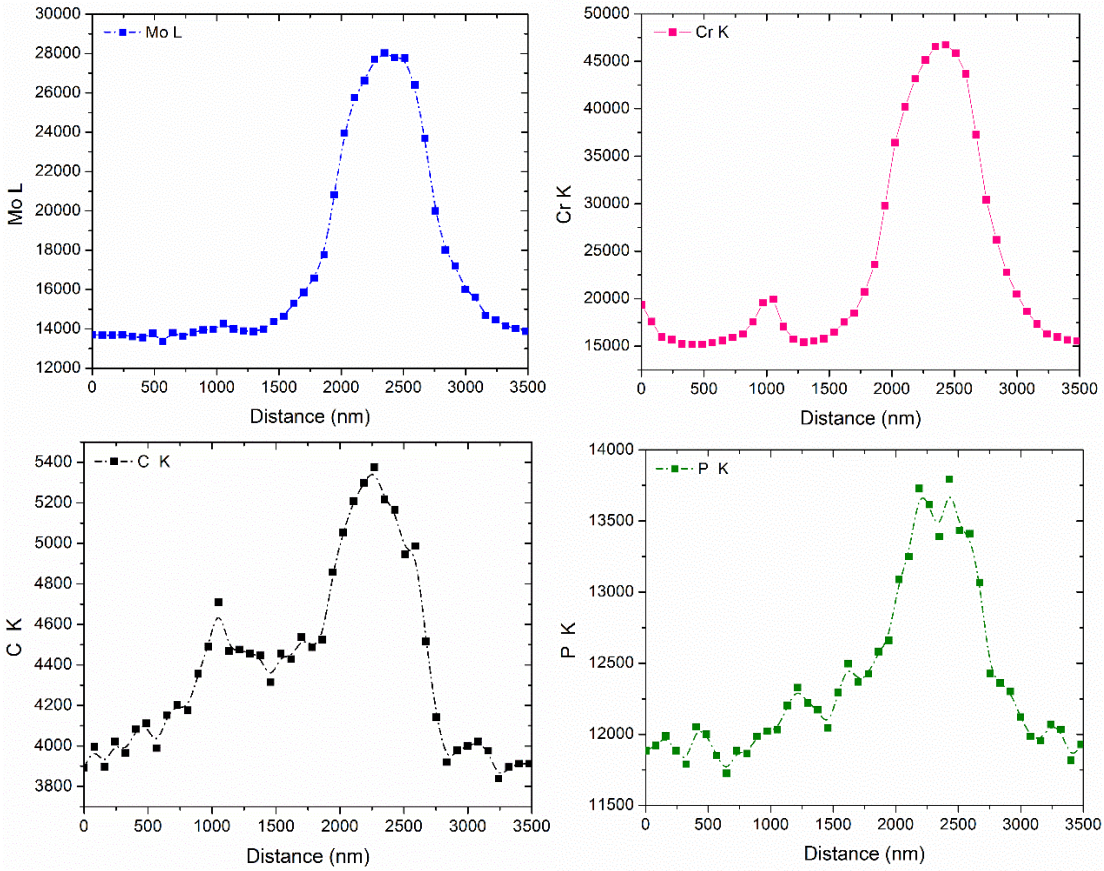

Figure 75: Chemical composition line scan (point counts) over an $M_{23}C_6$ carbide.

5.6 Carbide Aging and Dissolution – Metallographic Results

5.6.1 Aging after Austenitization

After quench from austenitization, a structure of un-tempered martensite with auto-temper carbides is present as shown in **Figure 76**, for HT#A treated at 843°C for 2 hours.

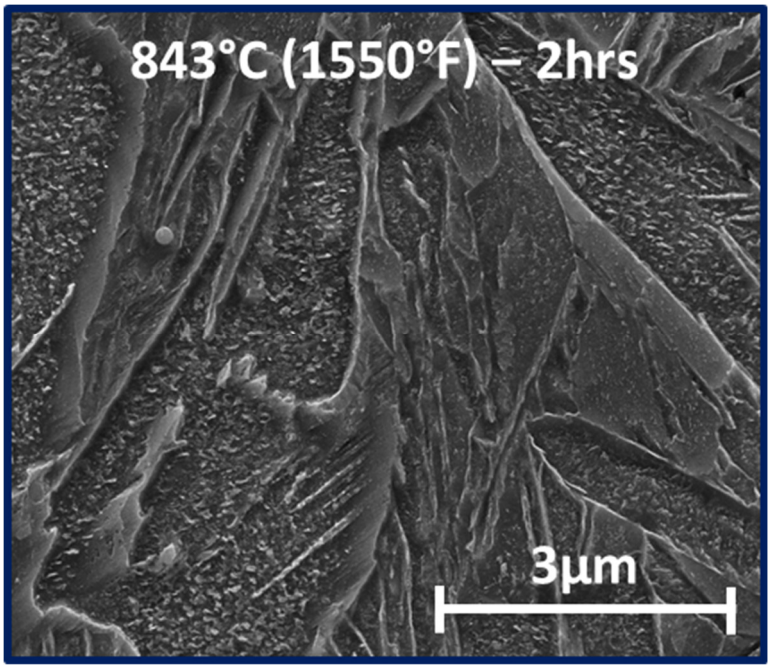

Figure 76: Auto-temper carbides after quench from austenitization (HT#A)

Figure 77 shows the influence of temperature on carbide aging through the temperature range of 426°C to 676°C, when aged for 10,000 minutes. It is immediately evident that the kinetics of coarsening are considerably faster at the higher end of the temperatures investigated, particularly at and above 621°C. The size of carbides at 676°C is perhaps an order of magnitude larger than those at 426°C.

Of equally important note is the lack of needle morphology M_7C_3 carbides at elevated temperatures and the general change in carbide interactions with grain boundaries. At lower temperatures, particularly at 482°C and 537°C, carbides are

observed painting the prior austenite and martensite lathe boundaries in addition to being prevalent throughout the inside of the grains. With increasing aging temperature, the carbides appear to coarsen at the grain boundaries such that the distance between each carbide is considerably larger than for lower temperatures. In addition, with increasing aging temperature, the density of carbides within the grain decreases and by 676°C carbides appear almost exclusively at boundaries within the structure.

The effect of aging time is shown in **Figure 78** for aging temperatures of 621°C and 676°C from 60 minutes up to 10,000 minutes. In each case, significant coarsening is evident, with a faster rate of coarsening at 676°C. It also becomes clear that at 676°C, M_7C_3 carbides are dissolving into the matrix at long time scales whereas a small fraction of M_7C_3 remains even at 10,000 minutes for aging at 621°C. A consequence of this could be an increased volume fraction of $M_{23}C_6$ carbides as more C, Cr, and Mo become available from the dissolving M_7C_3 carbides.

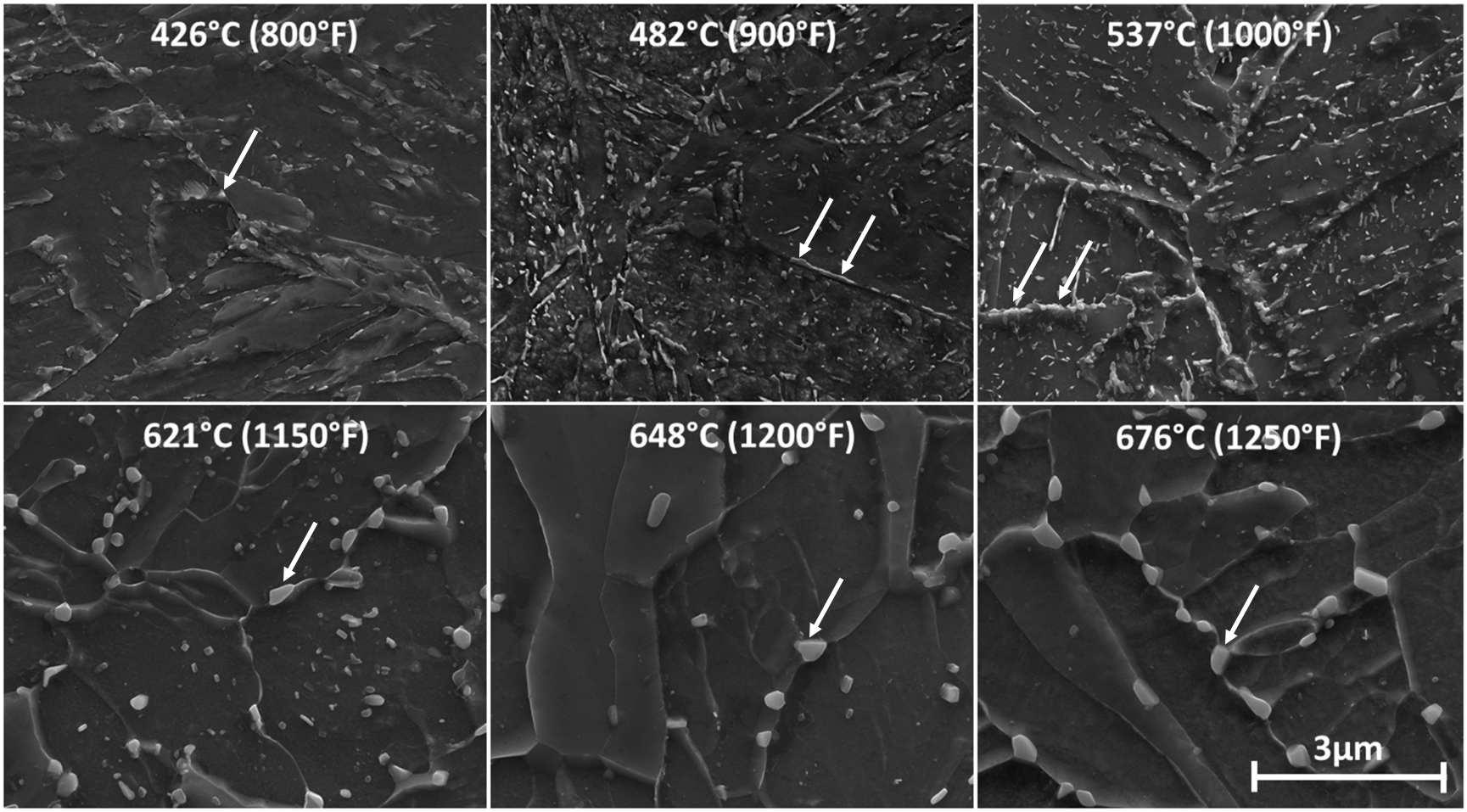

Figure 77: Aging after austenitization (HT# A) between 426°C and 676°C for 10,000 minutes. Initial treatment 853°C for 2 hrs. Imaging conditions: 15kv/ETD /40k mag/7.0 mm WD/2.5 SS [Carbide examples highlighted by white arrows clearly shows the large size increase in boundary carbides with increasing temperature; the continuous nature of carbides is also shown for 482 and 537°C]

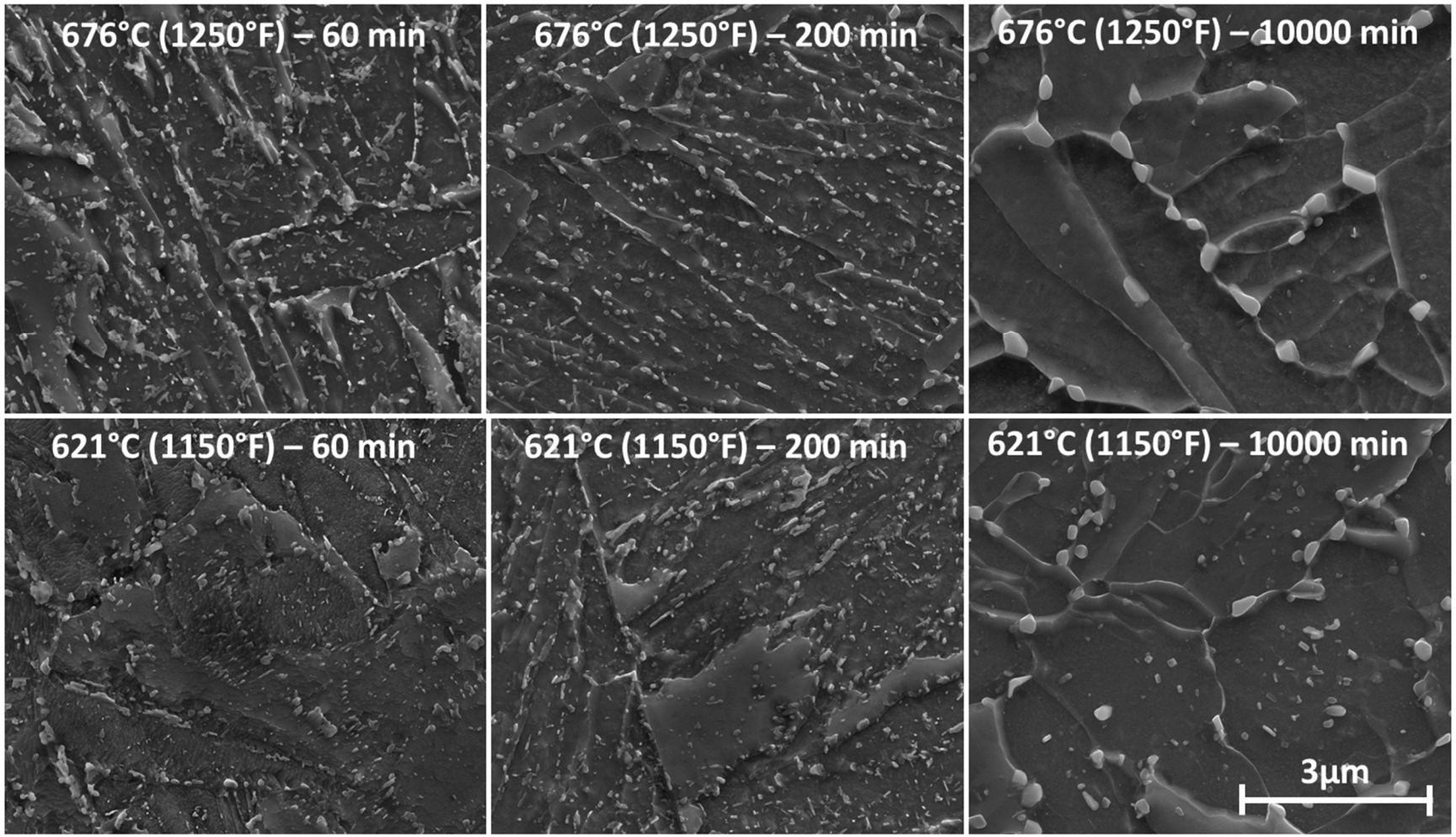

Figure 78: Carbide aging after austenitization (HT# A) between 621°C and 676°C from 60 min to 10,000 minutes. Imaging conditions: 15kv/ETD /40k mag/7.0 mm working distance /2.5 spot size

5.6.2 Aging after Tempering

HT#A and #4 were studied with aging in the embrittlement range between 426°C and 537°C. The starting structure for HT#A and #4 are shown in **Figure 79**. In both samples a tempered martensitic structure is apparent with a marginal concentration of carbides. Close inspection reveals that two different carbides are present, both $M_{23}C_6$ with a spherical morphology and M_7C_3 with a cigar/needle morphology. Both carbides in the control samples are present at the prior austenite grain and martensitic lathe boundaries within the grains.

After aging in the embrittlement range, an increase in the number of carbides is evident for both heats evaluated. This is easiest to observe visually with the samples treated for 40,000 minutes to intentionally bring out the effects of the aging treatment, shown in **Figure 80**. It is also noted that for aging at 482°C shown in **Figure 81** a large number of carbide clusters are apparent after 10,000 minutes of aging. These clusters are not as pronounced with increased aging time up to 40,000 minutes.

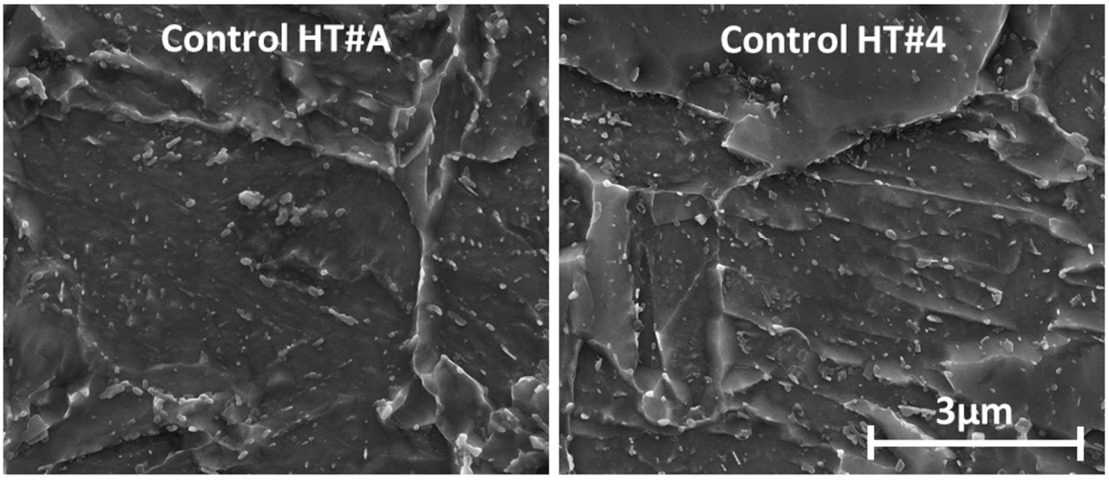

Figure 79: Control, HT#A and HT#7

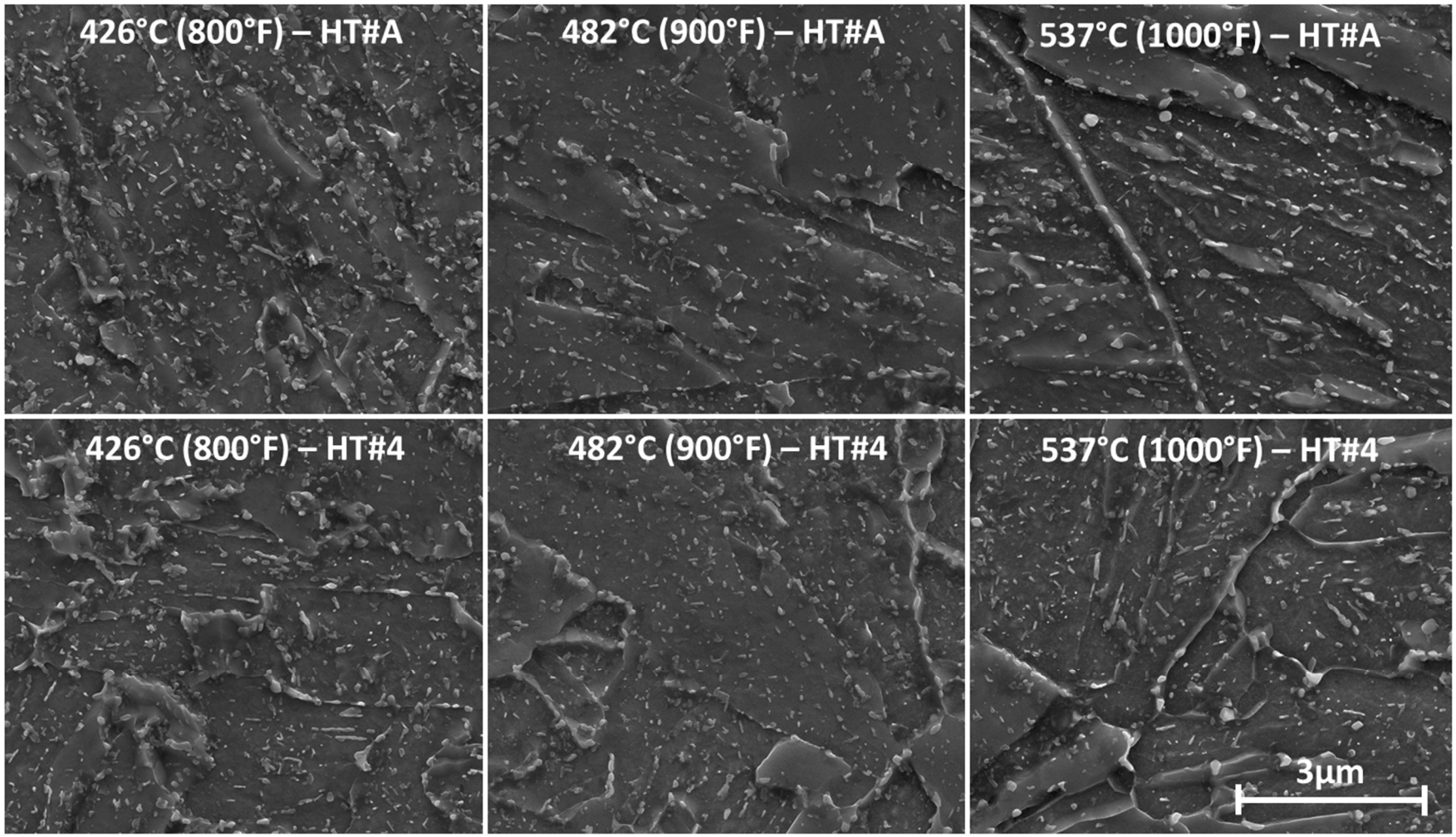

Figure 80: Carbide aging after austenitization and tempering (HT# A and HT# 4) between 426°C and 537°C for 40,000 minutes. Imaging conditions: 15kv/ETD /40k mag/7.0 mm WD/2.5 Spot

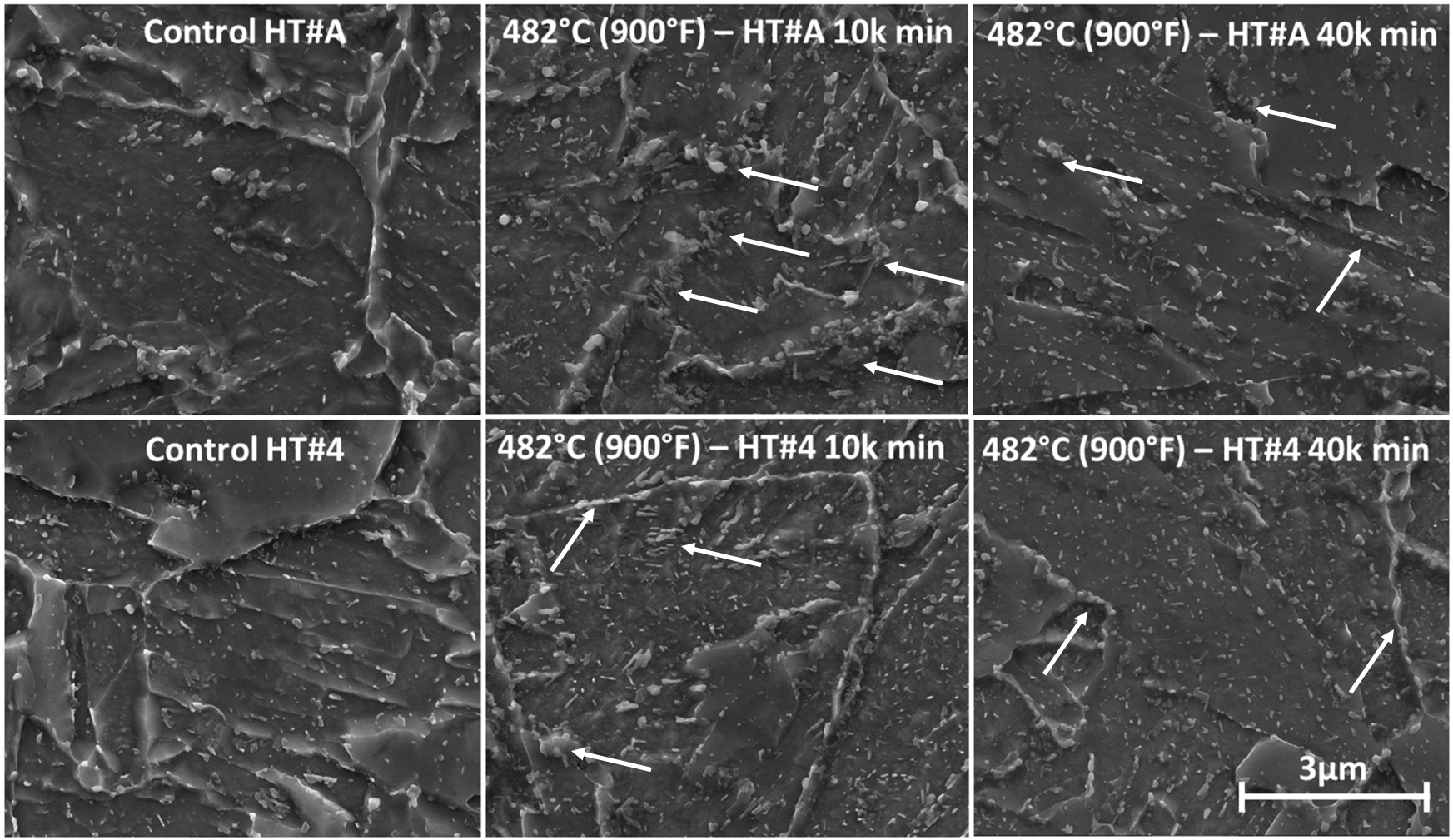

Figure 81: Carbide aging after austenitization and tempering (HT# A and HT# 4) at 482°C for 10,000 and 40,000 minutes. Imaging conditions: 15kv/ETD /40k mag/7.0 mm WD/2.5 Spot [Arrows highlight regions of clusters and/or semi-continuous boundary carbides]

5.6.3 Carbide dissolution after tempering

HT#A, #B, #2, and #4 were selected for evaluation of carbide aging after tempering, with a particular focus on examining the dissolution of the carbides and determining if the predictions of CALPHAD modeling would be observed in the microstructure. Each of the four heats were aged between 665°C and 699°C at times up to 600 hours in order to study the dissolution of the carbides and the influence of entering the inter-critical regime. A subset of those results is presented here-in that illustrates the impact of increasing temperature on carbide dissolution. **Figure 82** shows the incoming structure of the additional two heats studied, HT#B and HT#2. Of particular note with HT#B is the lack of M_7C_3 carbides, as evident by the lack of any carbides with a cigar morphology. This is consistent with CALPHAD predictions associated with the lower concentration of carbon in this heat.

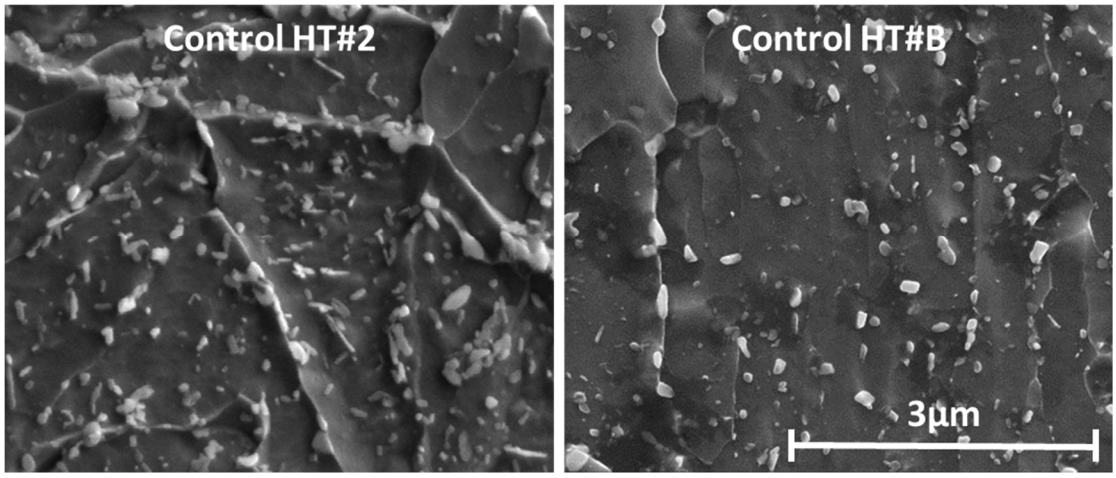

Figure 82: Control, HT#2 and HT#B

Figure 83 shows the carbide dissolution as predicted by CALPHAD modeling. Two characteristics are noted: (1) an overall decrease in the number and volume fraction of carbides with increasing temperature, and (2) a lack of needle like carbides

at 699°C. With extended aging time (**Figure 84**), the differences in carbide morphology are not immediately clear. Examination of carbide location for HT#A at higher temperatures shows that a subset of carbides is located within the un-tempered martensite region. This is consistent with the nucleation of austenite particles on the $M_{23}C_6$ carbides with which they are coherent. The influence of coherency appears more pronounced with increased aging time up to 600 hours as shown in **Figure 85**.

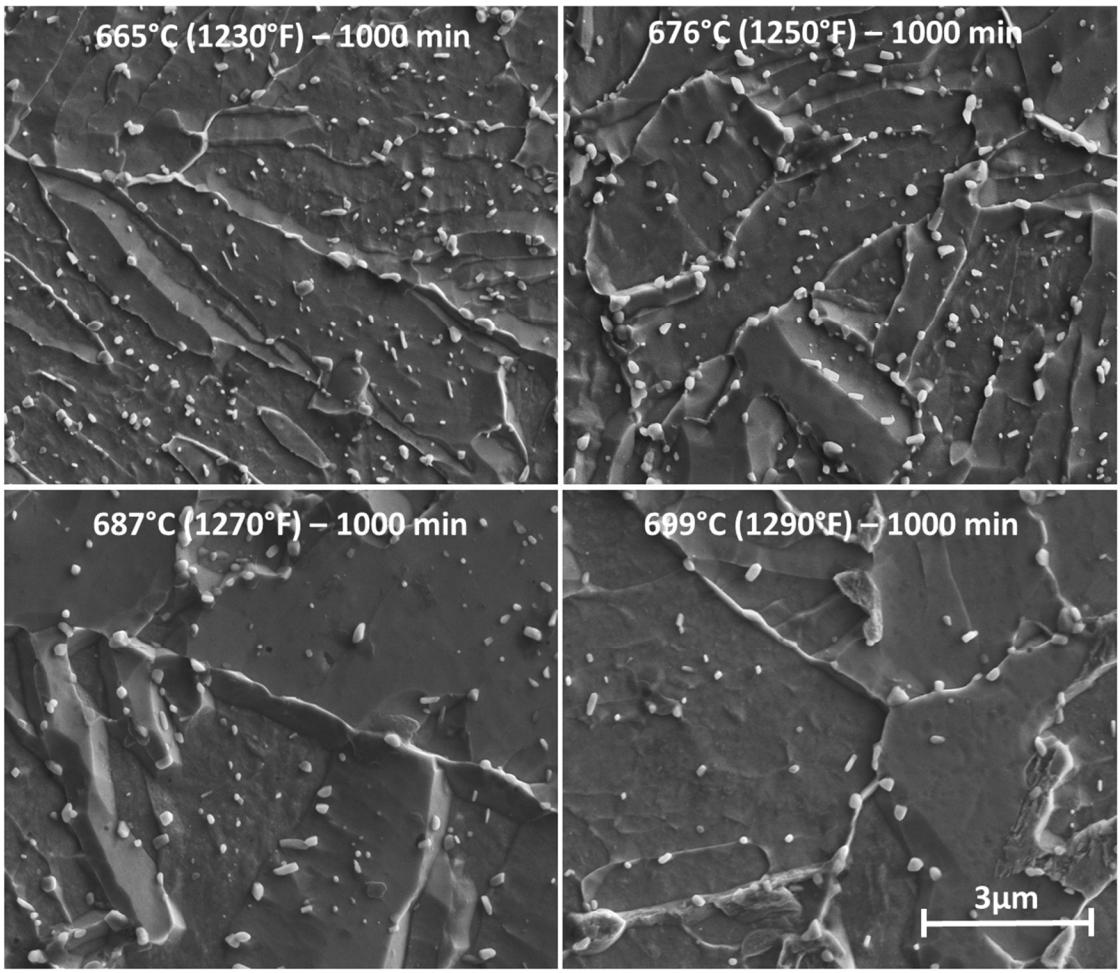

Figure 83: Carbide Dissolution (HT#2 - **Table 4**) – 7kv/ETD /10k mag/10.0 mm WD/2.5 Spot Size

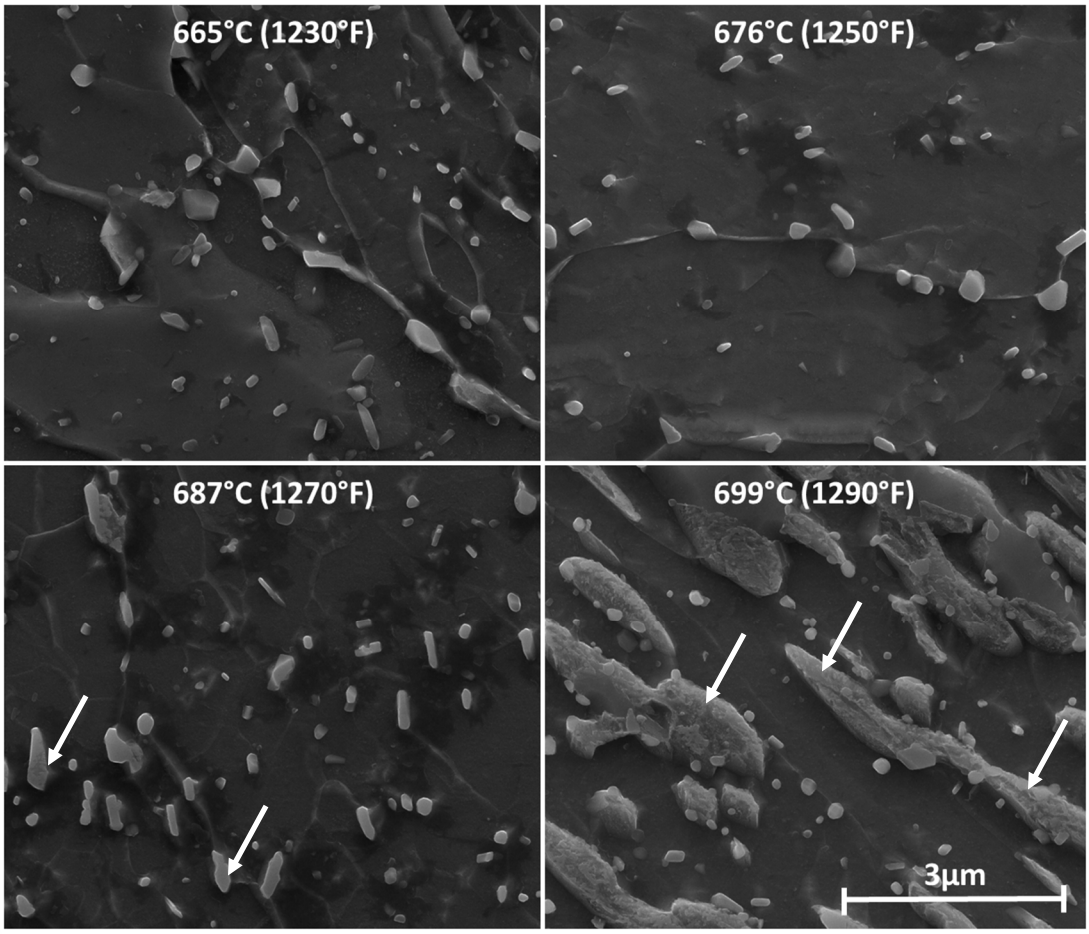

Figure 84: Carbide Aging, 43hr treatments (HT#A - **Table 4**) Imaging conditions: 15kv/ETD /40k mag/7.0 mm WD/2.5 Spot [Regions of untempered martensite highlighted by arrows, resulted from exceeding the AC1]

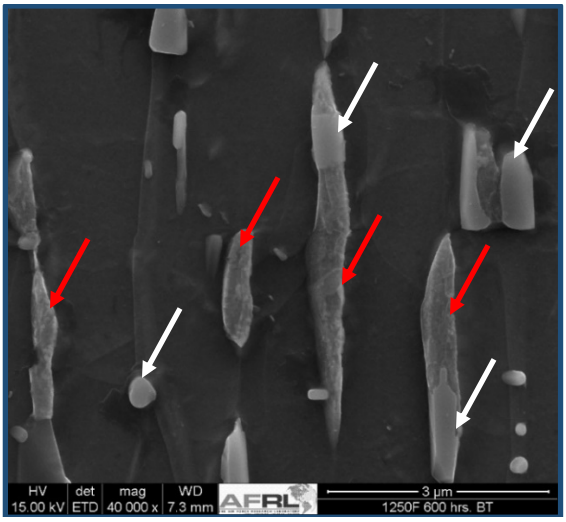

Figure 85: Carbide Aging, 600hr treatments at 676°C (HT#A - **Table 4**) Imaging conditions: 15kv/ETD /40k mag/7.0 mm WD/2.5 Spot [white arrow highlight carbides, red arrows highlight untempered martensite]

5.7 TEM Analysis of Carbides

5.7.1 Observations from Control Sample

Specimen E15 from HT#A is a control specimen in the austenitized and tempered condition. The occurrence of both M_7C_3 and $M_{23}C_6$ carbides is clear in TEM imaging. Also of interesting note is the preferential alignment of M_7C_3 to two orientations, approximately 70 degrees off set from one another from within a region of a single prior austenite grain as shown in **Figure 86**.

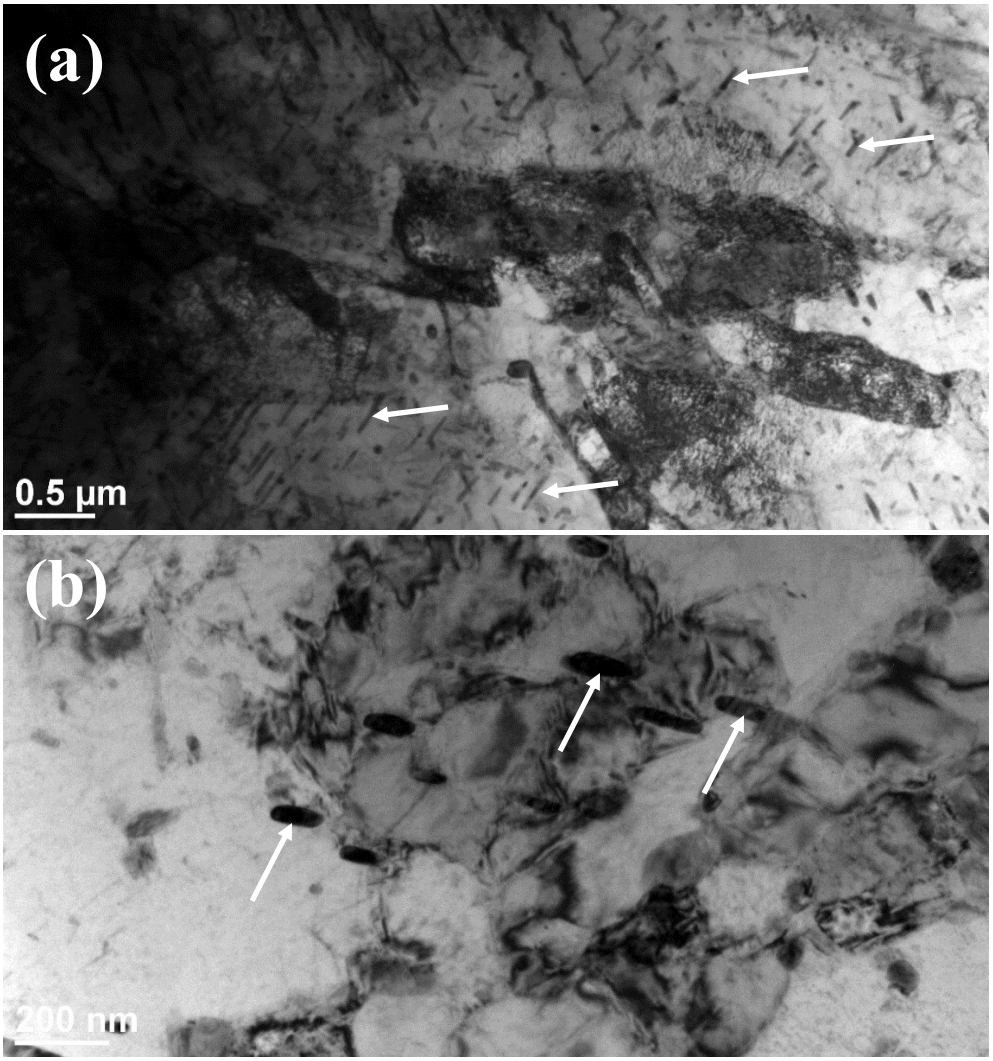

Figure 86: TEM image of preferential alignment of M_7C_3 carbides in control sample E15 (austenitized and tempered with no subsequent aging treatment) ; (a) lower mag. (b) higher mag. [carbide needle examples are indicated by arrows]

5.7.2 Observations of Embrittled Sample

Specimen E10 from HT#A has been intentionally aged at peak embrittlement temperature (482°C) for 10,000 minutes. The specimen was extracted using a FIB liftout in order to examine a region in the vicinity of a grain boundary. From these images it is even more clear than with SEM images that the M_7C_3 carbides are present primarily within the bulk and $M_{23}C_6$ carbides are located primarily along boundaries. Energy Dispersive Spectroscopy (EDS) was used on the carbides within the TEM foils in order to determine their elemental make-up.

β-Mo_2C has a close packed hexagonal crystal structure with the carbon atoms located in one half of the available octahedra interstices. The lattice parameters are a = 0.3007 nm and c = 0.4729 nm. They appear as needles in a tempered martensitic structure. It should be noted that the iron measurement is inflated, as Co, which has an overlapping peak with Fe, is present in the foil.

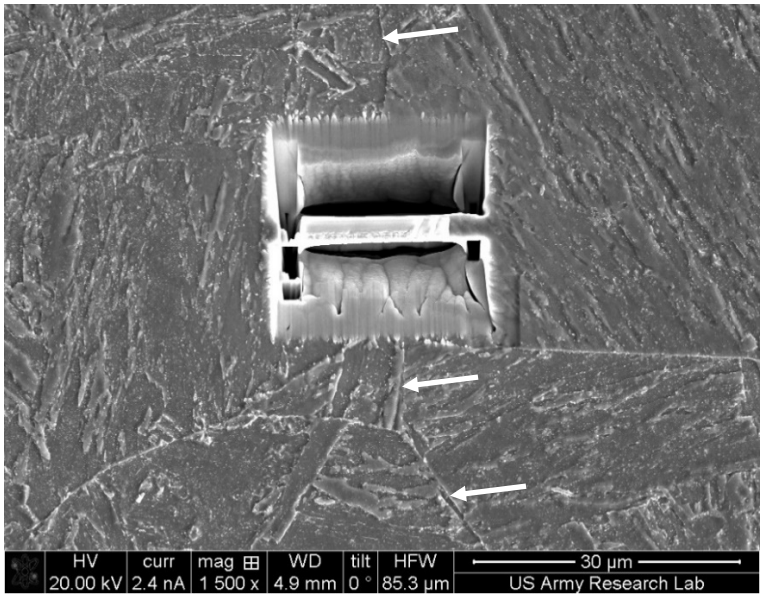

Figure 87: FIB liftout area. Specimen has been etched with 2% nital to reveal grain boundaries and carbides [Arrows highlights Grain Boundary on either side of liftout]

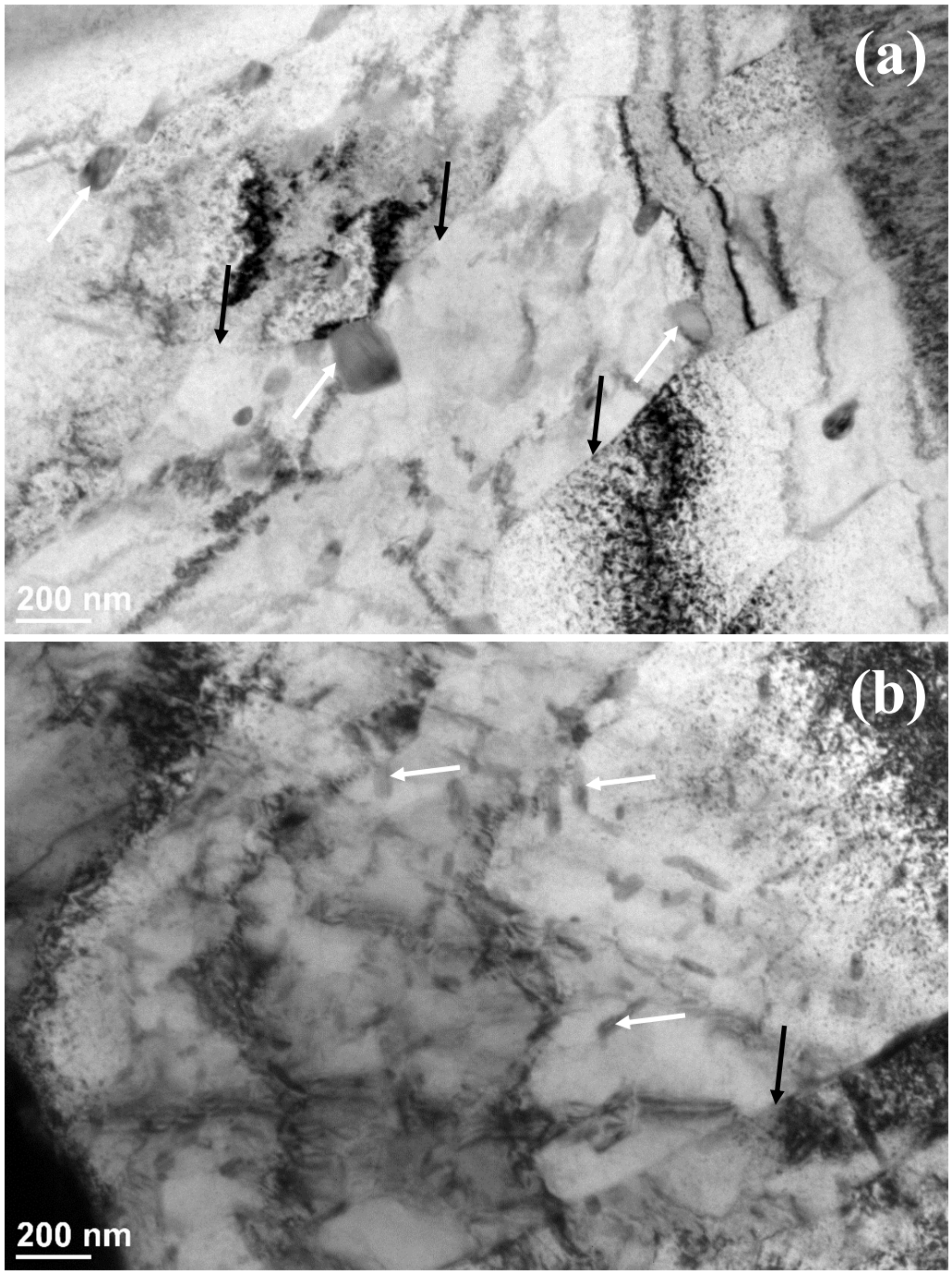

Figure 88: TEM Image of Specimen E10 (a) showing $M_{23}C_6$ carbides on boundaries and (b) showing M_7C_3 Carbides in the bulk. Carbides are observed in the vicinity of a prior austenite grain boundary; bright field images [white arrows highlight carbide examples in each image respectively, black arrows highlight boundary locations]

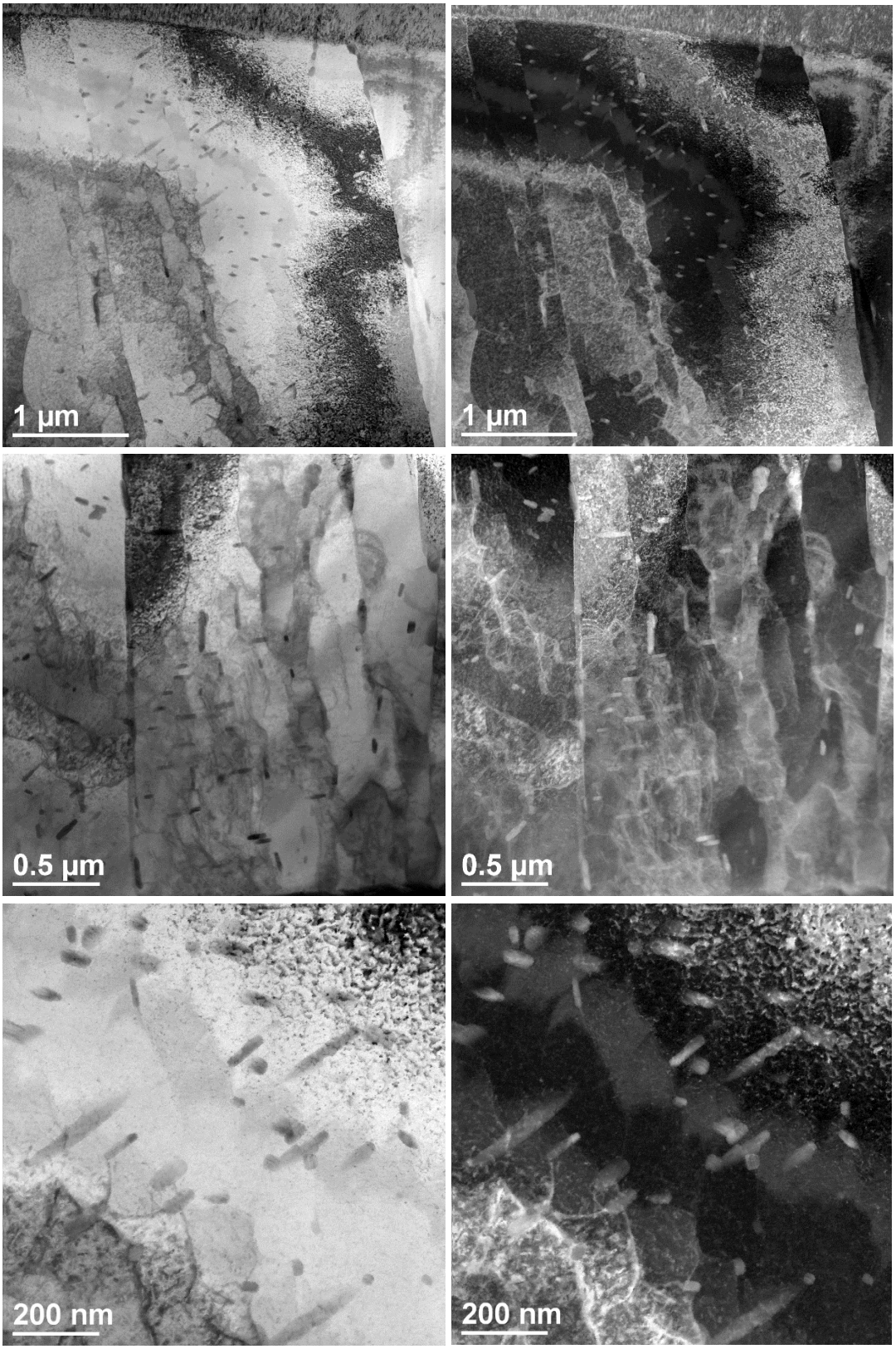

Figure 89: TEM Images of Specimen E10 showing M_7C_3 carbides in the bulk. Increasing magnification top to bottom [Left] Bright Field [Right] Dark Field

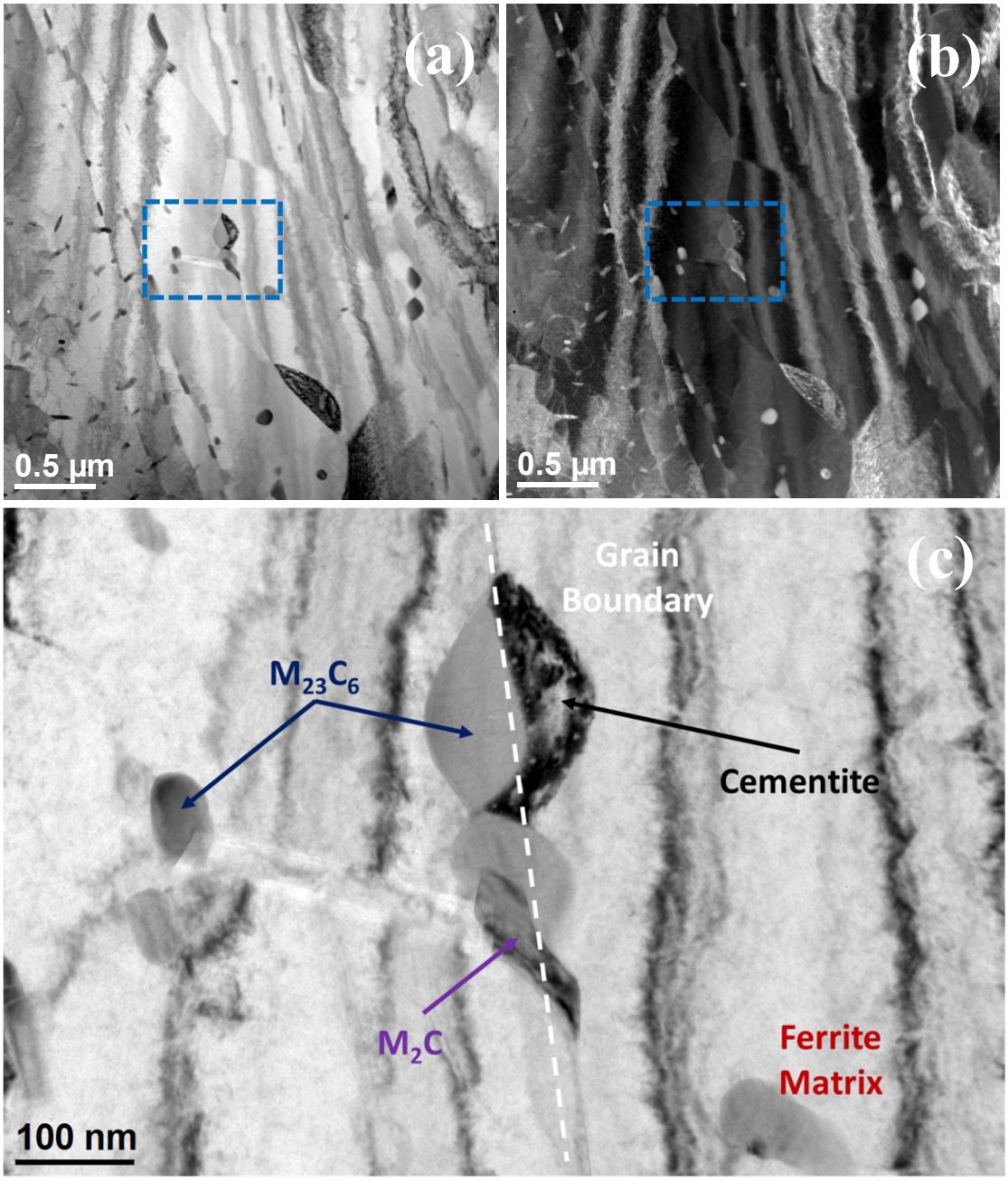

Figure 90: TEM Images of region of interest for EDS map analysis. Numerous carbide types present. Cementite is also shown along the prior austenite grain boundary (a) Bright Field (b) Dark Field (c) Higher magnification of blue box inset identifying phases

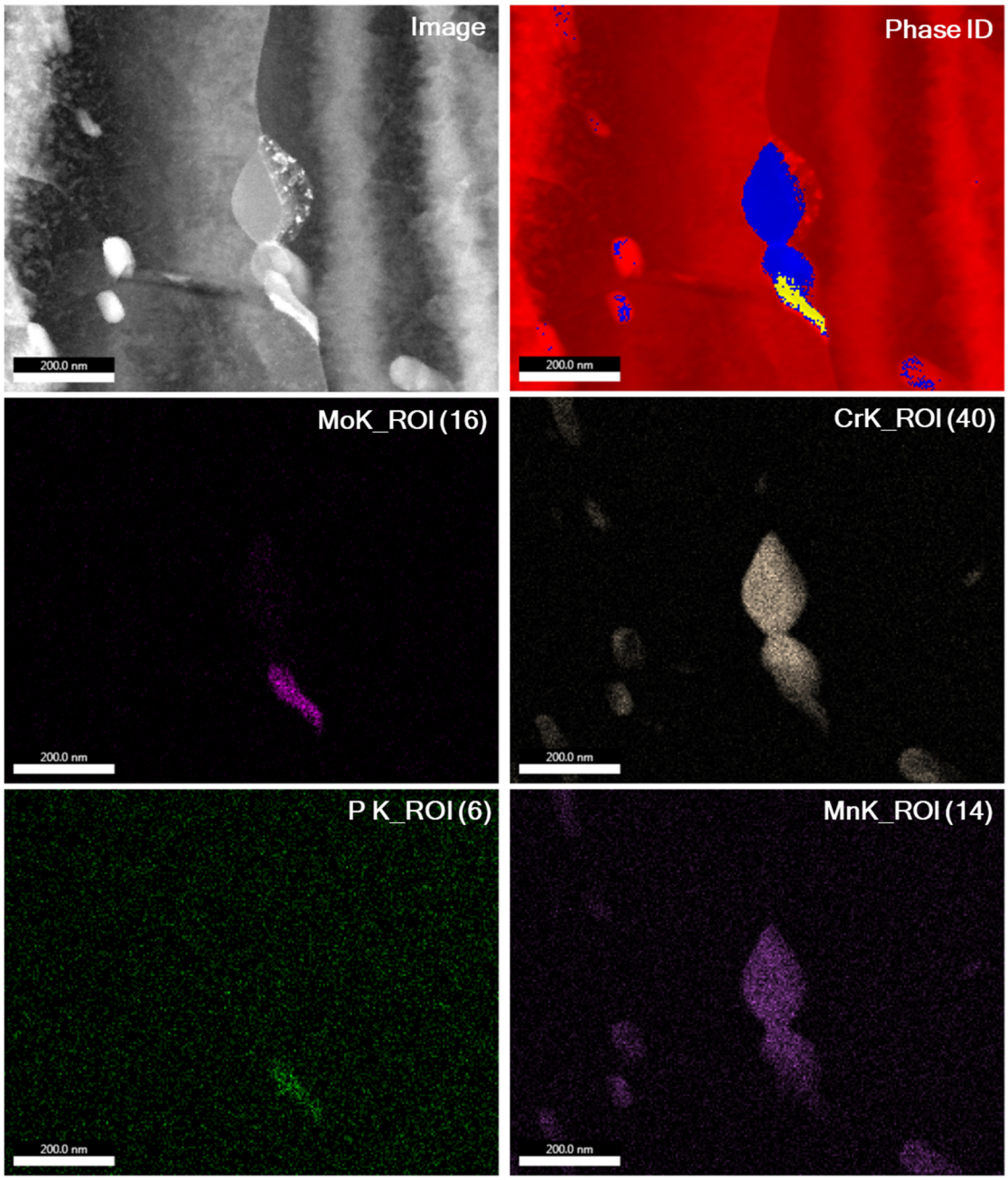

Figure 91: TEM Image and EDS showing three distinct phases in the region of a grain boundary. Specimen E10 aged at 482°C for 10,000 min. 1 hour scan.

Table 26: Chemical composition of phases in **Figure** 91 (wt%)

PHASE	CR	MN	FE	NI	MO
YELLOW	12.4	1.1	21.1	1.0	64.4
BLUE	31.0	4.3	56.0	1.5	7.1
RED	1.7	1.0	93.5	3.3	0.5

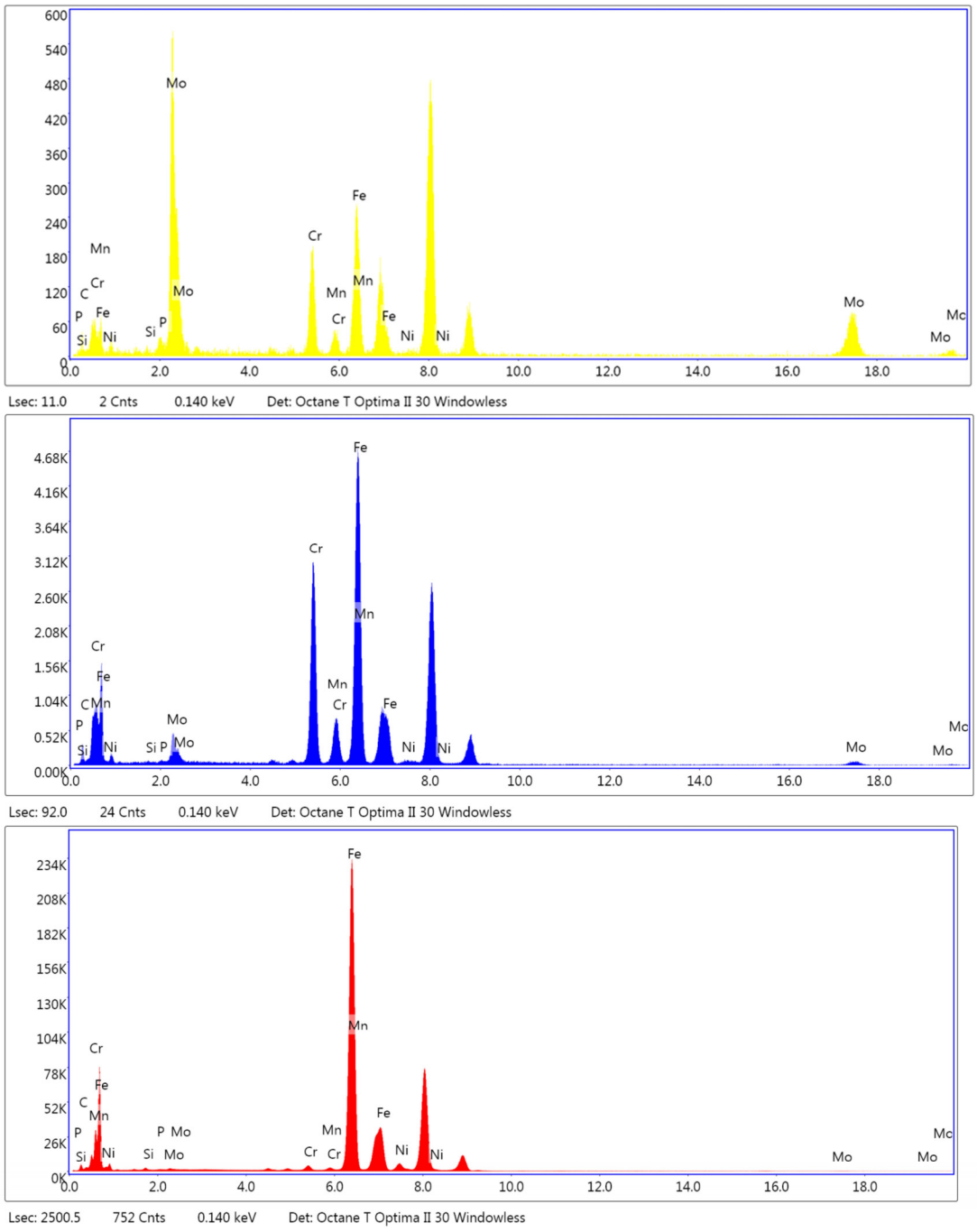

Figure 92: EDS spectra from three identified phases in **Figure 91**. Color of spectra corresponds to color of identified phase. Red is the bulk, blue is a Cr, Mn, Mo carbide, and yellow is a Mo, Cr carbide. Results of 1 hour scan.

Convergent beam diffraction patterns were taken of the blue phase along the grain boundary in **Figure 91**. These patterns (**Figure 93**) further support the earlier conclusion reached via morphology, location, and measurement of the chemical composition that these carbides are indeed $M_{23}C_6$. This technique could not be suitably exercised on the smaller carbides.

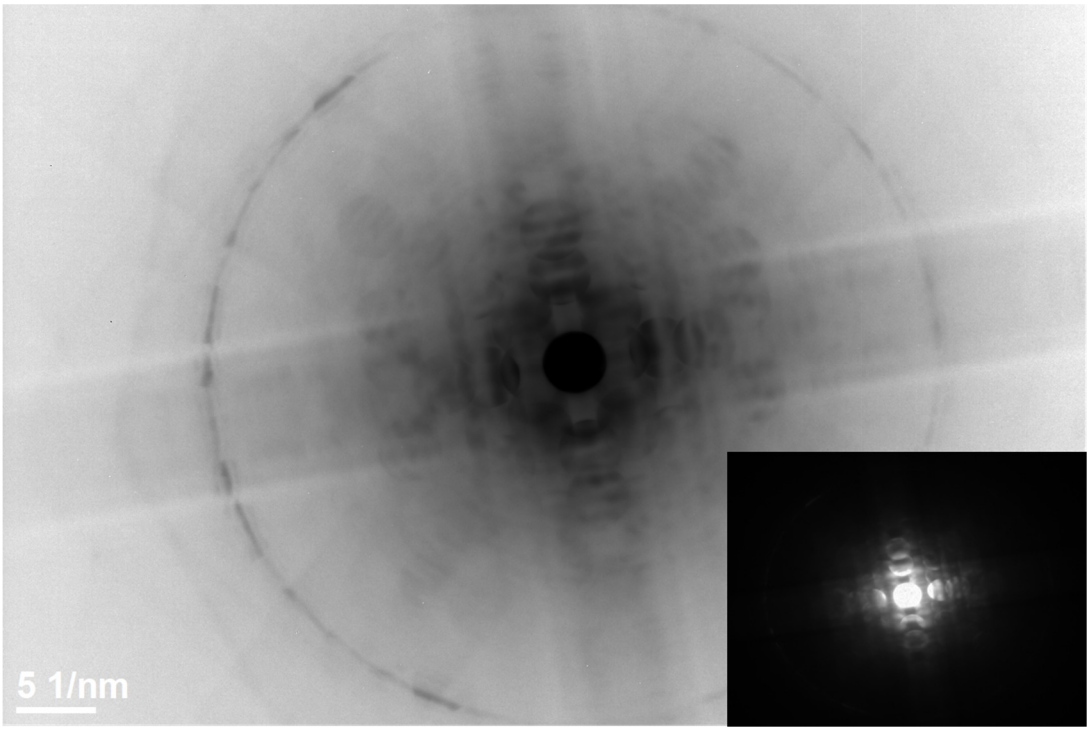

Figure 93: TEM convergent beam diffraction of blue phase in **Figure 91**. [001] major axis. Comparison to literature indicates this phase is $M_{23}C_6$. Inset is original diffraction pattern, main image has been processed in Gatan digital micrograph software to reveal weak reflections.

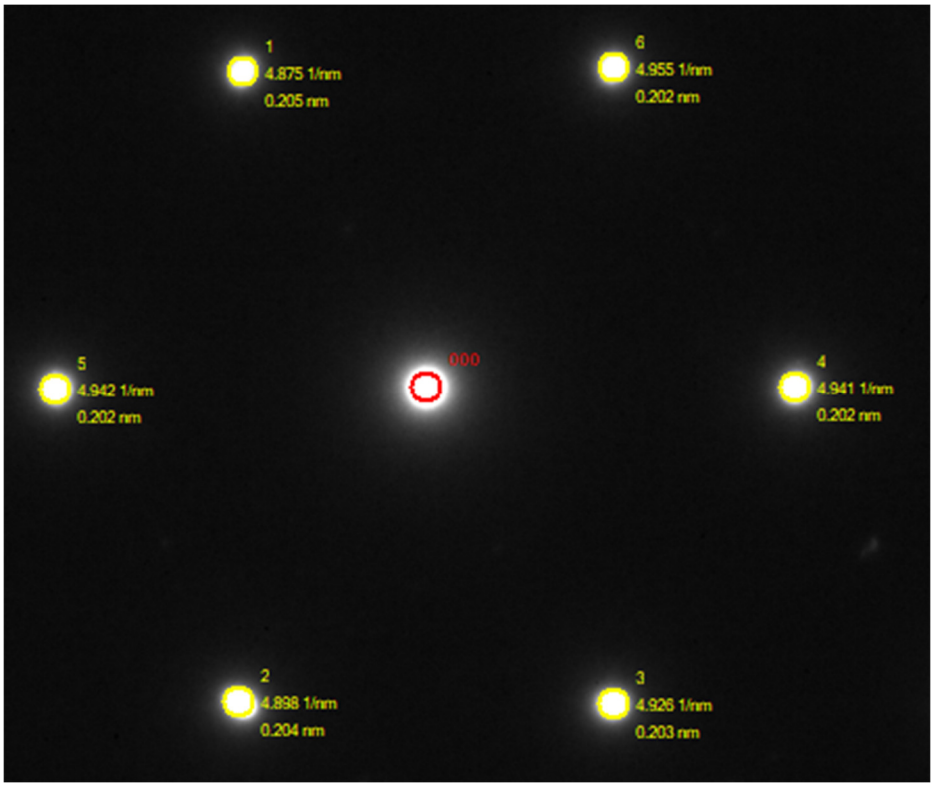

Figure 94: TEM diffraction of red matrix phase (ferrite) in **Figure 91** [111] major axis. Projected first 101 d spacing = 0.203nm, measured average =0.203nm

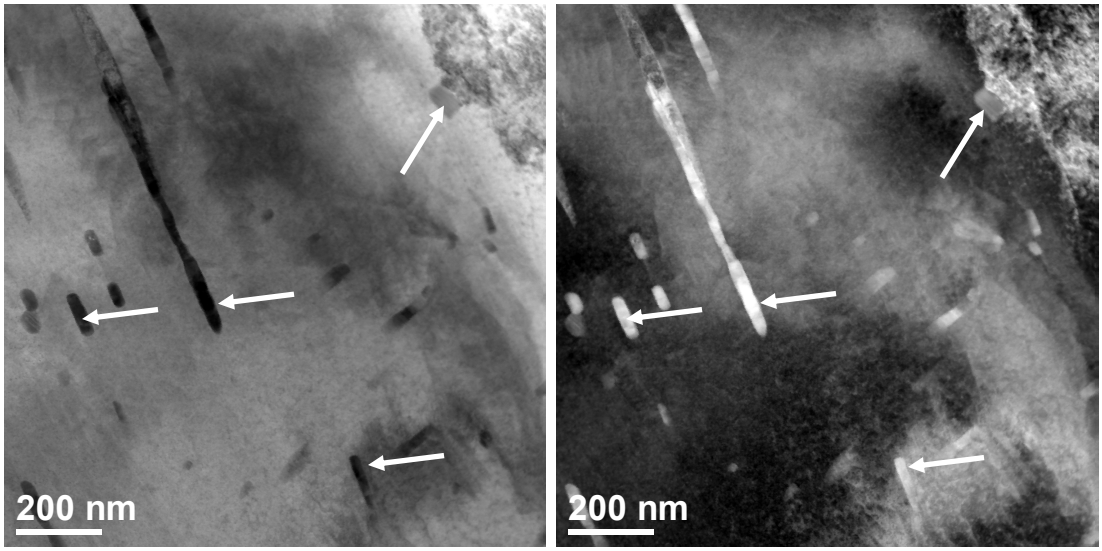

Figure 95: TEM Image in region of interest for EDS analysis of phases. Specimen E10 aged at 482°C for 10,000 min. [Arrows identify carbides examined]

Table 27: Chemical composition of phases in **Figure** 95 (wt%)

ELEMENT	BULK PHASE	GB PRECIPITATE	BULK PRECIPITATE
C K	0.1	0.3	0.4
CR K	1.2	40.5	8.3
MN K	0.7	3.9	2.8
FE K	94.6	48.9	85.6
NI K	2.3	0.4	1.3
MO K	1.1	6.0	1.6

Thus, from these results it is shown that three distinct precipitates exist when samples have been treated for extended time in the embrittlement range. An $M_{23}C_6$ carbide forms both on boundaries and in the bulk in vicinity of boundaries, and that carbide is primarily composed of Cr, Mn, Mo, and C with a measured stochiometric relationship of 8:1:1:1/3. An M_7C_3 carbide forms in the bulk that is also primarily Cr, Mn, Mo, and C but with a measured stochiometric relationship of 10:3:1:2. The third carbide is an M_2C carbide made up of Mo and Cr with a measured stochiometric relationship of 3:1. It is also noted that the Mo carbides are rich in P, whereas the Cr based carbides have P at their boundary but not within the carbide itself.

5.8 Carbide Aging and Dissolution – Analytical Results

This section provides a detailed overview of carbide measurements after varied aging treatments. The key summary for carbide volume fraction based on the phase identification performed in the proceeding sections is provided below:

Table 28: General characteristics of carbides as detailed by volume fraction

TREATMENT	HIGH CE (HT#A,2,D)		
	$M_{23}C_6$	M_7C_3	MoCr Phase
CONTROL	3%	3%	0%
482°C AGE (10K MIN)	4%	9%	<1%
650°C RECOVERY (1K MIN)	<2%	<2%	0%
700°C RECOVERY (1K MIN)	<2%	0%	0%

5.8.1 Aging after Austenitization

HT#A was austenitized at 871°C with subsequent aging treatments between 400°C and 700°C from 60 minutes to 10,000 minutes as detailed in section 3.6.2. These samples were prepared in accordance with the metallographic procedure detailed in section 3.2 and were imaged via SEM. Finally, the SEM images were processed via the image analysis methodology detailed in section 4.3 to determine critical carbide parameters of average carbide volume of an individual carbide, carbide volume fraction, and carbide density.

Image analysis of the control specimen after austenitization shows a high concentration of auto-temper carbides (Detailed in **Table 29**).

Table 29: Parameters of auto-temper carbides after austenitization (HT#A)

AVG CARBIDE VOLUME (μM^2)	VOLUME FRACTION (%)	CARBIDE DENSITY ($1/\mu M^2$)
0.001886	8.420117	40.92587

After aging for 60 minutes, a mixture of auto-temper and alloy carbides exists. The image analysis methodology developed for this work is not able to differentiate between auto-temper and alloy carbides, thus the volume fraction and density measurements for 60 minute aging is inflated. The raw results of image analysis for aging at 60 minutes are included below as **Figure 96**. The key characteristics of aging for 60 minutes are as follows:

- General unchanged carbide volume between 427°C and 621°C
- An increase in average boundary carbide volume above 621°C
- A similar increase in boundary carbide volume fraction above 621°C

- A significant delta between boundary and bulk carbide density
- A peak in bulk carbide density at 621°C

After 200 minutes of aging (**Figure 97**), the majority of auto-temper carbides have dissolved such that the carbide parameters determined through image analysis are largely representative of alloy carbides only. The key characteristics of aging for 200 minutes are as follows:

- Generally unchanged carbide volume across the entire temperature range
- Increasing carbide volume fraction with increasing temperature
- A decrease in volume fraction and carbide density at 648°C
- A delta between boundary and bulk carbide density
- Generally increasing carbide density with increasing temperature

Review of the SEM images along with the image analysis results reveals that apparent local decreases in volume fraction and carbide density noted at 648°C are indeed not local. Rather at 676°C a small fraction of un-tempered martensite appears in the microstructure that is being estimated as carbides by the image analysis program. Thus, both metallographic and image analysis methodologies are indicating that the AC1 has been exceeded. Note: Results at 676°C are not shown for longer aging times as the percentage of untempered martensite invalidated the measurement.

After aging for 10,000 minutes, the characteristics of carbide evolution are more easily discernable. Thus, the principle characteristics of carbide evolution after post austenitization tempering are as follows (detailed in **Figure 98**):

- Slightly increasing average bulk carbide volume up to 593°C followed by a slight decrease with increasing temperature
- Consistent near linear increase in average boundary carbide volume with increasing temperature

- A peak in bulk carbide volume fraction at 482°C
- A peak in boundary carbide volume fraction at 537°C
- A significant delta between bulk and boundary carbide density that decreases with increasing temperature
- A peak in bulk carbide volume fraction as 482°C with a significant decreasing trend with increasing temperature
- Decreasing boundary carbide density with increasing temperature

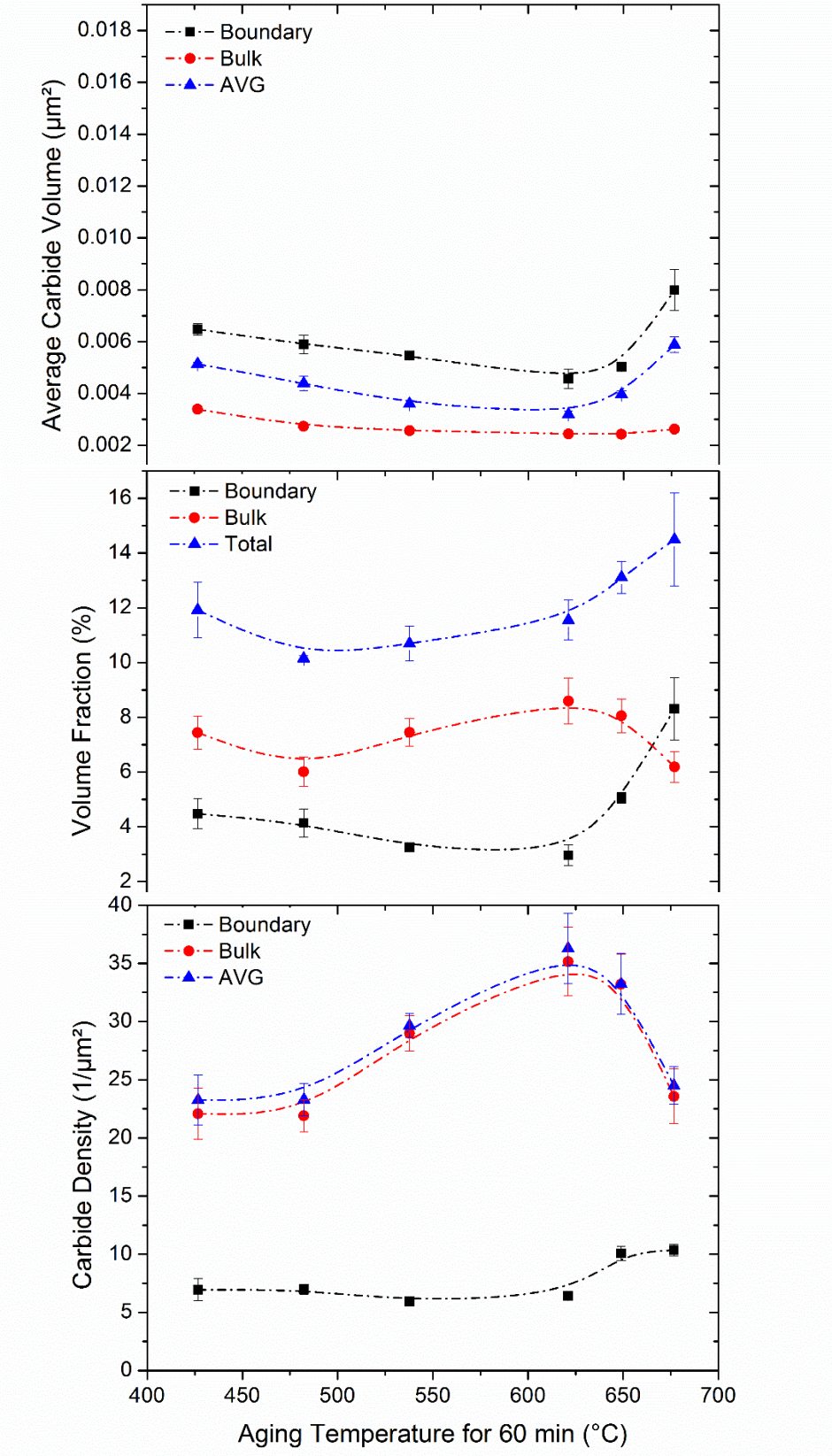

Figure 96: Carbide aging for 60 min. after austenitization (HT#A)

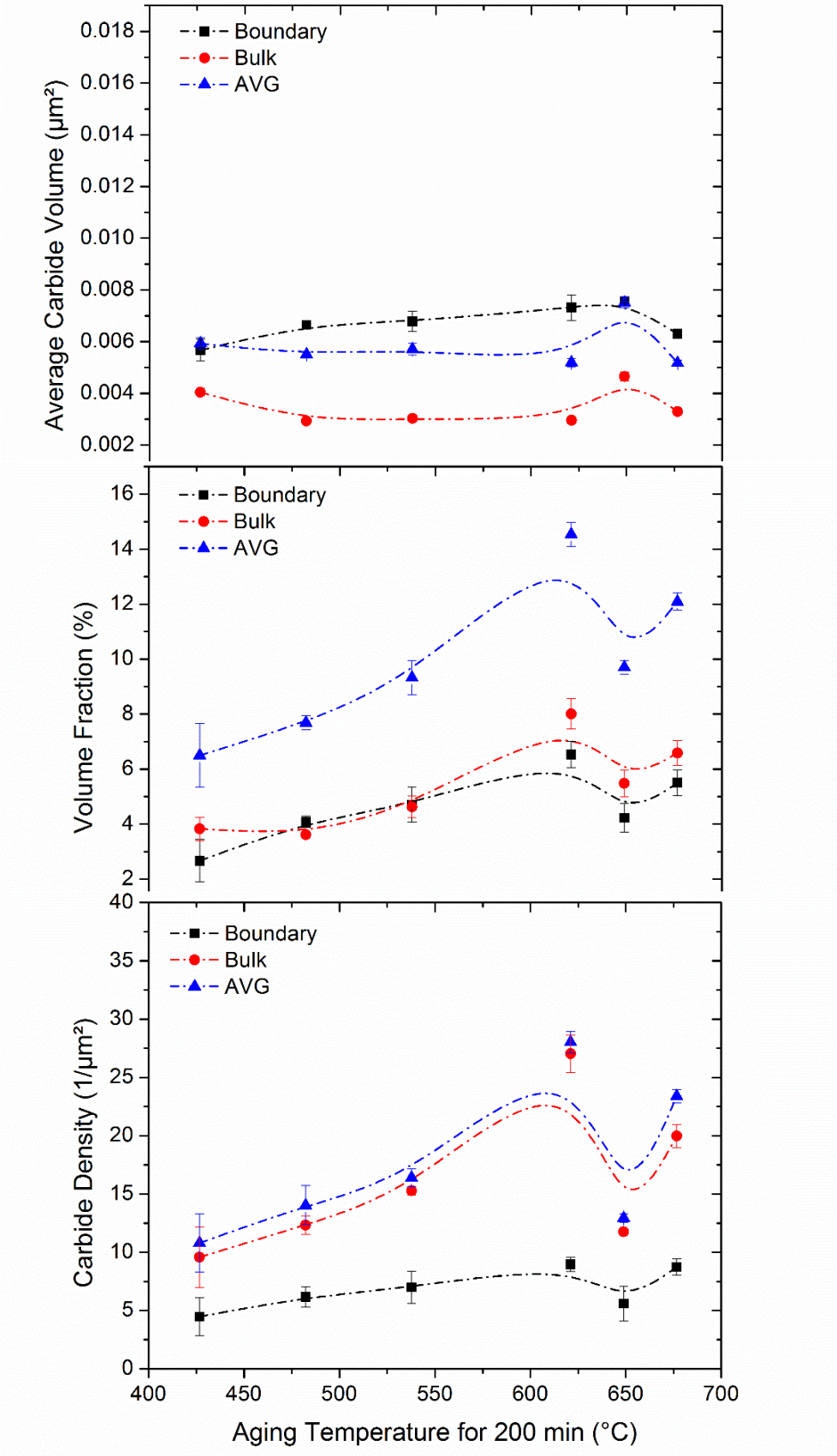

Figure 97: Carbide aging for 200 min. after austenitization (HT#A)

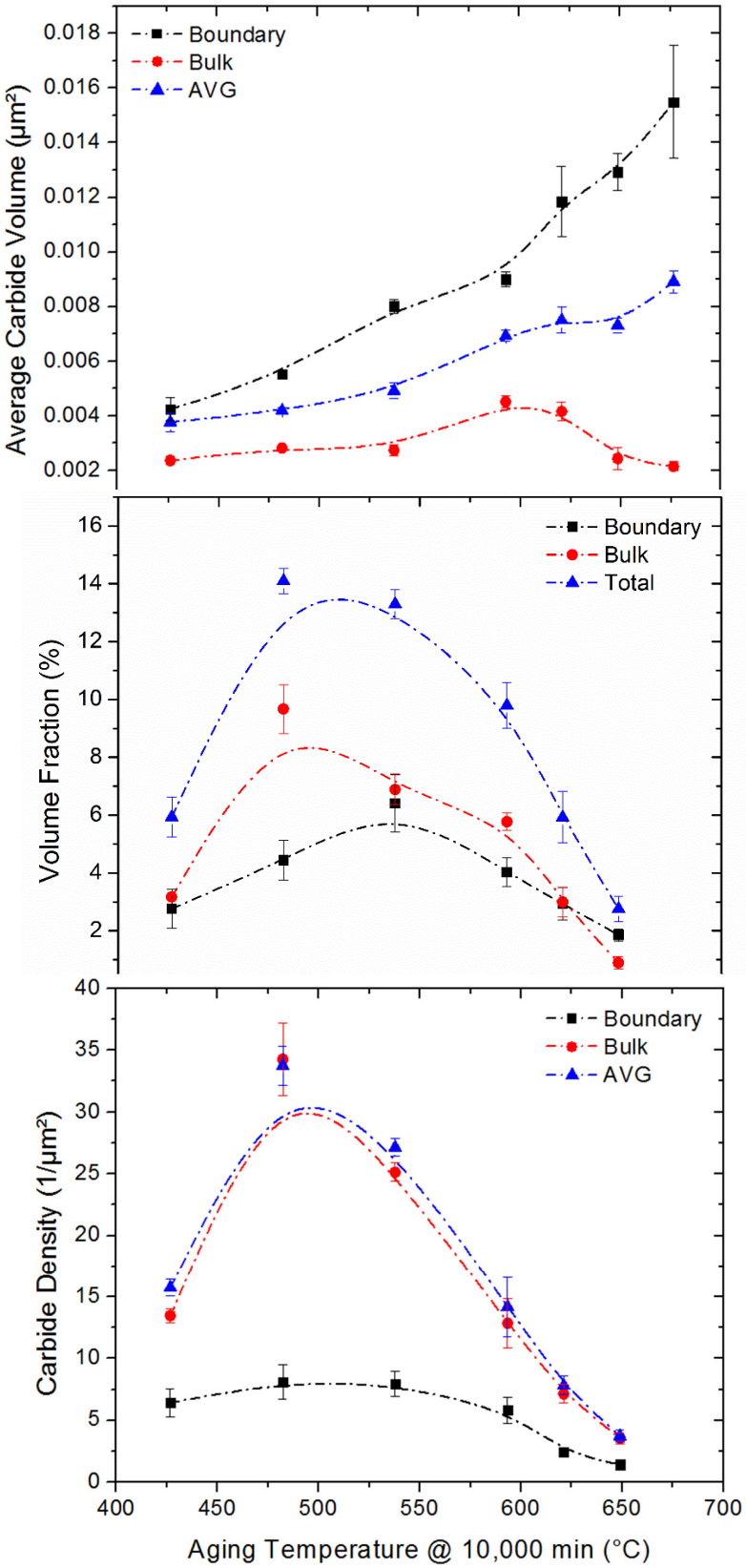

Figure 98: Carbide aging for 10,000 min. after austenitization (HT#A)

5.8.2 Aging after Tempering

HT#D and HT#4 were austenitized at 871°C and tempered at 643°C with subsequent aging treatments in the embrittlement range between 427°C and 538°C from 100 minutes to 40,000 minutes as detailed in section 3.6.2. These samples were prepared, imaged, and analyzed via the same procedure used on post austenitization aging samples in section 5.8.1. The results are shown below in **Figure 99** through **Figure 104**.

The most consistent results across all aging temperatures and both heats is an increase in carbide volume fraction with increasing aging time. In addition, the volume fraction of bulk carbides is always higher than that for boundary carbides. An increase in bulk carbide density across all samples with increasing time is also present, whereas the density of boundary carbides may increase slightly but remains relatively low by comparison. At 40,000 minutes the bulk carbide density across all samples is generally above 20 per μm^2, where the density for boundary carbides falls at or below 7 per μm^2. No easily discernable trends are observed in average carbide volume for the bulk carbides, with the only consistent trend being an increase in boundary carbide volume at 538°C. These results are all consistent with the nucleation of bulk carbides throughout this temperature range and coarsening of boundary carbides beginning at 482°C and clearly occurring at 538°C.

It is also noted that a slightly greater volume fraction of carbides is observed for HT#A comparted to HT#D. This may be a result of the increased level of carbon present in HT#A resulting in the nucleation of more carbides.

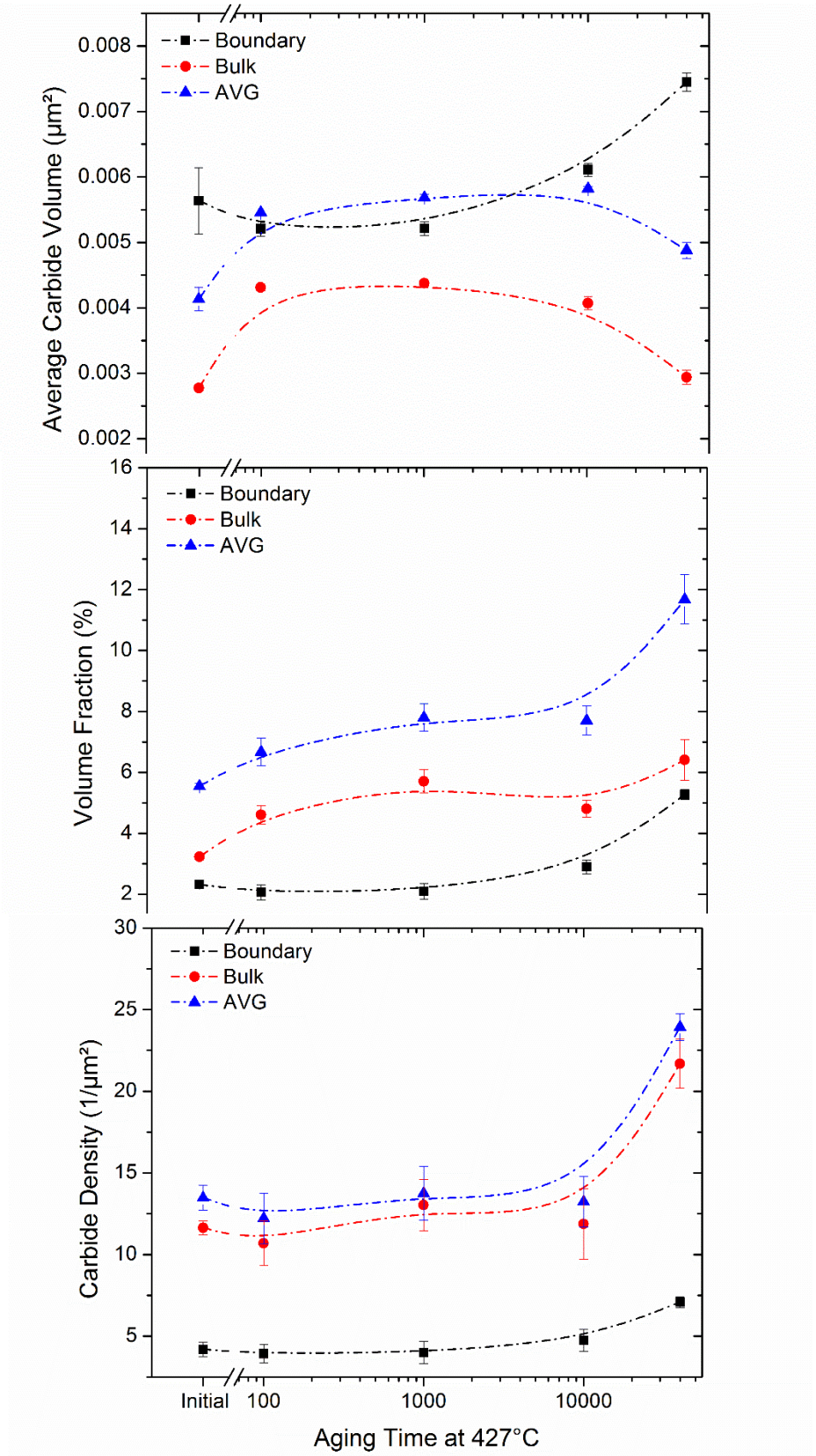

Figure 99: Carbide characteristics for aging at 427°C post tempering (HT#4)

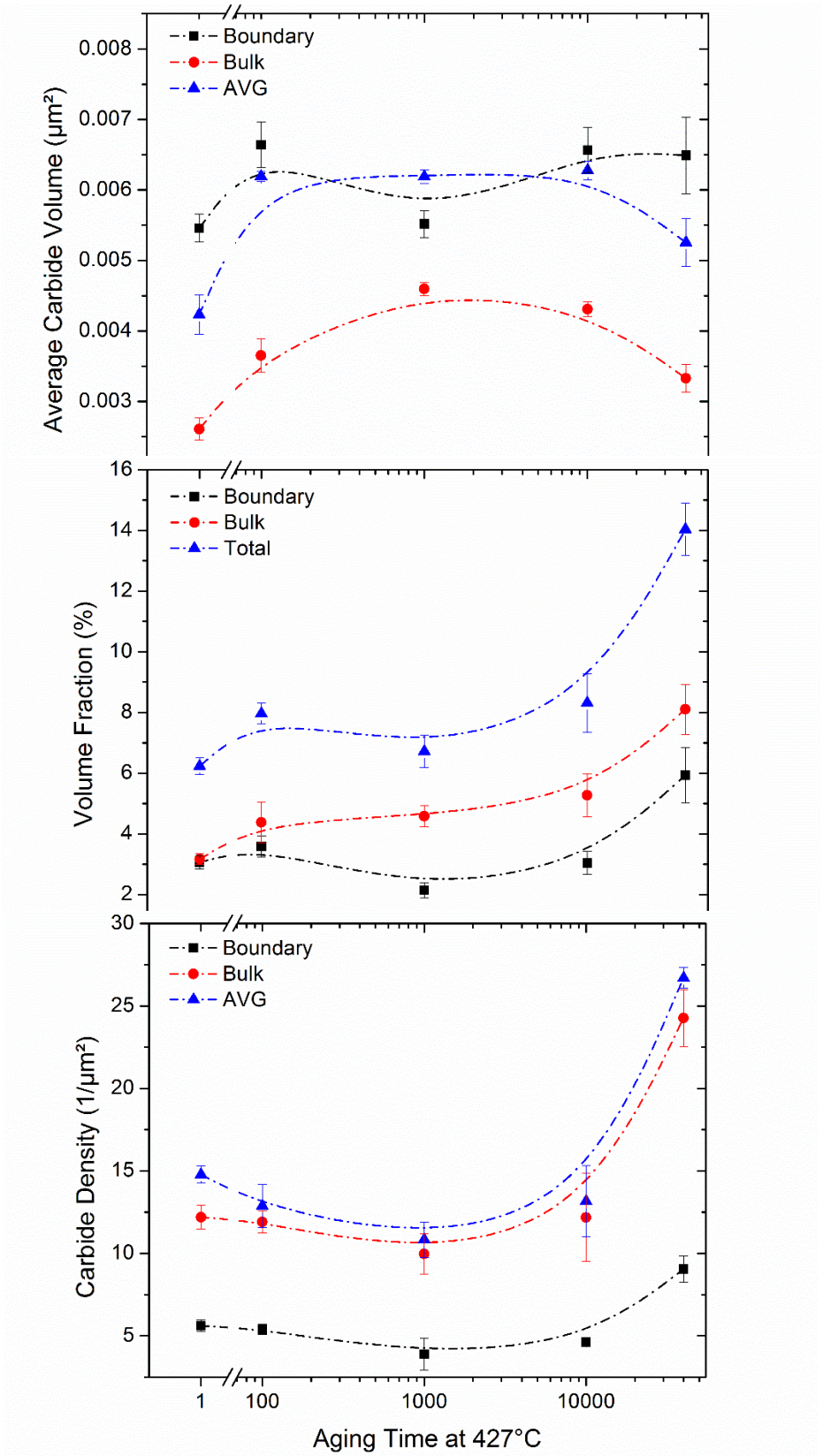

Figure 100: Carbide characteristics for aging at 427°C post tempering (HT#D)

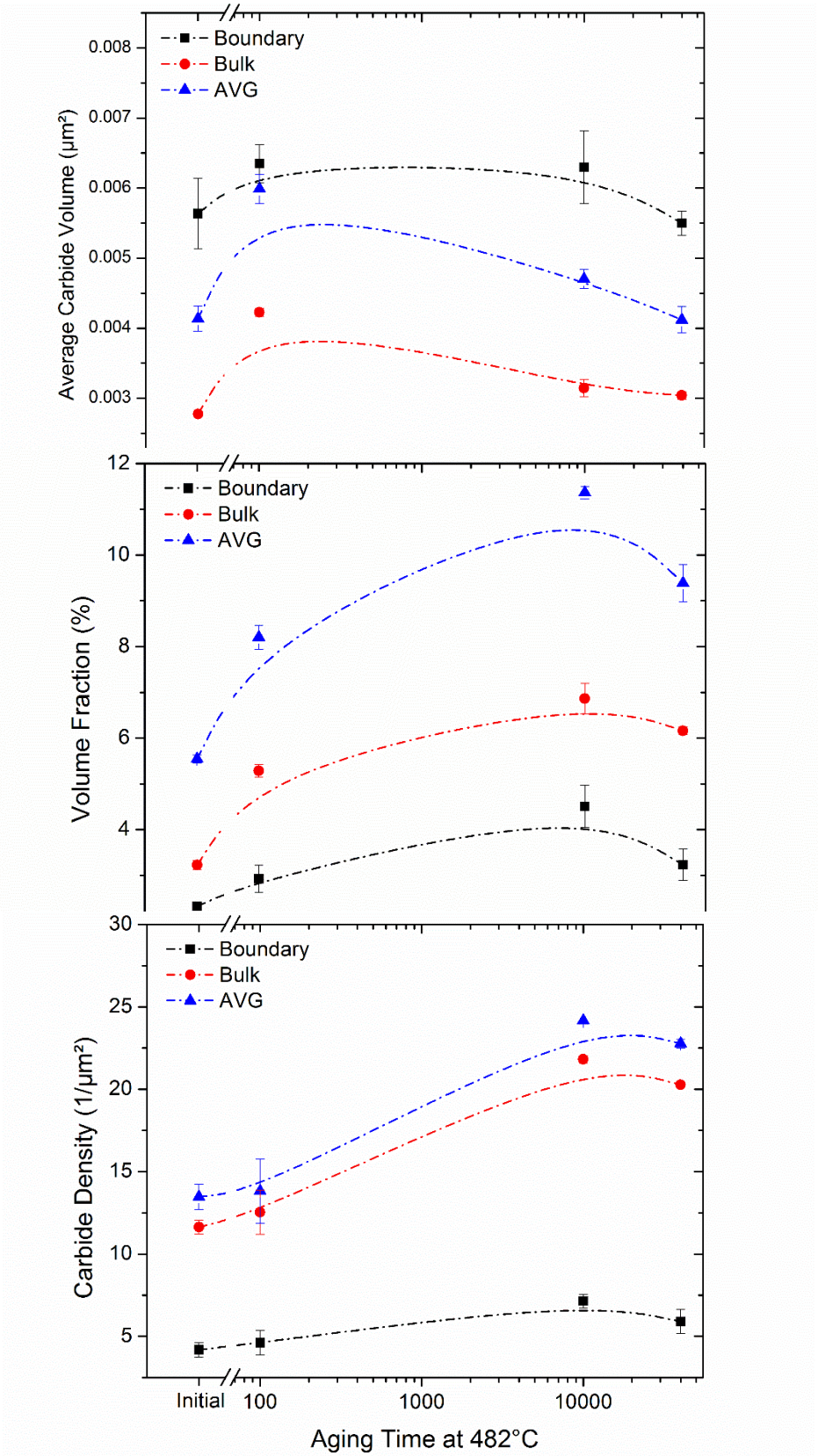

Figure 101: Carbide characteristics for aging at 482°C post tempering (HT#4)

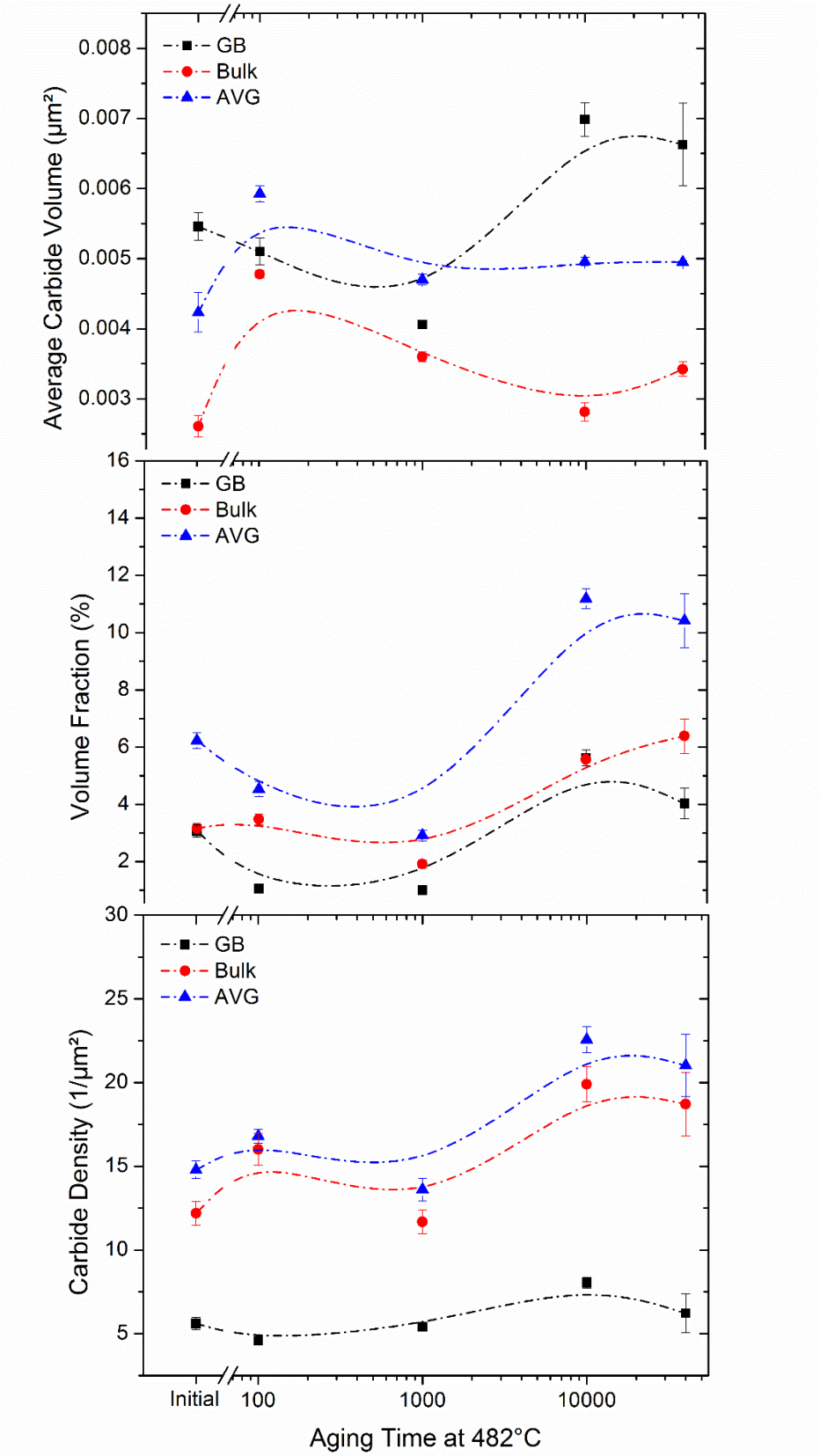

Figure 102: Carbide characteristics for aging at 482°C post tempering (HT#D)

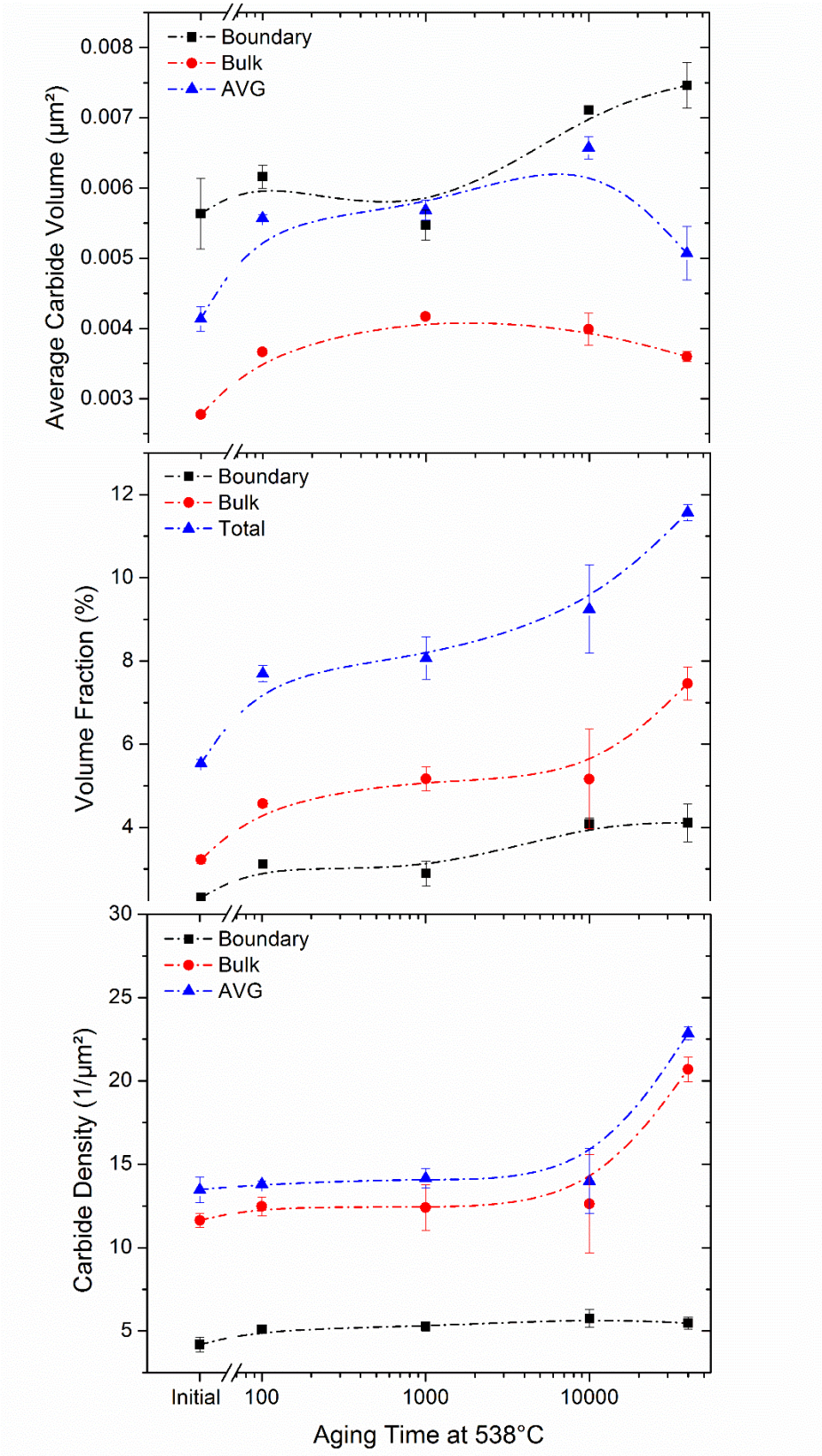

Figure 103: Carbide characteristics for aging at 538°C post tempering (HT#4)

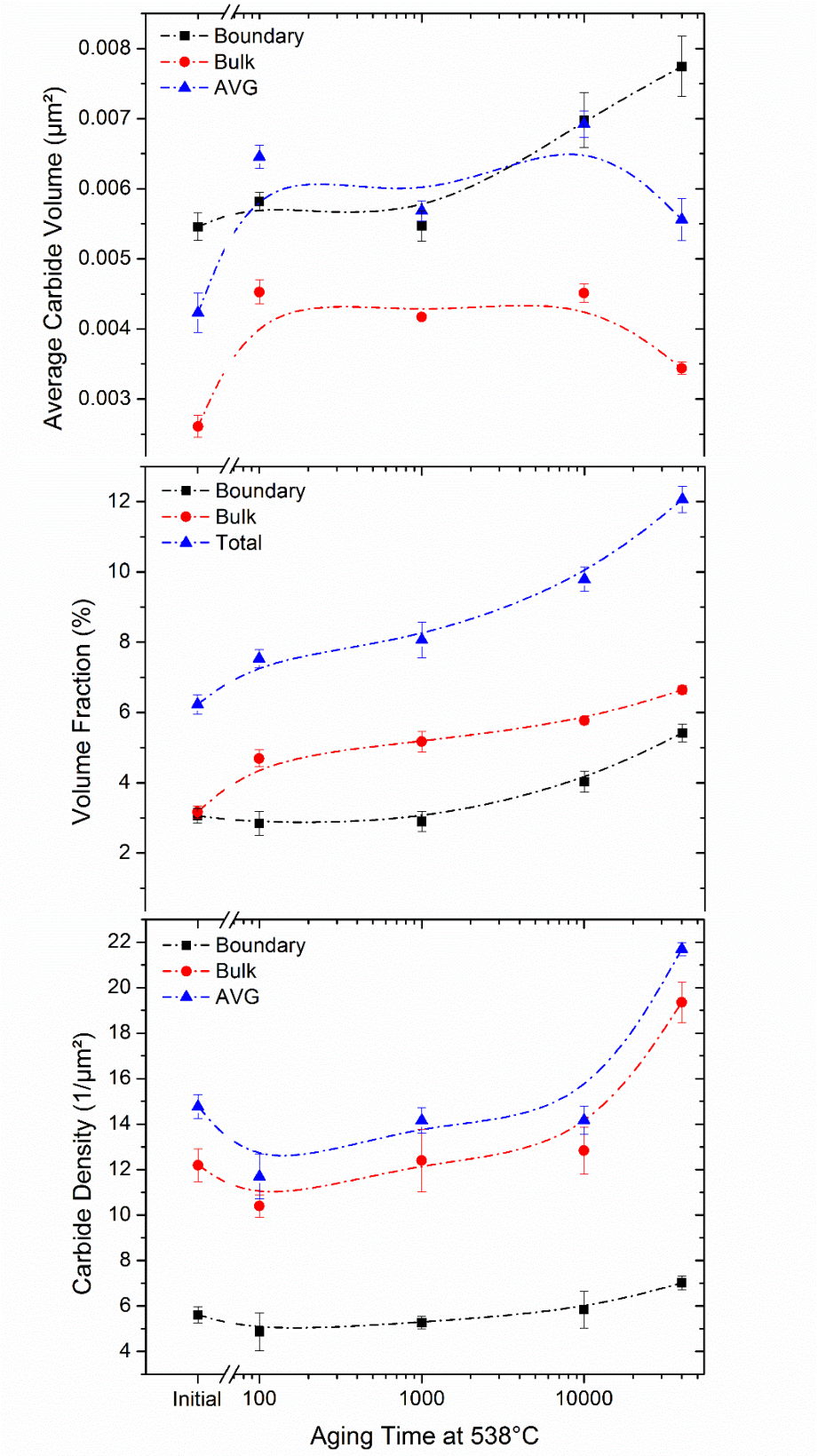

Figure 104: Carbide characteristics for aging at 538°C post tempering (HT#D)

5.8.3 Bulk carbide dissolution after tempering

HT#A, #B, #2, and #4 were austenitized at 871°C and tempered at 643°C with subsequent aging treatments in the tempering range between 665°C and 700°C from 1000 minutes to 40,000 minutes as detailed in section 3.6. These samples were prepared, imaged, and analyzed via the same procedure used on post austenitization aging samples in section 5.8.1. Image analysis of these specimens was particularly challenging as at 676°C and above at longer aging times, an increasing percentage of un-tempered martensite was present in the samples. As the image analysis routine struggles to segregate alloy carbides from local regions of un-tempered martensite, the results have numerous errors that must be considered when analyzing the raw results. An * is placed next to a raw result that is likely influenced by this measurement error. In general, the error results in inflated boundary volume fractions and deflated boundary average carbide volumes above 676°C.

The results of image analysis on HT#A aged for 43 hours (2580 minutes) are shown in **Figure 105**. The images used for this analysis are shown in **Figure 84**. The data points shown for aging at 643°C are the control specimen in the as austenitized and tempered condition with no subsequent aging. The key characteristics of note are as follows:

- Unchanging bulk average carbide volume
- Increasing boundary average carbide volume peaking at 676°C with a slight decrease with increasing temperature following the peak*
- Decreasing bulk carbide volume fraction with increasing temperature
- Increasing boundary carbide volume fraction with increasing temperature*
- A significant decrease in carbide density from the control

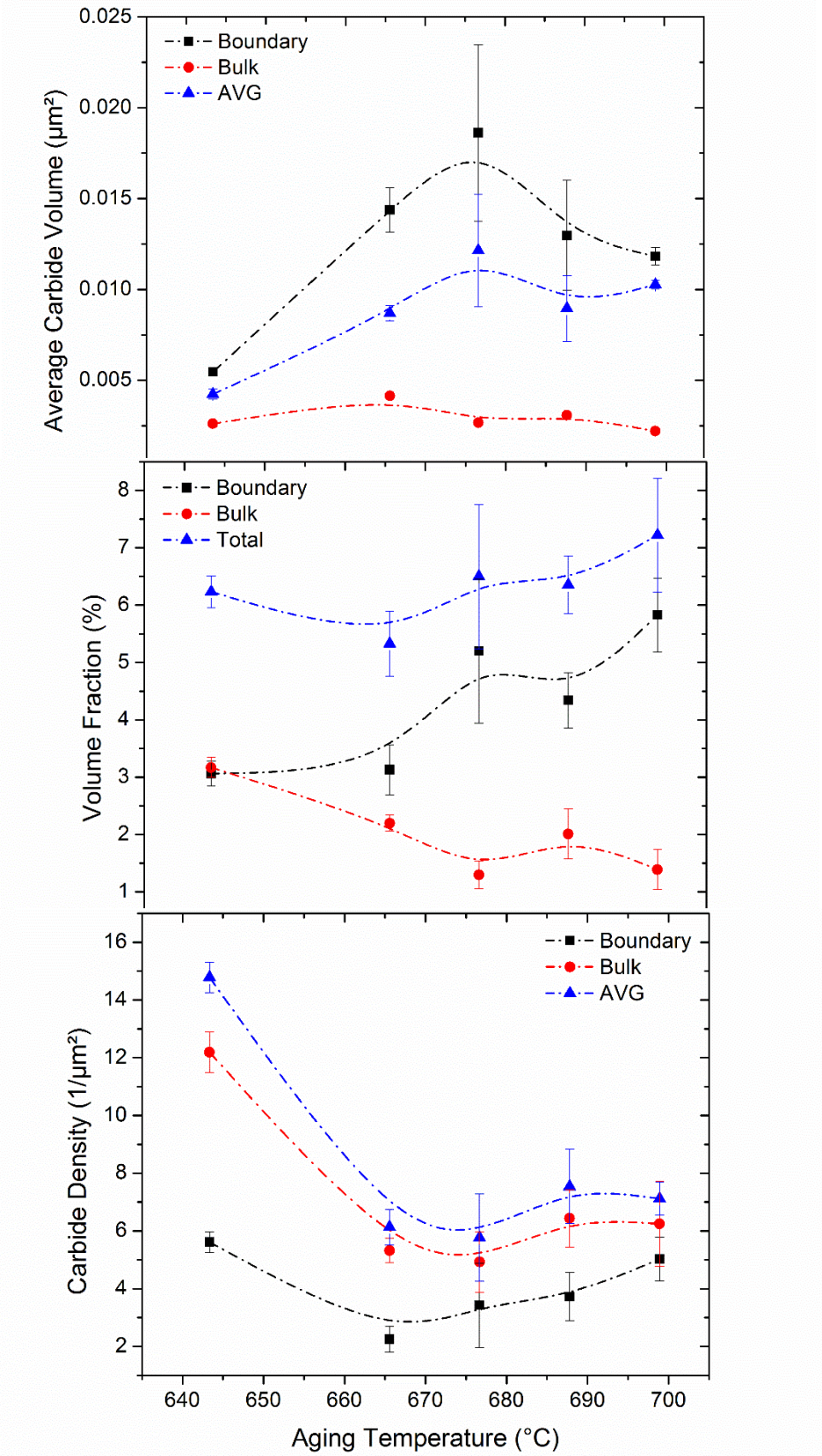

Figure 105: Carbide characteristics for aging after tempering for 43 hrs (HT#A)

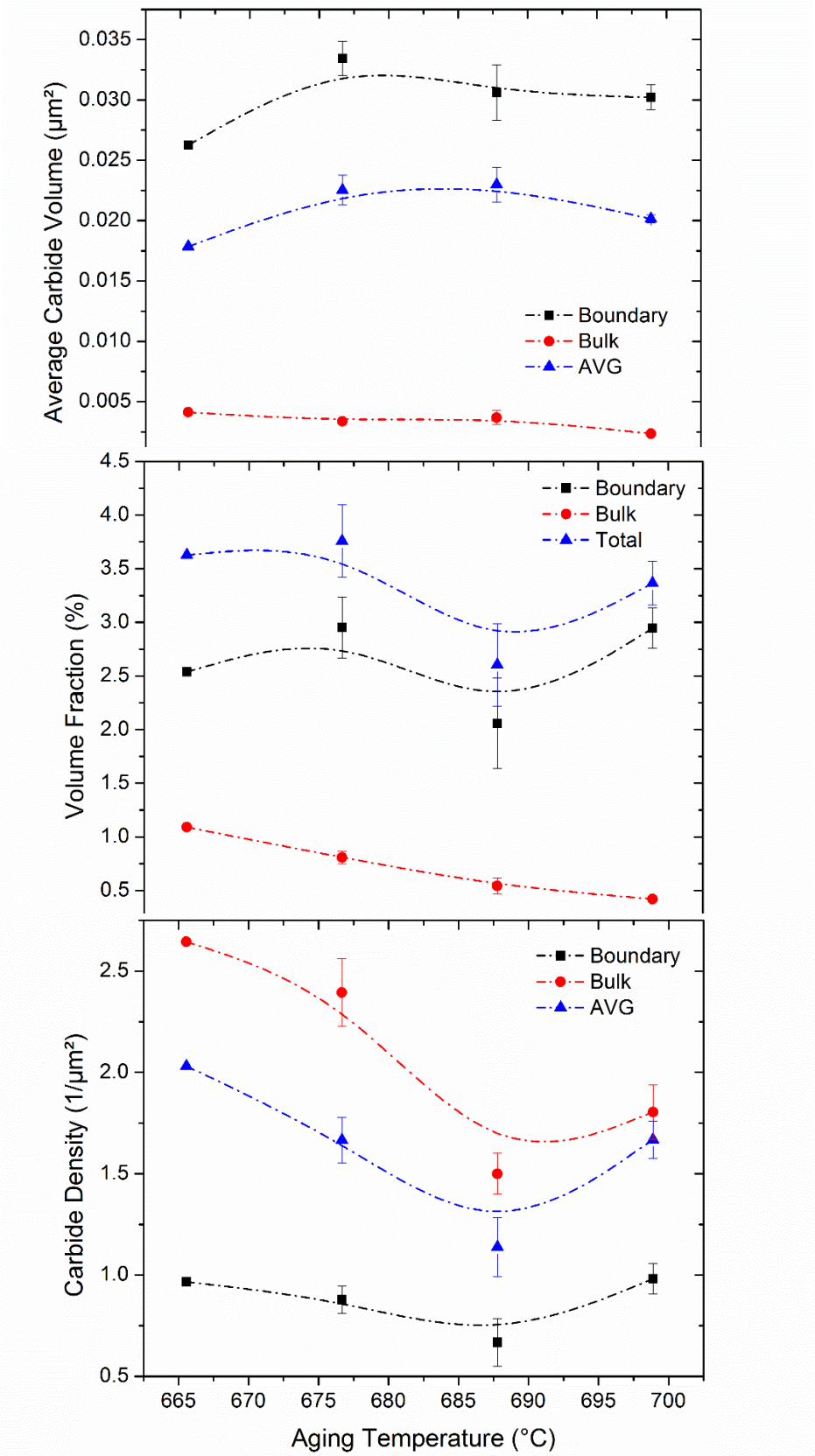

Figure 106: Carbide characteristics for aging after tempering for 14 hrs (HT#2)

Chapter 6: Analysis & Discussion

Through the systematic investigation of the HY alloy system, several conclusions can be drawn to advance the understanding of embrittlement and recovery. The preceding chapters provide a comprehensive characterization across length scales of the evolution of mechanical behavior and microstructure during thermal treatments for the HY-80 alloy system. An analytical image analysis method has been presented and executed to extract meaningful relationships for the evolution of alloy carbides through nucleation, growth, and dissolution. To expand on these results, the data obtained from the prior chapters can be used to inform models on the governing mechanisms of temper embrittlement and recovery, in addition to the speed of monatomic hydrogen diffusion.

This chapter will discuss the analysis of both mechanical and analytical results presented in Chapter 5 for the purposes of building a kinetic based model for thermal treatment of the alloy system. The form of this chapter is an introduction of all the key observations that will be discussed in a given section, followed by a discussion of the results in context with each other and the literature, associated solutions for kinetic constants, and presentation of modifications to key equations. Section 6.1 discusses the results of varied hydrogen aging treatments and the development of a modification to the Arrhenius solution of Fick's second law to predict the required aging time to migrate monatomic hydrogen to trapping sites. Section 6.2 discusses the results of temper embrittlement and recovery. Section 6.3 reviews the results of carbide analysis and the development of kinetic constants.

6.1 Mechanical Response of Hydrogen Aging Treatments

The main observations that will be discussed in this section are:

1. A peak increase in both T/4 and T/2 mechanical response at 482°C with a sub-critical anneal, re-austenitization, and temper (**Figure 58**)
2. Charpy impact strength results in excess of 110J regardless of aging time when a sub-critical anneal is followed by re-austenitization and temper (**Figure 59**)
3. A marginal increase of reduction of area, impact strength, tensile yield strength, and tensile ultimate strength after re-austenitization and tempering without any intentional hydrogen aging treatment. (**Figure 58** through **Figure 60**)
4. An increase of reduction of area with increasing hydrogen aging time and a post sub-critical anneal at 538°C (**Figure 61**)
5. A decrease in impact energy with increasing aging time at 538°C (**Figure 62**)
6. An increase of reduction of area at 482°C and Charpy impact strength above 70J without a sub-critical anneal and re-austenitization using only a post-aging treatment temper (**Figure 64** and **Figure 65**)

6.1.1 Aging below the embrittlement range

In order to compare results for low temperature aging, the mechanical response has been plotted as a function of equivalent aging time according to Fick's second law. In the analysis of this data reduction of area is used as an indirect measure for the level of diffusible monatomic hydrogen in the lattice. For the two assays executed with aging at 343°C and 371°C, the reduction of area is shown to increase with increasing soaking

time, as expected (**Figure 107**).[2] The speed of hydrogen thermal diffusion at 343°C matched that anticipated by the solution to Fick's law, with the exception of the longest time scale tested, where a slight drop in reduction of area was observed. This drop in mechanical response at longer soak times requires duplication to determine if it is a real performance impact or a testing artifact as a result of porosity, but at a minimum this demonstrates that the effectiveness of a hydrogen aging treatment may plateau at extended soaking time.

For aging at 371°C, a similar shape to the rate of increase in reduction of area is observed as compared to 343°C; however, for each equivalent aging time tensile ductility is slightly less than that observed at 343°C. This indicates that the predictive capability of the baseline solution to Fick's law is not adequate as a function of temperature.

Of particular note is the observation that both yield and ultimate strength increase with increasing aging time. In addition, there is an increased delta between YS and UTS at the centerline location for increased aging time as shown in **Figure 108**. This implies a change in the microstructure where one is not apparent with light metallography. Careful comparison of the microstructure under SEM imaging shows that the root causes could be explained by an increase in the number count and volume fraction of carbides further discussed in section 6.3. With these two observations it can be concluded that in this temperature range, new carbides are nucleating within the

[2] Note: Both T/2 tensile samples tested the underwent a 371°C soak for 28 hours had porosity on the fracture surface, lowering mechanical performance. These results were not utilized in calibration of the empirical hydrogen soak equation and are not shown on the graph. Raw data results can be found in data tables.

matrix and at boundary interfaces and that these carbides are responsible for the observed increase in tensile response.

That this increase in tensile response is observed primarily at the T/2 location implies that the nucleation of new carbides is associated with chemical composition, as the centerline location will have an alloy composition higher in carbon. This also implies a potential reason for the diffusion of hydrogen not following the expected diffusion models as carbides can serve as hydrogen trapping sites. Thus, in the presence of an increased concentration of hydrogen trapping sites the average required diffusion distance for monatomic hydrogen to be neutralized goes down.

The results were used to create an empirically based correction factor for the hydrogen aging time required to reach a minimum of 50% reduction of area and 20% elongation. These results showed the potential for a 49.6% reduction in required hydrogen aging time (from 450 hours to 227 hours) via increasing the soak temperature to 343°C for heavy section castings over 0.28m (11”). The empirically modified hydrogen aging time equation is given below:

$$t = Ch^n \exp\left[+\frac{Q}{RT}\right]$$

$$Correction\ Factor\ C = X * \left(\frac{4}{3}\ Ln(T) - \beta\right)\ \ Where\ \beta = 7.5219 \tag{48}$$

Note: X is defined in Chapter 2 and is a relative measure of the degassing of the material. This corrected hydrogen aging time equation was then used to calculate the required aging time for test specimens of 0.33m (13”) and 0.235m (9.25”) in thickness at both 329° and 343°C.

If the empirically modified hydrogen aging time equation was perfect, and one assumed that the manufacturing techniques for each sample were sufficiently similar, the resultant reduction of area would be identical for each specimen regardless of thickness, in **Figure 30**. This is not the case, but both the reduction of area and elongation exceeded specification requirements and thus the treatment can be considered successful. However, the empirically generated hydrogen equation does not adequately account for the increased amount of time required to diffuse monatomic hydrogen with increasing section size, particularly at the centerline location. This is likely associated with a greater starting concentration of hydrogen at the centerline resulting from the delta in solubility driving hydrogen to the center during solidification. Thus, an additional correction factor is needed to account for the varied starting concentration of hydrogen at different depths within a casting.

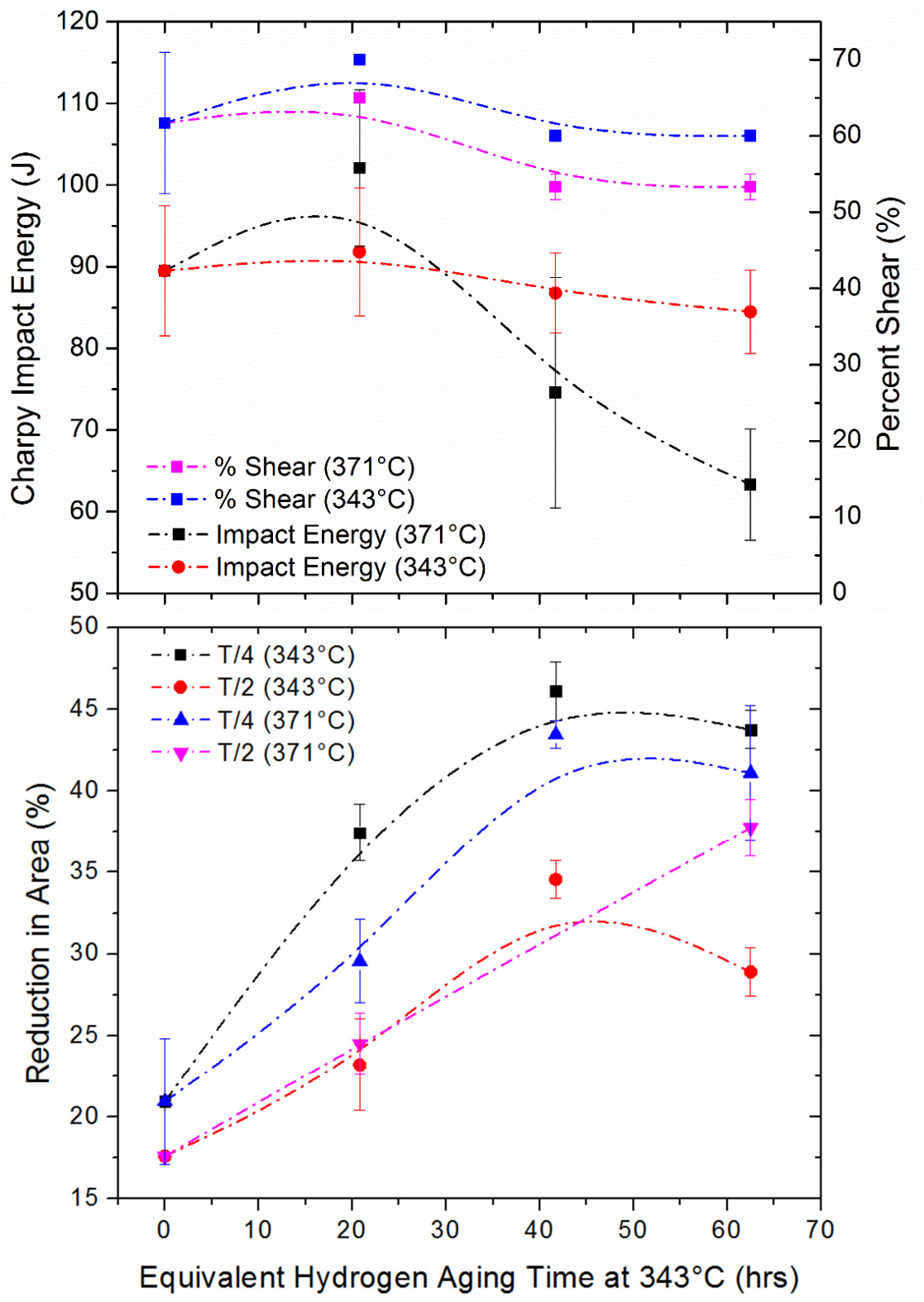

Figure 107: Charpy impact strength and tensile ductility for hydrogen aging below the embrittlement range *Note: Both tensile sample RoAs removed from 42 hour condition upon data filter at 371°C.

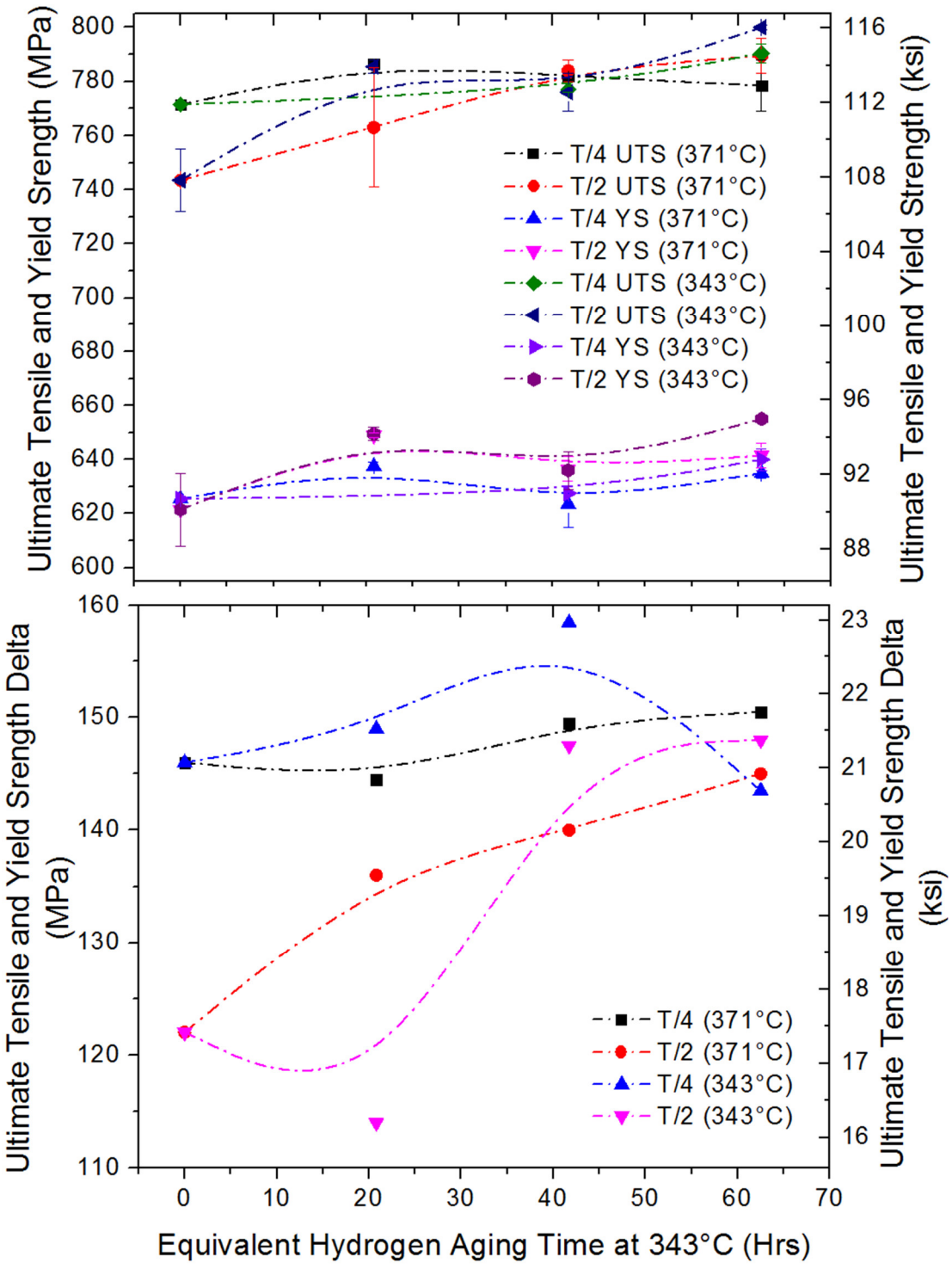

Figure 108: Tensile response for hydrogen aging treatments below the embrittlement range

6.1.2 Aging within the embrittlement range

In the development of aging trials within the embrittlement range, aging times were selected to be kinetically equivalent to each other based on Fick's second law. The empirically determined correction factor detailed above in section 6.1.1 was employed to attempt to account for the unquantified influences on the driving force for monatomic hydrogen diffusion. If that correction factor had been completely accurate one would expect the reduction of area and elongation measurements to be identical regardless of temperature for the time solutions to equation 72. However, experimentally, a depression in recovery of both the reduction of area and elongation measurements is observed for those treatments in excess of 482°C, where for treatments at 482°C and below the solution provided by equation 72 appears more accurate. This observation can be explained as a result of approaching the solubility limit for the critical ppm hydrogen the material must meet to exceed 50% reduction of area. For these cases, the driving force for hydrogen diffusion is decreased as the solubility limiting temperature is approached. Thus, an additional correction factor to that detailed in section 6.1.1 is needed to account for the influence the solubility limit has on the driving force for diffusion in addition to the correct factor that is needed to account for increased hydrogen levels at the centerline of thick sections.

That these treatments are able to increase the reduction of area to a factor in excess of specification requirements (and inherently below 1.2ppm monatomic hydrogen in the lattice) is particularly significant, as the treatments were performed on HT#A, which was intentionally hydrogen charged. Thus, it would be expected that, on a production heat of material containing less than half the starting concentration of

diffusible hydrogen contained within the matrix of HT#A, the treatment would be more effective and/or take less time to accomplish. This is demonstrated in the results of sub-embrittlement hydrogen aging treatments in **Figure 30** where for identical hydrogen aging at 329°C for 87 hours HT#A had 37% average reduction of area and standard industrial heat #3 had a response of 59% reduction of area at the centerline location.

It is also noted that the performance of a re-austenitization and re-temper on their own resulted in increases in both the reduction of area and elongation, indicating that these treatments served to move a significant portion of monatomic hydrogen atoms to trapping sites or free surfaces. This result on its own may appear to violate the ppm hydrogen solubility limit and is explained by: (1) Higher temperatures can be effective at diffusing some portion of monatomic hydrogen to trapping sites if the starting level of hydrogen exceeds the solubility limit for the temperature being used, which is true for the case of these assays; and (2) The material went through three cycles of heat up and cool down where the material would have observed temperature ranges both below the critical solubility limit and within ranges shown to be effective as a hydrogen aging treatment.

In addition to the slight increases in tensile ductility observed after re-austenitization and tempering, it is also noted that increases were observed in both impact strength and tensile yield and ultimate strength. This is consistent with double austenitization treatments for other low alloy steels and is a result of grain refinement and the Hall Petch relationship. It is inferred that the entire increase in impact strength for aging treatments within the embrittlement range is indeed a result of the double

austenitization and not a function of any mechanisms at play during treatment in the embrittlement regime. Further increases in tensile ultimate and yield strength are observed beyond that for the double austenitization during hydrogen aging. As with other observed increases in tensile response, this is explained by the presence of an increased volume fraction of discontinuous carbides within the bulk.

6.1.3 Proposed modified hydrogen aging equation

There are two primary modifications required to the baseline solution for required hydrogen aging time. The driving force for hydrogen diffusion is changing with both time and temperature, which is not accounted for in the baseline solution to Fick's law. With increasing time, the monatomic hydrogen content in the lattice goes down such that the decrease in the chemical potential deference decreases. The solubility also increases at higher temperatures similarly causing the chemical potential difference to decrease and thus decreasing the driving force for hydrogen diffusion.

First, the impact of the solubility limit on the driving force is considered. To modify this portion of the equation one must account for the activation energy for diffusion. The simplified solution to Fick's law used herein inherently assumes the activation energy will be constant with temperature and time, but this is not the case. Rather as the aging temperature approaches 580°C (the temperature where the solubility constant is equal to the target hydrogen content) the driving force will decrease and reach zero. A driving force factor can thus be defined as:

$$Driving\ Force\ Factor\ (F_T) = H_{critical} - Solubility\ Constant\ (T) \quad (49)$$

Where for HY-80 $H_{critical}$ = 1.2ppm to achieve a reduction of area of 50% (the specification minimum requirement for the alloy). An experimentally determined exponent, δ, is further proposed specific to the material that combines the influence of hydrogen trapping sites on the local driving force.

The proposed modification to the solution to Fick's law then becomes:

$$t = C^{\frac{1}{F^{\delta}}} h^{n} \exp\left[+\frac{Q}{RT}\right] \tag{50}$$

In this manner the modification detailed in equation 50 results in a function that decreases with increasing temperature until the aging temperature approaches the critical solubility limiting temperature for the material. The influence of the exponent drives both the degree of decrease in required aging time with increasing temperature and the delta between the solubility limiting temperature and the temperature at which the required aging time begins to increase.

Secondly, a correction factor is needed that addresses the variable starting concentration of monatomic hydrogen and trapping site densities throughout the cross section. This will be a thickness dependent variable that increases non-linearly with increasing thickness. For the case of HY-80, this can be solved from the assays executed on test samples of three different cross sections all treated at the same aging temperature with aging times based on the baseline solution.

The final proposed solution to the hydrogen aging time requirement combining the two modifications is as follows:

$$t_{H_c} = \left[LN \left\{ \frac{H_{current} - H_{critical}}{C_m} \frac{\pi^2}{8} \right\} \right]^{\frac{1}{F_T^{\delta}}} * \left(\frac{4}{3} Ln(T) - \beta \right) {h_i}^n \exp\left[+ \frac{Q}{RT} \right] \quad (51)$$

Where:
$\boldsymbol{H_c}$ = Critical hydrogen concentration to reach ductility target (ppm)
$\boldsymbol{C_m}$ = Starting maximum hydrogen concentration = 3.0ppm on average for HY steels
$\boldsymbol{h_i}$ = Casting local thickness (m)
n = 1.5 or 2 for planer or compact shapes respectively
Q = Activation Energy (kJ/mole)
β = Experimentally determined constant = 7.5219
F = Solubility limit influence driving force
R = The gas constant
T = Temperature (°K)
δ = local trapping site density & type exponent
t = time (hours)

It should be noted that this solution is not specific to HY-80. The driving force (F) can be determined for any alloy where the ${H^+}_{critical}$ to achieve the minimum tensile ductility is known (which can be determined experimentally as defined by Ref. [110]). Similarly, the δ exponent value can be solved experimentally following similar procedures as detailed here-in. In future research, it is recommended that solidification modeling be explored to computationally solve for the δ values of different alloys and cross sections. In addition, it is suspected that the δ exponent is influenced strongly by the density and type of hydrogen trapping sites. Such predictions cannot be accurately made using current models; however, the continuing work of the Beckerman group at the University of Iowa on inclusion and air entrapment modeling shows promise and may, upon its completion, be suitable for solving for the δ exponent of a given casting.

This trapping site exponent will also be influenced by the concentration and type of local carbides.

6.2 Mechanical Response of Temper Embrittlement and Recovery

The main observations that will be discussed in this section are:

1. The increase in impact strength at aging temperatures below 420°C for aging times of 2000 minutes or less (**Figure 38**)
2. The decrease in impact strength followed by a rise above the starting impact strength and then rapid fall off for aging at 482°C (**Figure 36**)
3. The shift in the start temperature for embrittlement of 50°C between the low and high phosphorus concentration heats studied (**Figure 37** and **Figure 39**)
4. The maximum embrittlement rate occurrence at 482°C for both heats investigated despite significant difference in composition (**Figure 37** and **Figure 39**)
5. A peak recovery rate and absolute recovery amount beyond the measured control impact strength at 649°C (**Figure 40** and **Figure 41**)
6. The reduction in impact energy with increasing aging time at 538°C with the application of an identical recovery treatment (**Figure 62**) with a simultaneous decrease in tensile response (**Figure 63**)

6.2.1 Embrittlement and Recovery Rate

In Chapter 5, the results for two heats of HY-80 (#B and #D) are detailed after treatment in the embrittlement range at logarithmic time intervals. **Figure 109** and **Figure 111** re-plot the results comparing the embrittlement rate for each heat at 399°C, 427°C, and 482°C. The delta in mechanical response is particularly evident for the treatment at 399°C for 5000 minutes of aging where HT#D has an impact strength

slightly above the control and HT#B has an impact strength of only less than 50% of that heat's control specimen.

When considering the results from HT#B containing a high concentration of phosphorus the initial starting impact energy was lower than anticipated. **Figure 36** shows clearly that the rate of embrittlement increases with increasing temperature and with HT#D. In addition, while a small amount of embrittlement may still be occurring at 347°C and 343°C (675°F and 650°F), at the time scales of a hydrogen aging treatment the loss in toughness is less than 10%. This result requires validation for a standard production heat as the degree of initial embrittlement observed prior to an aging treatment may influence the onset of follow on embrittlement. Furthermore, the rate of embrittlement and the onset temperature for observed embrittlement may be influenced by the starting content of embrittling elements already segregated to the grain boundary at the start of embrittlement measurements.

Both the low starting impact energy and the loss of toughness at the temper embrittlement barrier are an important observation as it indicates that the current specification defined limitations for embrittling elements are too high to ensure HY alloy steel is produced with acceptable mechanical performance. In the case of heat #B this appears to be the case, and while recovery from the embrittled condition was achieved for a lab scale sample, it is not likely that a thick cross section casting would be capable of complete embrittlement recovery. Based on this discovery, no further work was conducted with the high embrittling element heat #B. It is proposed for further study that a temper embrittlement equivalency equation is developed which

determines the relative impact of each element, such that a new requirement can be created to limit the total quantity of embrittling elements.

The significant and fast increase in impact toughness as measured at 649°C for embrittlement recovery rate assays conducted on HT#D (replotted below as **Figure 112**) indicates the potential for embrittling constituents such as phosphorous to be playing an active role in the embrittlement. However, the more gradual increase observed at slightly lower temperatures indicates that more than one embrittlement mechanism is likely at play, as the kinetics of phosphorous migration from the grain boundaries is not substantially lower between 649°C and 593°C. Rather this indicates that a slower diffusion-based process is active that is resulting in improvement in the mechanical response. In addition, it is noted that while HT#B begins embrittlement at significantly lower temperatures, each heat studied appears to have the same peak embrittlement temperature at 482°C that is clearly shown as an inflection point in **Figure 110** for HT#D. This inflection point implies a mechanistic change in the rate of embrittlement that is not explained by phosphorous segregation models.

For both heats studied, a slight peak in impact strength is observed at lower temperatures up to 420°C for HT#D and up to 370°C for HT#B (**Figure 110** and **Figure 111**). A potential explanation of these low temperature increases would be via the nucleation of new carbides that are discontinuous and thus provide a site for resistance to crack propagation. However, in the case of HT#B the higher concentration of embrittling elements overrides the beneficial effects that these carbides could have to impact strength. This slight peak in impact strength after short aging times was also observed in **Figure 107** for aging HT#A at 371°C prior to a depression in the impact

strength with increased aging time, and is even observed at higher embrittlement temperatures with very short aging times as shown in **Figure 36**.

In the literature the traditional mechanism of embrittlement and recovery is detailed as the migration of embrittling elements to the grain boundaries both via equilibrium and non-equilibrium segregation. In these cases, recovery from embrittlement is nearly instantaneous occurring over a period of only seconds associated with the migration of embrittling elements back into the bulk. However, while significant recovery from embrittlement is apparent over short periods of aging time, the fact that that the degree of embrittlement recovery both changes significantly with temperature, and that additional recovery is observed with increasing time verifies that an additional mechanism or mechanisms are at play.

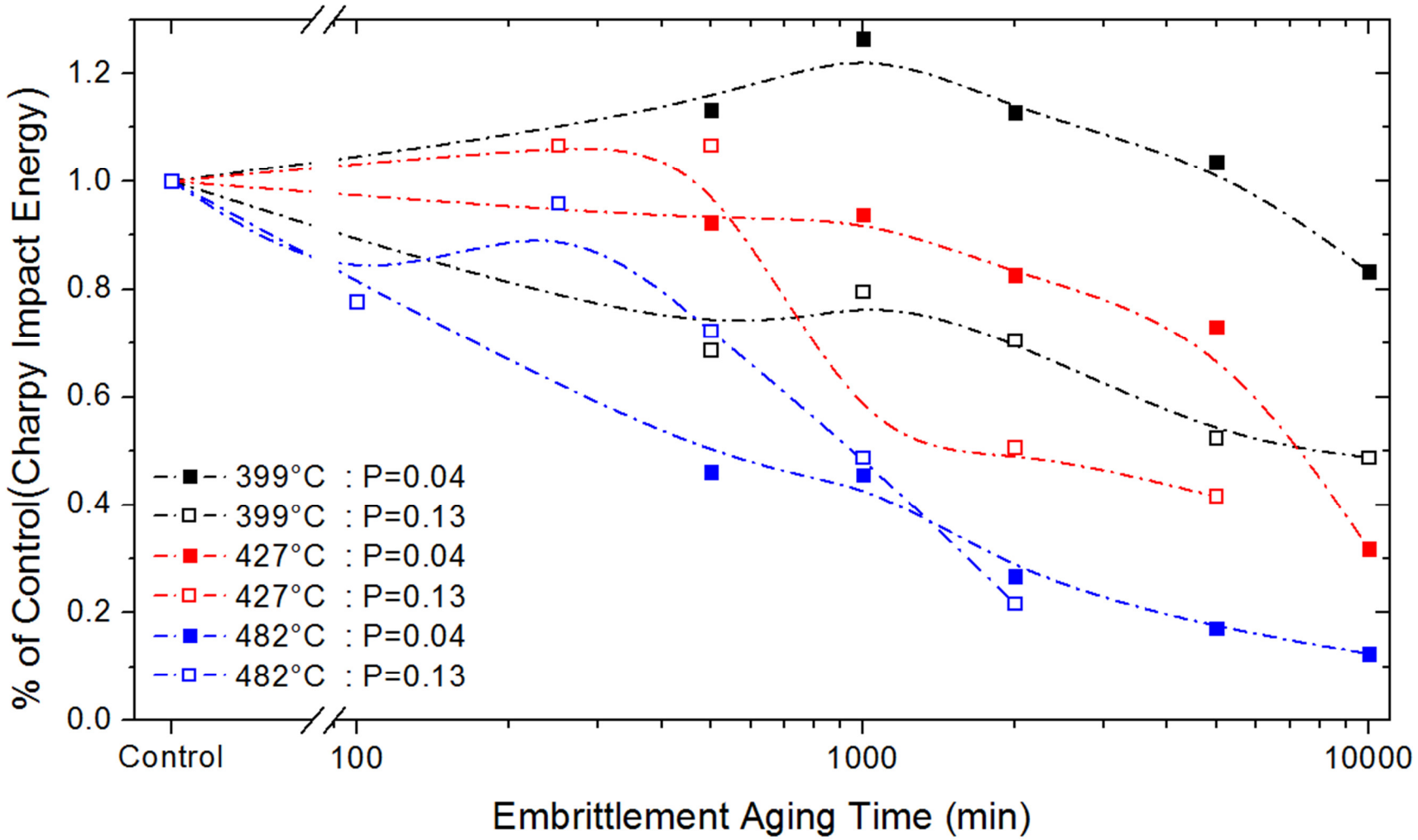

Figure 109: Embrittlement results as measured by the % of control from Charpy impact specimens tested at -73°C aged from 399°C to 482°C with two different heats containing phosphorus levels of 0.04 wt% and 0.13 wt%.

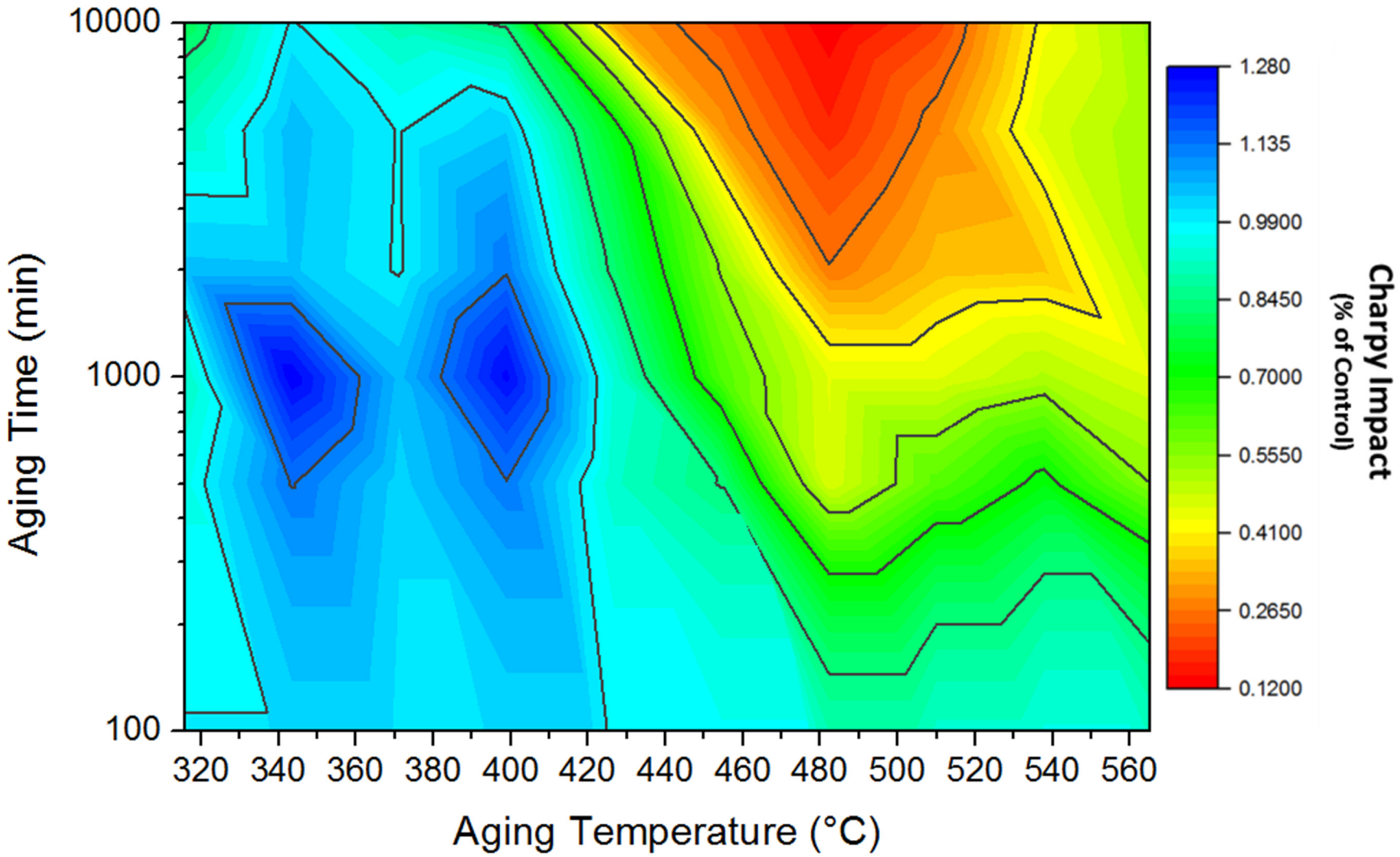

Figure 110: Embrittlement results as measured by the % of control from Charpy impact specimens tested at -73°C for HT#D.

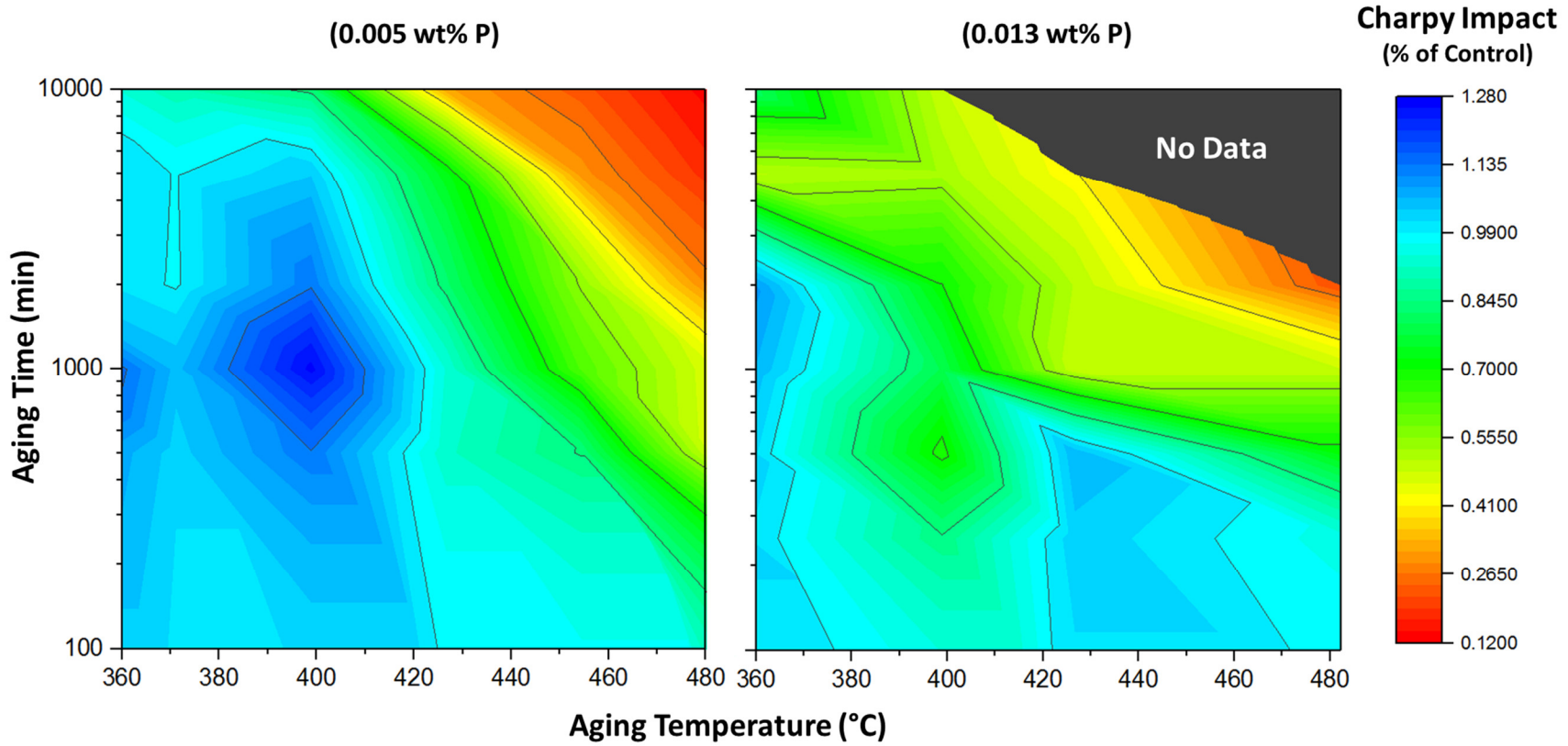

Figure 111: Embrittlement results as measured by the % of control from Charpy impact specimens tested at -73°C for both HT#D and HT#B

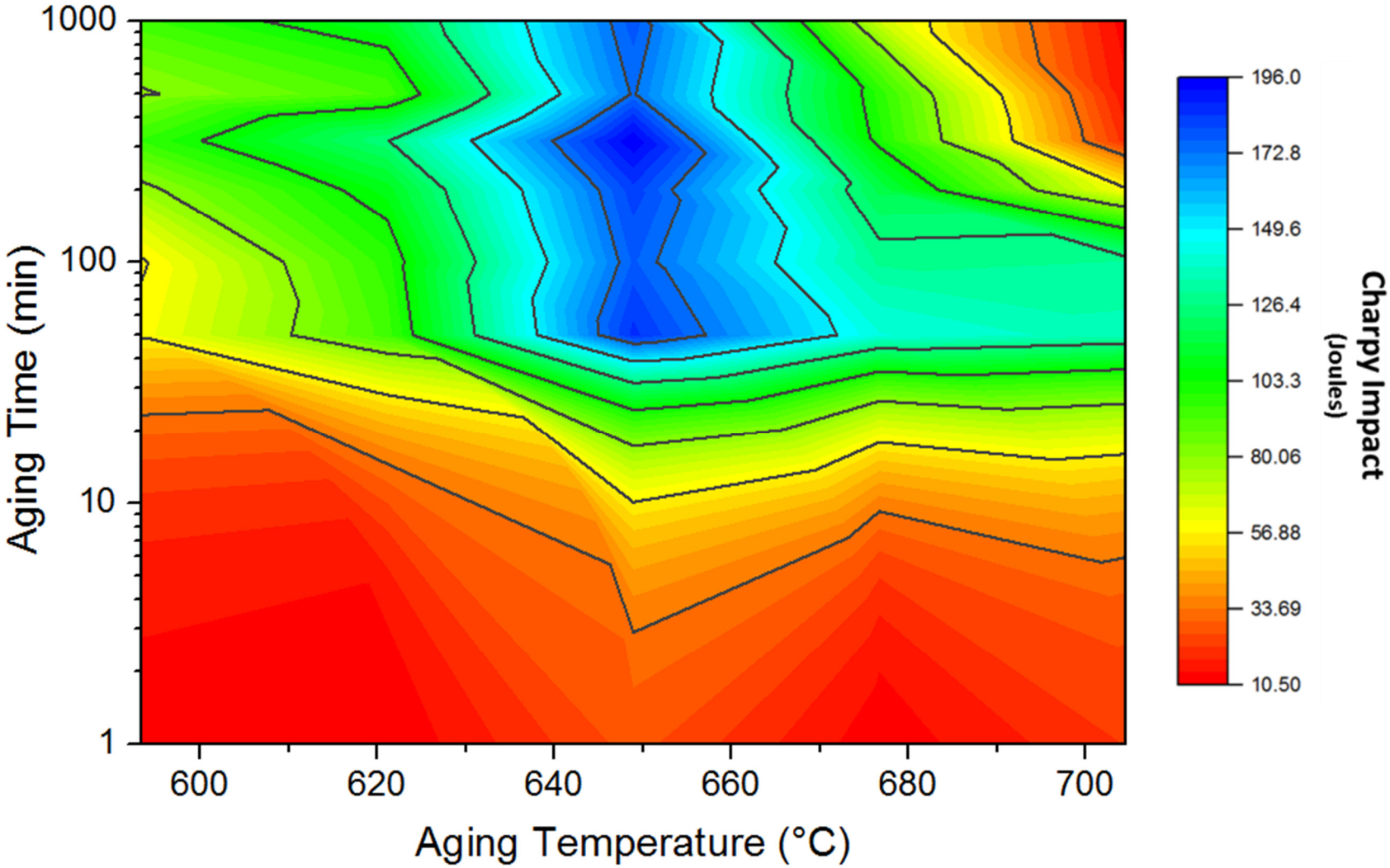

Figure 112: Embrittlement recovery rate results as measured by Charpy impact specimens tested at -73°C . HT#D.

6.2.2 Comparison of results with the McLean Model

The Mclean model for equilibrium segregation predicts a shift of 20°C between the critical temperature to reach 0.5 at% P (**Figure 19**). This is significant under the actual experimental observed shift in the onset of temper embrittlement (observed via Charpy impact results) of 50°C. Thus, the Mclean model results provides evidence that phosphorus may not be solely responsible for the shift in the onset temperature for temper embrittlement. Rather it is likely that a combination of several embrittling constituents are all contributing together to this shift.

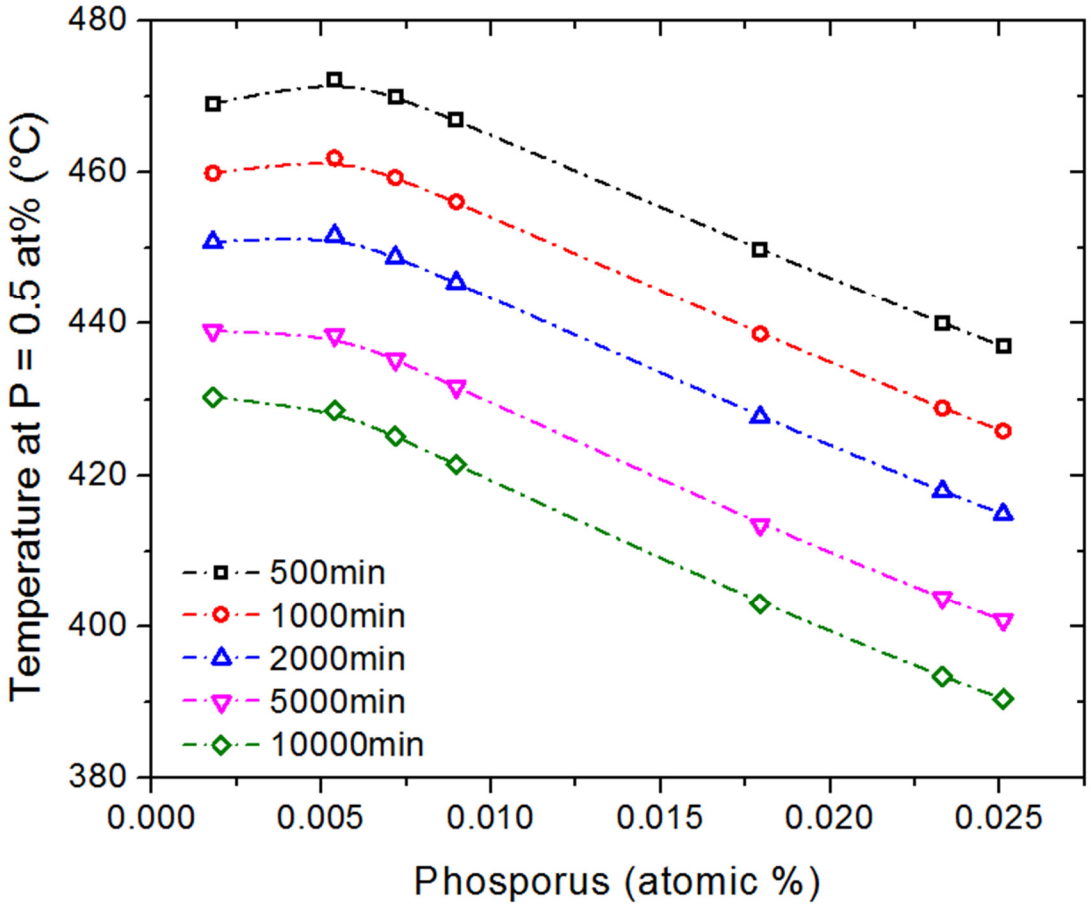

Figure 113: McLean model solution for equilibrium segregation of P to grain boundaries at an atomic concentration of 0.5% for the testing times used in the study of embrittlement rate. Model data points represent P levels present in study heats in addition to the lower limit of detection and the maximum permitted by specification.

6.3 Carbides as an Embrittlement Mechanism

The main observations that will be discussed in this section are:

1. The lack of any meaningful changes in the light metallographic microstructure for samples treated in the embrittlement range. (**Figure 42** and **Figure 43**)
2. The appearance of largely trans-granular cleavage fracture (and no intergranular fracture) on samples treated in the embrittlement range (**Figure 47**)
3. $M_{23}C_6$ Carbide painting and coarsening along prior austenite grain boundaries for samples within the embrittlement range (**Figure 52**, **Figure 53**, and **Figure 98**)
4. M_7C_3 Carbide nucleation in the bulk for samples treated in the embrittlement range (**Figure 79**, **Figure 80**, and **Figure 98**)
5. The appearance of carbide clusters for aging in the embrittlement range (**Figure 50**, **Figure 51**, and **Figure 81**) and the lack of carbide clusters after treatment in the tempering/embrittlement recovery range (**Figure 83**)
6. Phosphorous surrounding and concentrated within carbides after aging in the embrittlement range (**Figure 75**)
7. The alignment of maximum embrittlement rate as measured by Charpy impact strength (**Figure 110**) and peak nucleation rate of M_7C_3 carbides at 482°C (**Figure 98**)
8. The different carbide volume fractions with identical impact strengthens observed during examination of hydrogen aging process sequence for a low carbon heat of HY-80 where the matrix is largely free from any M_7C_3 carbides as observed after tempering (**Figure 70**)

6.3.1 Carbide observations coinciding with embrittlement

Metallographic along with computational work supports a conclusion that the observed embrittlement and subsequent recovery cannot be solely explained by the segregation of phosphorus and other embrittling elements to grain boundaries as has been previously suspected in this and other steel alloy systems. Rather it is shown that alloy carbides play a key role in embrittlement whereas $M_{23}C_6$ carbides coarsen and, in some regions, appear as a continuous or semi-continuous structure at the prior austenite grain boundaries in the embrittling temperature range. The placement of these carbides at the boundary serves both to create initiation sites where cracks can nucleate and to deplete the matrix of Mo, a P scavenger, thus introducing additional P at the grain boundary beyond that anticipated by equilibrium and non-equilibrium segregation. In addition, M_7C_3 carbides are seen nucleating in the embrittlement range as evidenced by doubling to quadrupling the volume fraction. Recovery from embrittlement is thus proposed to be a result of two independent, but interacting, mechanisms related to both the removal of P from the boundary and the dissolution of carbides from the system.

The earlier historical work on the development of process parameters for HY-80 has clearly established that lowering of the content of embrittling constituents does impact the onset of temper embrittlement as measured by a reduction in the impact strength of the material. This work further supports that conclusion. HT#B with higher P content (0.013 wt%) is shown to start embrittlement at approximately 340°C whereas the start of embrittlement is shifted up to approximately 420°C in this material with P content of 0.005 wt%. However, the prior work on this alloy does not report the presence of any carbides, whether in the bulk or at the grain boundaries. This lack of

study is likely a result of both the lack of characterization tools available at the time and the presence of largely intergranular fracture with temper embrittlement, which supported the researchers' conclusions of embrittlement due to grain boundary segregation.

With the lowering of embrittling constituents in current industrial heats, it is now more easily discernible that carbides also play a role in embrittlement. That these carbides are made up of Mo as a primary element is also significant. Mo is known to be a co-segregate with and a scavenger of P [111] such that the addition of Mo to the matrix will delay the onsite of embrittlement. However, when Mo carbides form, the matrix is depleted of Mo. This has two impacts of removing a P scavenger from the overall matrix and of depositing free P in the vicinity of the nucleated carbide. The work with atom probe tomography on similarly alloyed systems containing Ni, Cr, and Mo [98] supports the conclusion of depositing and segregation of P to the carbide/matrix interface.

The appearance of only cleavage fracture further supports a conclusion that the presence of carbides changes the primary fracture path during embrittlement, particularly when carbide clusters form that can serve as nucleation embryos for cleavage. The embrittlement due to carbides is likely exacerbated by the depletion of Mo from the bulk and the additional P deposited in the vicinity and/or within a carbide as it nucleates. Of interesting note for higher carbon heat of HY is that the nucleation of M_7C_3 occurs along a limited number of preferential planes within the matrix, indicating interphase precipitation for this carbide. As a result, as these carbides are

needle like in morphology and would also have P surrounding them, preferential trans-granular cracking paths may be formed via this alignment. (**Figure 114**).

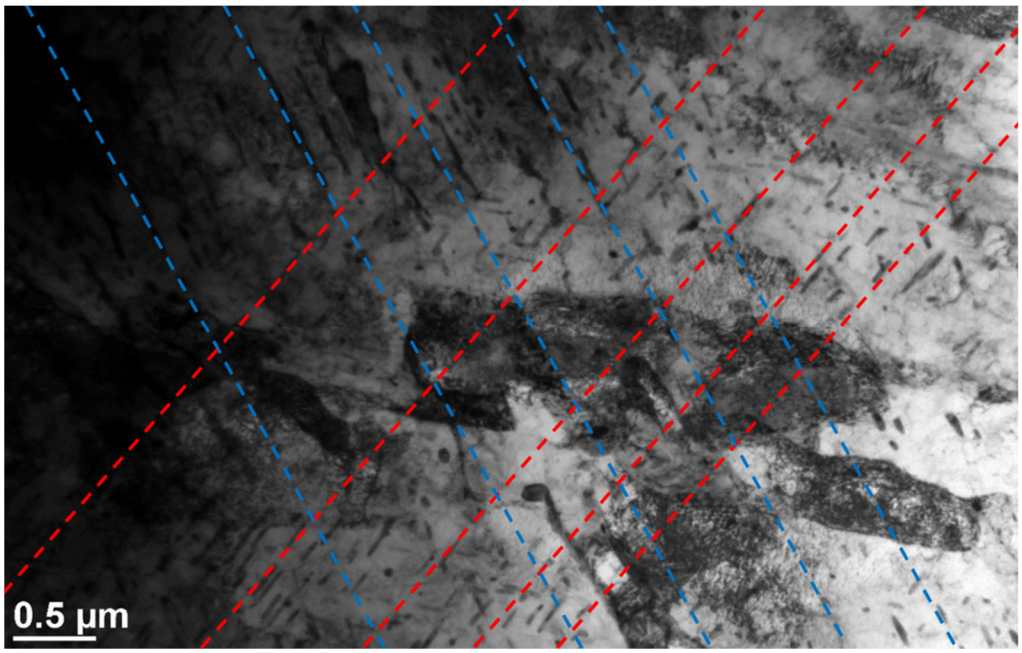

Figure 114: Preferential planes for M_7C_3 carbides in the bulk shown in a bright field TEM image. Planes outlined in red and blue dotted lines (HT#A)

It should also be noted that the unexpected increase in impact toughness observed with aging at low temperatures between 320°C and 420°C is likely also associated with carbides as discussed above. Moreover, for nearly all hydrogen aging studies, increases in the ultimate and tensile strength are observed with increasing treatment time in the embrittlement range, particularly at centerline locations with higher alloying content. Thus, when developing treatments it is important to strike a balance between avoiding the detrimental impacts observed due to carbides of certain types and morphologies and the potential beneficial increases in tensile and Charpy mechanical response.

The observed change in structure due to the addition of the annealing treatment when examining process sequence, being accompanied by a reduction in both ultimate

and yield strength and an increase in the -18°C Charpy impact strength is of note. It indicates that as long as the carbides are (1) not in semi-continuous links at the prior austenite grain boundaries and martensite lath boundaries, (2) not forming in clusters, and (3) predominately $M_{23}C_6$ carbides at boundaries rather than M_7C_3. The total volume fraction of carbides being higher does not necessarily have a detrimental impact on Charpy impact strength. Rather, a decrease in total volume fraction appears to be linked to a reduction in the ultimate and tensile strength, which in the case of sample 5 decreased its yield strength to 34 MPa below the specification requirements.

6.3.2 Carbide Nucleation, Growth, and Coarsening Kinetics

The analytical results from carbide analysis can be used to determine numerous kinetic constants for the diffusion, coarsening, and dissolution of alloy carbides are their constituents in the HY system. The most straight forward of these is a calculation of the nucleation rate of new bulk carbides, which are predominantly M_7C_3 carbides shown in **Figure 115** over the temperature range from 426°C to 537°C. The rate for HT#4 and HT#D is for those specimens which were austenitized, tempered, and then aged within the embrittlement range. The aging treatment for HT#A directly preceded the austenitization treatment. As expected the nucleation rate is considerably higher, by an order of magnitude, for aging directly after austenitization. Also of note, is that HT#D had a slightly higher nucleation rate than HT#4. This is likely explained by the increased level of carbon present in in HT#D. The most consequential observation is that throughout the embrittlement range there is nucleation of new bulk M_7C_3 carbides.

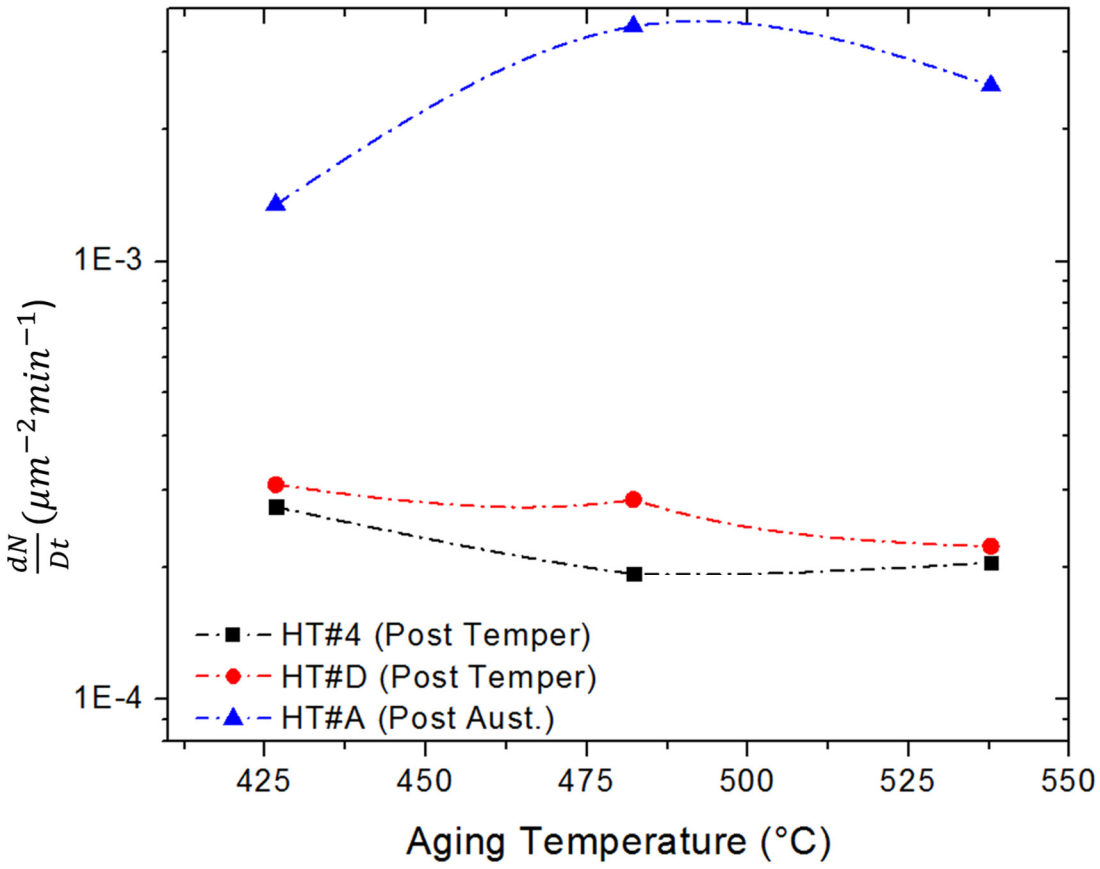

Figure 115: Nucleation rate vs. temperature for bulk (M_7C_3) carbides.

Coarsening is apparent for grain boundary $M_{23}C_6$ carbides through examination of the microstructure via SEM for aging temperatures at the upper limit of the embrittlement range and above. When examining the carbide parameters over time for a given treatment temperature the coarsening constant n can be determined. With increasing temperature the coarsening constant indicates a transition from dislocation, to grain boundary, to bulk diffusion mechanisms (**Figure 116** and **Table 30**).

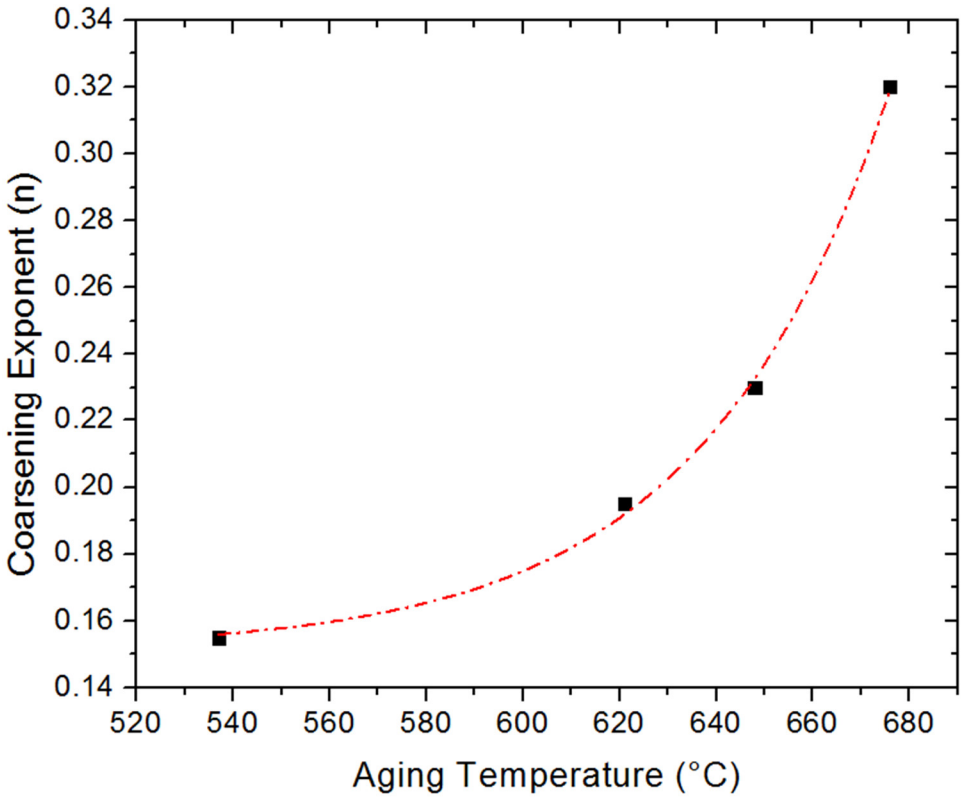

Figure 116: Experimentally determined coarsening exponent (n) as a function of temperature for boundary (predominantly $M_{23}C_6$) carbides

Table 30: Diffusion mechanism based on coarsening constant adapted from Ankem [112]

COARSENING CONSTANT	DIFFUSION MECHANISM
0.2	Dislocation Diffusion Control
0.25	Grain Boundary Diffusion Control
0.33	Bulk Diffusion Control
0.5	Interface Control

In order to calculate the activation energy for coarsening (diffusion of rate-limiting Cr) of the observed grain boundary $M_{23}C_6$ carbides, the following treatment is used adopted from Grewal and Ankem [113], [114]:

The particle size can be expressed as a function of a growth parameter, the aging time, and the coarsening exponent as follows:

$$\delta_{\alpha}^{\alpha-\beta} = K_{\alpha}^{\alpha-\beta} t^{n} \quad (52)$$

$$\delta_{\beta}^{\alpha-\beta} = K_{\beta}^{\alpha-\beta} t^{n} \quad (53)$$

Where:
$K_{\alpha}^{\alpha-\beta}, K_{\beta}^{\alpha-\beta}$ = growth paramaters of the α and β phases
$\delta_{\alpha}^{\alpha-\beta}, \delta_{\beta}^{\alpha-\beta}$ = particle size of the α and β phases (microns)
t= time (hours)
n = coarsening exponent
α phase = carbide, β phase = matrix

The growth parameters can be expressed by the following empirical equations:

$$K_{\alpha}^{\alpha-\beta} = K_{\alpha}/V_{\beta}^{m_{\beta}} \quad (54)$$

$$K_{\beta}^{\alpha-\beta} = K_{\beta}/V_{\alpha}^{m_{\alpha}} \quad (55)$$

Where:
K_{α}, K_{β} = growth constants of the α and β phases
V_{α}, V_{β}= volume percent of the α and β phases
m_{α}, m_{β} = retardation exponents of the α and β phases

Using the model proposed by Grewal and Ankem where based on LSW theory the solute and solvent atoms move in opposite directions resulting the in the mutual conversion of α to β and vice versa, the $K_{\alpha}^{\alpha-\beta}$ parameter can be related temperature dependent terms defining the evolution of particle sizes as follows:

$$\ln K_{\alpha}^{N} = \ln\left[T\,\frac{\left(K_{\alpha}^{\alpha-\beta}\right)^{\frac{1}{n}}\left(X_{Cr}^{\beta}-X_{Cr}^{\alpha}\right)^{2}}{X_{Cr}^{\beta}}\right] = \ln K_{\alpha}' - Q/RT \quad (56)$$

Where:
$X_{Cr}^{\beta}, X_{Cr}^{\alpha}$ = equilibrium mole fractions of Cr in the α and β phases

In this work, the values for the equilibrium mole fractions of Cr in the carbide and matrix have been calculated via Thermocalc CALPHAD analysis (See Appendix C). The values for volume fraction and carbide size at a given temperature are taken from the image analysis of 10,000 min. aging trials presented in Chapter 5 Section 8.

The coarsening exponents are as detailed above. The results of $lnK_\alpha^N \; vs. Inverse\ Temperature$ are plotted below in **Figure 117**.

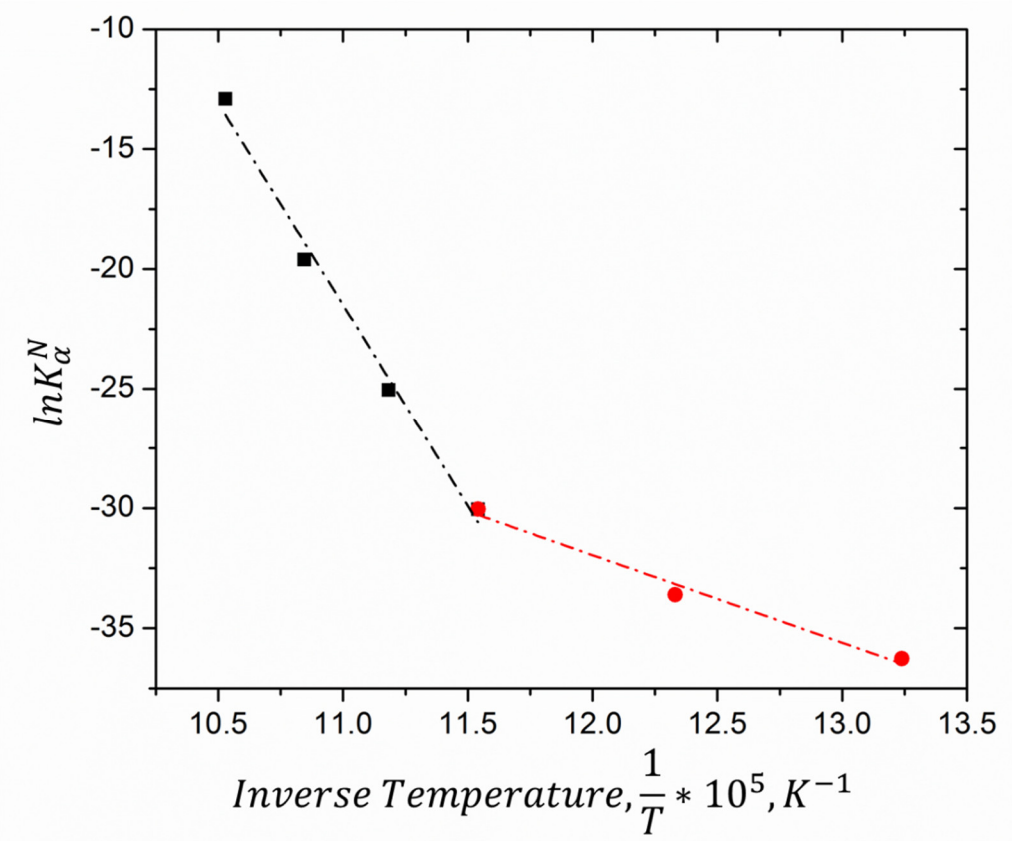

Figure 117: Dependency of parameter lnK_α^N on inverse temperature for grain boundary $M_{23}C_6$ carbides in the ferrite matrix. The change in slope indicates a likely change in coarsening mechanism.

The change in slope clearly suggests that the rate-controlling mechanism for coarsening changes as the temperature is increased. It is also seen that the activation energy for the lower temperature range is significantly reduced. As the activation energy for grain-boundary diffusion is expected to be smaller than that of bulk diffusion, it is suspected that grain boundary diffusion is at least one of the major rate-controlling mechanism. That these carbides coarsen on the grain boundaries also supports such a conclusion in addition to the calculated coarsening constant.

PARAMETER	HIGH T	LOW T
K'_α	163.438	11.816
Q (KJ/MOLE FROM FIGURE 117)	139.7	30.3

In the literature activation energies for Cr diffusion between a $M_{23}C_6$ and a ferrite matrix are reported between 75 and 230 kJ/mole in duplex stainless steels where $M_{23}C_6$ carbides form and coarsen at the ferrite/austenite phase boundary. [115], [116] Thus, while the activation energies at higher temperatures are in the alignment with the literature, the reported values at low temperatures are considerably lower than previously reported. However, it should be noted that these previous studies of duplex steels are influenced by the austenite matrix, where Cr has an activation energy of as much as twice that for ferrite. It is also noted that the reported activation energies are significantly less than that of Fe self-diffusion in BCC iron of 251 kJ/mol. [117]

It is interesting to note that in the temperature range where the activation energy of coarsening is low, microstructurally the formation of a semi-continuous system of carbides is observed forming at the boundary. However, when the activation energy is elevated carbides become discontinuous along the boundary.

A plot of Ln(average carbide volume) vs. 1/T for both boundary and bulk carbides in HT#A that have been aged for 10,000 minutes at varied temperatures throughout the embrittlement and tempering regime is shown as **Figure 118**. For negative slopes coarsening dominates and for positive slopes dissolution dominates. When the slope approaches zero, nucleation of new carbides becomes dominant. Over the entire temperature range the slope for $M_{23}C_6$ carbides remains relatively consistent. The bulk carbides, that are predominantly M_7C_3 with a small percentage of $M_{23}C_6$, show three distinct regions. At low temperatures the slope is low and is consistent with

the apparent nucleation of new carbides in this temperature range. With slightly increased temperature the slope of Ln(carbide volume) vs 1/T changes significantly indicating a small temperature range for coarsening. Finally, at higher temperatures the slope changes direction indicating the onset of carbide dissolution.

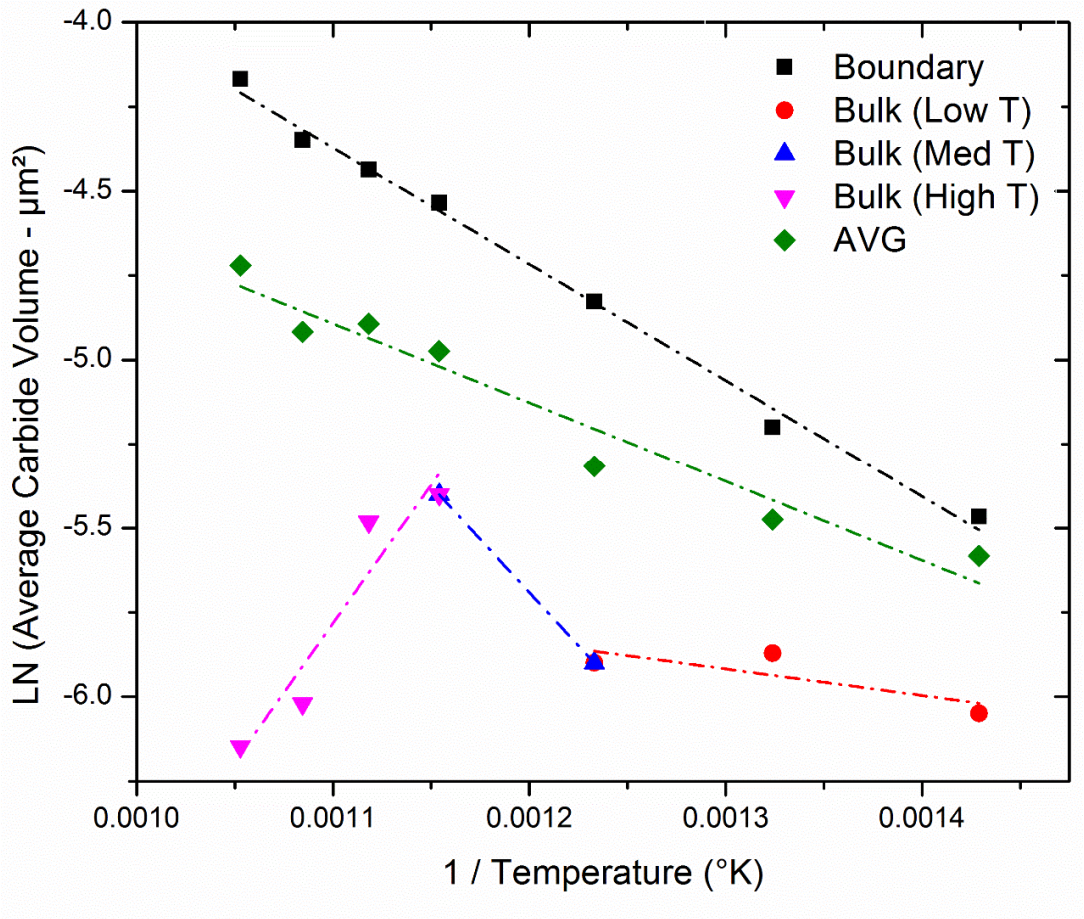

Figure 118: Plot of Ln(average carbide volume) vs 1/T for carbide aging after austenitization for 10,000 minutes. Results indicate a low barrier to nucleation of new bulk M_7C_3 carbides.

6.3.3 Carbide Dissolution Kinetics

In order to examine the kinetics of carbide dissolution one must consider the chromium diffusion in the surrounding matrix such that is has to be described in the same manner as the diffusional-controlled growth of particles, as chromium is the

diffusion limiting species in M_7C_3 carbides. [118] Using the approach of Sozykina *et. al*. based on the Zener [119], Hillert [120], and Wert and Zener [99], [121] models, the following treatment is used for the determination of dissolution activation energy:

The rate of interface propagation is defined as:

$$\frac{dr}{dt} = \frac{1}{r}\, D\, \frac{C^{m/c} - C_{\infty}^{m}}{C^{c} - C_{\infty}^{m}} \tag{57}$$

Where:
$C^{m/c}$ is the concentration of chromium at the carbide matrix interface
C^{c} is the concentration of chromium in the carbide particle
C_{∞}^{m} is the concentration of chromium in the matrix far from the particle
D is the diffusion coefficient of chromium
R is the radius of the half-width of the particle
t is time

During the dissolution process C will increase towards the equilibrium value C, while obeying the balance equation:

$$(1 - f_c)C_{\infty}^{m} + f_c C^{c} = C_0 \tag{58}$$

Where C_0 is the overall concentration of chromium in the alloy. Combining equation 76 and 77:

$$r dr = \frac{f_c - f_c^{eq}}{1 - f_c^{eq}} D dt \tag{59}$$

Where f_c and f_c^{eq} are the current and equilibrium volume fraction of carbide. On holding f_c will decrease from the initial f_c^{in} at time = 0 up to f at time = infinity.

For the case of small particles, such as the M_7C_3 carbides in question, then r in equation 78 is simply the average radius of the particles and the following simplification can be made:

$$f_c^{in} - f_c = \frac{1}{V}\frac{4\pi}{3} r^3 \tag{60}$$

Where V is the average volume of the alloy per one particle.

As a function of time and diffusivity the volume fraction may be found according to the Avrami equation:

$$f_c = f_c^{eq} + \left(f_c^{in} - f_c^{eq}\right) * \exp(-(\alpha D t)^n) \tag{61}$$

Taking the double logarithm of equation 80:

$$\ln\left\{-ln\left(\frac{f_c - f_c^{eq}}{f_c^{in} - f_c^{eq}}\right)\right\} = nln\alpha D + nlnt\ ;\ where\ \varphi = \frac{f_c - f_c^{eq}}{f_c^{in} - f_c^{eq}} \tag{62}$$

Such that a plot of experimental data plotted on a ln(-ln(1- φ)) vs ln t would lie on a straight line with a slope of n and an intercept of $nln(\alpha D)$. In order to find the activation energy equation 81 must be re-written and solved for a parameter z as follows:

$$z = 2\ln\left\{-ln\left(\frac{f_c - f_c^{eq}}{f_c^{in} - f_c^{eq}}\right)\right\} - ln\frac{f_c^{in\frac{4}{3}} * t}{\left(f_c^{in} - f_c^{eq}\right) * \left(1 - f_c^{eq}\right)} = ln2D_0\left(\frac{36\pi}{V}\right)^{\frac{2}{3}} - \frac{Q}{RT} \tag{63}$$

Given this solution z can be plotted against 1/T to solve for the activation energy of dissolution of the M_7C_3 carbide (via diffusion of Cr across the carbide/matrix interface) (**Figure 119**) as 296.3 +/- 24.8 kJ/mol. To derive this solution the in initial and current volume fractions are taken from experimental measurements after carbide image analysis and the equilibrium volume fraction is determined via Thermocalc CALPHAD (See Appendix C) results. This activation energy for Cr diffusion between M_7C_3 carbides and a ferrite matrix is in close agreement to that previously reported in the literature at 280 kJ/mol. [122]

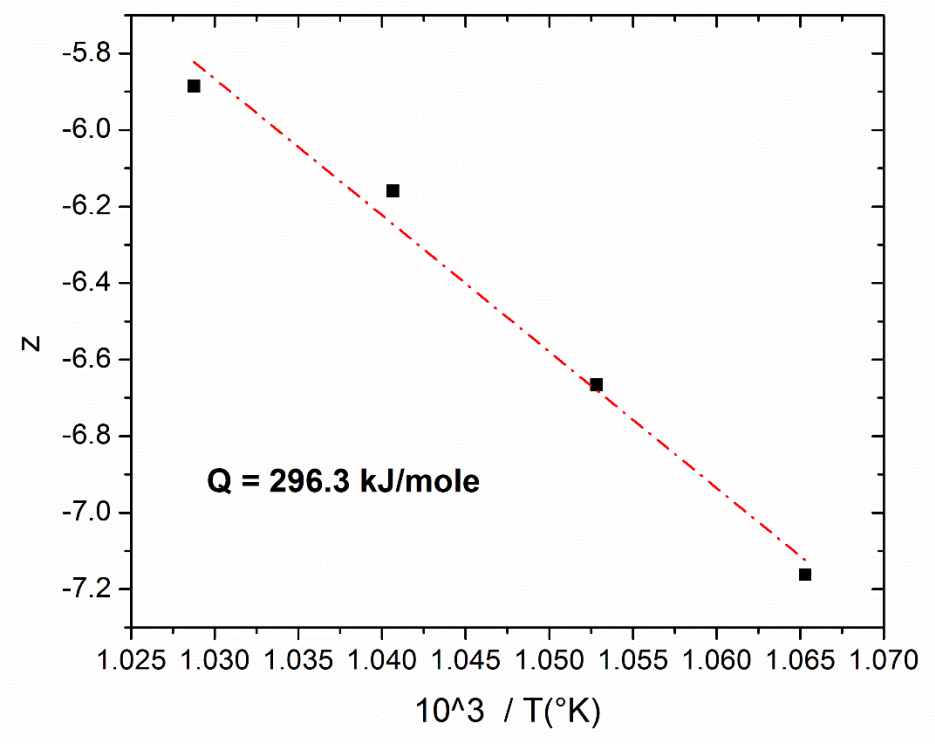

Figure 119: Activation energy calculation for dissolution

6.3.4 Precipitate Phase Identification

On the basis of the results presented in Chapter 5 two precipitate phases were identified as follows:

(1) Boundary $M_{23}C_6$ carbides identified based on CALPHAD analysis, morphology, location (at boundaries), dissolution temperature, EDS measured composition, and convergent beam diffraction patterns.

(2) Bulk M_7C_3 carbides identified based on CALPHAD analysis, morphology, location (in the bulk), dissolution temperature, and EDS measured composition.

However, a third precipitate phase with Mo was found with no clear identification, partially due to its low volume fraction.

Laves phases with Mo are primarily of the form Fe_2Mo with a hexagonal structure and a lattice parameters of a = 0.473nm and c = 0.772 nm [123]. The Mo phase identified in this study has extremely low levels of Fe and thus does not have the stoichiometric relationship that would be expected with such as phase. Thus, it is likely that this Mo rich phase is not a laves phase. Far more likely is that the Mo rich phase is an M_2C carbide or M_2X which has been shown to precipitate at 500°C in other steel systems with Mo contents that do not exceed 1wt. %, but only when these steels were overaged (as we done in this study) [124]. Both have a hexagonal close packed structure and commonly precipitate as fine needles parallel to $<100>_{\alpha}$. The composition in the literature varied widely with Mo, Cr, and V soluble in high quantities. When Cr contents are low (or locally low) M_2X is often close to the ideal Mo_2C composition (70wt% Mo). Other researchers have documented the ratio of metallic elements to be 0.91Mo : 0.06Mn : 0.02Fe in alloys not containing Cr.

Thus, the third precipitate phase is proposed to be:

(3) Boundary M_2C carbides identified based on morphology, and EDS measured composition (specifically the stoichiometric relationship).

Chapter 7: Conclusions and Future Work

7.1 Summary

This research addresses gaps in understanding of both hydrogen embrittlement and thermal embrittlement of high strength low alloy steels used in naval ship hulls and other demanding applications requiring high yield strength and impact toughness. In addition to work developing a new manufacturing treatment, an objective was to model the microstructural evolution and determine the interrelationship between the microstructure and resultant mechanical properties. Samples of HY-80 were manufactured at four different industrial manufacturers and thermally processed with a variety of experimentally designed heat treatments. A thorough set of mechanical and structural characterization was performed via Charpy and Tensile testing along with optical metallography, SEM, and TEM analysis. In summary, the work performed over the course of this project provides a clear, thorough approach for the characterization of this alloy system with regard to hydrogen and temper embrittlement over the entire range of temperatures used in industrial manufacture and several never previously reported. The results and analysis have provided definitions for new more cost-effective processing methodologies as well as valuable insights into the mechanisms governing the evolution of structure and the associated relationships with mechanical performance for the HY steel system during thermal treatments.

7.2 Research Contributions

Research contributions on the heat treatment and modeling of high yield low alloy steels include:

- Development of an understanding of the mechanisms of embrittlement between 300°C and 565°C and embrittlement recovery between 593°C and 704°C in the HY alloy system
- Development and validation of a new more cost-effective processes for the mitigation of monatomic hydrogen embrittlement in high yield low alloy steels, with applicability to a wide range of low alloy steels
- Development of a novel image analysis technique for the characterization of alloy carbides to enable the development of kinetic constants and the segregation of boundary and bulk carbide characteristics
- Determination of the effect on composition on the precipitation of carbides in the HY alloy system
- Determination of kinetic constants which assist with the prediction of the coarsening, nucleation, and dissolution rate of $M_{23}C_6$ and M_7C_3 carbides via CALPHAD techniques, and the resultant impact on mechanical response
- Development of a kinetic model for the required time for neutralization of monatomic hydrogen to concentrations low enough to preclude detrimental hydrogen damage that results in a reduction in tensile ductility

7.3 Conclusions

Over the course of this work the following key conclusions have been drawn from the results and analysis presented in detail in the preceding chapters.

General Conclusions on the HY Alloy System

- For the first time, it has been shown that both $M_{23}C_6$ and M_7C_3 carbides are present in the HY alloy system when carbon levels are sufficiently high. The volume fraction of M_7C_3 decreases to the point of no presence for carbon levels of 0.15 wt% and under.
- Also for the first time it is shown that the presence of these carbides correlate with embrittlement in the material as an additional contributor to the reduction in impact energy beyond the diffusion of embrittling constituents such as phosphorous.
- This work demonstrated that it is possible that heat made within the specification limits can generate an alloy with unusably high embrittlement rates that will fail specification requirements as measured by non-compliant Charpy mechanical response.
- It has been shown that a second austenitization followed by tempering results in increases of all mechanical response parameters including reduction of area, elongation, Charpy impact strength, yield strength, and ultimate strength; even for cases of extreme hydrogen charging.

On Hydrogen Aging

- Through rigorous experimentation it has been shown that hydrogen aging treatments can be used within the temper embrittlement range to significantly accelerate the diffusion of monatomic hydrogen from the lattice to trapping sites within the steel such that the detrimental effect on ductility due to hydrogen is mitigated. This newly developed treatment reduces the required time to perform a hydrogen age in heavy

section HY steel castings > 0.28m from 450 hours to less than 50 hours which can result in significant industrial cost savings.

- It is shown through mechanical testing that the diffusion of hydrogen is significantly influenced by the critical solubility limit of hydrogen with increasing influence as the aging temperature approaches the solubility limited temperature.
- It is demonstrated that the use of ductility measurements on tensile specimens, specifically the reduction of area, can be used as a good indicator of the level of monatomic diffusible hydrogen in the lattice of a steel alloy.
- It is shown that the starting concentration of hydrogen at the centerline of a thick cross section casting is increased such that the kinetically predicted critical diffusion times are not accurate without modifications to the baseline equations. A modification to the Arrhenius solution to Fick's second law has been proposed to account for this.
- Metallography results show that for alloy compositions where M_7C_3 carbides are not thermodynamically stable or only present in small concentrations, the final tempering operation is sufficient to mitigate the deleterious impacts of treatment in temper embrittlement regime.

On Temper Embrittlement and Recovery

- For the first time it is shown that embrittlement in HY-80 steels occur throughout the temperature range from 315°C to 565°C whereas Charpy V-notch impact energy (CVN) decreases at all temperatures across the embrittlement range with a peak embrittlement rate at 482°C.
- SEM fractography of Charpy impact specimens after embrittlement has shown a trans-granular cleavage rather than the historically anticipated intra-granular fracture,

indicating embrittlement is not primarily due to migration of embrittling constituents to grain boundaries.

- After embrittlement, a sub-critical anneal below the AC1 and above the embrittlement range increases the impact toughness of the alloy significantly, with a peak in recovery at 649°C up to and beyond the original control impact strength with adequate time. This recovery is attributed to both the dissolution of detrimental carbides such that they are both lower in volume fraction and no longer forming continuous or semi-continuous chains along grain boundaries. Furthermore, the diffusion of embrittling constituents away from the grain and carbide boundaries also contributes to the recovery from embrittlement.
- This work has shown that the mechanisms of embrittlement in the HY steel system are multifaceted including:
    - Diffusion of phosphorous and other embrittling constituents to grain boundaries and carbides via the energy reduction resulting from equilibrium and non-equilibrium segregation.
    - The nucleation of needle-shaped M_7C_3 carbides in the bulk at peak embrittlement temperatures creating initiation sites for crack propagation, as shown via the presence of cleavage fracture on the surface of embrittled Charpy impact specimens.
    - The morphology of $M_{23}C_6$ and M_7C_3 carbides along prior austenite grain and martensite lath boundaries creating a localized semi-continuous system, which when more continuous result in increased depression in the measured Charpy impact energy.

- The nucleation of carbide clusters both within the bulk and at grain and martensite lathe boundaries which serve as initiate sites for cleavage fracture.

- Furthermore, this work has shown that the mechanisms of embrittlement recovery in the HY steel system are similarly multifaceted and include:
  - The dissolution of M_7C_3 carbides, and carbide clusters (which serve as initiation sites for cleavage).
  - The coarsening of $M_{23}C_6$ carbides at prior austenite grain boundaries and martensite lathe boundaries such that the boundary area occupied by carbides is significantly reduced.
  - The segregation of phosphorous away from prior austenite grain boundaries and the interface between carbides and the matrix.

On Alloy carbides

- Kinetic coarsening constants calculated during this work indicate that the primary diffusion mechanisms for the constituents of alloy carbides in HY steel are dislocation and grain boundary based.
- Metallographic results show that M_7C_3 carbides nucleate along a limited number of preferential orientations within the bulk of the material. These are thought to create preferential pathways for trans-granular fracture when these carbides are surrounded by embrittling elements such as phosphorous.
- The measured dissolution temperatures in this study for alloy carbides match closely with those predicted by Thermocalc CALPHAD modeling, but require extended aging times in excess of those used for industrial scale heat treatments to realize the thermodynamically stable condition. This is also true for the AC1 temperature where

it is only apparent at extremely long aging times on the length scale of months that the AC1 falls within the traditional tempering temperature range.

- A Mo rich phase is shown to occur experimentally that is suspected to be an M_2C carbide at very small volume fractions after long time aging at 482°C. This phase is not predicted by CALPHAD modeling and may be associated with the incorrect assumption of homogenous elemental concentrations within the material that will not be the case in thick cross section castings due to segregation at the solidification front.

7.4 Future Suggestions

There are several challenges that need to be addressed in studying the HY alloys system and other similar alloys in further work. The following suggestions are provided for future experimental assays and for the further development of thermodynamic and kinetic models.

- The role of the M_7C_3 carbide is not completely understood for the HY alloy system, specifically the influence of the preferential alignment of carbides along specific planes within the bulk, and the resultant influence on mechanical response. Additional study is recommended that investigates the initiation sites for cleavage fracture to determine the influence of the M_7C_3 carbide, specifically whether the alignment of carbides influences the initiation and connection of cleavage embryos.
- During low temperature aging, a slight increase in impact strength was observed when embrittling constituents are of sufficiently low concentration. The mechanisms behind this increase in impact strength were not explicitly studied as part of this work. While it is proposed here-in that this increase is a result of carbide nucleation, it is recommended that compositions with increasing concentrations of vanadium be

studied, as thermodynamic work indicates the formation of a vanadium carbide may be responsible for this slight increase in impact strength despite the very low concentrations of vanadium present in the experimental heats used.

- The current work provides the embrittlement and recovery rate from both the effects of embrittling constituents and carbides. Future work should endeavor to determine the independent contribution of each embrittlement mechanism. It is proposed that this could be accomplished via use of a Gleeble or Macro-Rita system to heat a thin strip of initially embrittled material to the recovery temperature range for times less than 1 minute. It has been reported that over this time frame embrittling constituents will migrate away from the grain boundary; however, such a short treatment would not permit significant dissolution or evolution of carbides. In this manner mechanical testing could be performed on specimens that had the influence of alloy carbides on mechanical response isolated.
- Recent work has shown that neutron bombardment can be used to directly observe hydrogen atoms within a lattice. The use of these techniques could be employed to determine numerous aspects of hydrogen trapping including trapping site affinity, density, and type which could be used to further refine kinetic models for hydrogen diffusion.
- Results for dislocation-based studies indicate that dislocation motion may be capable of being used to transport hydrogen in a steel lattice. However, the techniques employed in this study were not able to mitigate hydrogen damage to a level needed in order to manufacture HY-80 with technically acceptable mechanical performance or to the degree of repeatability required (such that the results are not presented here-in).

Further fundamental study and validation is needed on this hydrogen transport phenomenon in order for it to be used as an industrial scale process or to understand its influence on hydrogen diffusion. It is recommended alternate dislocation motion inducing techniques be investigated by the characterization capabilities available for the study of hydrogen via neutron bombardment.

- The results of this work should be further validated over a range of chemical compositions and starting thermal histories to ensure the embrittlement mechanisms identified here-in are valid for all industrially used compositions, solidification rates, and pre-intentional thermal processing.
- The influence of solidification rate on the local composition (as a result of segregation between primary and secondary dendrites) is not specifically addressed in this work. Controlled experiments are recommended whereas the solidification rate is controlled via placing an induction heat coil around the solidifying material sample. In this manner the influence of the degree of local segregation on carbide nucleation, coarsening, and dissolution; and the associated impact on mechanical response, can be studied.
- Development of a temper embrittlement equivalency equation is recommended that determines the relative impact of each embrittling element, such that a new requirement can be created to limit the total quantity of embrittling elements.
- The image analysis technique developed by this study for the analysis of carbide parameters could be improved via the implementation of neural network and machine learning methodologies. Specifically, the challenges of properly identifying carbide parameters for treatments that exceeded the AC1, such that a mixture of un-tempered martensite is present, could be attacked via these enhanced methods. In addition, the

methodologies developed in this work could be further expanded to TEM image analysis.

- The detected Mo rich phase at the grain boundary after aging in the embrittlement regime, while strongly suspected to be and M_2C carbide, could not be definitively identified due to its small size and volume fraction. It is recommended that identification be attempted at a Synchrotron radiation source via x-ray diffraction such as the facility located at Argonne National Laboratory in Illinois. This would also serve to perform additional validation of the identified carbides from this study.
- While HY has served the industry well over the past decades, increasing demand for ever more complex articles of increasing thickness will drive the need for iterations of the composition of HY steel. It is therefore recommended that new alloy formulations be studied in future work using the results and techniques developed in this work as the foundation for further study. This work indicates that the use of increasing concentrations of Cr drives the formation of the apparently deleterious M_7C_3 carbides. It is therefore suggested that compositions be investigated that lower Cr content and replace it with increases in Mo, Ni, and/or V to compensate for the lost contributions to hardenability. In addition, further work to understand the inter-critical heat treatment regime is recommended for its ability to intentionally partition the composition such that different stable bulk phase compositions and associated alloy carbides could be designed to specifically occur in segregated regions of the microstructure.

- Finally, it is recommended that the new treatment developed here-in for accelerated hydrogen aging be validated with a full scale first article test per specification requirements, and if ultimately shown successful as predicted, that it be implemented in the casting industrial base with the associated savings passed on to the U.S. DoD and U.K. MoD.

Appendix A: Statistical Analysis

Each T/4 and T/2 trial had two replicates to enable both increased fidelity of the results and the ability remove an erroneous result from the data set. Removal of specimen from the data set was required on several occasions normally due to the excessive presence of porosity on the fracture surface of a tensile specimen. The replicates were averaged with empirically determined trends applied to engender a relationship between hours and reduction of area of a tensile specimen for a specific hydrogen removal treatment.

The standard deviation in many cases is not useful in a predictive model obtained from a linear type regression, as these regressions could be too varied to come to any reasonable forecast for reduction of area at that treatment's time. In a statistical regression analysis, the product is a function with predictive capability derived from the data, such that most data points should fall within the range of the predictive function plus or minus an error.

$$Data = f(x) \pm \varepsilon \tag{64}$$

Using the standard deviation as the "error," or ε, would not be suitable because the possible values for an extrapolated data point would be too far ranging to be practically useful. Therefore it was deemed necessary to create an error function that could replace the standard deviation and that could be used to extrapolate possible future points in conjunction with a regression function.

A.1.1 Modifications to the Error Function

The modification to the error function was needed to increase slowly with time since it would be used to estimate a reduction of area for an untested amount of time beyond

the upper limit of hours from the experimental data. Therefore, the function must account for all of these constraints, and should be producible using only the provided hours versus reduction of area data, so that a procedure for production of this function may be created. Along with the alternate error function, a method to quantitatively test it against the standard deviation was devised to provide sufficient evidence that it is generally superior for modeling purposes than the standard deviation. Equation 54 below and represents the modified error function as ε, the error term seen in Equation 53.

$$\varepsilon = b * \ln(x)\,; b = constant\,, x = time\ (hrs) \tag{65}$$

A logarithmic base function of time multiplied by a constant was selected to satisfy the increasing range of predicted reduction of area values with increasing time. This function increases slowly with increases in time due to the fact that the natural log of the hours spent in the furnace is taken. First, a linear trendline was fitted to the set of T/4 and T/2 reduction of area measurements. Then, an error value "E" was calculated by taking the absolute value of the real data point subtracted by the corresponding point on the line of best fit. Following that, b*ln(x) columns were made with b1 and b2 values equaling 1 as an initial guess for iterative solving to be used later. An Error of the Error, EOE term was created by subtracting E and b*ln(x) and squaring that value. These EOEs were then summed to make the Sum of the Error of the Error, SEOE.

$$\begin{gathered}\text{(T/4) } E1 = |data\ point - LOBF\ point| \\ \text{(T/2) } E2 = |data\ point - LOBF\ point|\end{gathered} \tag{66}$$

$$\begin{gathered}\text{(T/4) } New\ Error(T/4) = b1 * \ln(x) \\ \text{(T/2) } New\ Error\ (T/2) = b2 * \ln(x)\end{gathered} \tag{67}$$

$$\begin{gathered}\text{(T/4) } EOE1 = (E1 - b1\ln(x))^2 \\ \text{(T/2) } EOE2 = (E2 - b2\ln(x))^2\end{gathered} \tag{68}$$

$$\text{(T/4) } \sum_{i=1}^{n} EOE1_i \tag{69}$$

$$(T/2)\sum_{i=1}^{n} EOE2_i$$

The SEOE was used as the target parameter to minimize, and the b value was used as the variable cell (with an initial guess of 1). The Generalized Reduced Gradient non-linear solver algorithm was then used to fit a b value that best reduced the SEOE. This algorithm is an iterative process that uses derivatives and gradients to change variable cells so that the target cell (SEOE) is optimized (minimized in this case). Finding the b constant using this method is similar to the linear-least squares method of linear regression used universally.

A.1.2 Percent Deviations

The reduction of area data could not be separated into subsets based on control factors such as temperature and time because of the number of data points for each test condition. Different control factors resulted in numerous expected reduction of areas and average reduction of area results between replicates in sets of specimens. This meant that a different metric had to be used to describe and encompass all of the specimen sets, regardless of treatment or control factors. Therefore, averages and standard deviations were not accurate metrics to use. Instead, percent standard deviation was used since then only specimens in the same set were compared to each other; as opposed to standard deviation which would theoretically scale with the raw averages. Equation 28 shows the calculation necessary to derive the percent standard deviation that was used in this study.

$$\%\ Standard\ Deviation = \left[\frac{Standard\ Deviation\ of replicates}{Average\ of replicates}\right] = \left[\frac{(s)}{(\bar{x})}\right] = \frac{\left[\sqrt{\left(\frac{1}{n}\right) * \sum_{i=1}^{n}(x_i - \bar{x})^2}\right]}{\left[\frac{\sum_{i=1}^{n} x_i}{n}\right]} \quad (70)$$

Using the percent standard deviation allows for use of data from specimens of varying control factors, increasing the data pool available for simultaneous analysis. The data was separated into these categories because any trends specific to T/4 or T/2 samples would easily be seen, and generalizations could be made about the characteristics of T/4 and T/2 specimens. A filter to flag potential outlier specimens was made using analysis of the percent deviations found using Equation 28.

Based on these previous observations of the influence of porosity on tensile ductility it was deemed necessary to create a filter for tensile data collected as a part of this study to quickly determine whether or not a specimen failing the requirements for HY-80 required further examination, and whether it was valid for use in the development of models.

The result of this statistical analysis and subsequent fractography of suspect fracture surfaces was the removal of seven specimens from the data sets, all at the T/2 centerline depth. In each case it was found that these data points represented an outliner with loss of ductility due to localized porosity on the edge of a fracture surface, effectively resulting in a notched tensile specimen. At the onset of this work, the potential for the loss of ductility due to porosity was accounted for via the testing of two tensile specimens at each location and testing condition. In all cases but one, only one of the two tensile specimens was impacted by local porosity and the single tensile data point is used for graphing data trends and development of models throughout the rest of this work. The results of that analysis identifying the specimens for removal from models is detailed below.

A.2.1 Measuring Percent Deviations

The data was tested for normality so that statistically based conclusions could be made about these tensile ductility response.

Table 31: Percent Deviation Statistics

STATISTIC	T/4	T/2
AVERAGE	0.063875	0.173622
ST. DEV.	0.057307	0.189922

In **Table 31** the averages and standard deviations of the percent deviations for the entire T/4 and T/2 data sets is shown. The deviations for the T/2 depth are greater than those for T/4 as expected, likely associated with the great propensity for solidification voids at the centerline vs quarter line. Probability plots were created to test the data sets for normality and showed that the data was highly non-normal at each testing depth (Figure 28 Probability Plot of T/4 and Figure 29 Probability Plot of T/2). In order to use an effective metric for a filter, the data had to be transformed into a normal set. The Anderson Darling (AD) values for both were very high, and the P-Values were below the desired range of above 0.05. The histograms also did not follow a normal curve (**Figure 121**). Therefore, a transformation of the data was needed.

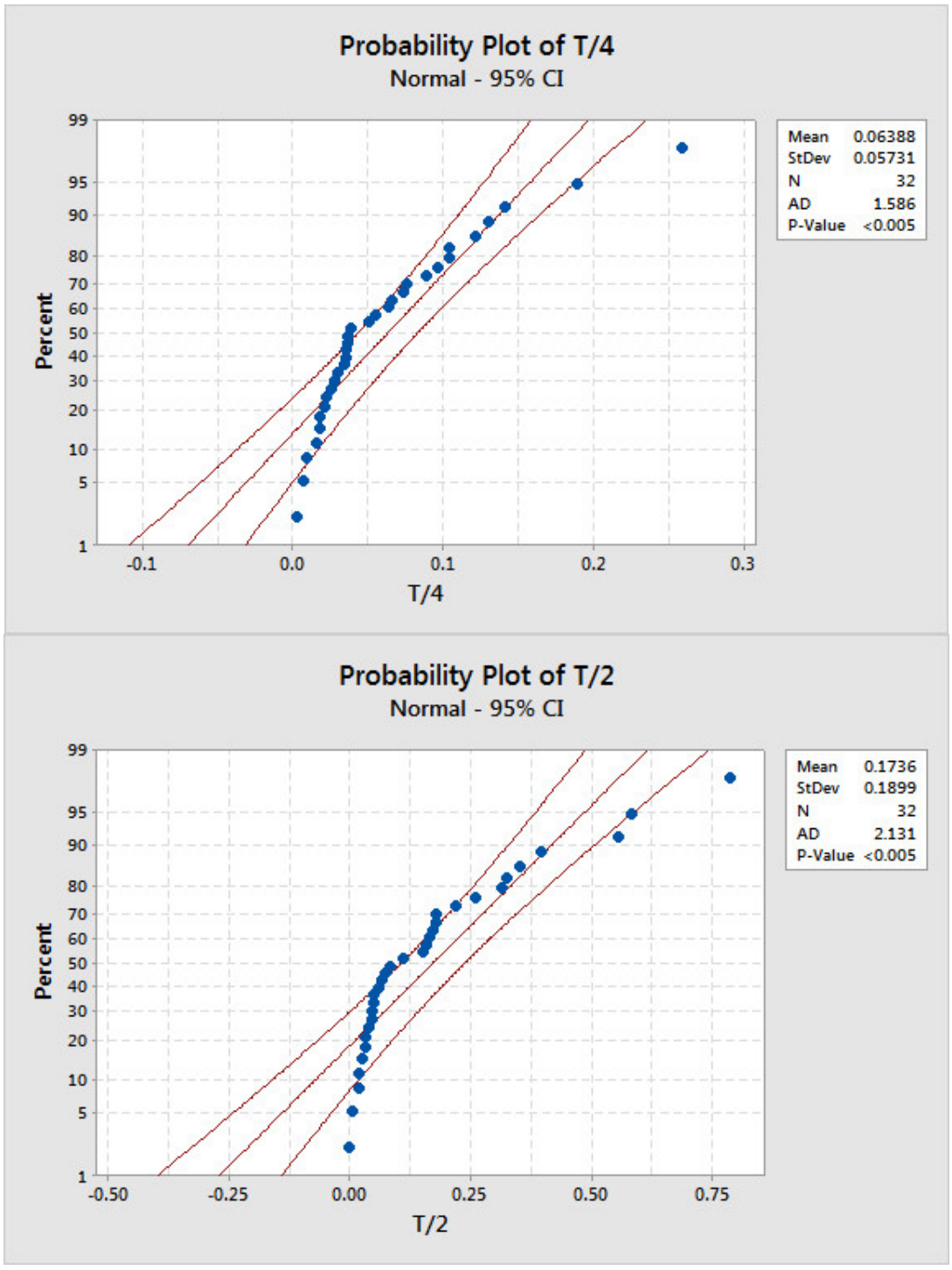

Figure 120: Probability Plot of T/4 and T/2 testing depths

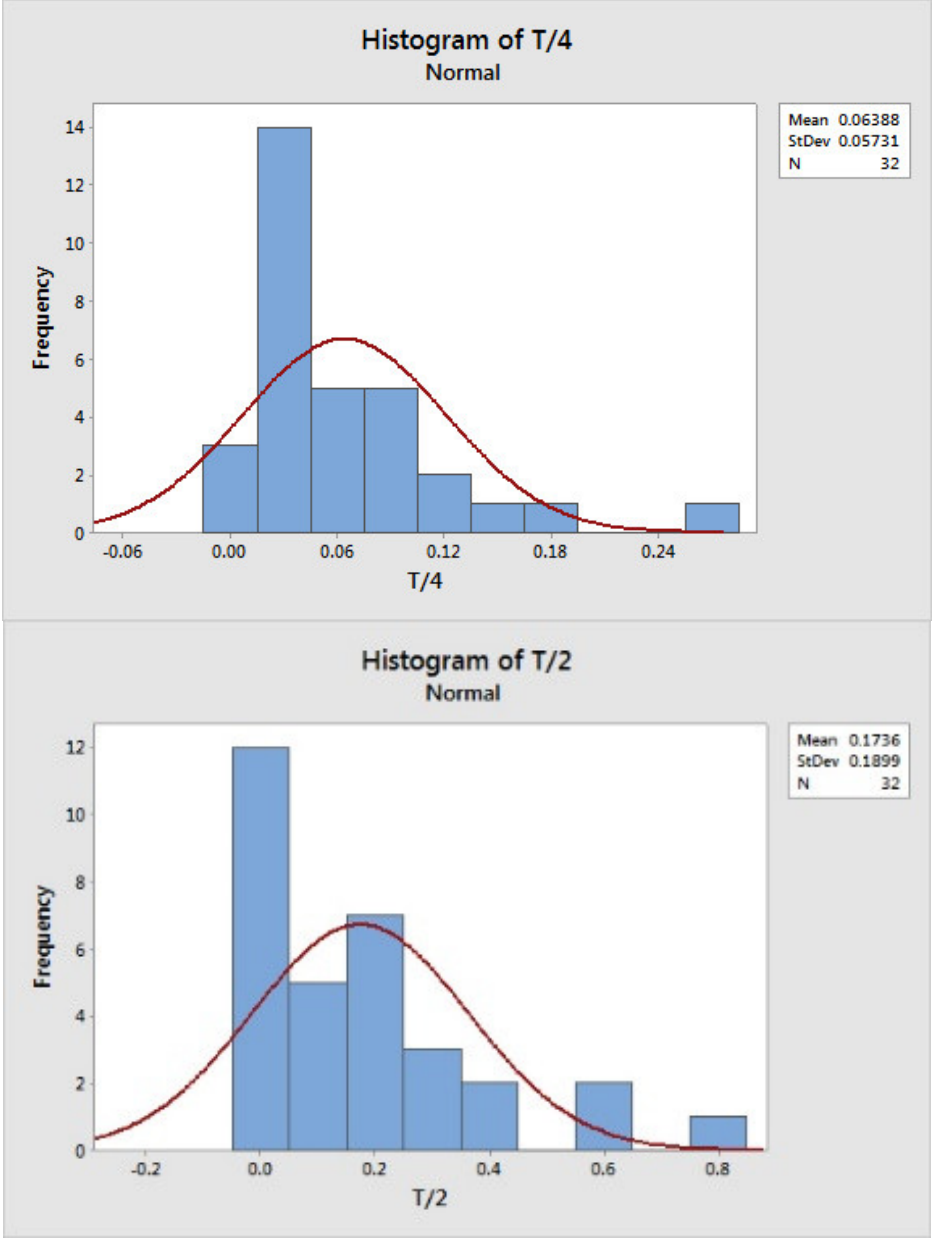

Figure 121: Histogram of T/4 and T/2 testing depths

Determining what type of distribution this data followed was crucial in finding a suitable transform. In order to resolve the correct distribution the data sets were fit to individual distributions and given Anderson-Darling and P-Values. Criteria for choosing a distribution or transform are a low Anderson-Darling value, and a P-Value above 0.05. In addition, both T/4 and T/2 data sets must have the same transform type or distribution, so

that the same processes discussed here-in can be applied to tensile samples extracted from all sizes of casting test blocks. Therefore, the AD values were targeted to be as low as possible, and the P value as high as possible so long as both criterion are met in both T/4 and T/2 sets of data. **Table 32** is provided to condense the information and clarify the results. The distribution highlighted in blue is the best distribution to describe the data. A blank cell means that the distribution was not tested for because it was deemed unnecessary, since a related distribution was a better fit. **Figure 122** and **Figure 123** show comparisons between the Johnson Transformation and other distributions for the T/4 and T/2 data respectively.

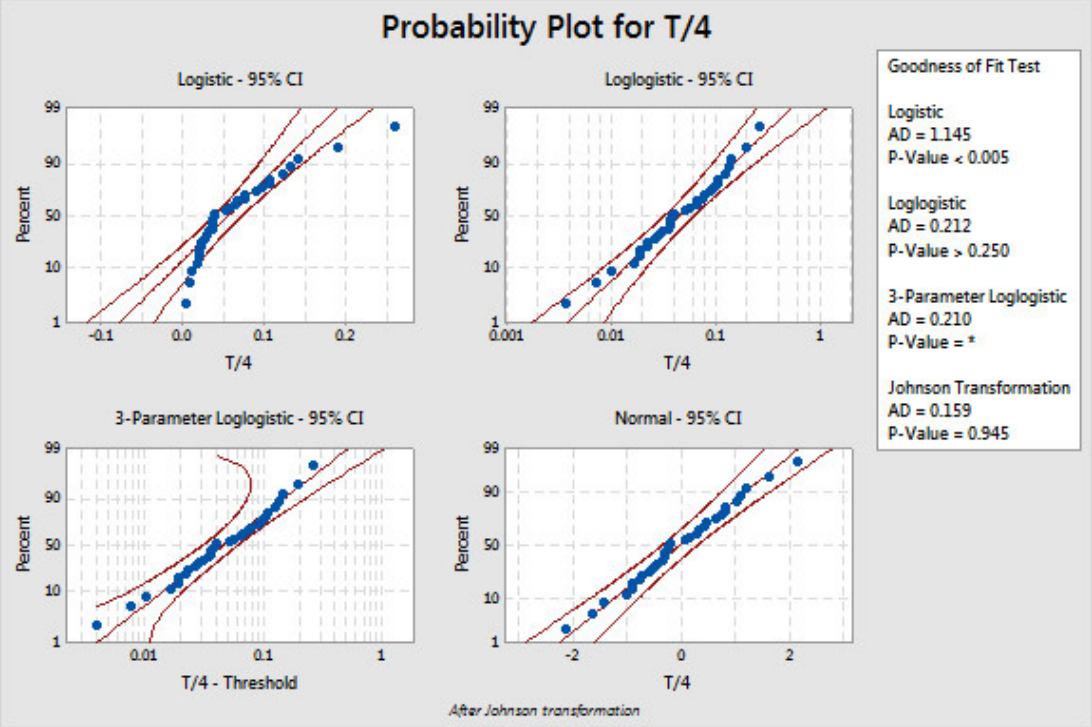

Figure 122: Probability Plots for T/4

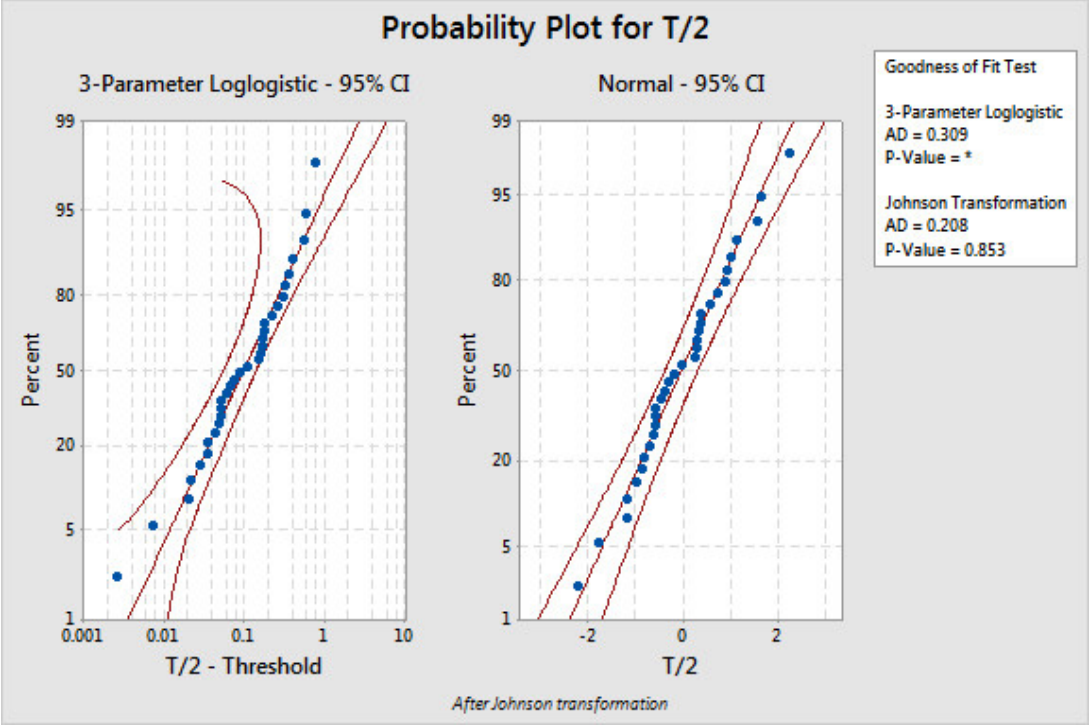

Figure 123: Probability Plots for T/2

Table 32: Individual Distribution Identification

DISTRIBUTION	T/4		T/2	
	AD	**P-Value**	**AD**	**P-Value**
NORMAL	1.586	<0.005	2.131	<0.005
3-PARAMETER LOGNORMAL	0.175	*	0.264	*
2-PARAMETER EXPONENTIAL	0.368	>0.250	0.363	>0.250
3-PARAMETER WEIBULL	0.264	>0.500	0.327	>0.500
SMALLEST EXTREME VALUE	2.95	<0.010	3.228	<0.010
LARGEST EXTREME VALUE	0.732	0.05	1.29	<0.010
3-PARAMETER GAMMA	0.234	>0.250	0.376	*
LOGISTIC	1.145	<0.005	1.621	<0.005
3-PARAMETER LOGLOGISTIC	0.21	*	0.309	*
JOHNSON TRANSFORMATION	0.159	0.945	0.208	0.853
BOX-COX TRANSFORMATION	0.221	0.817		
LOGNORMAL	0.221	0.817		
EXPONENTIAL	0.515	0.47		
WEIBULL	0.263	>0.250		
GAMMA	0.234	>0.250		
LOGLOGISTIC	0.212	>0.250		

A.2.2 Data Transformations

The Johnson Transformation was found to be the best fit for both T/4 and T/2 data sets with AD values of 0.159 and 0.208 respectively. The P-Values of 0.945 and 0.853 were concurrently the highest values for T/4 and T/2.

Johnson transforms exist as three types of curves: bounded, log-normal, and unbounded (Equations 71 - 74).

$$Bounded\ System\ (SB): y = \gamma + \eta * \ln\left[\frac{x - \varepsilon}{\lambda + \varepsilon - x}\right] \quad (71)$$

$$Log - noraml\ System\ (SL): y = \gamma + \eta * \ln\left[\frac{x - \varepsilon}{\lambda}\right] \quad (72)$$

$$Unbounded\ System\ (SU): y = \gamma + \eta * \mathrm{Sinh}^{-1}\left[\frac{x - \varepsilon}{\lambda}\right] \quad (73)$$

Where:

$$Sinh^{-1}(z) = \ln\left(z + \sqrt{(1 + z^2)}\right) \quad (74)$$

And:
y is the transformed value
γ is the shape 1 parameter
η is the shape 2 parameter
ε is the location parameter
λ is the scale parameter

Minitab and numerous other statistical software packages calculate the parameters and type of Johnson curve the same manner. The goal of the transformation is to turn a non-normal variable "x", the set of data from experimental studies, into a normal variable "z". The Minitab Johnson Transformation algorithm first considers almost all potential transformation functions from the Johnson system. Using the "Method of Percentiles" multiple z values are considered. The optimal z value is found using a grid search procedure with a z increment of smaller than 0.01, which achieves larger P-Values.

Minitab replaces the Shapiro-Wilk test with the Anderson-Darling test statistic (AD) to create uniformity within the individual distribution identification analysis; the other distributions are evaluated based on the AD value as well. The AD value is used to evaluate how well a set of data fits a certain distribution, and in this case how well the J1 and J2 sets fit a normal distribution. A low AD value is preferred and indicates higher conformation to the normal distribution. Minitab selects the transformation with the highest P-Value and provides the AD statistic alongside the chart produced from analysis of the transformation, producing a J1 and J2 representing the T/4 and T/2 testing locations respectively.

Figure 124 and **Figure 125** provide plots for the transformed data sets for each T/4 and T/2. The Z Value plot provides P Values as a function of Z values in order to find the optimal transformation. The probability plots from the original data are provided to compare with the probability plots for the transformed data. Both AD value and P-Values are much improved in the Probability Plots for Transformed Data. Minitab also provides the Johnson equations with the best-fit parameters. The best transformation type for T/4 and T/2 was a bounded system, or SB and the transformation functions are provided below as Equations 75 and 76.

The percent deviations are the input, “x”, and the output of Equations 33 and 34 are the transformed values, J1 and J2 respectively. J1 and J2 can then be analyzed as normal sets of data, however the characteristics obtained must be back-transformed into percent deviations. Normality allows for population spanning assumptions to be made, as well as for a probability density function. Basing a filter on means and standard deviations derived from untransformed, non-normal data would be error prone; therefore the filter should be

based on means and standard deviations derived from the transformed data. The transformed data was used to find a "true average" percent deviation, and any set of replicates that had a higher average percent deviation than the true average was flagged for inspection and physical examination.

$$\frac{T}{4}: J1 = 2.03045 + 0.936163 * \ln\left[\frac{x + 0.00219141}{0.495339 - x}\right] \quad (75)$$

$$\frac{T}{2}: \ J2 = 1.49753 + 0.719772 * \ln\left[\frac{x + 0.00583917}{1.06544 - x}\right] \quad (76)$$

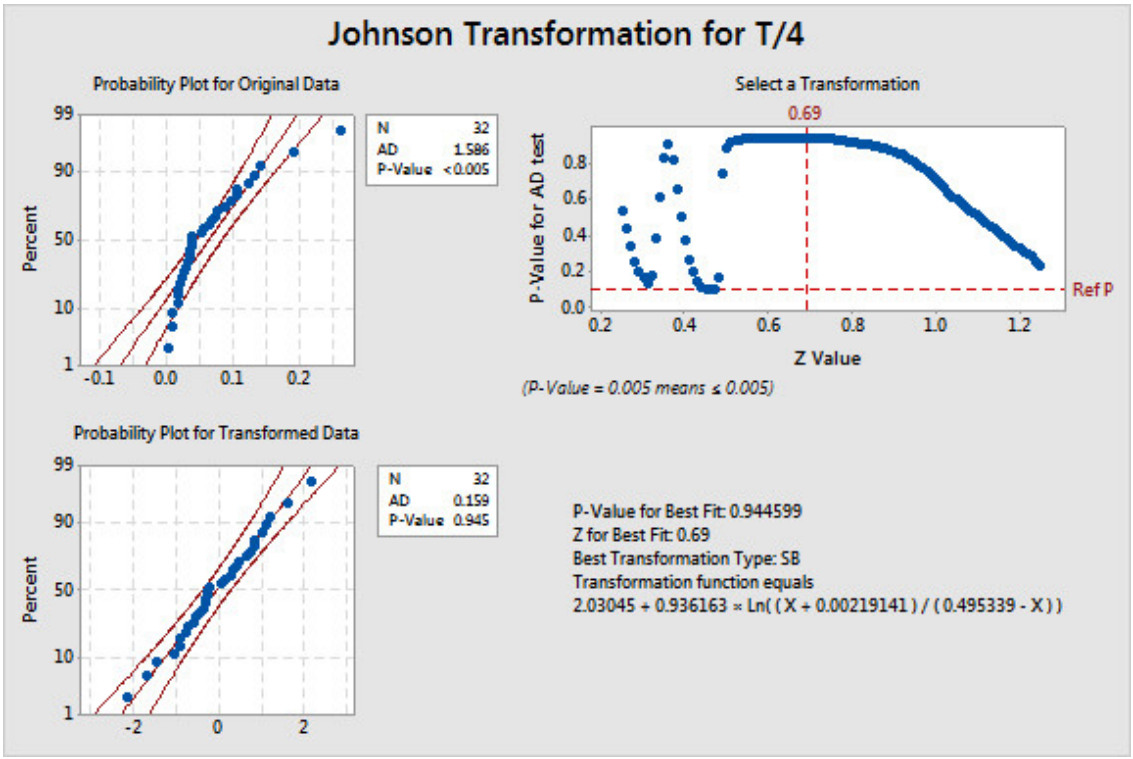

Figure 124: Johnson Transformation for T/4

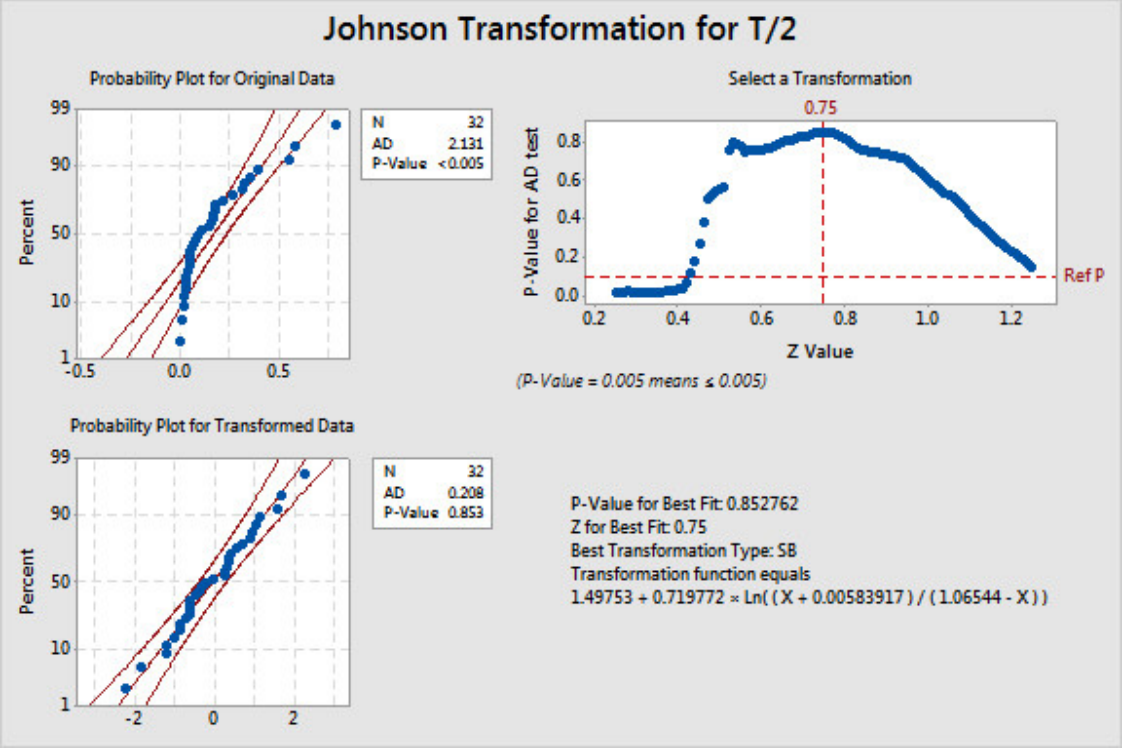

Figure 125: Johnson Transformation for T/2

A.2.3 The Probability Density Function

The average percent deviation was found using the Normal Distribution Probability Density Function (PDF) as opposed to simply taking the average of the transformed values and back-transforming to get that value in percent deviation. The ability to tabulate and plot J1, J2, and the probability density as a function of incremental percent deviation was the key factor in this decision. Percent deviations were incremented by 0.01 from 0 to 1. These values were transformed using Equations 16 and 17 to produce values for J1 and J2. Using J1 and J2, the probability density function values were calculated.

The maximum value found in the P(J1) and P(J2) columns correspond to the maxima. The maximum of a normal distribution's PDF lies on the mean of the population being studied. It is interesting to note that the peak of the T/2 graph is much wider than

the peak of the T/4 graph, indicating there is a higher probability of having a large range of percent deviations. Because the process was tabulated, the maxima of the Probability Density Functions can easily be linked to the percent deviation; the tables and graphs provided allow for ease of use.

The integral of the PDF between two deviations equals the probability that a sample will fall within the range of those deviations, as shown in Equation 35. Hence the area under the curve of an entire PDF is equal to 1, which is the sum of all probabilities possible. In this case, it must be kept in mind that the input variable for the density function is going to be the transformed variable, not the percent deviations themselves. The integral of the PDF was not used here, since all that was required was the maximum of the PDF curve as a function of the percent deviation.

$$Probability\ \ X\ takes\ a\ value\ in\ interval\ [a,b] = P(a \leq X \leq b) = \int_a^b f(x)dx \tag{77}$$

Where:
J = J1 or J2
μ = J1 or J2 mean
σ = J1 or J2 standard deviation

$$Normal\ Distribution\ PDF = f(J) = \left(\frac{1}{\sigma\sqrt{2\pi}}\right) e^{-\frac{(J-\mu)^2}{2\sigma^2}} \tag{78}$$

The percent deviation coordinate of the maximum is the true average percent deviation of the data set. For T/4 this value was 0.04, and for T/2 this value was 0.11. If a set of replicates had a higher average percent deviation than the true averages, the set was flagged. Inside the set, steel tensile samples that had reduction of areas below the average of the set were identified for further analysis.

Upon physical examination, a sub-set of the filtered samples had small notches adjacent to the breakage interface where the samples were broken apart. These notches could have been responsible for atypically low reduction of area results, and were random manufacturing defects. Samples that were filtered and had these notches were regarded as true outliers and removed from the data for the purposes of developing predictive models for hydrogen aging.

Appendix B: Chemical Composition Results

HT#	ID	C	SI	NI	CR	MO	MN	CO	W	V	NB	P	S	CU	AL	TI	CA	SN	ZR	FE
C	1-T2	0.137	0.309	2.96	1.414	0.588	0.644	0.0041	0.0058	0.0057	0.0138	0.0098	0.0028	0.0075	0.0187	0.0059	0.0065	0.0022	0.0486	93.80
C	1-T4	0.147	0.310	2.95	1.407	0.598	0.648	0.0041	0.0061	0.0051	0.0142	0.0096	0.0023	0.0079	0.0190	0.0064	0.0053	0.0005	0.0497	93.80
C	2-T2	0.140	0.309	2.96	1.398	0.583	0.635	0.0027	0.0060	0.0050	0.0142	0.0101	0.0031	0.0071	0.0190	0.0059	0.0091	0.0000	0.0444	93.80
C	2-T4	0.139	0.306	2.95	1.404	0.609	0.638	0.0018	0.0063	0.0052	0.0126	0.0094	0.0034	0.0076	0.0189	0.0064	0.0075	0.0000	0.0488	93.80
C	3-T2	0.132	0.293	2.83	1.372	0.576	0.648	0.0020	0.0069	0.0050	0.0125	0.0090	0.0033	0.0071	0.0194	0.0063	0.0061	0.0000	0.0435	94.00
C	3-T4	0.139	0.302	2.91	1.388	0.582	0.629	0.0006	0.0028	0.0054	0.0136	0.0088	0.0043	0.0083	0.0195	0.0051	0.0120	0.0000	0.0531	93.90
C	4-T2	0.143	0.302	2.95	1.403	0.617	0.622	0.0027	0.0085	0.0052	0.0123	0.0097	0.0042	0.0076	0.0209	0.0066	0.0089	0.0149	0.0477	93.80
C	4-T4	0.147	0.310	2.96	1.414	0.620	0.645	0.0028	0.0070	0.0058	0.0128	0.0100	0.0025	0.0081	0.0188	0.0067	0.0040	0.0000	0.0440	93.80
C	5-T2	0.141	0.315	2.98	1.422	0.633	0.652	0.0035	0.0081	0.0053	0.0141	0.0107	0.0029	0.0080	0.0193	0.0066	0.0062	0.0000	0.0451	93.70
C	5-T4	0.142	0.312	2.96	1.409	0.598	0.646	0.0022	0.0068	0.0059	0.0133	0.0104	0.0027	0.0081	0.0195	0.0067	0.0048	0.0007	0.0441	93.80
C	6-T2	0.137	0.302	2.86	1.398	0.599	0.621	0.0026	0.0100	0.0052	0.0132	0.0094	0.0063	0.0075	0.0189	0.0059	0.0172	0.0000	0.0463	93.90
C	6-T4	0.146	0.313	2.97	1.416	0.632	0.643	0.0029	0.0070	0.0058	0.0133	0.0118	0.0032	0.0071	0.0190	0.0068	0.0038	0.0008	0.0455	93.70
C	7-T2	0.137	0.302	2.88	1.382	0.573	0.613	0.0033	0.0075	0.0055	0.0131	0.0084	0.0043	0.0077	0.0188	0.0064	0.0128	0.0000	0.0445	94.00
C	7-T4	0.144	0.307	2.95	1.400	0.589	0.638	0.0021	0.0015	0.0047	0.0137	0.0086	0.0027	0.0080	0.0188	0.0064	0.0057	0.0008	0.0509	93.80
C	8-T2	0.140	0.318	2.94	1.421	0.604	0.664	0.0025	0.0053	0.0055	0.0145	0.0107	0.0028	0.0079	0.0199	0.0059	0.0048	0.0017	0.0517	93.80
C	8-T4	0.144	0.308	2.87	1.414	0.619	0.646	0.0032	0.0061	0.0052	0.0139	0.0100	0.0040	0.0076	0.0185	0.0075	0.0085	0.0099	0.0556	93.80
D	R1	0.182	0.419	2.92	1.389	0.387	0.646	0.0033	0.0038	0.0059	0.0109	0.0046	0.0020	0.1040	0.0126	0.0075	0.0013	0.0232	0.0360	93.90
D	R2	0.189	0.411	2.99	1.396	0.379	0.677	0.0014	0.0023	0.0060	0.0099	0.0047	0.0018	0.1040	0.0102	0.0065	0.0003	0.0216	0.0368	93.90
D	R3	0.185	0.412	2.97	1.382	0.368	0.663	0.0027	0.0033	0.0060	0.0098	0.0043	0.0020	0.1030	0.0114	0.0062	0.0008	0.0156	0.0368	94.00
D	R4	0.185	0.415	2.96	1.396	0.372	0.676	0.0038	0.0045	0.0061	0.0105	0.0047	0.0015	0.1050	0.0107	0.0068	0.0003	0.0196	0.0380	93.90
D	R5	0.179	0.405	2.94	1.346	0.359	0.685	0.0022	0.0038	0.0052	0.0105	0.0041	0.0013	0.1010	0.0114	0.0061	0.0005	0.0189	0.0378	94.00

HT#	ID	C	SI	NI	CR	MO	MN	CO	W	V	NB	P	S	CU	AL	TI	CA	SN	ZR	FE
D	R6	0.175	0.417	3.03	1.364	0.384	0.657	0.0019	0.0016	0.0050	0.0098	0.0048	0.0022	0.1020	0.0103	0.0065	0.0003	0.0188	0.0381	93.90
D	R7	0.176	0.415	2.93	1.389	0.379	0.672	0.0039	0.0064	0.0060	0.0107	0.0048	0.0019	0.1030	0.0109	0.0065	0.0007	0.0195	0.0375	94.00
D	R8	0.176	0.416	3.03	1.366	0.381	0.646	0.0035	0.0003	0.0052	0.0100	0.0042	0.0009	0.1040	0.0108	0.0065	0.0004	0.0209	0.0388	93.90
D	R9	0.170	0.403	2.91	1.350	0.365	0.656	0.0020	0.0016	0.0046	0.0105	0.0038	0.0015	0.0995	0.0110	0.0062	0.0005	0.0196	0.0407	94.10
D	R10	0.183	0.411	2.96	1.388	0.382	0.676	0.0038	0.0036	0.0057	0.0112	0.0042	0.0017	0.1040	0.0106	0.0059	0.0004	0.0213	0.0393	93.90
D	R11	0.172	0.413	2.95	1.375	0.377	0.628	0.0038	0.0030	0.0051	0.0105	0.0046	0.0017	0.1020	0.0105	0.0070	0.0004	0.0166	0.0408	94.00
D	R12	0.171	0.405	2.92	1.386	0.376	0.666	0.0040	0.0070	0.0063	0.0118	0.0043	0.0013	0.1020	0.0106	0.0066	0.0004	0.0187	0.0351	94.00
D	R13	0.175	0.410	2.91	1.389	0.367	0.659	0.0019	0.0061	0.0059	0.0109	0.0039	0.0019	0.1010	0.0101	0.0071	0.0003	0.0167	0.0345	94.10
D	R14	0.188	0.420	3.09	1.372	0.360	0.653	0.0003	0.0010	0.0062	0.0093	0.0041	0.0015	0.1030	0.0105	0.0063	0.0002	0.0119	0.0330	93.90
D	R15	0.172	0.414	2.90	1.379	0.363	0.658	0.0028	0.0070	0.0061	0.0105	0.0045	0.0018	0.1020	0.0112	0.0070	0.0006	0.0143	0.0335	94.10
D	R16	0.188	0.415	3.02	1.359	0.362	0.657	0.0003	0.0026	0.0049	0.0089	0.0044	0.0012	0.1020	0.0105	0.0071	0.0005	0.0159	0.0367	93.90
D	R17	0.169	0.409	2.87	1.373	0.359	0.649	0.0019	0.0075	0.0058	0.0109	0.0043	0.0015	0.0984	0.0103	0.0071	0.0003	0.0202	0.0338	94.10
D	R18	0.180	0.418	3.02	1.379	0.381	0.671	0.0011	0.0035	0.0054	0.0097	0.0040	0.0020	0.1030	0.0111	0.0073	0.0002	0.0161	0.0371	93.90
D	R19	0.179	0.416	3.00	1.364	0.375	0.665	0.0011	0.0066	0.0054	0.0091	0.0050	0.0017	0.1000	0.0102	0.0067	0.0003	0.0162	0.0337	93.90
D	R20	0.184	0.420	2.95	1.404	0.385	0.680	0.0019	0.0078	0.0059	0.0111	0.0047	0.0014	0.1020	0.0096	0.0069	0.0002	0.0182	0.0358	93.90
D	R21	0.179	0.417	2.97	1.399	0.368	0.676	0.0023	0.0069	0.0065	0.0107	0.0041	0.0016	0.1030	0.0103	0.0063	0.0004	0.0180	0.0314	93.90
D	R22	0.186	0.411	2.95	1.393	0.373	0.677	0.0013	0.0033	0.0059	0.0103	0.0046	0.0019	0.1020	0.0102	0.0075	0.0003	0.0174	0.0369	94.00
D	R23	0.172	0.412	2.90	1.395	0.368	0.661	0.0020	0.0087	0.0060	0.0107	0.0045	0.0015	0.1010	0.0113	0.0070	0.0006	0.0201	0.0330	94.00
D	R24	0.175	0.421	3.01	1.371	0.379	0.669	0.0003	0.0026	0.0049	0.0096	0.0051	0.0017	0.1020	0.0102	0.0069	0.0005	0.0152	0.0356	93.90
D	R25	0.174	0.411	2.89	1.395	0.382	0.664	0.0024	0.0088	0.0058	0.0108	0.0046	0.0023	0.1010	0.0106	0.0071	0.0005	0.0214	0.0357	94.00
D	R26	0.182	0.418	3.03	1.356	0.374	0.655	0.0000	0.0012	0.0042	0.0094	0.0047	0.0017	0.1010	0.0106	0.0070	0.0005	0.0180	0.0333	93.90
D	R27	0.188	0.417	2.96	1.405	0.380	0.681	0.0008	0.0044	0.0057	0.0102	0.0051	0.0023	0.1020	0.0103	0.0071	0.0004	0.0183	0.0358	93.90
D	R28	0.189	0.429	3.06	1.420	0.403	0.700	0.0018	0.0047	0.0060	0.0101	0.0057	0.0016	0.1060	0.0098	0.0062	0.0002	0.0187	0.0313	93.70
D	R29	0.176	0.407	2.99	1.340	0.359	0.652	0.0007	0.0034	0.0059	0.0092	0.0042	0.0009	0.0991	0.0111	0.0062	0.0005	0.0152	0.0296	94.00
D	R30	0.182	0.411	2.97	1.399	0.383	0.665	0.0030	0.0074	0.0060	0.0101	0.0048	0.0018	0.1030	0.0102	0.0070	0.0005	0.0180	0.0298	93.90

HT#	ID	C	SI	NI	CR	MO	MN	CO	W	V	NB	P	S	CU	AL	TI	CA	SN	ZR	FE
A	17B	0.169	0.331	2.86	1.338	0.377	0.670	0.0050	0.0094	0.0059	0.0115	0.0039	0.0012	0.0888	0.0103	0.0056	0.0004	0.0116	0.0437	94.20
A	17D	0.158	0.330	2.85	1.317	0.378	0.710	0.0056	0.0074	0.0057	0.0109	0.0034	0.0023	0.0870	0.0104	0.0057	0.0003	0.0104	0.0395	94.20
A	21A	0.181	0.375	2.88	1.319	0.387	0.714	0.0198	0.0064	0.0065	0.0119	0.0040	0.0021	0.0233	0.0064	0.0069	0.0004	0.0085	0.0438	94.20
A	21C	0.189	0.390	3.03	1.269	0.427	0.657	0.0189	0.0049	0.0069	0.0123	0.0054	0.0026	0.0249	0.0046	0.0076	0.0002	0.0019	0.0384	93.90
A	22C	0.187	0.394	2.95	1.340	0.404	0.691	0.0198	0.0087	0.0068	0.0130	0.0042	0.0022	0.0246	0.0057	0.0069	0.0003	0.0058	0.0405	94.00
A	22TA	0.182	0.379	2.88	1.333	0.409	0.681	0.0211	0.0058	0.0064	0.0131	0.0043	0.0020	0.0236	0.0073	0.0070	0.0004	0.0080	0.0430	94.10
A	231A	0.181	0.382	2.89	1.323	0.391	0.680	0.0196	0.0088	0.0066	0.0119	0.0050	0.0028	0.0233	0.0083	0.0073	0.0008	0.0085	0.0423	94.20
A	231C	0.185	0.388	2.90	1.326	0.413	0.626	0.0195	0.0059	0.0060	0.0116	0.0044	0.0022	0.0240	0.0066	0.0064	0.0004	0.0105	0.0399	94.10
A	232A	0.179	0.389	2.96	1.244	0.418	0.632	0.0198	0.0085	0.0066	0.0123	0.0047	0.0024	0.0240	0.0051	0.0069	0.0002	0.0028	0.0424	94.00
A	232C	0.186	0.385	2.93	1.246	0.419	0.649	0.0199	0.0054	0.0065	0.0125	0.0047	0.0027	0.0239	0.0058	0.0064	0.0003	0.0029	0.0453	94.00
A	233A	0.186	0.396	2.98	1.341	0.427	0.645	0.0213	0.0067	0.0068	0.0123	0.0046	0.0027	0.0242	0.0126	0.0072	0.0009	0.0116	0.0423	93.90
A	233C	0.187	0.385	2.94	1.246	0.407	0.641	0.0197	0.0064	0.0067	0.0128	0.0048	0.0026	0.0236	0.0079	0.0065	0.0005	0.0025	0.0424	94.00
A	234A	0.180	0.384	2.93	1.325	0.411	0.623	0.0209	0.0092	0.0067	0.0114	0.0045	0.0028	0.0234	0.0078	0.0070	0.0005	0.0062	0.0399	94.10
A	234C	0.183	0.397	2.93	1.251	0.414	0.647	0.0188	0.0061	0.0065	0.0125	0.0045	0.0023	0.0242	0.0074	0.0068	0.0004	0.0047	0.0429	94.00
A	235A	0.183	0.383	2.92	1.303	0.395	0.650	0.0196	0.0019	0.0063	0.0134	0.0043	0.0026	0.0240	0.0056	0.0072	0.0003	0.0069	0.0418	94.10
A	235C	0.186	0.389	2.96	1.243	0.401	0.639	0.0209	0.0062	0.0067	0.0126	0.0049	0.0020	0.0241	0.0056	0.0069	0.0002	0.0037	0.0440	94.00
A	236A	0.184	0.383	2.90	1.332	0.417	0.630	0.0206	0.0041	0.0063	0.0125	0.0050	0.0035	0.0241	0.0075	0.0076	0.0005	0.0097	0.0413	94.10
A	236C	0.189	0.389	3.00	1.260	0.411	0.649	0.0196	0.0024	0.0069	0.0128	0.0055	0.0022	0.0248	0.0058	0.0070	0.0003	0.0055	0.0416	93.90
A	241A	0.184	0.384	2.95	1.256	0.394	0.680	0.0189	0.0022	0.0059	0.0121	0.0039	0.0023	0.0233	0.0096	0.0061	0.0007	0.0085	0.0397	94.10
A	241C	0.189	0.388	2.96	1.325	0.415	0.623	0.0197	0.0092	0.0067	0.0117	0.0051	0.0027	0.0231	0.0061	0.0069	0.0004	0.0088	0.0410	94.00
A	242A	0.185	0.384	2.93	1.318	0.400	0.673	0.0187	0.0060	0.0061	0.0115	0.0044	0.0022	0.0251	0.0117	0.0065	0.0008	0.0049	0.0421	94.10
A	242A	0.182	0.390	2.93	1.335	0.415	0.653	0.0215	0.0073	0.0072	0.0127	0.0049	0.0022	0.0240	0.0079	0.0070	0.0005	0.0045	0.0427	94.00
A	242C	0.190	0.398	3.05	1.265	0.442	0.653	0.0196	0.0056	0.0068	0.0121	0.0048	0.0028	0.0241	0.0061	0.0076	0.0003	0.0088	0.0426	93.80
A	243A	0.186	0.404	3.00	1.344	0.417	0.637	0.0200	0.0006	0.0070	0.0123	0.0048	0.0025	0.0235	0.0087	0.0070	0.0006	0.0131	0.0373	93.90

HT#	ID	C	SI	NI	CR	MO	MN	CO	W	V	NB	P	S	CU	AL	TI	CA	SN	ZR	FE
A	243C	0.189	0.392	3.00	1.334	0.405	0.683	0.0184	0.0050	0.0066	0.0115	0.0045	0.0019	0.0238	0.0058	0.0067	0.0003	0.0079	0.0394	94.00
A	251A	0.183	0.384	2.90	1.245	0.404	0.635	0.0204	0.0085	0.0063	0.0123	0.0043	0.0028	0.0235	0.0070	0.0069	0.0006	0.0070	0.0416	94.10
A	251C	0.182	0.377	2.88	1.281	0.378	0.668	0.0187	0.0054	0.0062	0.0116	0.0040	0.0030	0.0225	0.0070	0.0067	0.0004	0.0040	0.0441	94.20
A	252A	0.183	0.389	2.95	1.250	0.416	0.644	0.0192	0.0072	0.0069	0.0125	0.0046	0.0024	0.0242	0.0064	0.0075	0.0004	0.0055	0.0393	94.00
A	252C	0.186	0.387	2.90	1.230	0.406	0.620	0.0183	0.0079	0.0064	0.0112	0.0040	0.0022	0.0231	0.0065	0.0068	0.0004	0.0027	0.0389	94.10
A	253A	0.185	0.384	2.95	1.234	0.386	0.629	0.0186	0.0052	0.0066	0.0118	0.0043	0.0023	0.0230	0.0072	0.0063	0.0004	0.0038	0.0441	94.10
A	253A	0.164	0.377	2.93	1.341	0.310	0.670	0.0039	0.0037	0.0054	0.0113	0.0035	0.0014	0.1580	0.0081	0.0064	0.0012	0.0136	0.0372	94.10
A	253C	0.185	0.388	2.92	1.233	0.385	0.646	0.0187	0.0026	0.0065	0.0120	0.0042	0.0022	0.0230	0.0057	0.0068	0.0003	0.0038	0.0441	94.10
A	253D	0.154	0.376	2.88	1.235	0.312	0.671	0.0051	0.0061	0.0050	0.0115	0.0036	0.0018	0.1590	0.0097	0.0063	0.0018	0.0086	0.0385	94.20
A	254A	0.183	0.386	2.92	1.334	0.406	0.726	0.0189	0.0012	0.0071	0.0126	0.0049	0.0030	0.0237	0.0088	0.0071	0.0008	0.0106	0.0390	94.10
A	254C	0.185	0.383	2.93	1.238	0.413	0.677	0.0201	0.0061	0.0063	0.0127	0.0046	0.0026	0.0236	0.0062	0.0064	0.0003	0.0048	0.0443	94.00
A	255A	0.183	0.397	3.03	1.319	0.433	0.651	0.0209	0.0074	0.0070	0.0119	0.0049	0.0028	0.0238	0.0061	0.0066	0.0004	0.0157	0.0422	93.90
A	255A	0.171	0.331	2.93	1.322	0.546	0.634	0.0027	0.0041	0.0053	0.0107	0.0047	0.0022	0.1190	0.0107	0.0065	0.0000	0.0143	0.0354	93.90
A	255C	0.188	0.401	3.05	1.258	0.426	0.659	0.0188	0.0073	0.0067	0.0128	0.0047	0.0018	0.0250	0.0048	0.0074	0.0003	0.0088	0.0432	93.80
A	255C	0.169	0.327	2.89	1.316	0.535	0.632	0.0025	0.0037	0.0047	0.0110	0.0038	0.0022	0.1170	0.0111	0.0063	0.0000	0.0124	0.0382	94.00
A	256A	0.187	0.382	2.89	1.218	0.392	0.677	0.0187	0.0073	0.0064	0.0117	0.0043	0.0023	0.0237	0.0106	0.0067	0.0006	0.0055	0.0488	94.10
A	256C	0.181	0.392	2.90	1.296	0.407	0.632	0.0191	0.0072	0.0062	0.0119	0.0048	0.0025	0.0244	0.0065	0.0070	0.0004	0.0044	0.0406	94.10
A	262C	0.169	0.369	2.88	1.314	0.494	0.635	0.0067	0.0092	0.0050	0.0112	0.0043	0.0020	0.0917	0.0129	0.0067	0.0010	0.0065	0.0430	94.00
A	391A	0.164	0.369	2.99	1.280	0.452	0.634	0.0149	0.0082	0.0061	0.0115	0.0047	0.0030	0.0601	0.0084	0.0066	0.0000	0.0071	0.0412	93.90
A	391C	0.166	0.359	2.97	1.256	0.425	0.706	0.0146	0.0057	0.0066	0.0115	0.0044	0.0023	0.0576	0.0097	0.0055	0.0000	0.0063	0.0423	94.00
A	392A	0.166	0.346	2.91	1.239	0.399	0.691	0.0133	0.0061	0.0059	0.0106	0.0039	0.0022	0.0554	0.0105	0.0057	0.0000	0.0052	0.0428	94.20
A	392C	0.158	0.350	2.91	1.257	0.422	0.697	0.0120	0.0062	0.0061	0.0113	0.0041	0.0022	0.0581	0.0092	0.0062	0.0000	0.0007	0.0411	94.10
A	427A	0.172	0.373	2.86	1.320	0.483	0.643	0.0041	0.0061	0.0052	0.0108	0.0035	0.0016	0.0899	0.0107	0.0067	0.0002	0.0153	0.0393	94.00
A	427C	0.195	0.387	2.99	1.269	0.426	0.653	0.0204	0.0035	0.0064	0.0127	0.0053	0.0025	0.0246	0.0062	0.0064	0.0004	0.0074	0.0418	93.90

HT#	ID	C	SI	NI	CR	MO	MN	CO	W	V	NB	P	S	CU	AL	TI	CA	SN	ZR	FE
A	63A	0.181	0.389	2.92	1.339	0.405	0.688	0.0197	0.0066	0.0070	0.0130	0.0048	0.0027	0.0245	0.0072	0.0065	0.0006	0.0063	0.0415	94.10
A	63C	0.190	0.384	2.95	1.236	0.395	0.634	0.0196	0.0063	0.0065	0.0112	0.0046	0.0027	0.0239	0.0060	0.0064	0.0004	0.0000	0.0434	94.10
A	81A	0.187	0.388	2.97	1.324	0.414	0.653	0.0197	0.0068	0.0063	0.0113	0.0051	0.0024	0.0234	0.0073	0.0074	0.0005	0.0130	0.0400	94.00
A	81D	0.187	0.389	2.93	1.325	0.402	0.718	0.0199	0.0028	0.0069	0.0119	0.0045	0.0025	0.0237	0.0063	0.0065	0.0004	0.0142	0.0404	94.10
A	82A	0.183	0.386	2.93	1.318	0.406	0.678	0.0193	0.0061	0.0060	0.0118	0.0041	0.0022	0.0234	0.0079	0.0064	0.0006	0.0154	0.0429	94.10
A	82C	0.184	0.380	2.89	1.314	0.376	0.665	0.0197	0.0058	0.0067	0.0122	0.0035	0.0018	0.0231	0.0087	0.0063	0.0005	0.0062	0.0391	94.20
A	83A	0.184	0.391	2.99	1.341	0.404	0.631	0.0181	0.0017	0.0074	0.0122	0.0046	0.0016	0.0236	0.0044	0.0069	0.0002	0.0076	0.0359	94.00
A	83D	0.186	0.384	2.91	1.320	0.397	0.675	0.0202	0.0059	0.0060	0.0118	0.0049	0.0018	0.0228	0.0075	0.0070	0.0005	0.0071	0.0443	94.10
A	84B	0.180	0.391	2.98	1.336	0.406	0.670	0.0182	0.0019	0.0069	0.0119	0.0046	0.0021	0.0233	0.0051	0.0073	0.0002	0.0121	0.0341	94.00
A	84C	0.188	0.389	2.98	1.244	0.398	0.636	0.0191	0.0059	0.0062	0.0116	0.0045	0.0019	0.0240	0.0062	0.0073	0.0003	0.0046	0.0434	94.00
A	85A	0.186	0.398	3.01	1.283	0.430	0.648	0.0197	0.0068	0.0067	0.0124	0.0053	0.0022	0.0244	0.0061	0.0065	0.0003	0.0052	0.0432	93.90
A	85C	0.188	0.386	2.94	1.322	0.394	0.674	0.0200	0.0045	0.0064	0.0123	0.0034	0.0024	0.0235	0.0063	0.0064	0.0003	0.0059	0.0409	94.10
A	86A	0.183	0.386	3.00	1.336	0.412	0.636	0.0192	0.0055	0.0061	0.0120	0.0046	0.0022	0.0242	0.0048	0.0065	0.0003	0.0121	0.0422	94.00
A	86C	0.187	0.395	3.02	1.339	0.413	0.635	0.0183	0.0015	0.0070	0.0116	0.0048	0.0024	0.0240	0.0052	0.0066	0.0002	0.0137	0.0397	94.00

Appendix C: HT #A Computational Results

The following details the results of CALPHAD analysis to predict the stable phases at 316°C, 482°C, and 649°C.

SYSTEM				
MOLES	1			
MASS	55.31616	[g]		
TEMPERATURE	589.15	[K]		
TOTAL GIBBS ENERGY	-21165.3346	[J]		
ENTHALPY	6928.39389	[J]		
VOLUME	7.14E-06	[m3]		
COMPONENT	Mole Fraction	Mass Fraction	Activity	Potential
C	0.00944	0.00205	0.21662	-7492.69491
P	0.00009	0.00005	6.99E-18	-1.94E+05
S	0.00005	0.00003	4.82E-08	-82531.97341
SI	0.00808	0.0041	1.15E-14	-1.57E+05
V	0.00004	0.00004	4.20E-11	-1.17E+05
MN	0.00644	0.0064	0.00027	-40209.82205
MO	0.00242	0.0042	0.00001	-55531.62506
AL	0.00014	0.00007	2.39E-15	-1.65E+05
CR	0.01575	0.0148	0.00035	-38966.2051
NI	0.02969	0.0315	0.00131	-32508.46786
FE	0.92786	0.93676	0.0199	-19186.6745

	Moles	Mass	Volume Fraction
BCC_A2#1	0.94604	52.67681	0.95137
COMPOSITION			
COMPONENT	Mole Fraction	Mass Fraction	
FE	0.96414	0.96701	
NI	0.02447	0.02579	
SI	0.00804	0.00406	
MN	0.00258	0.00255	
CR	0.00047	0.00044	
AL	0.00015	0.00007	
P	0.00009	0.00005	
S	0.00005	0.00003	
MO	1.98E-06	3.42E-06	
V	1.64E-07	1.50E-07	
C	3.45E-08	7.45E-09	
	Moles	Mass	Volume Fraction
FCC_A1#1	0.0152	0.8523	0.01514
COMPOSITION			
COMPONENT	Mole Fraction	Mass Fraction	
FE	0.46135	0.45953	
NI	0.41232	0.4316	
MN	0.09461	0.09271	
SI	0.03067	0.01537	
CR	0.00068	0.00063	
AL	0.00032	0.00015	
P	0.00002	0.00001	
C	0.00002	4.94E-06	
MO	2.20E-06	3.77E-06	
V	6.75E-09	6.13E-09	
S	1.80E-11	1.03E-11	

	Moles	Mass	Volume Fraction
FCC_A1#2	0.00008	0.00269	0.00007
COMPOSITION			
COMPONENT	Mole Fraction	Mass Fraction	
V	0.40562	0.62547	
FE	0.10229	0.17292	
C	0.47371	0.17223	
CR	0.01768	0.02783	
MO	0.00032	0.00092	
MN	0.00038	0.00063	
NI	6.83E-08	1.21E-07	
S	2.61E-10	2.53E-10	
P	5.26E-13	4.93E-13	
SI	5.26E-13	4.47E-13	
AL	5.26E-13	4.30E-13	
	Moles	Mass	Volume Fraction
M23C6#1	0.02364	1.16957	0.02112
COMPOSITION			
COMPONENT	Mole Fraction	Mass Fraction	
CR	0.35316	0.37114	
FE	0.32233	0.36383	
MO	0.10059	0.19506	
C	0.2069	0.05023	
NI	0.01117	0.01325	
MN	0.00585	0.0065	
V	6.49E-07	6.68E-07	
AL	0	0	
SI	0	0	
S	0	0	
P	0	0	

	Moles	Mass	Volume Fraction
M7C3#1	0.01504	0.6148	0.0123

COMPOSITION		
COMPONENT	Mole Fraction	Mass Fraction
CR	0.46143	0.58686
MN	0.16131	0.21677
FE	0.07318	0.09997
C	0.3	0.08814
MO	0.00278	0.00653
NI	0.00062	0.00089
V	0.00068	0.00085
SI	7.00E-13	4.81E-13
AL	7.00E-13	4.62E-13
S	0	0
P	0	0

SYSTEM		
MOLES	1	
MASS	55.31616	[g]
TEMPERATURE	755.15	[K]
TOTAL GIBBS ENERGY	-29824.2	[J]
ENTHALPY	12839.76	[J]
VOLUME	7.20E-06	[m3]

COMPONENT	Mole Fraction	Mass Fraction	Activity	Potential
C	0.00944	0.00205	0.16489	-11317.4
P	0.00009	0.00005	1.87E-15	-2.13E+05
S	0.00005	0.00003	3.84E-08	-1.07E+05
SI	0.00808	0.0041	3.09E-12	-1.66E+05
V	0.00004	0.00004	8.95E-10	-1.31E+05
MN	0.00644	0.0064	0.00015	-55316.4
MO	0.00242	0.0042	0.00003	-65005.6
AL	0.00014	0.00007	3.43E-13	-1.80E+05
CR	0.01575	0.0148	0.00048	-48036.6
NI	0.02969	0.0315	0.00066	-45986.8
FE	0.92786	0.93676	0.01218	-27678.8

STABLE PHASES			
	Moles	Mass	Volume Fraction
BCC_A2#1	0.96055	53.48277	0.96609
COMPOSITION			
COMPONENT	Mole Fraction	Mass Fraction	
FE	0.95315	0.95602	
NI	0.03049	0.03213	
MN	0.00506	0.00499	
SI	0.00841	0.00424	
CR	0.00256	0.00239	
AL	0.00015	0.00007	
MO	0.00004	0.00007	
P	0.00009	0.00005	
S	0.00005	0.00003	
V	2.13E-06	1.95E-06	
C	4.59E-06	9.91E-07	
	Moles	Mass	Volume Fraction
M23C6#1	0.02576	1.26741	0.02278
COMPOSITION			
COMPONENT	Mole Fraction	Mass Fraction	
FE	0.3759	0.42663	
CR	0.30053	0.31756	
MO	0.08868	0.1729	
C	0.2069	0.0505	
NI	0.01506	0.01796	
MN	0.01293	0.01444	
V	4.45E-06	4.60E-06	
AL	0	0	
SI	0	0	
S	0	0	
P	0	0	

	Moles	Mass	Volume Fraction
M7C3#1	0.01369	0.56597	0.01113

COMPOSITION		
COMPONENT	Mole Fraction	Mass Fraction
CR	0.40521	0.50972
FE	0.1916	0.25886
MN	0.09153	0.12166
C	0.3	0.08717
MO	0.00731	0.01697
V	0.00301	0.00372
NI	0.00134	0.0019
SI	7.00E-13	4.76E-13
AL	7.00E-13	4.57E-13
S	0	0
P	0	0

SYSTEM		
MOLES	1	
MASS	55.31616	[g]
TEMPERATURE	922.15	[K]
TOTAL GIBBS ENERGY	-39979.03523	[J]
ENTHALPY	20296.48481	[J]
VOLUME	7.24E-06	[m3]

COMPONENT	Mole Fraction	Mass Fraction	Activity	Potential
C	0.00944	0.00205	0.1347	-15370.37819
P	0.00009	0.00005	5.29E-14	-2.34E+05
S	0.00005	0.00003	2.07E-08	-1.36E+05
SI	0.00808	0.0041	9.84E-11	-1.77E+05
V	0.00004	0.00004	4.86E-09	-1.47E+05
MN	0.00644	0.0064	0.00004	-77331.4757
MO	0.00242	0.0042	0.00006	-74271.21283
AL	0.00014	0.00007	7.81E-12	-1.96E+05
CR	0.01575	0.0148	0.00041	-59719.93021
NI	0.02969	0.0315	0.00025	-63593.92535
FE	0.92786	0.93676	0.00747	-37547.10912

STABLE PHASES			
	Moles	Mass	Volume Fraction
BCC_A2#1	0.87998	48.98217	0.88673
COMPOSITION			
COMPONENT	Mole Fraction	Mass Fraction	
FE	0.95482	0.95797	
NI	0.0255	0.02689	
CR	0.00623	0.00582	
MN	0.00447	0.00441	
SI	0.00821	0.00414	
MO	0.00033	0.00057	
AL	0.00016	0.00008	
P	0.0001	0.00005	
S	0.00006	0.00003	
C	0.00013	0.00003	
V	8.76E-06	8.01E-06	
	Moles	Mass	Volume Fraction
FCC_A1#1	0.08204	4.54117	0.08062
COMPOSITION			
COMPONENT	Mole Fraction	Mass Fraction	
FE	0.86365	0.8714	
NI	0.08349	0.08853	
MN	0.02363	0.02345	
CR	0.00927	0.0087	
SI	0.01034	0.00524	
C	0.00915	0.00199	
MO	0.00035	0.00061	
AL	0.00007	0.00003	
P	0.00005	0.00003	
S	6.83E-06	3.95E-06	
V	3.61E-06	3.32E-06	

	Moles	Mass	Volume Fraction
M23C6#1	0.03021	1.46653	0.02634
COMPOSITION			
COMPONENT	Mole Fraction	Mass Fraction	
FE	0.47583	0.54749	
CR	0.22829	0.24456	
MO	0.06515	0.12878	
C	0.2069	0.0512	
NI	0.01286	0.01555	
MN	0.01096	0.0124	
V	0.00002	0.00002	
AL	0	0	
SI	0	0	
S	0	0	
P	0	0	
	Moles	Mass	Volume Fraction
M7C3#1	0.00776	0.32629	0.0063
COMPOSITION			
COMPONENT	Mole Fraction	Mass Fraction	
CR	0.33575	0.4153	
FE	0.30975	0.41152	
C	0.3	0.08572	
MN	0.03153	0.04121	
MO	0.01693	0.03863	
V	0.00448	0.00543	
NI	0.00157	0.00219	
SI	1.97E-11	1.31E-11	
AL	6.06E-12	3.89E-12	
S	0	0	
P	0	0	

Appendix D: Carbide Image Analysis Routine

Routine 1 – Basic Detection Program:
0001 'Grain Boundary Removal'
0002 Set Process Frame to 0,0 2560x1920 pixels
Position : 0, 0 µm
Size : 12 x 9 µm
Display frame : don't change
Pause on run : no
[]
0003 Set Guard Frame to 0,0 2560x1920 pixels
Position : 0, 0 µm
Size : 12 x 9 µm
0004 Clear => All
0005 Smooth x3
0006 Contrast Thresholding -> BPL1
Contrast : Very High
Sensitivity : 59 %
Fill objects : Yes
0007 Contrast Thresholding -> BPL2
Contrast : High
Sensitivity : 79 %
Fill objects : Yes
0008 Contrast Thresholding -> BPL3
Contrast : Normal
Sensitivity : 46 %
Fill objects : Yes
0009 Relative Gray Threshold
BPL4 : C1 = [1.178, 3.127] C2 = [0, 0]
Background : Bright
Reference : Mean
Method : (C1 x Mean) + C2
[]
0010 Relative Gray Threshold
BPL5 : C1 = [1.178, 3.153] C2 = [0, 0]
Background : Bright
Reference : Mean
Method : (C1 x Mean) + C2
[]
0011 Object Transfer BPL5 -> BPL6
Length greater than 0.27µm
0012 Border Transfer BPL6 (All) -> BPL7
0013 Combine (BPL6, BPL7) -> BPL8
0014 Combine (BPL1, BPL2, BPL3) -> BPL9

0015 (BPL4 XOR BPL8) -> BPL10
0016 ' Grain Boundary Carbide Finder’
0017 Combine (BPL9, BPL10) -> BPL11
0018 Copy BPL8 -> BPL14
0019 Dilate CIRC x1 => BPL14
0020 (BPL8 XOR BPL14) -> BPL14
0021 Convex Hull CIRC x1 => BPL14
0022 Convex Hull CIRC x1 => BPL14
0023 Propagate 2 Levels => BPL14
0024 Convex Hull CIRC x1 => BPL14
0025 Invert BPL14 -> BPL15
0026 Opening CIRC x2 => BPL15 Extend
0027 Copy BPL15 -> BPL16
0028 Opening CIRC x7 => BPL16 Extend
0029 (BPL15 AND BPL16) -> BPL14
0030 (BPL11 OR BPL14) -> BPL11
0031 ' Carbide Refining’
0032 Bridge Removal => BPL11
Bridge thickness : 10 µm
Contour roughness : 2
Computation method : slow but accurate
0033 Bridge Removal => BPL11
Bridge thickness : Infinite
Contour roughness : 10
0034 Copy BPL9 -> BPL12
0035 Dilate CIRC x2 => BPL9
0036 (BPL9 XOR BPL12) -> BPL13
0037 Convex Hull CIRC x2 => BPL13
0038 Separate Manually BPL11
Marking plane : BPL13
Editing tool : Line
Clear marking bitplane on entry : False
Outline thickness : 2
Message :
0039 ' Total Volume Fraction of Carbides
0040 Set Process Frame to 0,0 2560x1790 pixels
Position : 0, 0 µm
Size : 12 x 9 µm
Display frame : don't change
Pause on run : no
[]
0041 Set Guard Frame to 0,0 2560x1790 pixels
Position : 0, 0 µm
Size : 12 x 9 µm
0042 Field Measures (BPL11) -> FLDM1
Area Percent

0043 ' Histograms ‘
0044 Object Measures (BPL11) -> OBJM4
Length
Circular Diameter
Spherical Diameter
0045 Object Measures (BPL11) -> OBJM2
Aspect Ratio
Area
Spherical Area

References:

[1] J. P. Hirth, "Effects of hydrogen on the properties of iron and steel," *Metallurgical Transactions A*, vol. 11, no. 6, pp. 861–890, Jun. 1980.

[2] C. D. Beachem, "A new model for hydrogen-assisted cracking (hydrogen 'embrittlement')," *Metallurgical and Materials Transactions B*, vol. 3, no. 2, pp. 441–455, Feb. 1972.

[3] H. K. Birnbaum and P. Sofronis, "Hydrogen-enhanced localized plasticity—a mechanism for hydrogen-related fracture," *Materials Science and Engineering: A*, vol. 176, no. 1, pp. 191–202, Mar. 1994.

[4] S.-K. Kim, C.-S. Lee, M.-H. Kim, and J.-M. Lee, "Numerical Analysis of Hydrogen Transport using a Hydrogen-Enhanced Localized Plasticity Mechanism," p. 4, 2012.

[5] I. M. Robertson, H. K. Birnbaum, and P. Sofronis, "Chapter 91 Hydrogen Effects on Plasticity," in *Dislocations in Solids*, vol. 15, J. P. Hirth and L. Kubin, Eds. Elsevier, 2009, pp. 249–293.

[6] T. Tabata and H. K. Birnbaum, "DIRECT OBSERVATIONS OF HYDROGEN ENHANCED CRACK PROPAGATION IN IRON," in *Perspectives in Hydrogen in Metals*, M. F. ASHBY and J. P. HIRTH, Eds. Pergamon, 1986, pp. 723–728.

[7] H. K. Birnbaum, "Hydrogen Embrittlement," in *Encyclopedia of Materials: Science and Technology*, K. H. J. Buschow, R. W. Cahn, M. C. Flemings, B. Ilschner, E. J. Kramer, S. Mahajan, and P. Veyssière, Eds. Oxford: Elsevier, 2001, pp. 3887–3889.

[8] C. J. McMahon, "Hydrogen-induced intergranular fracture of steels," *Engineering Fracture Mechanics*, vol. 68, no. 6, pp. 773–788, Apr. 2001.

[9] S. Wang, M. L. Martin, P. Sofronis, S. Ohnuki, N. Hashimoto, and I. M. Robertson, "Hydrogen-induced intergranular failure of iron," *Acta Materialia*, vol. 69, pp. 275–282, May 2014.

[10] A. R. Troiano, "The Role of Hydrogen and Other Interstitials in the Mechanical Behavior of Metals: (1959 Edward De Mille Campbell Memorial Lecture)," *Metallography, Microstructure, and Analysis*, vol. 5, no. 6, pp. 557–569, Dec. 2016.

[11] A. Nagao, M. Dadfarnia, B. P. Somerday, P. Sofronis, and R. O. Ritchie, "Hydrogen-enhanced-plasticity mediated decohesion for hydrogen-induced intergranular and 'quasi-cleavage' fracture of lath martensitic steels," *Journal of the Mechanics and Physics of Solids*, vol. 112, pp. 403–430, Mar. 2018.

[12] A. Nagao, C. D. Smith, M. Dadfarnia, P. Sofronis, and I. M. Robertson, "The role of hydrogen in hydrogen embrittlement fracture of lath martensitic steel," *Acta Materialia*, vol. 60, no. 13, pp. 5182–5189, Aug. 2012.

[13] C. Zapffe and C. Sims, "Hydrogen Embrittlement, Internal Stress and Defects in Steel," *Transactions, American Institute of Mining and Metallurgical Engineers*, vol. 145, pp. 225–259, 1941.

[14] D. G. Westlake, "Hydrides of intermetallic compounds: A review of stabilities, stoichiometries and preferred hydrogen sites," *Journal of the Less Common Metals*, vol. 91, no. 1, pp. 1–20, May 1983.

[15] I. M. Robertson, "The effect of hydrogen on dislocation dynamics q,qq," *Engineering Fracture Mechanics*, p. 22, 2001.

[16] D. S. Shih, I. M. Robertson, and H. K. Birnbaum, "Hydrogen embrittlement of α titanium: In situ tem studies," *Acta Metallurgica*, vol. 36, no. 1, pp. 111–124, Jan. 1988.

[17] J. Lufrano, P. Sofronis, and H. K. Birnbaum, “Elastoplastically accommodated hydride formation and embrittlement,” *Journal of the Mechanics and Physics of Solids*, vol. 46, no. 9, pp. 1497–1520, Sep. 1998.
[18] J. Lufrano, P. Sofronis, and H. K. Birnbaum, “Modeling of hydrogen transport and elastically accommodated hydride formation near a crack tip,” *Journal of the Mechanics and Physics of Solids*, vol. 44, no. 2, pp. 179–205, Feb. 1996.
[19] P. J. Ferreira, I. M. Robertson, and H. K. Birnbaum, “Hydrogen effects on the interaction between dislocations,” *Acta Materialia*, vol. 46, no. 5, pp. 1749–1757, Mar. 1998.
[20] P. Sofronis, Y. Liang, and N. Aravas, “Hydrogen induced shear localization of the plastic flow in metals and alloys,” *European Journal of Mechanics - A/Solids*, vol. 20, no. 6, pp. 857–872, Nov. 2001.
[21] J. LUFRANO and P. SOFRONIS, “ENHANCED HYDROGEN CONCENTRATIONS AHEAD OF ROUNDED NOTCHES AND CRACKSÐCOMPETITION BETWEEN PLASTIC STRAIN AND HYDROSTATIC STRESS,” p. 8.
[22] M. V. RODRIGUEZ and P. J. FICALORA, “The Mechanism of a Hydrogen-Dislocation Interaction in B.C.C. Metals: Embrittlement and Dislocation Motion,” p. 10.
[23] W. A. Counts, C. Wolverton, and R. Gibala, “First-principles energetics of hydrogen traps in α-Fe: Point defects,” *Acta Materialia*, vol. 58, no. 14, pp. 4730–4741, Aug. 2010.
[24] A. Oudriss *et al.*, “Grain size and grain-boundary effects on diffusion and trapping of hydrogen in pure nickel,” *Acta Materialia*, vol. 60, no. 19, pp. 6814–6828, Nov. 2012.
[25] Y. Tang and J. A. El-Awady, “Atomistic simulations of the interactions of hydrogen with dislocations in fcc metals,” *Physical Review B*, vol. 86, no. 17, Nov. 2012.
[26] S. Taketomi, R. Matsumoto, and N. Miyazaki, “Atomistic simulation of the effects of hydrogen on the mobility of edge dislocation in alpha iron,” *Journal of Materials Science*, vol. 43, no. 3, pp. 1166–1169, Feb. 2008.
[27] A. Barnoush, M. Asgari, and R. Johnsen, “Resolving the hydrogen effect on dislocation nucleation and mobility by electrochemical nanoindentation,” *Scripta Materialia*, vol. 66, no. 6, pp. 414–417, Mar. 2012.
[28] Y. Jagodzinski, H. Hänninen, O. Tarasenko, and S. Smuk, “Interaction of hydrogen with dislocation pile-ups and hydrogen induced softening of pure iron,” *Scripta Materialia*, vol. 43, no. 3, pp. 245–251, Jul. 2000.
[29] I. M. Robertson and H. K. Birnbaum, “DISLOCATION MOBILITY AND HYDROGEN – A BRIEF REVIEW,” p. 6.
[30] J. Ćwiek and J. Michalska-Ćwiek, “Evaluation of hydrogen degradation of high-strength weldable steels,” *Journal of Achievements in Materials and Manufacturing Engineering*, vol. 42, p. 8, 2010.
[31] A. Begi, “THE INFLUENCE OF MICROSTRUCTURE ON HYDROGEN DIFFUSION IN DUAL PHASE STEEL,” *Acta Metallurgica Slovaca*, vol. 17, no. 2, p. 9, 2011.
[32] H. K. Birnbaum, “Mechanisms of Hydrogen Related Fracture of Metals:,” Defense Technical Information Center, Fort Belvoir, VA, May 1989.

[33] Y. Katz, N. Tymiak, and W. W. Gerberich, “The dynamic nature of hydrogen assisting crack extension,” *Journal of Achievements in Materials and Manufacturing Engineering*, vol. 18, no. 1, p. 4, 2006.
[34] P. Sofronis and R. M. McMeeking, “Numerical analysis of hydrogen transport near a blunting crack tip,” *Journal of the Mechanics and Physics of Solids*, vol. 37, no. 3, pp. 317–350, Jan. 1989.
[35] I. Y. Telitchev and O. Vinogradov, “Numerical tensile tests of BCC iron crystal with various amounts of hydrogen near the crack tip,” *Computational Materials Science*, vol. 36, no. 3, pp. 272–280, Jun. 2006.
[36] A. Barnoush and H. Vehoff, “Recent developments in the study of hydrogen embrittlement: Hydrogen effect on dislocation nucleation,” *Acta Materialia*, vol. 58, no. 16, pp. 5274–5285, Sep. 2010.
[37] C. V. Di Leo and L. Anand, “Hydrogen in metals: A coupled theory for species diffusion and large elastic–plastic deformations,” *International Journal of Plasticity*, vol. 43, pp. 42–69, Apr. 2013.
[38] S. Wang, K. Takahashi, N. Hashimoto, S. Isobe, and S. Ohnuki, “Strain field of interstitial hydrogen atom in body-centered cubic iron and its effect on hydrogen–dislocation interaction,” *Scripta Materialia*, vol. 68, no. 5, pp. 249–252, Mar. 2013.
[39] P. Sofronis, Y. Liang, and N. Aravas, “Hydrogen induced shear localization of the plastic flow in metals and alloys,” *European Journal of Mechanics - A/Solids*, vol. 20, no. 6, pp. 857–872, Nov. 2001.
[40] Y. Liang, P. Sofronis, and N. Aravas, “On the effect of hydrogen on plastic instabilities in metals,” *Acta Materialia*, vol. 51, no. 9, pp. 2717–2730, May 2003.
[41] M. C. Draper, “Control of Monatomic Hydrogen in High Strength Steel Castings,” in *Steel Founders Society of America T&O Proceedings*, 2013, p. 17.
[42] I. Maroef, D. L. Olson, M. Eberhart, and G. R. Edwards, “Hydrogen trapping in ferritic steel weld metal,” *International Materials Reviews*, vol. 47, no. 4, pp. 191–223, Aug. 2002.
[43] S. Frappart, X. Feaugas, J. Creus, F. Thebault, L. Delattre, and H. Marchebois, “Hydrogen solubility, diffusivity and trapping in a tempered Fe–C–Cr martensitic steel under various mechanical stress states,” *Materials Science and Engineering: A*, vol. 534, pp. 384–393, Feb. 2012.
[44] NAVSEA, “BASE MATERIALS FOR CRITICAL APPLICATIONS: REQUIREMENTS FOR LOW ALLOY STEEL PLATE, FORGINGS, CASTINGS, SHAPES, BARS, AND HEADS OF HY-80/100/130 AND HSLA-80/100.” COMMANDER, NAVAL SEA SYSTEMS COMMAND, 18-Dec-2012.
[45] H. Dong, G. Li, B. Tipton, P. Konkol, Y. Pang, and J. J. Valencia, “Enhanced Processing for High Strength Steel Castings and Forgings for Naval Components: Optimum Thermal Soaking Treatment for Hydrogen Removal.” National Center for Excellence in Metalworking Technology, 24-Mar-1999.
[46] A. McNabb and Foster, P., “A New Analysis of the Diffusion of Hydrogen in Iron and Ferritic Steels,” *The American Institute of Mining, Metallurgical, and Petroleum Engineers*, p. 10, 1963.
[47] A. Turnbull, “4 - Hydrogen diffusion and trapping in metals,” in *Gaseous Hydrogen Embrittlement of Materials in Energy Technologies*, vol. 1, R. P. Gangloff and B. P. Somerday, Eds. Woodhead Publishing, 2012, pp. 89–128.

[48] J. Toribio and V. Kharin, “A generalised model of hydrogen diffusion in metals with multiple trap types,” *Philosophical Magazine*, vol. 95, no. 31, pp. 3429–3451, Nov. 2015.
[49] R. Kirchheim and A. Pundt, “25 - Hydrogen in Metals,” in *Physical Metallurgy (Fifth Edition)*, D. E. Laughlin and K. Hono, Eds. Oxford: Elsevier, 2014, pp. 2597–2705.
[50] A. V. Gapontsev and V. V. Kondrat’ev, “Hydrogen diffusion in disordered metals and alloys,” *Physics-Uspekhi*, vol. 46, no. 10, pp. 1077–1098, Oct. 2003.
[51] R. C. Brouwer, E. Salomons, and R. Griessen, “Diffusion of hydrogen in alloys,” *Phys. Rev. B*, vol. 38, no. 15, pp. 10217–10226, Nov. 1988.
[52] A. Biscarini, B. Coluzzi, and F. M. Mazzolai, “Application of statistical mechanics to solid solutions of interstitial impurities in binary alloys,” *Acta Materialia*, vol. 47, no. 12, pp. 3447–3455, Sep. 1999.
[53] T. Xu, L. Zheng, K. Wang, and R. D. K. Misra, “Unified mechanism of intergranular embrittlement based on non-equilibrium grain boundary segregation,” *International Materials Reviews*, vol. 58, no. 5, pp. 263–295, Jun. 2013.
[54] R. M. Horn and R. O. Ritchie, “Mechanisms of tempered martensite embrittlement in low alloy steels,” *Metallurgical Transactions A*, vol. 9, no. 8, pp. 1039–1053, Aug. 1978.
[55] R. Pilkington *et al.*, “Trace element embrittlement in a 2.25%Cr-1%Mo steel,” *Materials Science and Engineering: A*, vol. 212, no. 2, pp. 191–205, Jul. 1996.
[56] M. M. Fetisova and I. Pleshakov, “Mechanism underlying the reduction in the strength of an intergranular bond during the development of reversible temper embrittlement in steels,” *Soviet Materials Science*, vol. 11, no. 3, pp. 309–311, 1976.
[57] Z. QU and C. J. McMAHON, “The effects of tempering reactions on temper embrittlement of alloy steels,” p. 8.
[58] A. Joshi, “Segregation at selective grain boundaries and its role in temper embrittlement of low alloy steels,” *Scripta Metallurgica*, vol. 9, no. 3, pp. 251–260, Mar. 1975.
[59] N. Bandyopadhyay and C. J. McMahon, “The micro-mechanisms of tempered martensite embrittlement in 4340-type steels,” *Metallurgical Transactions A*, vol. 14, no. 7, pp. 1313–1325, Jul. 1983.
[60] S. Shenhua and X. Tingdong, “Combined equilibrium and non-equilibrium segregation mechanism of temper embrittlement,” *Journal of Materials Science*, vol. 29, no. 1, pp. 61–66, 1994.
[61] R. G. Faulkner, “Combined grain boundary equilibrium and non-equilibrium segregation in ferritic/martensitic steels,” *Acta Metallurgica*, vol. 35, no. 12, pp. 2905–2914, Dec. 1987.
[62] M. A. V. Chapman and R. G. Faulkner, “Computer modelling of grain boundary segregation,” *Acta Metallurgica*, vol. 31, no. 5, pp. 677–689, May 1983.
[63] R. G. Faulkner, “Segregation to Boundaries,” in *Encyclopedia of Materials: Science and Technology*, K. H. J. Buschow, R. W. Cahn, M. C. Flemings, B. Ilschner, E. J. Kramer, S. Mahajan, and P. Veyssière, Eds. Oxford: Elsevier, 2001, pp. 8290–8294.

[64] R. Wu, D. Wang, and A. J. Freeman, “First principles investigations of MCD spectra and sum rules for 3d transition metal surfaces,” *Journal of Magnetism and Magnetic Materials*, vol. 132, no. 1, pp. 103–123, Apr. 1994.
[65] R. Wu and A. J. Freeman, “Magnetism at metal-ceramic interfaces: effects of a Au overlayer on the magnetic properties of Fe/MgO(001),” *Journal of Magnetism and Magnetic Materials*, vol. 137, no. 1, pp. 127–133, Oct. 1994.
[66] J. R. Rice and J.-S. Wang, “Embrittlement of interfaces by solute segregation,” *Materials Science and Engineering: A*, vol. 107, pp. 23–40, Jan. 1989.
[67] M. Yamaguchi, “First-Principles Study on the Grain Boundary Embrittlement of Metals by Solute Segregation: Part I. Iron (Fe)-Solute (B, C, P, and S) Systems,” *Metallurgical and Materials Transactions A*, vol. 42, no. 2, pp. 319–329, Feb. 2011.
[68] M. . Jokl, V. Vitek, and C. . McMahon, “A microscopic theory of brittle fracture in deformable solids: A relation between ideal work to fracture and plastic work,” *Acta Metallurgica*, vol. 28, no. 11, pp. 1479–1488, Nov. 1980.
[69] M. Guttmann, “Temper embrittlement and ternary equilibrium segregation,” *Materials Science and Engineering*, vol. 42, pp. 227–232, Jan. 1980.
[70] M. Guttmann, “The Role of Residuals and Alloying Elements in Temper Embrittlement.”
[71] R. Viswanathan and A. Joshi, “Effect of microstructure on the temper embrittlement of Cr-Mo-V steels,” *Metallurgical Transactions A*, vol. 6, no. 12, Dec. 1975.
[72] M. Draper, E. Rozzero, and K. Rackers, “Unpublished Work - Temper Embrittlement of Forged HY-80.” 2018.
[73] Bureau Of Ships Washington Dc, “BUREAU OF SHIPS CONFERENCE. HY-80 STEEL FABRICATION IN SUBMARINE CONSTRUCTION, AT BUREAU OF SHIPS 21-22 MARCH 1960:,” Defense Technical Information Center, Fort Belvoir, VA, Dec. 1960.
[74] S. D. Funni, M. G. Koul, and A. L. Moran, “Evaluation of properties and microstructure as a function of tempering time at intercritical temperatures in HY-80 steel castings,” *Engineering Failure Analysis*, vol. 14, no. 5, pp. 753–764, Jul. 2007.
[75] P. Yayla, E. Kaluc, and K. Ural, “Effects of welding processes on the mechanical properties of HY 80 steel weldments,” *Materials & Design*, vol. 28, no. 6, pp. 1898–1906, Jan. 2007.
[76] J. E. Holthaus, M. G. Koul, and A. L. Moran, “Property and microstructure evaluation as a function of processing parameters: Large HY-80 steel casting for a US Navy submarine,” *Engineering Failure Analysis*, vol. 13, no. 8, pp. 1397–1409, Dec. 2006.
[77] M. Salive, “Effects of Microstructure, Composition, and Strength on the NIL Ductility Transition (NDT) Temperature of HY-80 Steel,” *Naval Ship Research and Development Center*, Jan. 1972.
[78] A. R. Willner and M. L. Salive, “The effects of autenitizing and tempering on the mechanical properties of fully quenched HY-80 steels,” *Naval Ship Research and Development Center*, Dec. 1961.
[79] A. R. Willner and M. L. Salive, “Evalutation of commercially produced HY-80 Steel,” *Naval Ship Research and Development Center*, Jul. 1964.

[80] M. L. Salive and A. R. Willner, “COMPARISON OF STANDARD AND SUBSIZE HY-80 DROPWEIGHT SPECIMENS FOR VARIOUS CONDITIONS OF HEAT TREATMENT,” p. 18.
[81] A. R. Willner and M. L. Salive, “EFFECTS OF TEMPERING ABOVE THE LOWER CRITICAL TEMPERATURE A SUB C1 ON THE PROPERTIES OF AN HY-80 STEEL:,” Defense Technical Information Center, Fort Belvoir, VA, Jan. 1966.
[82] A. R. Willner and M. L. Salive, “The effects of tempered nonmartensitic products on the notch toughness and mechanical properties of an HY-80 steel,” *Naval Ship Research and Development Center*, Mar. 1965.
[83] Y. Xu *et al.*, “Study on the nucleation and growth of M23C6 carbides in a 10% Cr martensite ferritic steel after long-term aging,” *Materials Characterization*, vol. 111, pp. 122–127, Jan. 2016.
[84] N. I. Medvedeva, D. C. Van Aken, and J. E. Medvedeva, “Stability of binary and ternary M23C6 carbides from first principles,” *Computational Materials Science*, vol. 96, pp. 159–164, Jan. 2015.
[85] L. Dong, Z. Ding, B. Liang, and Z. Xu, “Structural characterization of M $_7$ C $_3$ -type carbide precipitated in the aging treated 100Mn13 steel,” *Phase Transitions*, vol. 88, no. 11, pp. 1054–1061, Nov. 2015.
[86] C. M. Garzón, A. R. Franco Jr., and A. P. Tschiptschin, “Thermodynamic Analysis of M_7C_3 Carbide Dissolution during Plasma Nitriding of an AISI D2 Tool Steel,” *ISIJ International*, vol. 57, no. 4, pp. 737–745, 2017.
[87] D. H. Jack and K. H. Jack, “Invited review: Carbides and nitrides in steel,” *Materials Science and Engineering*, vol. 11, no. 1, pp. 1–27, Jan. 1973.
[88] P. Phetlam and V. Uthaisangsuk, “Microstructure based flow stress modeling for quenched and tempered low alloy steel,” *Materials & Design*, vol. 82, pp. 189–199, Oct. 2015.
[89] N. Bandyopadhyay, C. L. Briant, and E. L. Hall, “Carbide precipitation, grain boundary segregation, and temper embrittlement in NiCrMoV rotor steels,” *Metallurgical Transactions A*, vol. 16, no. 5, pp. 721–737, May 1985.
[90] A. Salemi and A. Abdollah-zadeh, “The effect of tempering temperature on the mechanical properties and fracture morphology of a NiCrMoV steel,” *Materials Characterization*, vol. 59, no. 4, pp. 484–487, Apr. 2008.
[91] Y. Tanaka, T. Azuma, and N. Yaegashi, “Isothermal aging test results (up to 100 000 h) of NiCrMoV steels for low-pressure steam turbine,” *International Journal of Pressure Vessels and Piping*, vol. 59, no. 1, pp. 71–81, Jan. 1994.
[92] K. Wieczerzak, P. Bala, M. Stepien, G. Cios, and T. Koziel, “Formation of eutectic carbides in Fe–Cr–Mo–C alloy during non-equilibrium crystallization,” *Materials & Design*, vol. 94, pp. 61–68, Mar. 2016.
[93] S. Dépinoy *et al.*, “Carbide Precipitation in 2.25 Cr-1 Mo Bainitic Steel: Effect of Heating and Isothermal Tempering Conditions,” *Metallurgical and Materials Transactions A*, vol. 48, no. 5, pp. 2164–2178, May 2017.
[94] V. A. Korablev, Y. I. Ustinovshchikov, and I. G. Khatskelevich, “Embrittlement of chromium steels on formation of special carbides,” *Metal Science and Heat Treatment*, vol. 17, no. 1, pp. 15–18, Jan. 1975.

[95] N. A. Giang, M. Kuna, and G. Hütter, “Influence of carbide particles on crack initiation and propagation with competing ductile-brittle transition in ferritic steel,” *Theoretical and Applied Fracture Mechanics*, vol. 92, pp. 89–98, Dec. 2017.
[96] J. Guan, L. Wang, Z. Zhang, X. Shi, and X. Ma, “Fatigue crack nucleation and propagation at clustered metallic carbides in M50 bearing steel,” *Tribology International*, vol. 119, pp. 165–174, Mar. 2018.
[97] A. D. Erak, E. A. Kuleshova, A. S. Kiselev, A. S. Kiselev, and A. P. Bandura, “Correlation of local parameters of brittle crack initiation and propagation with the fracture toughness of VVER-1000 pressure vessel steels,” *Engineering Fracture Mechanics*, vol. 202, pp. 162–173, Oct. 2018.
[98] L. Lundin and B. Richarz, “Atom-probe study of phosphorus segregation to the carbide / matrix interface in an aged 9% chromium steel,” *Applied Surface Science*, vol. 87–88, pp. 194–199, Mar. 1995.
[99] C. Zener, “Theory of Growth of Spherical Precipitates from Solid Solution,” *Journal of Applied Physics*, vol. 20, no. 10, pp. 950–953, Oct. 1949.
[100] R. Wagner and R. Kampmann, “Homogeneous Second Phase Precipitation,” *Phase Transformations in Materials*, vol. 4, pp. 213–303, 1991.
[101] I. M. Lifshitz and V. V. Slyozov, “The kinetics of precipitation from supersaturated solid solutions,” *Journal of Physics and Chemistry of Solids*, vol. 19, no. 1, pp. 35–50, Apr. 1961.
[102] M. Zuo, G. Renman, J. P. Gustafsson, and W. Klysubun, “Phosphorus removal by slag depends on its mineralogical composition: A comparative study of AOD and EAF slags,” *Journal of Water Process Engineering*, vol. 25, pp. 105–112, Oct. 2018.
[103] Steel Founders Society of America, *Steel Castings Handbook, 6th Edition*. ASM International, 1995.
[104] Z. Stokowiec, R. McLellan, and D. Gray, “The Uses of Argon And Nitrogen in the Argon-Oxygen Decarburisation Process, Stirring, Purging and in Casting Pit Practice.” Wiggin Alloys Ltd.
[105] R. Aucott, D. Gray, and C. Holland, “The Theory and practice of the Argon /Oxygen Decarburizing Process,” vol. 79, 1971.
[106] U. R. Kattner, “The thermodynamic modeling of multicomponent phase equilibria,” *JOM*, vol. 49, no. 12, pp. 14–19, Dec. 1997.
[107] Z.-K. Liu, “First-Principles Calculations and CALPHAD Modeling of Thermodynamics,” *Journal of Phase Equilibria and Diffusion*, vol. 30, no. 5, pp. 517–534, Oct. 2009.
[108] E. Kozeschnik, “2 - Thermodynamic Basis of Phase Transformations,” in *Computational Materials Engineering*, K. G. F. JANSSENS, D. RAABE, E. KOZESCHNIK, M. A. MIODOWNIK, and B. NESTLER, Eds. Burlington: Academic Press, 2007, pp. 7–46.
[109] M. Hillert, “Phase Equilibria, Phase Diagrams and Phase Transformations: Their Thermodynamic Basis, Second Edition,” p. 526.
[110] B. Tipton *et al.*, “Enhanced Processing for High Strength Steel Castings and Forgings for Naval Components: Enhanced Tools to Predict Residual Stresses and Hydrogen Distribution: TR No. 99-83.” National Center for Excellence in Metalworking Technology, 06-Dec-1999.

[111] M. Guttmann, P. Dumoulin, and M. Wayman, “The thermodynamics of interactive co-segregation of phosphorus and alloying elements in iron and temper-brittle steels,” *Metallurgical Transactions A*, vol. 13, no. 10, pp. 1693–1711, Oct. 1982.
[112] S. Ankem, “ENMA 661: Kinetics of Reactions in Materials,” University of Maryland, 2015.
[113] G. Grewal and S. Ankem, “Isothermal particle growth in two-phase titanium alloys,” *Metallurgical Transactions A*, vol. 20, no. 1, pp. 39–54, Jan. 1989.
[114] G. GREWAL and S. Ankem, “Particle Coarsening Behavior of alpha-beta Titanium Alloys,” *METALLURGICAL TRANSACTIONS A*, vol. 21A, pp. 1645–1654, Jun. 1990.
[115] H. M. Chung and O. K. Chopra, “ACCELERATED AGING EMBRITTLEMENT OF CAST DUPLEX STAINLESS STEEL - ACTIVATION ENERGY FOR EXTRAPOLATION,” p. 35.
[116] Z. B. Wang, N. R. Tao, W. P. Tong, J. Lu, and K. Lu, “Diffusion of Cr in Nanostructured Fe and Low Carbon Steel Produced by means of Surface Mechanical Attrition Treatment,” *Diffusion in Solids*, vol. 249, p. 8.
[117] Brandes and Brook, *Smithells Metals Reference Book, 7th Edition*. Oxford: Butterworth-Heinemann, 1992.
[118] A. S. Sozykina, K. Y. Okishev, A. G. Grebenshchikova, and D. A. Mirzaev, “Kinetic Description of $(Cr, Fe)_7C_3$ Carbide Dissolution in Austenite of High-Carbon Fe-Cr-C Ternary Alloys,” *Materials Science Forum*, vol. 870, pp. 409–415, Sep. 2016.
[119] C. Zener, “Kinetics of the decomposition of austenite,” *Trans. AIME*, vol. 167, pp. 550–583, 1946.
[120] M. Hillert, “Solid state phase transformations,” *Jernkontoret Annaler*, vol. 141, pp. 757–790, 1957.
[121] C. Wert and C. Zener, “Interference of growing spherical precipitate particles,” *J. Appl. Phys.*, vol. 21, pp. 5–8, 1950.
[122] J. Bratberg, J. Ågren, and K. Frisk, “Diffusion simulations of MC and M_7C_3 carbide coarsening in bcc and fcc matrix utilising new thermodynamic and kinetic description,” *Materials Science and Technology*, vol. 24, no. 6, pp. 695–704, Jun. 2008.
[123] M. I. Isik *et al.*, “The nucleation of Mo-rich Laves phase particles adjacent to M23C6 micrograin boundary carbides in 12% Cr tempered martensite ferritic steels,” *Acta Materialia*, vol. 90, pp. 94–104, May 2015.
[124] D. Jain, D. Isheim, A. H. Hunter, and D. N. Seidman, “Multicomponent High-Strength Low-Alloy Steel Precipitation-Strengthened by Sub-nanometric Cu Precipitates and M2C Carbides,” *Metallurgical and Materials Transactions A*, vol. 47, no. 8, pp. 3860–3872, Aug. 2016.